TECHNISCHE UNIVERSITÄT MÜNCHEN

Lehrstuhl für Werkzeugmaschinen und Fertigungstechnik am
Institut für Werkzeugmaschinen und Betriebswissenschaften (*iwb*)

Managing Form Deviation in Laser Beam Melting by Pre-Deformation

Fabian Alexander Bayerlein

Vollständiger Abdruck der von der Fakultät für Maschinenwesen der Technischen Universität München zur Erlangung des akademischen Grades eines

Doktor-Ingenieurs (Dr.-Ing.)

genehmigten Dissertation.

Vorsitzende: Prof. Dr.-Ing. Katrin Wudy

Prüfer der Dissertation: 1. Prof. Dr.-Ing. Michael F. Zäh
                           2. Prof. Dr.-Ing. Alexander Kaplan

Die Dissertation wurde am 19.02.2020 bei der Technischen Universität München eingereicht und durch die Fakultät für Maschinenwesen am 24.07.2020 angenommen.

Contents

Contents

Contents

Abstract

With the high temperature gradients occurring during the laser beam melting manufacturing process, workpieces are prone to exhibit form deviations that hinder their production. It was investigated whether the application of a simulation-based pre-deformation methodology is able to reduce these deviations to an acceptable magnitude and how much confidence can be placed in these predictions. A comparison with experimentally determined form deviations suggests that the finite-element-based approach for the prediction of form deviations is suitable for industrially relevant workpieces. The assessed level of predictive capability of the model indicates a wide range of applicability. Additionally, an iterative method for pre-deformation enables an automated way towards first-time-right design. This methodology will contribute to the manageability of form deviations in laser beam melting.

Kurzfassung

Aufgrund der hohen Temperaturgradienten, die während des Laserstrahlschmelzens auftreten, neigen die damit gefertigten Werkstücke zu Formabweichungen, welche ihre Produktion erschweren. Es wurde untersucht, ob eine simulationsbasierte Vordeformation diese Abweichungen auf ein akzeptables Maß reduzieren kann und wie viel Vertrauen in die Vorhersagen des Simulationsmodells gesetzt werden kann. Der Vergleich mit experimentell ermittelten Formabweichungen legt nahe, dass der Ansatz zur Vorhersage von Formabweichungen industriell relevanter Werkstücke geeignet ist. Durch Methoden der Unsicherheitsbewertung und Sensitivitätsanalyse wurde die Vorhersagefähigkeit des Modells bewertet. Das entwickelte iterative Verfahren zur Vordeformation liefert automatisiert eine modifizierte Eingangsgeometrie mit möglichst geringen Abweichungen von der Zielgeometrie. Die vorliegende Arbeit leistet damit einen wesentlichen Beitrag zur Beherrschbarkeit von Formabweichungen beim Laserstrahlschmelzen.

Acknowledgment

Abbreviations

AM	additive manufacturing
AMP	additive manufacturing process
ANOVA	analysis of variance
CAD	computer-aided design
CAE	computer-aided engineering
CDF	cumulative probability density function
CDPM	cool-down phase model
CLI	common layer interface
DE	distortion engineering
DOF	degree of freedom
EDF	empirical probability density function
EDM	electric discharge machining
EOS	EOS GmbH
FE	finite element
FEM	finite element method
FTR	first-time-right
GCI	grid convergence index
GD&T	geometric dimensioning and tolerancing
HT	heat treatment
IGA	isogeometric analysis
IN718	Inconel 718 (trademark of Special Metals Corporation), material-number 2.4668, a nickel-base superalloy
iwb	institute for machine tools and industrial management of TU Munich, Institut für Werkzeugmaschinen und Betriebswissenschaften der TU München
JS	jackknife samples
LBM	laser beam melting
MCS	Monte Carlo sampling
MPA	material testing laboratory, Materialprüfungsanstalt
OAT	one-at-a-time
OP	operation
PBA	probability bounds analysis
PCMM	predictive capability maturity model
PD	pre-deformation
PDF	probability density function
PP	post-processing
QA	quality assurance
RMS	root mean square
SA	sensitivity analyis
SEP	separation
SI	Sobol' index
SRA	stress relief annealing
SRQ	system response quantity
STL	standard-tesselation-language
TGM	temperature gradient mechanism
UQ	uncertainty quantification
V&V	verification and validation
WP	workpiece

Latin symbols

Symbol	Description	Unit
a	Layer number	
A	Sampling matrix A	-
B	Sampling matrix B	-
Ab	Sampling matrix Ab	-
A	Constant in the Norton creep model	$\mathrm{s^{-1}\,MPa^{-n}}$
b	Step number	
Ba	Sampling matrix Ba	-
c	Complexity factor	-
d	Dimensionality, i. e. number of factors	-
E	Young's Modulus	GPa
E_x	Expectation operator	-
EE	Elementary effect	-
f	General model evaluation function	-
f_c	Solution on the coarse mesh	-
f_f	Solution on the fine mesh	-
F_s	Safety factor for the grid convergence index	-
GCI	Grid convergence index	-
h_c	Height of the layer compound in the simulation	mm
$h_{Plate,side}$	Film coefficient for the side of the build plate	$\mathrm{mW\,mm^{-2}\,K^{-1}}$
$h_{WP,side}$	Film coefficient for the side of the workpiece	$\mathrm{mW\,mm^{-2}\,K^{-1}}$
$h_{WP,top}$	Film coefficient for the top side of the workpiece	$\mathrm{mW\,mm^{-2}\,K^{-1}}$
i	Counter for iterative pre-deformation	-
i_{nec}	Number of necessary development cycles	-
i_{sav}	Number of saved development cycles	-
i_{sim}	Number of simulated development cycles	-
k	Counter one for factors in an analysis	-
K_{AMM}	Costs for an AM machine	€/h
K_{AMO}	Costs for an AM operator	€/h
K_{CAEE}	Costs for a CAE engineer	€/h
K_{COMP}	Costs for the comparison between actual and target geometry	€
K_{CS}	Cost savings for the simulation-based process chain	€
K_{GCX}	Costs for a software for comparison of target and actual comparison, e. g. Geomagic Control X	€/h
K_{GDX}	Costs for a re-engineering software, e. g. Geomagic Design X	€/h
K_{HM}	Costs for a CAE package, e. g. Altair Hypermesh	€/h

Latin symbols

Symbol	Description	Unit
K_{MAN}	Costs for the manufacturing of the part	€
$K_{MAN,tot}$	Cost for the manufacturing-based development cycle	€
K_{ME}	Costs for a measurement expert	€/h
K_{MEAS}	Costs for the measurement procedure	€
K_{MME}	Costs for the measurement equipment	€/h
K_{POST}	Costs for the simulation-based post-processing	€
K_{PRE}	Costs for the simulation-based pre-processing	€
K_{REFIT}	Costs for the refit from measurement data	€
K_{RM}	Costs for the raw material	€
K_{SIM}	Costs for the actual simulation	€
$K_{SIM,tot}$	Cost for the simulation-based development cycle	€
K_{WS}	Costs for a workstation	€/h
l	Second counter for factors in an analysis	-
l_e	Target length for the element edges	-
n	Exponent in the Norton creep model	-
$n_{Samples}$	Number of samples	-
Obj	Objective function in a least squares algorithm	
P	Point of a workpiece	-
P'	Point of a workpiece after a process or a set of processes	-
p_e	Element order	-
p	Probability	-
R	Number of trajectories in a Morris analysis	-
r	Index of the current trajectory	-
R^2	Pearson's correlation coefficient	-
Res	Residual in a least squares algorithm	
r_f	Refinement factor between two numerical meshes	-
S	Sobol' index	-
S_1	First order Sobol' index	-
S_T	Total Sobol' index	-
SD	Standard deviation	-
t	Time	s
T	Temperature	°C
T_m	Melting point	°C
T_{Conv}	Reference temperature for the convection	°C
Tol	Exemplary tolerance range	-
T_{Pre}	Pre-heating temperature	°C
T_{Pro}	Temperature in the heat affected zone	°C
T_{Room}	Room temperature	°C

Symbol	Description	Unit
T_{SRA}	Temperature during the stress relief annealing procedure	°C
u	Displacement	mm
u_{other}	Displacement fraction not attributable to translation, rotation or scaling	mm
$u_{rotation}$	Displacement fraction attributable to a rotational rigid body motion	mm
u_{scale}	Displacement fraction attributable to a scaling operation	mm
$\underline{\underline{u}}$	Displacement matrix for all points in the workpiece	mm
$u_{translation}$	Displacement fraction attributable to a translational rigid body motion	mm
$\underline{u}$	Displacement vector	mm
u_x	Displacement fraction in the direction of the x-axis	mm
u_y	Displacement fraction in the direction of the y-axis	mm
u_z	Displacement fraction in the direction of the z-axis	mm
v	Factor in an analysis	-
V	Variance or variance share attributable to the factors given by the index	-
v_1	Factor one in an analysis	-
v_2	Factor two in an analysis	-
v_3	Factor three in an analysis	-
v_4	Factor four in an analysis	-
$\underline{v}$	Vector of all factors in an analysis	-
W	Workpiece	-
x	Spatial coordinate in the build plane	mm
x'	Spatial coordinate in the build plane after a process or a set of processes	mm
x_{opt}	Optimal input position to yield a workpiece within tolerance after manufacturing	mm
$\underline{\underline{x}}_{opt}$	Optimal input position of all points of a workpiece to yield a manufacturing result within tolerance	mm
x_{target}	Target value for the x-coordinate, i. e. the initial value in the designed model	mm
$\underline{\underline{x}}_{target}$	Target value for the spatial coordinates, i. e. the initial coordinates of the designed model	mm
$\underline{\underline{x}}$	Spatial coordinates of all points in a workpiece	mm
$\underline{\underline{x}}'$	Spatial coordinates of all points in a workpiece after a process or a set of processes	mm
$\underline{x}$	Spatial coordinates of a point in a workpiece	mm

Latin symbols

Symbol	Description	Unit
y	Spatial coordinate in the build plane, perpendicular to the x-axis	mm
Y	System response quantity for a given sampling vector	-
z	Spatial coordinate perpendicular to the build plane, i. e. in build-up direction	mm
$\tilde{z}$	Local coordinate in build-up direction	mm

Greek symbols

Symbol	Description	Unit
α	Thermal expansion coefficient	K^{-1}
c	Specific heat capacity	$\mathrm{mJ\,t}^{-1}\,\mathrm{K}^{-1}$
$\underline{\underline{\Delta}}$	Form deviation, spatial difference between current and target coordinate	-
δ	Change in a factor or variable	-
Δ_I	Deviation by projection to the input geometry	-
Δ_O	Deviation by projection to the output geometry	-
ϵ	Strain	-
ϵ_{cr}	Strain fraction attributable to creep mechanisms	-
$\dot{\epsilon}_{cr}$	Creep strain rate	-
ϵ_{el}	Elastic strain fraction	-
ϵ_{pl}	Plastic strain fraction	-
ϵ_{th}	Thermal strain fraction	-
ϵ_x	Strain introduced via phase changes	-
γ	Value of the system response quantity (SRQ) of interest	-
γ_c	Chosen value of the SRQ of interest	-
κ	5-95-spread of the normal distribution	%
K_c	Constant factor for the creep regression fit	-
K_ϵ	Linear creep strain factor for the creep regression fit	-
$K_{\epsilon2}$	Quadratic creep strain factor for the creep regression fit	-
$K_{\epsilon3}$	Cubic creep strain factor for the creep regression fit	-
$K_{\epsilon,T}$	Linear creep strain and temperature factor for the creep regression fit	-
K_σ	Linear stress factor for the creep regression fit	-
$K_{\sigma2}$	Quadratic stress factor for the creep regression fit	-
$K_{\sigma3}$	Cubic stress factor for the creep regression fit	-
$K_{\sigma\epsilon}$	Linear stress and creep strain factor for the creep regression fit	-
$K_{\sigma,T}$	Linear stress and temperature factor for the creep regression fit	-
K_T	Linear temperature factor for the creep regression fit	-
K_{T2}	Quadratic temperature factor for the creep regression fit	-
λ	Conductivity	$\mathrm{mW\,mm}^{-1}\,\mathrm{K}^{-1}$
μ_{Morris}	Mean effect of a variable in a Morris analysis	-
μ^*_{Morris}	Mean absolute effect of a variable in a Morris analysis	-

Greek symbols

Symbol	Description	Unit
ν	Poisson's ratio	-
$\underline{\psi}$	Pre-scaling factor	-
Ψ	Pre-scaling function	-
ϱ	Density	$\mathrm{t\,mm^{-3}}$
σ	Stress	MPa
σ_{Morris}	Variability in a Morris analysis	-
σ_{vM}	von-Mises stress	MPa
σ_y	Yield stress	MPa
Θ	Distortion function	-
$\tilde{\zeta}$	Pre-deformation factor	-
Ξ	Pre-deformation function	-

1 Introduction

" 'Simulate before you create' really is a key factor to ensure a successful laser sintering process with metal materials, right from the start." (STEUER 2018). This insight, shared by a manager of a manufacturer of laser beam melting (LBM) systems, emphasizes the role of simulation for the metal-based additive manufacturing (AM) processes. With high costs for manufactured workpieces, predicting the outcome in order to make sensible design choices, may mark the difference between LBM being an economically viable instead of a promising manufacturing alternative to conventional processes. Simulative efforts may target different system response quantities (SRQs), but with AM drawing its main advantage from near-net-shape manufacturing, form deviation is among the primary quantities of interest. This thesis is intended to supply a methodology to manage this quantity with a simulation-based pre-deformation approach.

1.1 Motivation

In contrast to conventional processes, AM in general and LBM in particular are intended to increase resource utilization by additively creating workpieces close to their final form in a layerwise fashion, reducing material formation that is machined in a later process step. The layers consist of small laser welded seams, which are fused with the previous layers as well as with each other, creating a coherent workpiece. The economic potential led to high rates of growth over the last decade, but there are still hindrances prohibiting wide-spread usage. HUANG et al. (2015) mention that among the most important challenges concerning technology and research in AM are the poor accuracy due to the stress build-up as well as the high variability of this quantity in the produced workpieces. Similarly, BAUMERS et al. (2016) also mention poor dimensional accuracy as well as lacking predictability and repeatability among the main challenges. The key benefit of AM processes is their capability to provide near-net-shape workpieces. Depending on the requirements, these workpieces may either be used directly or with a significantly lower effort in post-processing compared to workpieces from normal machining processes. However, current approaches to dimensional accuracy are characterized by manufacturing-based trial and error approaches, excessive use of support structures or high post-processing allowances. In some cases, e. g. for the latter, these methods may not lead to satisfactory results even when applied correctly: the turbine blade shown in Figure 1.1 experiences high levels of distortion and features a hollow region. Even when machine allowance is added to both sides of the blade, the hollow part is likely not machineable to the right position.

Similarly, manufacturing-based trial and error approaches provide significant drawbacks both in terms of effort and repeatability, as the results are e. g. dependent on the designer

(a) Nominal geometry (meshed) on the build plate *(b) Actual workpiece after machining*

Figure 1.1: *For workpieces with internal features, such as this turbine blade primitive, the strategy of adding machine allowances to the design may not yield satisfactory results: even if machined to measurement, the hollow region is still not at the right position. The cross-section at the tip is highlighted in red.*

and the accessibility of the respective workpiece to the measurement technique. While the effect of redesign loops on the cost effectiveness of a workpiece may be negligible for large production series, the lead time may still be significantly reduced with a simulation-based design process (see Figure 1.2). In contrast, this first-time-right (FTR) manufacturing may be crucial for smaller production series.
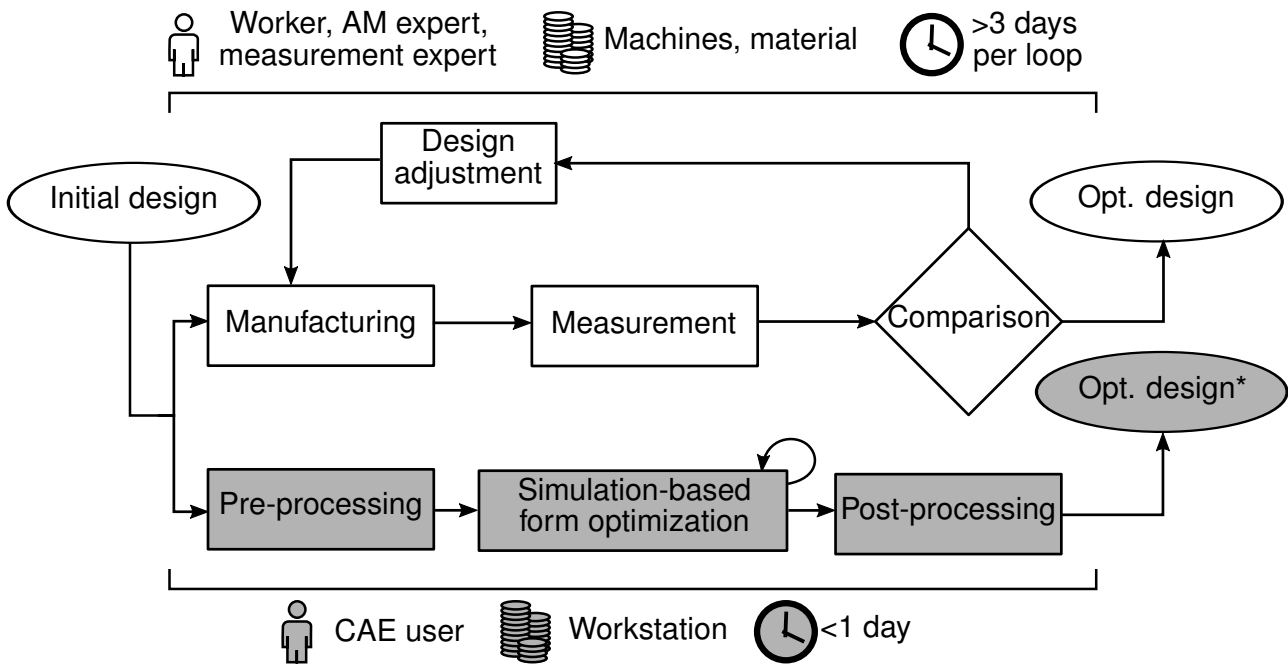
Figure 1.2: *Comparison of a manufacturing- and a simulation-based process chain for the redesign of a geometry in order to yield reduced form deviations after a set of processes.*
* Since a model can only provide an approximation of the response of the real process, the result of the digital pre-process depends on the predictive capability of the model (adjusted from BAYERLEIN et al. (2015)).

1.2 Goal

The goal of this thesis is to facilitate the manufacturing of workpieces via LBM that exhibit tolerable form deviations before post processing. With the high temperature gradients occurring in an LBM process, distortion is likely to occur and can only be avoided to some extent. Thus, the goal in this thesis is not to avoid this distortion but to compensate the design by the predicted effect. Due to the complexity of the process and the geometries, a simulation-based methodology is favored to heuristic or empirical methods. In order to provide the intended benefit, the simulation model is required to correctly predict the mechanical response along the process chain and the results need to be usable for a pre-deformation. Additionally, variability and uncertainties should be properly addressed.

The basic suitability of a simulation-based pre-deformation algorithm in order to increase dimensional accuracy is shown by multiple authors (AFAZOV et al. 2017; BRANNER 2010; KELLER 2017; SEIDEL 2016). Thus, this thesis is intended to provide additional insights into the controllability and effectivity of the process by means of modeling, simulation and validation.

1.3 Structure

The overall structure of this work is based on the SIMILAR process known from systems engineering (BAHILL and GISSING 1998). The letters of the acronym refer to different phases within a product development process: state the problem, investigate alternatives, model the system, integrate, launch the system, assess performance and re-evaluate constantly. These are explained in the following in more detail. Additionally, Figure 1.3 on the following page provides a compact overview of the structure of this thesis in combination with the SIMILAR process. However, the proposed step of constantly revisiting and re-evaluating the model performance is omitted for conciseness.

The first step is to convert the customer needs into a suitable problem statement. This is covered within the current chapter and all necessary terminology is given in Chapter 2. Subsequently, Chapter 3 provides information on both the underlying phenomena, neighboring investigations and the suitability of alternative approaches to solve the problem. The scope as well as the goal of this thesis are then presented in Chapter 4 in more detail. The developed methodology is separated into three solution components that each cover the phases of *modeling the system*, *integration* and *launching the system*, i.e. producing results by model execution. Chapter 5 presents the developed simulation method for the prediction of form deviations of industrial workpieces. Subsequently, the predictive capability of this model was investigated according to Chapter 6. Lastly, a method for an optimized input design is presented in Chapter 7. Additionally, the performance of the components is assessed

individually within the respective chapters and in summary in Chapter 8. The latter evaluates the overall efficacy, efficiency and effectivity of the developed method.
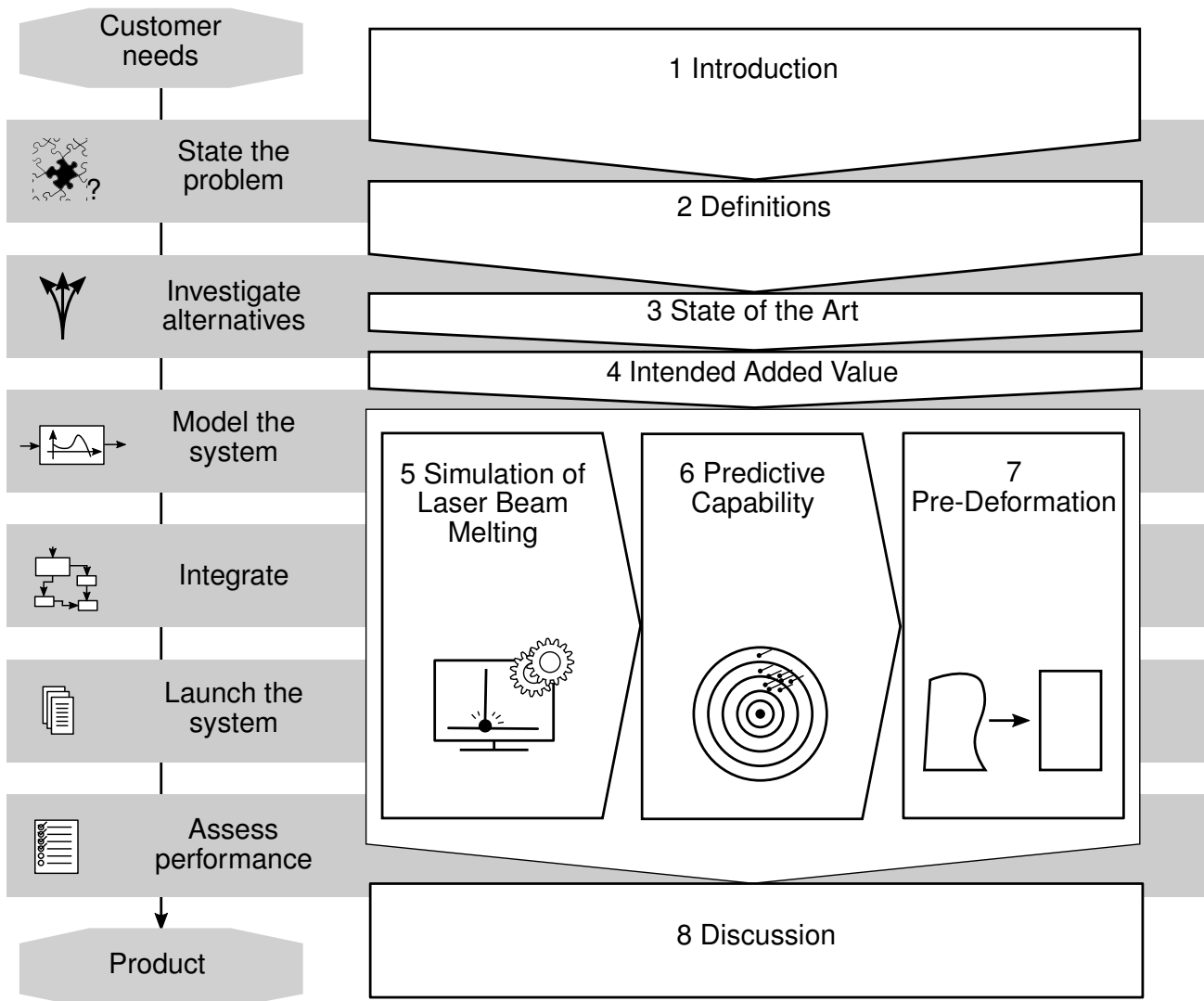
Figure 1.3: *The structure of this thesis is based on the SIMILAR process, referring to the respective phases of a product development process. The constant re-evaluation of model performance is not depicted in this figure.*

2 Basics and Definitions

This chapter is intended to provide all necessary definitions to allow for an unambiguous terminology to be used. The covered topics are: the LBM process, dimensional accuracy, simulation in the context of LBM as well as the area of model and simulation verification and validation (V&V).

2.1 Laser Beam Melting

While the developed methodology may be applicable to other processes, all data were generated by LBM. Thus, the following subsections provide an overview of its principle, the corresponding chain of processes to yield industrially usable workpieces and details of the relevant data streams.

2.1.1 Principle and Basic Quantities

LBM is characterized by a circular process map that uses a laser source to melt alloyed metal powder in a layerwise fashion in a defined spatial sequence so that a near-net-shape workpiece is generated upon re-solidification. Figure 2.1 on the next page shows the manufacturing sequence. The LBM process has a multitude of interconnected parameters that significantly affect the quality of the resulting workpiece that may be quantified by e.g. workpiece porosity, surface quality or other SRQs. In the following, only the fundamental parameters are discussed.

In order for the material to be fully melted (the distinctive feature of LBM), the absorbed energy must lead to a temperature that surpasses the melting point for all particles. To this end, high power laser sources are used. Together with specific optical components, they enable an efficient delivery of the laser power to the powder bed. Since the purpose of the LBM process is the creation of highly complex workpieces, the used spot size of the laser beam is adjusted close to the lower bound of the geometrical resolution which is defined by the higher end of the particle size distribution of the used powder material, e. g. between 50 to $100\,\mu m$. With typical build envelopes of 300 by $300\,mm^2$ in the build plane, the focus spot travels over the cross-section with a high velocity (around $1\,m/s$) to enable the production of workpieces in a reasonable time frame. Derived from the motion being realized by so-called laser scanners, the corresponding quantity is frequently referred to as scan speed. The pattern in which the focus spot is moved over the area to be melted is called the hatch pattern. Another key characteristic is the distance between neighboring scan tracks, i. e. the hatch distance. Depending on the used pattern, e. g. stripes or chess, further parameters may be necessary for an unambiguous description. In combination, scan speed, laser power and hatch distance determine the area specific energy density (J/m^2). Additionally, for most materials, a
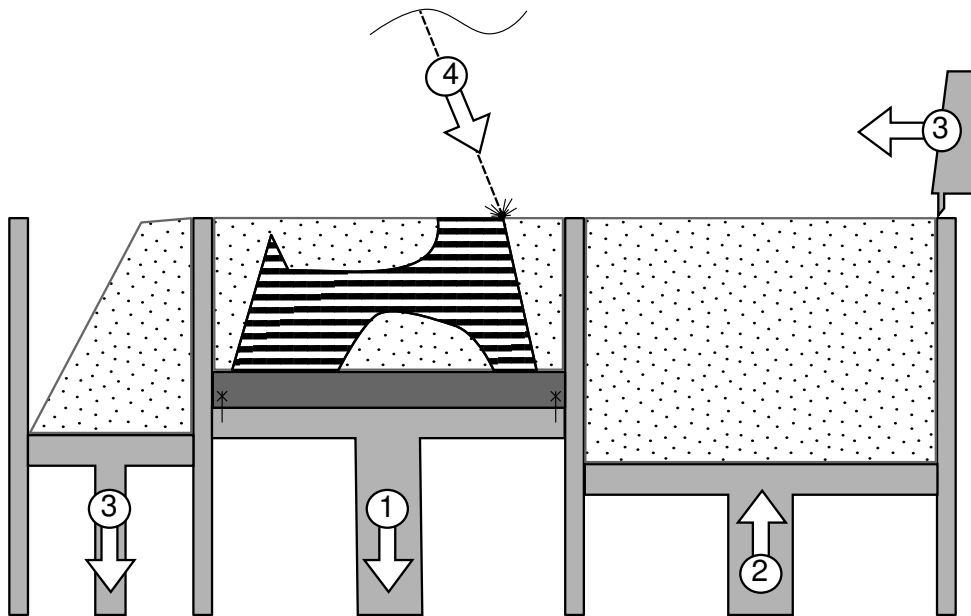
Figure 2.1: *Schematic overview of the LBM manufacturing cycle: the build plate is lowered by one layer height (1), the powder reservoir is raised (2) in order for the coating mechanism to spread the newly available powder on the build envelope (3) and last, the focused laser beam melts the powder (4).*

preceding or subsequent exposure in the form of the workpiece contour is beneficial to the surface quality. This contour exposure is frequently characterized by a variation in energy density in order to improve surface quality.

The process is characterized by steep temperature gradients both spatially and temporally, i. e. between pre-heating and melting temperature of the material. Inhomogeneous heating and cooling of the material introduces stresses which in turn may cause distortions.

2.1.2 Process Chain

Despite the early terminology of additive manufacturing processes (AMPs) commonly being referred to as "rapid" prototyping, tooling or manufacturing, the duration of the actual process may be high, i. e. up to multiple days. The origin of "rapid" stems from the fact that the generation of near net shape parts can significantly reduce the time and effort for all subsequent steps in the process chain before the operation phase. For prototyping, the AMP is often the only process step. However, for the production of end-use parts, subsequent process steps are usually needed. The typical process chain for workpieces made from nickel-base superalloys that are manufactured via LBM is depicted in Figure 2.2 on the facing page. All experiments in this thesis were conducted with Inconel 718 (trademark of Special Metals Corporation), material-number 2.4668, a nickel-base superalloy (IN718).

Computer-aided design (CAD) This step refers to the design process of the workpiece. In order to fully use the potential of AM and to provide an economical benefit, a redesign of conventional workpieces is typically necessary. It may be the result of a topology
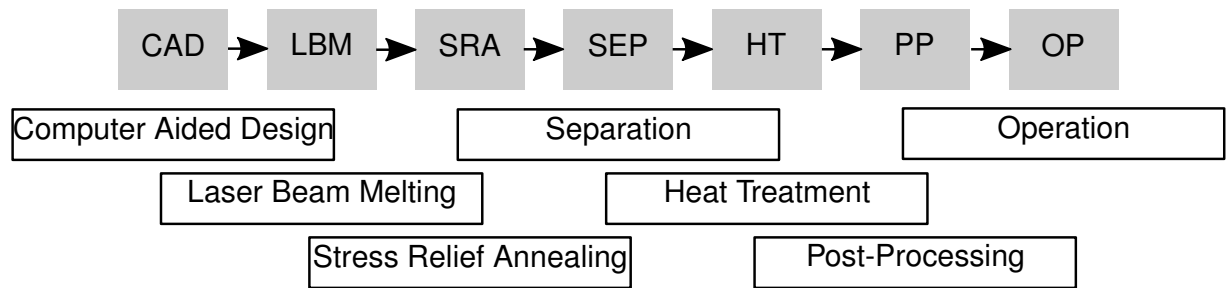
Figure 2.2: *Process chain for workpieces from IN718 that are manufactured via LBM: after the design and the manufacturing process, the parts are heat treated for a first time in order to reduce residual stresses, separated from the build plate, heat treated a second time for precipitation and post-processed, i. e. machined, to the respective requirements before going into operation.*

optimization, but as a minimal requirement it should respect the design guidelines for AM (THOMAS 2009). The result of this stage is the workpiece without manufacturing-specific adjustments.

Laser beam melting (LBM) The actual manufacturing process of a near net shape workpiece as described in the previous subsection is contained in this step. Additionally, for this thesis, the build job preparation is also included: virtually slicing the workpiece, possible support generation, positioning and orientation on the build plate as well as providing a build plate and powder. This step also includes the cool-down of the workpiece in the machine to room temperature and the subsequent removal of all remaining powder (in the accessible cavities). If not specified differently, the step is conducted according to the specification of the machine manufacturer, including all settings for the process parameters.

Stress relief annealing (SRA) Workpieces typically exhibit high levels of residual stresses after the LBM process (see Chapter 3). In order to improve dimensional and mechanical stability in subsequent process steps, a heat treatment to relief the main fraction of these stresses is often conducted. If skipped, the residual stresses may either lead to excessive deformation or cause material failure in the form of cracks when super-positioned with external loads. Within all experiments in the context of this thesis, the system of build plate and workpiece was subjected to the following annealing procedure: Heating with $10\,\mathrm{K\,min^{-1}}$ up to $955\,°\mathrm{C}$. Subsequently, annealing at $955\,°\mathrm{C}$ for $1\,\mathrm{h}$ and, finally, controlled cooling with $-10\,\mathrm{K\,min^{-1}}$. This process is from here on referred to as stress relief annealing (SRA), although it is rather a combination of both stress relief and solution annealing (SPECIAL METALS CORPORATION 2018). The increased temperature level was also chosen to increase ductility for subsequent process steps such as machining.

Separation (SEP) The separation process can be conducted via machining, i. e. sawing, or via electric discharge machining (EDM). If not mentioned otherwise, parts were removed

from the build plate via EDM, since that requires less machining allowance and has less influence on distortion (see Chapter 3).

Heat treatment (HT) The material used in the context of this thesis is a precipitation hardening nickel-base superalloy. For heat treatment SPECIAL METALS CORPORATION (2018) defines two possibilities that both consist of a solution annealing and a precipitation hardening phase. For this thesis, the following procedure was employed: Solution annealing at 955 °C/ 1 h/ Argon Quenching, double ageing at 720 °C/ 8 h and 620 °C/ 8 h, respectively / Air Cooling.

Post-processing (PP) Since the surface finish of LBM workpieces does typically not conform to required tolerances, a subsequent machining may be necessary. This includes the removal of support structures, if applicable.

Operation (OP) In the context of this work, this is the final process step. By allowing new lightweight designs for the actual operation of the workpiece, AM may pose an alternative to conventional manufacturing even if the production is significantly more expensive (WEBER and LAKOMIEC 2017).

In the following, the mentioned abbreviations will not only be used to refer to the corresponding process but also to distinguish the state of a workpiece in the process chain indicated by a subscript.

2.1.3 Material Properties

This subsection presents general information on LBM-related material characteristics and details on the main alloy under investigation, i. e. IN718. While the methodology of managing form deviations is transferable, individual modeling decisions are based on material specific characteristics.

The localized heat input in combination with the low ambient temperature level of LBM results in high spatial and temporal cooling gradients which lead to a fine grain structure (FARSHIDIANFAR et al. 2016). This microstructure is beneficial for mechanical toughness in a lower temperature regime but reduces strength and creep resistance at higher temperatures (TROSCH et al. 2016). However, since the LBM process is characterized by differing thermal conditions, with e. g. the local conductivity depending on workpiece geometry and powder-to-solid fraction, it is possible that a different microstructure is created at different areas within the workpiece, resulting in non-homogeneous material characteristics. Especially for filigree areas of the workpiece, with significantly altered cooling gradients, the microstructure may differ from that of the bulk material (ANTONSSON and FREDRIKSSON 2005).

IN718 is a precipitation-hardening nickel-base superalloy. Due to its high mechanical toughness and creep resistance at high temperature levels of up to 700 °C it is suitable for gas turbine applications. For the material to exhibit these advantages, it is necessary to properly adjust the microstructure in general (γ-matrix) and the precipitation phases (γ', γ'' and δ) in particular.

While the γ' is a stable phase, the transformation of the γ'' phase into the embrittling δ phase starting at 650 °C limits the application at higher temperatures (see e. g. REPPER (2010, pp. 11ff.) for further details).

The alloy specification for IN718 poses rather loose restrictions on its composition, with a spread of e. g. 5 % in its nickel content or 4 % for chromium (DIN EN 10302). Correspondingly, the resulting thermophysical properties may vary: For the solidus temperature, e. g., both POTTLACHER et al. (2002) and ANTONSSON and FREDRIKSSON (2005) mention values from different studies ranging from 1075 °C to 1260 °C with the latter distinguishing between solidus on heating and cooling. While the high material toughness is beneficial during the operation phase, it poses a challenge for traditional machining, causing high tool wear and increased monetary effort. With AM promising a decreased necessity for post-processing by creating near net-shape workpieces, IN718 is a prime example for the evaluation of AM cost effectiveness.

The microstructure of LBM manufactured workpieces from IN718 is characterized by the sequential adding of micro weld seams. A columnar grain structure in build-up direction and, depending on the process strategy, more or less pronounced γ'' as well as the absence of γ' precipitations lead to an anisotropic behavior and reduced mechanical strength compared to forged material (AMATO et al. 2012). However, subsequent heat treatment of LBM manufactured workpieces leads to a superior tensile strength at room temperature compared to both forged and cast material as well as equal (forged) or superior (cast) performance at elevated temperatures (TROSCH et al. 2016). D. ZHANG et al. (2015) report similar findings: The strength of as-manufactured material lies between cast and wrought material with significantly higher elongation at break. Subsequent heat treatment reduces ductility, but only to a level comparable to that of cast or wrought material, and increases toughness. In addition to the variability of thermophysical properties attributable to the material composition of the IN718 superalloy, the variability of properties may also be introduced by differing processing strategies and ambient conditions, e. g. machine types. The magnitude of the overall spread of mechanical properties was investigated for IN718 within a round robin test (VDI 3405 2.2). The findings yield, e. g., a spread of ± 28 % in the Young's Modulus of as-built specimens that stems from the confounded variation of both feedstock material and processing conditions. There is no information on how the resulting variation relates to the individual contributors, but, considering the magnitude, it is likely that the mechanical properties of workpieces built on different LBM machines may differ significantly even for the same feedstock material.

2.2 Form Deviation

This section is intended to explain what the target quantity of this thesis, i. e. form deviation, exactly refers to and how this quantity relates to established rules for geometric dimensioning and tolerancing (GD&T). The following terminology will be used:

True surface The surface that separates the body from its surrounding medium (DIN 4760). For this thesis, this quantity is of limited use as it cannot be determined with a reasonable amount of effort and time.

Measured surface The surface as captured by the measuring equipment with both random (noise) and systematic (faulty calibration) error sources (DIN 4760). Quantities from measurements are depicted with a tilde symbol (˜) as they are an approximation of the true surface.

Geometric surface The definition of the surface from the technical specification, i. e. the computer-aided design (CAD) model in the context of this thesis (DIN 4760). Geometrically defined quantities, i. e. points on a CAD model, are depicted with a bar symbol (¯) to represent their idealized character in comparison to the potentially rough true surface. Nodal coordinates of a finite element (FE) model are marked in the same way. While generic mesh creation may allow for coarse and inaccurate geometry representation, a tightly constrained mesh generation is assumed within the context of this work. Thus, the form deviations between a workpiece built from the CAD data and one built from the exported surface data of the nominal FE model (see next item) are assumed to be negligible.

Calculated surface The most accurate definition of the surface of the workpiece that can be generated from the information of the FE model. Quantities that are calculated via simulation, i. e. predicted, are an estimate of the true quantity and are thus distinguished by a hat symbol (ˆ).

Size, shape and form While the size describes the extent of a workpiece represented via its bounding box, the shape defines the summary of all inter-surface angles and proportions of lengths. Together, they provide the form of a workpiece.

However, all given symbols are only used if a distinction is necessary.

The geometrical product specification is well standardized with a matrix model defined in ISO 14638. This fundamental standard structures sub-standards according to their coverage of different geometrical aspects, e. g. position, direction or surface imperfection, and their role within the measurement chain, e. g. requirement specification, definitions for measurement equipment or calibration.

The goal of this thesis is a global optimization towards minimal form deviation of the final workpiece compared to its definition in the CAD model. In terms of GD&T, this is equivalent to a tolerance requirement for all comparison points, i. e. nodes of the computational mesh before and after the process. Further details are given in Chapter 7. The GD&T system of ISO 14638 will thus not be discussed further.[1]

---

[1]There are, however, applications in which certain aspects of GD&T may be of paramount importance and a weighted cost function may provide results that are easier to process: If, for an exemplary workpiece, e. g. only one surface is to be perfectly aligned, the corresponding optimization may be limited to this one surface.

In order to clarify the scale of the methodology proposed in this thesis, DIN 4760 provides a suitable distinction of different orders of form deviations: While first order form deviations are only apparent by looking at the workpiece in its totality, an excerpt of the surface is sufficient to characterize second to sixth order deviations. From here on, only those of the first order are discussed in this thesis.

2.2.1 Stress and Strain

In the absence of external forces, a body reaches an equilibrium between stresses and plastic strains. Depending on the mechanical constraint, a previously introduced load will result in deformations or stresses or a mixture of both (see Fig. 2.3).

Residual stresses exist on different length scales, e. g. self-equilibration occurs over individual grains or over the whole workpiece, and are classified accordingly. For this thesis, if not mentioned otherwise, residual stresses refer to the so-called macro-stresses, i. e. type I, that self equilibrate over the whole workpiece. However, when comparing macro-stress levels, it is essential that the corresponding micro-stress states are also comparable. (HUTCHINGS et al. 2005)

With AM typically only being an economically viable and eco-friendly choice if high material usage rates can be achieved (PARIS et al. 2016), AM workpieces are expected to provide low local stiffness, i. e. mechanical constraint, which in turn favors the development of higher deformation levels during manufacturing. This is independent from the overall workpiece
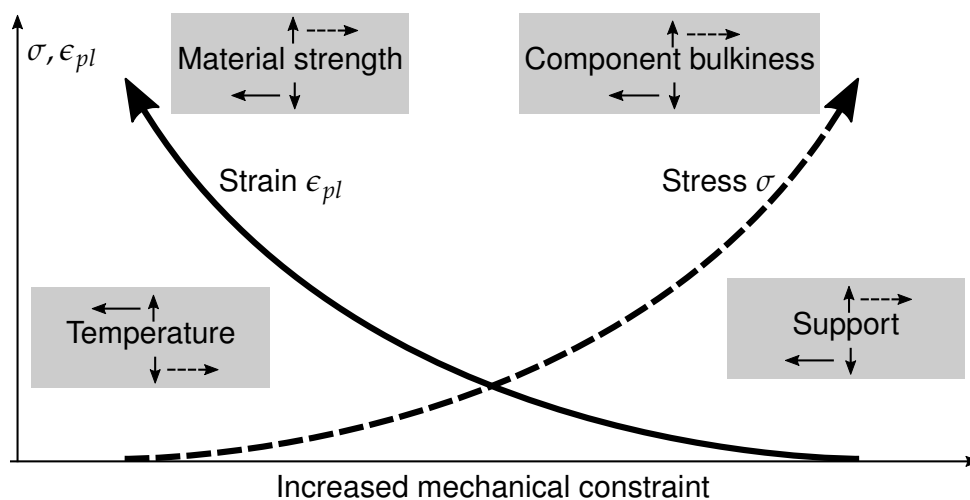
Figure 2.3: *The balance between stress and strain in a workpiece depends on the mechanical constraint (adapted from NITSCHKE-PAGEL and WOHLFAHRT (2002)). Additionally, the influence of four exemplary quantities on said balance, from the environment (e. g. temperature in the building chamber and the amount of support structures), the material (material strength) and the workpiece (component bulkiness), is presented. The arrows should be interpreted as follows: An increase of e. g. the bulkiness of the component (arrow above) will lead to more stresses being stored (dashed right arrow) and vice versa.*

behavior under load where new design possibilities offered by AM may enable tailored levels of compliance.

This distinction can also be represented in terms of fractions of the strain in a material: The total strain ϵ can be subdivided into an elastic fraction ϵ_{el}, that corresponds with the stored stresses, and a plastic fraction ϵ_{pl}, i.e. the irreversible deformation. Further, if temperature changes are involved, thermal expansion will provide ϵ_{th}, and possible phase transformations may yield ϵ_x. Lastly, the plastic strain may be subdivided according to its origin from a materials perspective: rate-independent, i.e. plastic ϵ_{pl}, and rate-dependent, i.e. viscous or creep phenomena related strain ϵ_{cr} (RUST 2015, p. 181). In the following, the latter definition of ϵ_{pl} is used, resulting in the strain decomposition:

$$\epsilon = \epsilon_{el} + \epsilon_{pl} + \epsilon_{cr} + \epsilon_{th} + \epsilon_x \tag{2.1}$$

Rate-dependent strain introduction may, depending on the boundary conditions, lead to two different macroscopic phenomena that are governed by the same microstructural processes. An increase in strain under constant stress is referred to as creep, while relaxation (see Figure 2.4a on the next page) describes the lowering of stress under constant strain (RUST 2015, p. 181). Both phenomena are characterized by three distinct phases (see Figure 2.4b):

- During primary creep (I) the initially high creep rate continuously decreases due to a disproportionate increase in hardening effects. This phase is concluded
- when hardening and softening are in balance, resulting in a constant creep rate. This secondary creep (II) phase thus marks the minimum of the creep rate.
- The last phase, i.e. tertiary creep (III), characterizes the final increase of the creep rate due to a disproportionate increase in softening effects, eventually leading to failure.

However, when an applied temperature induces microstructural changes, the stationary phase, i.e. secondary creep, may not appear. Instead, the creep strain rate continuously increases just after reaching a minimum. This happens, e.g., in precipitation hardening materials due to a coarsening of the respective particles. (RÖSLER et al. 2012, p. 391)

The rate at which a creep strain is introduced is dependent on different driving forces, i.e. stress σ and temperature level T, and the history of the creep process, i.e. either passed time t or accumulated creep strain ϵ_{cr}:

$$\dot{\epsilon}_{cr} = f\left(\sigma, T, t, \epsilon_{cr}\right) \tag{2.2}$$

When creep occurs over a range of stress levels, a time-dependent description of the process may lead to a premature assumption of creep strain saturation. Thus, strain-based descriptions are more suitable for variable load scenarios. (RUST 2015, pp. 182ff.)
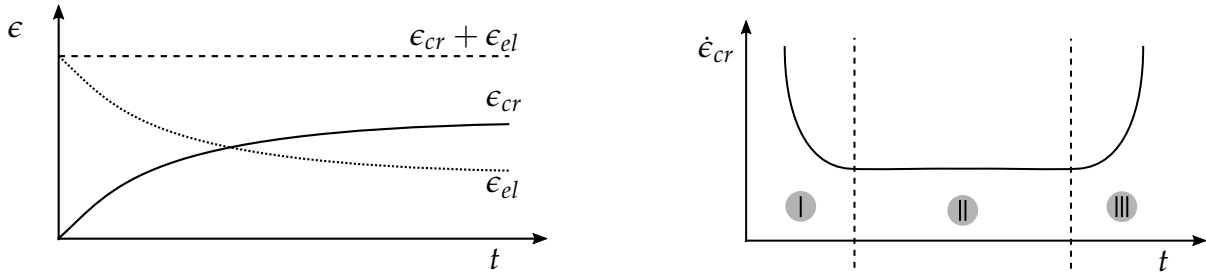
(a) *Transformation from elastic to creep strain during a relaxation experiment (adjusted from* Rust *(2015, p. 182))*

(b) *Different phases of creep: primary (I), secondary (II) and tertiary (III) (adjusted from* Rösler *et al. (2012, p. 386))*

Figure 2.4: *Illustrations of characteristic quantities for both typical creep phenomena: loading via constant strain (relaxation, a) and constant stress (creep, b)*

2.2.2 Distortion

Let a workpiece W be a set of points P with coordinates $(x, y, z) = \underline{x}$. The LBM process or any set of process can then be interpreted as a function Θ that yields a new point P' for all points P in the given workpiece W:

$$\Theta(P) = P' \quad \forall\, P \in W \quad \text{with e. g.} \tag{2.3}$$

$$\Theta(x) = x + u_x \quad \text{in } x\text{-direction for a given point } P \tag{2.4}$$

with the displacement vector $\underline{u} = (u_x, u_y, u_z)$. In the following, quantities relating to the ensemble of all points in the workpiece are denoted with two underlines, e. g. $\underline{\underline{x}}$. The displacement can be subdivided into fractions that relate to specific transformations: translation, rotation, scaling and shape changes. For this thesis, these fractions will be governed by:

$$u = \underbrace{\underbrace{u_{translation} + u_{rotation}}_{\text{rigid body motion}} + \underbrace{\underbrace{u_{scale}}_{\text{size change}} + \underbrace{u_{other}}_{\text{shape change}}}_{\substack{\text{form change = deformation, distortion}}} }_{\text{displacement}} \tag{2.5}$$

The quantities of interest for this work, i. e. displacement $\underline{u}$ and form deviation $\underline{\underline{\Delta}}$, are thus defined by:

$$\underline{\underline{u}} = \Theta(\underline{\underline{x}}) - \underline{\underline{x}} = \underline{\underline{x}}' - \underline{\underline{x}} \tag{2.6}$$

$$\underline{\underline{\Delta}} = \Theta(\underline{\underline{x}}) - \underline{\underline{x}}_{target} = \underline{\underline{x}}' - \underline{\underline{x}}_{target} \tag{2.7}$$

To illustrate the difference between these two quantities, Figure 2.5 depicts two exemplary ways of comparison for a simple workpiece and its deformed version:

- The displacement u can only be obtained when both geometries are within the same coordinate system and the mapping between deformed point P' and undeformed point

P is known. For the measured geometry, the second condition can, in general, not be met. While it is possible to design specific markers to track certain areas of the workpiece, these additional markers may influence distortion behavior or may not be suitable for the intended use.

- For the form deviation $\underline{\underline{\Delta}}$, the direction and magnitude are dependent on the relationship of the two coordinate systems (deformed and reference configuration) and the way of comparison[2]. Thus, the applicability of a comparison between a simulation result that shows the displacements of the nodes ($\underline{\hat{u}}$) and a calculation of form deviations from e.g. a 3-D-scanning result ($\underline{\tilde{\Delta}}$) needs careful consideration (see the beginning of this section for details on notation). For this thesis the coordinate system is defined so that the x-y-plane coincides with the upper surface of the build plate and the z-axis points in build-up direction. The placement of the origin in the x-y-plane is assumed to be central with respect to the build plate. This coordinate system is also used when the workpiece is separated from the build plate.

One of the goals of this thesis is the determination of a pre-deformation (PD) function Ξ that yields the right coordinates $\underline{x}$ for all points P in order for the final workpiece to exhibit a
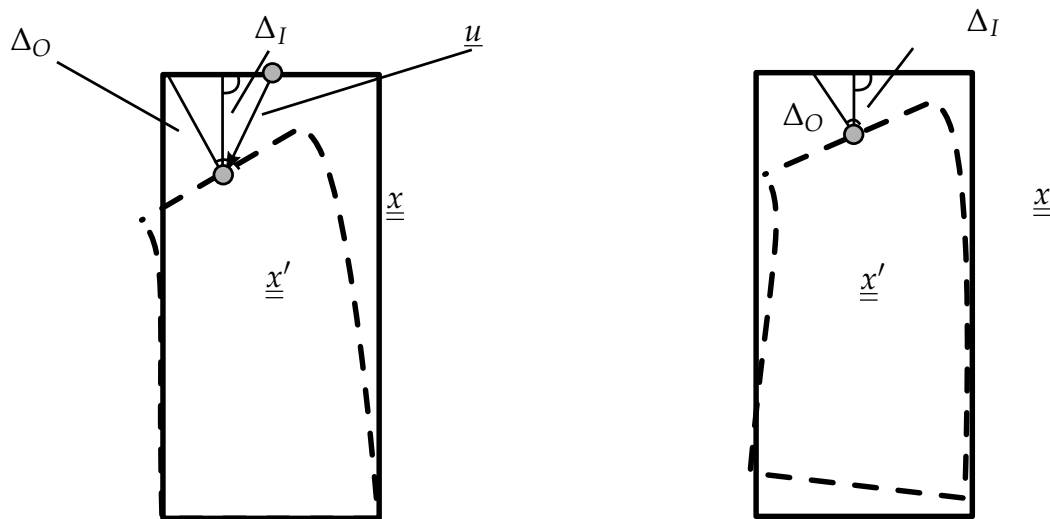
Figure 2.5: *Difference between displacement and dimensional deviation: when both configurations are given in the same coordinate system, the displacement $\underline{u}$ maps the input $\underline{x}$ to the output position $\underline{x}'$ (left). For a given sample point, u describes the displacement. Additionally, the form deviation for this point is given by Δ_I or Δ_O depending on whether it is generated by projecting on the input or the output configuration, respectively. If e.g. a best-fit alignment of the geometries is carried out before the comparison, the displacement cannot be identified. There are still multiple interpretations of the form deviation (right).*

---

[2]Most software packages that are able to visualize form deviation use either the projected distance along the face normals of one of the surfaces or the shortest distance as a measure.

deviation from the target geometry that lies within a given tolerance range *Tol*:

$$\Xi(\underline{\underline{x}}') = \underline{\underline{x}}_{opt} \quad \text{so that} \tag{2.8}$$

$$\Theta(\underline{\underline{x}}_{opt}) \leq \underline{\underline{x}}_{target} \pm Tol \tag{2.9}$$

In summary, the PD does not minimize the displacement but the form deviation of the workpiece.

2.3 Computer Aided Engineering

This section defines all necessary terminology corresponding to modeling and simulation efforts and presents the framework for the predictive capability analysis that is used within the context of this work.

2.3.1 Modeling and Simulation

Since the following terms are defined differently in many works, their definition as used within the context of this thesis is mentioned explicitly here and their role within the work is described. For a detailed discussion on the historical background and other definitions, see Chapters 2 and 3 of OBERKAMPF and ROY (2010).

A System is "a set of physical entities that interact and are observable, where the entities can be a specified quantity of matter or a volume in space" (OBERKAMPF and ROY 2010, p. 84). The main system of interest in this work is an individual workpiece in the LBM process. Modeling aspects require that the system is expanded to include the build plate (see Chapter 5).

A Model is "a representation of a physical system or process intended to enhance our ability to understand, predict, or control its behavior" (OBERKAMPF and ROY 2010, p. 92). In the context of this thesis, two types of models are distinguished: the conceptual model that defines all equations, boundary conditions and other necessary ingredients to represent a real system, and the numerical or computerized model, i. e. the implementation of this information. This thesis e. g. employs a thermo-mechanical finite-element-method-based numerical model. Additionally, similar to most currently employed models, the model is deterministic, i. e. all inputs are provided as fixed values and evaluations of the model will, except for numerical errors, always yield the same, deterministic result if provided with the same inputs.

Simulation is "the exercise or use of a model to produce a result" (OBERKAMPF and ROY 2010, p. 92). In order to gain knowledge from a model, it is necessary to study the interrelationship of input and output quantities. The latter are, from here on out, referred

to as SRQs. In the context of this thesis, this simulation refers to the execution of the aforementioned, sequentially coupled thermal and thermo-mechanical, FE-model.

Verification is "the process of determining that a model implementation accurately represents the developer's conceptual description and specifications" (DoD 5000.59). This is commonly referred to as answering the question "Are we doing things right?" in contrast to validation (see next point), which answers the complementary question "Are we doing the right thing?". Verification must precede validation in order to avoid two errors canceling out each other and assuming validity of a model that is in fact faulty (V&V10).

Validation is "the process of determining the degree to which a model is an accurate representation of the real-world from the perspective of the intended uses of the model" (DoD 5000.59). While there are other definitions without the need for real word data, e. g. SARGENT (2013), where an additional, accurate and validated model may serve as reference, only experimental results are used for validation within this thesis.

Prediction is the "use of a computational model to foretell the state of a physical system under conditions for which the computational model hast not been validated" (OBERKAMPF and ROY 2010, p. 39). If the primary targets of the simulation model are predictions of the SRQs, simply reproducing experimental outcomes provides limited benefit. Correspondingly, the developed methodology in this thesis is intended to be applicable to a wide range of input geometries and even materials, not just the ones it has been applied to before.

Aleatory uncertainty is "uncertainty due to inherent randomness" (OBERKAMPF and ROY 2010, p. 51). In general, all physical quantities of a workpiece, e. g. its Young's Modulus of Elasticity, are subject to a non-reducible variability. Even workpieces originating from well-controlled processes exhibit differences in their macroscopic behavior stemming from the stochastic nature of material formation. If enough data is available, the probabilistic nature may then be characterized by a probability density function (PDF) which accurately captures the knowledge without sacrificing correctness. Since the interpretation and comparison of multiple PDFs may result in unreadable depictions, only their cumulative equivalents, i. e. cumulative probability density functions (CDFs), are used within the context of this thesis. See Figure 2.6 on the facing page for a comparison between those two depictions.

Epistemic uncertainty is "uncertainty due to lack of knowledge" (OBERKAMPF and ROY 2010, p. 53) During the development of a simulation model, constraints in computational resources and development budget frequently require assumptions and simplifications. In case there is insufficient data to justify the assumption of a specific PDF, uncertainty is typically provided as an interval in which the true value is assumed to lie. This is

especially common for quantities that are hard to measure, e. g. material properties at hight temperatures.

P-box Due to the different nature of aleatory and epistemic uncertainty and their respective handling, i. e. probability theory and interval analysis, a suitable approach for their combined handling is necessary. This, so-called probability bounds analysis (PBA), approach represents the knowledge about the true value of a quantity by a probability box, i. e. a p-box. The concept is shown in Figure 2.7 on the next page for an SRQ prediction: Individual CDFs resulting from multiple evaluations of the system at distinct values for all epistemic inputs are combined. Depending on the type of parameters in the model, different types of p-boxes may result (see Figure 2.8 on the following page). (OBERKAMPF and ROY 2010, pp. 98ff.)

The Error in a quantity is "a deviation from the true value of the quantity" (OBERKAMPF and ROY 2010, p. 57). Since the true value is never known, errors can only be reduced but never quantified. One possible distinction separates the systematic error, referred to as the bias, from the random error, i. e. the fluctuations of e. g. measurement results (ISO/IEC Guide 98-3). See Figure 2.9 on the next page for a visualization of these quantities. Additionally, errors may stem from various other sources. When comparing simulative and experimental results of form deviations e. g., multiple contributors add up: the solution error from using a computer with finite resources, algorithm and coding errors, model errors from faulty assumptions about the real world and, lastly, measurement errors (OBERKAMPF and ROY 2010, p. 383).
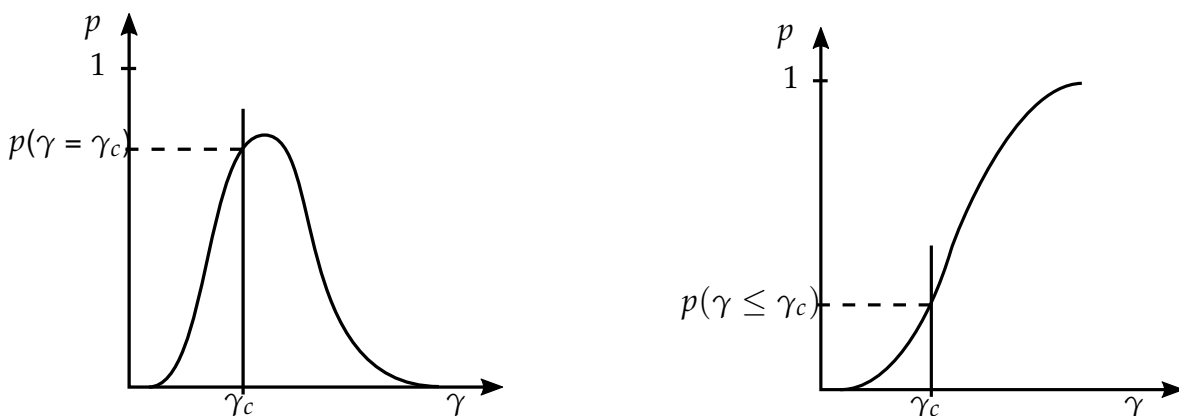
(a) PDF showing the probability that a given result γ matches γ_c

(b) CDF showing the probability that a given result γ is smaller than or equal to a threshold γ_c

Figure 2.6: *Visualization of an aleatory uncertainty via (a) the probability density function and (b) its cumulative equivalent*
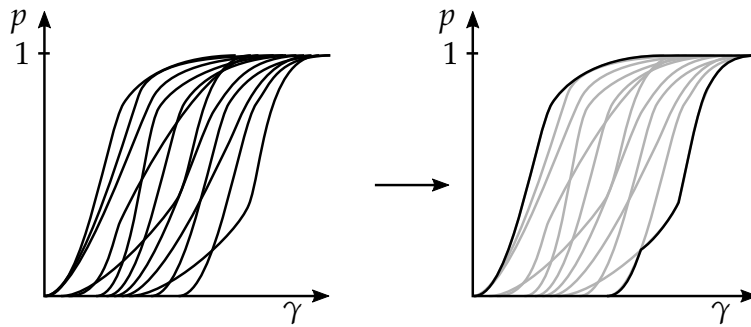
Figure 2.7: *Visualization of the results of a PBA: multiple CDFs for different system conditions (left) are summarized into a p-box (right). Since no additional information should be drawn from the distribution of the CDFs, the p-box, constructed from the outermost data, accurately represents the complete knowledge about the system.*

(a) *Purely aleatory*   **(b)** *Purely epistemic*   **(c)** *Empirical*   **(d)** *Generic*
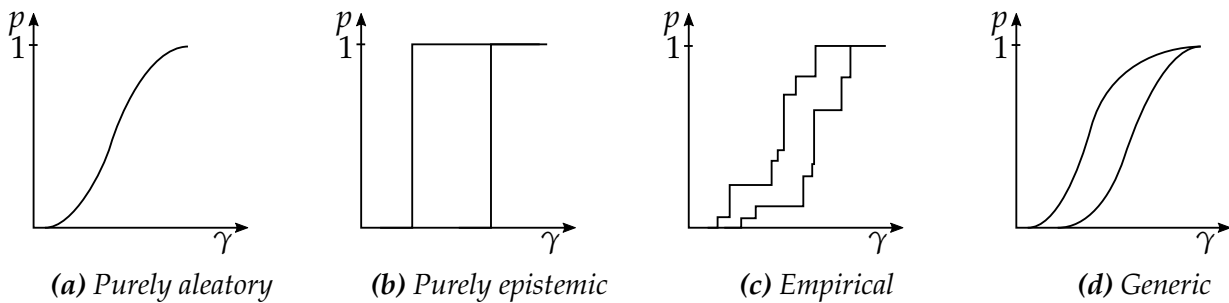
Figure 2.8: *Different types of p-boxes that result from the varying types of uncertainty: (a) when all uncertainty in the system is properly characterized by probability distributions, the SRQ is also characterizable as a CDF. (b) In contrast, if no probability information exists and only intervals are supplied, the SRQ will also be a pure interval. (c) For experimental trials, there is typically only a limited number of executions resulting in a staircase-like CDF for the SRQ that, if different conditions are applied, may also be of interval character. (d) Lastly, if both aleatory and epistemic uncertainties are present and the system is executed a high number of times, a generic p-box results.*
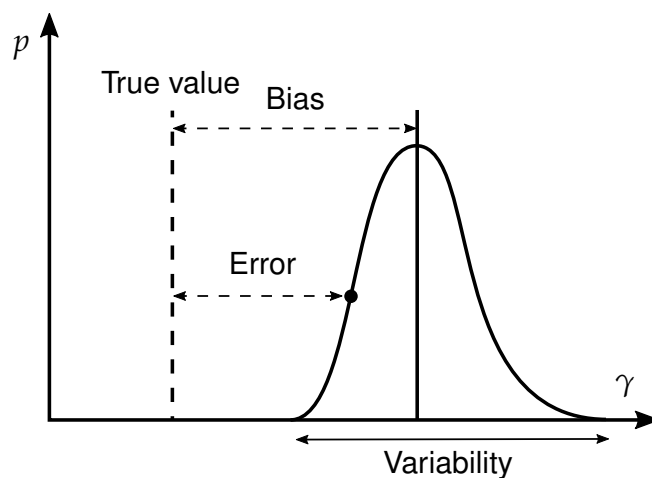
Figure 2.9: *Definitions for error, bias and variability within this thesis: since the true value is never known, error and bias can only be estimated.*

2.3.2 Predictive Capability

When results from simulation models are intended to serve as a basis for decisions, it is essential to convey the level of certainty of the predictions for the SRQs. Similarly to experimental results, this data is necessary for a risk-informed decision-making process. However, due to limited computational resources, uncertainty in simulation models is typically not explicitly accounted for. Instead, the predominant strategies of either multiplying the result with a safety factor or the assumption of a worst case as well as the combination thereof can be described as the de-facto standard. With rising system complexity, correctly identifying and characterizing the aforementioned worst case may not be possible in many cases. Fortunately, more generalized methods for handling uncertainty in a computational model are available: By using statistical methods in combination with a repeated execution of a deterministic model, non-deterministic information about the system in question is gained. These methods aim to assess and increase the predictive capability of a model by explicitly respecting the imperfections in knowledge about different aspects of the simulation process[3]. In the context of this work, the predictive capability maturity model (PCMM) established by researchers from the Sandia National Laboratory is used (SAND2007-5948): A self-assessment in the categories representation and geometric fidelity, physics and material model fidelity, code verification, solution verification, model validation, as well as uncertainty quantification and sensitivity analysis allows to discern whether the current maturity of the simulation model meets the previously defined requirements[4]. These requirements are mainly dependent on the criticality of the decision that the simulation is intended to support. This criticality may stem from various factors, e. g. public safety[5] or economic constraints.

A different view is provided by SARGENT (2013): The verification and validation aspects of the predictive capability in the simulation setting are oriented in a circular map (see Figure 2.10). Solution and code verification are summarized into computerized model verification, while model validation is split into operational as well as conceptual model validation. Additionally, the areas of bias and uncertainty are subsumed in the aspect of data validity, which affects all activities. In summary, SARGENT (2013) introduces a different view but recognizes similar sources of error.

In conclusion, assessing the predictive capability is necessary in order to ensure decision makers of the soundness of the modeling approach and the risk associated with different options. Additionally, the gathered information may also be used to determine whether the model is suitable for the intended use: When, e. g. the model predictions of the final form

---

[3]As a bonus, results may also indicate whether a reduction of specific sources of error are beneficial. For example, decreasing the effect of computational errors may only slightly change the shape of a PDF which already exceeds the tolerance range by multiple magnitudes. In this case, the model formulation itself should first be considered for improvement.

[4]The full model is provided in Appendix A.4 on page 155.

[5]The PCMM was developed by engineers working in the field of nuclear safety.
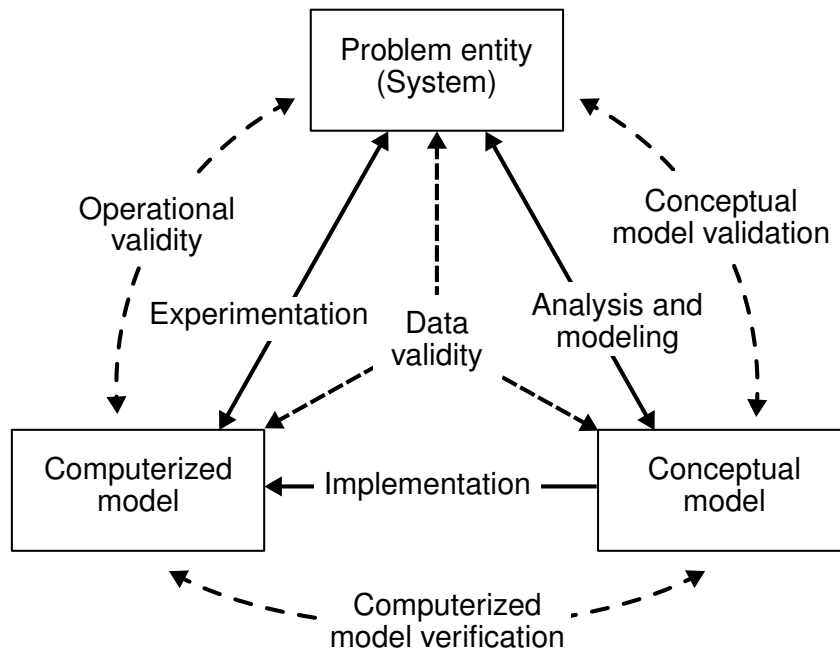
Figure 2.10: *The Sargent cycle consists of three domains, the respective actions to get from one to the other and the V&V activities that are related to these domains (adjusted from* SARGENT *(2013)).*

deviation of an exemplary workpiece are given as $\pm 2\,\mathrm{mm}$, but the tolerance range as well as the experimentally determined variation are smaller than a tenth of a millimeter, the model cannot be deemed suitable.

3 State of the Art

The research on both distortion and simulation in the field of AM is extensive. The following sections present a structured view on all major conclusions from the currently existing research on both distortion in, and the simulation of, LBM. Many research groups have devoted multiple studies to this topic and, accordingly, it is not sensible to describe all relevant efforts in this chapter in full detail. The chapter is closed by a summary and gap analysis that inspires the intended added value of this thesis.

3.1 Distortion in LBM

Since distortion in LBM stems from various sources and has many influencing factors, a categorization scheme is employed here. The following subsection introduces the methodology of distortion engineering (DE) as one of the possible schemes for structuring information on this phenomenon.

3.1.1 Distortion Engineering

DE was developed as a methodology to research and handle distortion in a process chain consisting of different potentially distortion-inducing manufacturing steps (ZOCH 2012). The underlying concept is the acknowledgment that the distortion of a workpiece is not a single-source phenomenon but rather a quantity that affects and is affected by the whole process chain. Figure 3.1 on the next page provides an overview on the main aspects.

For a workpiece, the way from CAD to operation consists of various processing steps that may affect its geometrical shape (cf. Figure 2.2 on page 7). In order to gain an understanding of the various influences of the process parameters and the environmental variables on an SRQ, the first step is to either collect information during production or to design an experimental study in order to generate input-output-interdependencies. Depending on the behavior of the processes, e. g. whether they are linear or chaotic, the number of samples required to yield meaningful information can range from only a few evaluations to an unreasonable amount of experiments. Thus, techniques from the domain of design of experiments are employed in order to efficiently uncover whether simple models, e. g. linear or quadratic (regression), can be employed to correctly describe the variability in the output. This level of understanding, how input parameters affect the output, is defined as the first level in the DE methodology.

The second level requires an understanding of the underlying mechanisms and aims to identify the carriers of distortion potential. The typical tools in order to develop this understanding
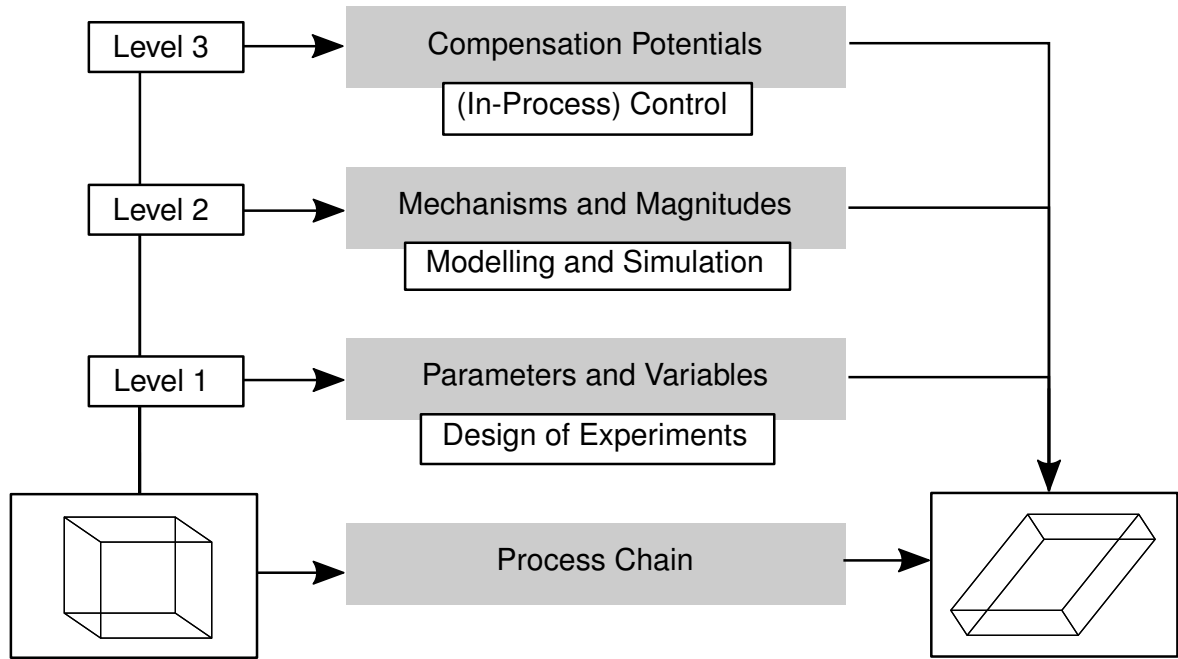
Figure 3.1: *Depiction of the main concept of distortion engineering: for a workpiece that is handled along a process chain, certain parameters and variables affect the distortion potential that can be identified via experimental studies. In a subsequent step, e. g. modeling and simulation can help to identify and quantify the underlying mechanisms. Last, with this knowledge, compensation potentials can be used to control certain aspects of the process chain or individual processes in order to match the requirements for form deviation. The different levels are introduced as a way of grading the knowledge about the distortion behavior of a workpiece in a process chain (adapted from ZOCH (2012)).*

are modeling[6] and simulation, in either a bottom-up or a top-down like approach, i. e. by starting from sub-models and sub-processes and connecting those or by modeling the main processes and subsequent detailing. The goal is to know which mechanisms contribute in which magnitude to which carrier of distortion potential. For a typical workpiece for the transmission industry, e. g., the following carriers of distortion potential were identified by ZOCH (2012): geometry, chemical composition, microstructure, residual stresses, temperature history and mechanical history.

Lastly, the identified mechanisms can be, simply put, inversely applied in order to balance the distortion potential with a compensation potential (ZOCH 2012, p. 12). The suitability of these compensation measures is then determined by the magnitude of their effect and the controllability of the corresponding input-output-relationship. The original methodology only mentions in-process control, which is extended in this thesis to control in general, i. e. also pre-

---

[6]While regression models are also models according to the given definition in Section 2.3, they are not rooted in a physical understanding and are thus not considered adequate for level two. If, however, a regression model, e. g. a linear relationship between two quantities, can be justified by a physical interrelation, it is satisfactory. Additionally, regression models may hint at a hidden relationship that may otherwise not have been identified.

and post-process. The following subsections deal with the application of this methodology to the topic of LBM and structure the current state of the art accordingly.

3.1.2 Parameters and Variables

There are a multitude of parameters and variables connected to the LBM process. This section provides an overview on studies that investigated the relationship between the resulting distortion and parameters, i. e. controllable factors, as well as other variables, i. e. factors that are typically not in control of the operator.

Parameters Before any choice on processing parameters is made, the designer is provided with the largest lever on the distortion of the final workpiece. Depending on the bulkiness of the workpiece and the material, significantly differing form deviations will result (cf. Section 2.2.1). For information on suitable guidelines to be followed in AM design, the reader is referred to the corresponding literature (e. g. THOMAS (2009) and THOMPSON et al. (2016)). Other direct parameters for form deviation management comprise the orientation of the workpiece in the build job and the use and design of support structures (KROL 2019). Furthermore, the digital data chain prior to the actual manufacturing may affect the resulting build job (ZENG et al. 2013).

There are many studies on how a change in process parameters affects the introduction of residual stresses and distortion in a simple structure (KRAUSS and ZAEH 2013; MUGWAGWA et al. 2018; MÜLLER et al. 2015; MUNSCH 2013; VRANCKEN 2016). Firstly, inconclusive results are reported for the LBM process parameters, i. e. laser power, scanning speed and layer thickness (MUNSCH 2013, p. 41). In this context, MUGWAGWA et al. (2018) bring attention to the fact that changing the melting parameters may result in an altered microstructure or porosity, clouding the influence on the distortion. Similarly, KRAUSS and ZAEH (2013) present that a multi-target optimization towards e. g. microstructure and dimensional accuracy leads to conflicts and that trade-offs are necessary.

Secondly, concerning the pattern of exposure, different studies (MÜLLER et al. 2015; MUNSCH 2013) agree that it is more often than not possible to find an optimized strategy with respect to a minimized final workpiece distortion. However, the right strategy is dependent on the material as well as the geometry and the magnitude of the effect is limited. KRAUSS and ZAEH (2013) could not determine a significant influence of the exposure pattern on dimensional accuracy for IN718. The effect of distortion from the placement of the workpiece on the build plate was examined by CASAVOLA et al. (2008). They report a difference in residual stress levels up to a factor of two for a simple cylindrical specimen. Additionally, VRANCKEN (2016, p. 173) reports that the influence of process parameters on the residual stress state may be material dependent.

Lastly, DENLINGER et al. (2015) investigated the effect of a varying layer dwell time, i. e. the time between subsequent exposures, in a directed energy deposition process on a titanium-base and a nickel-base superalloy. While their results suggest a highly material dependent response and a significant magnitude, the transferability to LBM is assumed to be small as the thermal household of the powder-based processes is much more stable. In summary, an alteration of the process parameters may lead to a change of the distortion behavior, but no simple relationship can be established. The influence can either be solely attributed to an altered thermal household or even differing microstructure and mechanical properties.

Variables A study on LBM workpieces built from Ti-6Al-4V feedstock shows that characteristics of the powder distribution may affect the resulting mechanical properties in a non-negligible magnitude (SEYDA et al. 2017). A difference of 8 % in (Vickers) hardness points to a significantly altered material state that may influence the distortion behavior (cf. Figure 2.3 on page 11). However, MÜLLER et al. (2015) experimented with different particle size distributions and could not detect a significantly altered distortion behavior of cantilever structures for both nickel- and aluminum-base alloys. In conclusion, feedstock properties exert influence on the microstructure which may in turn affect distortion behavior.

With LBM requiring workpieces to be built on a build plate, the geometry of said build plate also influences the distortion behavior of the workpiece. MERCELIS and KRUTH (2006) explained the effect with a theoretical model, resulting in the conclusion that a thicker design of the build plate leads to lower overall residual stresses in the workpiece.

Lastly, the method of separating the workpiece from the build plate, i. e. sawing or EDM, may affect the distortion behavior. While EDM is known to only introduce changes of the microstructure and the residual stress state up to a depth of 0.1 mm in IN718 (EKMEKCI 2007; KOLARIK et al. 2009; REPPER et al. 2012), sawing may provide differing results. Independent from the separation method and possible added stresses, especially for large workpieces, the direction of separation may significantly affect the distortion behavior, but there are no suitable studies available on this issue.

Additionally, there may be other less controllable factors contributing to an unavoidable variability in distortion behavior, e. g. thermal drift in the scanner system, positional differences due to backlash in the axes of the LBM system or completely unknown sources (MEINERS 1999, p. 81). There is currently no data available to quantify the unassignable variability of distortion behavior from e. g. job to job or machine to machine.

Table 3.1 summarizes the available information on both the expected effect size and predictability of the mentioned parameters and variables. The given estimates are based on the provided sources and are subject to change with new information being gathered.

Table 3.1: *Identified main parameters and variables, their estimated effect size and predictability as reported in the literature (○ = no influence/unpredictable effect, ◔ = small influence/material-dependent nonlinear effect, ◑ = medium influence/effect can be estimated by expert, ◕ = large influence/effect can be estimated, ● = paramount influence/effect can be calculated)*

Parameter/Variable	Maximum estimated effect size	Estimated effect predictability
Design of the WP	●	◑
Orientation of the WP	◕	◑
Design of support structures	◕	◕
Data conversion	◔	●
Process parameters	◑	○
WP position on the build plate	◑	◔
Powder particle size distribution	◔	◔
Geometry of the build plate	◑	◕
Separation method	◔	◑
Separation direction	◔	◑
Unassignable variability	?	○

3.1.3 Mechanisms and Magnitudes

The next step within the DE methodology is the identification of the driving mechanisms behind the distortion and to relate them to carriers of distortion potential. For LBM, the same carriers as found in ZOCH (2012) are assumed (cf. Subsection 3.1.1). The first investigation into underlying mechanisms for the development of residual stresses in LBM was published by MERCELIS and KRUTH (2006). Their study presents two mechanisms, namely the temperature gradient mechanism (TGM) known from laser forming and the cool-down of the molten top layer, in this thesis referred to as cool-down phase model (CDPM). Additionally, this subsection mentions other distortion-inducing mechanisms in the LBM context and classifies them according to the scale they act on: Local effects affect only areas of the workpiece, while global effects act on the whole workpiece.

Temperature Gradient Mechanism For a solid body in which one area is being heated to a significantly elevated temperature, the thermal expansion of said area will result in stresses that lead to distortion. If the stresses surpass the yield strength of the material, which may be significantly lowered due to the increased temperature, plastic strains are introduced that remain even after the system returns to an isothermal state. Despite LBM producing workpieces that are made up of kilometers of weld seams, the knowledge about the introduced strains cannot be directly applied, since powder with negligible macroscopic mechanical properties is involved in LBM. Also, in contrast to normal welding processes, the layers are re-melted multiple times over the course of the subsequent layer build-up.

However, KELLER (2017, p. 37) shows that, similar to welding, the introduced strains are anisotropic in the *x-y*-plane for a normal process, i. e. not just a single seam in powder. As

most of the machine manufacturers currently employ elaborated exposure strategies, i.e. rotating patterns, that lead to a homogenization of the heat input, this anisotropy is deemed negligible for bulky areas of the workpiece. Thus, this effect is expected to act on a local scale. However, with an increased interest in process quality, tendencies towards skipping exposure directions that may lead to spatters landing on to-be-solidified cross-sections emerge, this may change.

Cool-Down Phase Model The subsequent solidification and cooling of layers is another mechanism of distortion introduction. With the top layer reducing its volume during cooling due to the vanishing thermal expansion and the bottom layer counteracting this deformation, a bending moment is introduced. Since the workpiece is mechanically clamped by the build plate, this leads to high tensile stresses in the outer regions of the workpiece. This expectation is in line with investigations of the residual stress field of LBM produced workpieces (BAYER-LEIN et al. 2016, 2018; SOCHALSKI-KOLBUS et al. 2015). Since the whole process is based on the layerwise addition of material, this effect is to be categorized as global.

Solid State Phase Transformation Another possible source of strain and thus distortion are solid state phase transformations. DENLINGER and MICHALERIS (2016) show that modeling the phase transformation is not necessary for IN718, since the possible precipitation does not lead to a strain introduction. However, for build plates made from other materials, e.g. steel, phase transformations may occur, especially during post-process heat treatments. The introduced transformation strains may influence the mechanical equilibrium for the whole workpiece.

Thermal Expansion Besides phenomena that introduce distortion due to spatially and temporally varying thermal expansion, there is also the pure volumetric effect of thermal expansion. Depending on the temperature during the manufacturing process, i.e. the pre-heating temperature as the process is not expected to significantly raise the ambient temperature in the process chamber even for large build jobs, the effect needs to be accounted for. For a normal IN718 based LBM process with a pre-heating temperature of $80\,°C$ this effect is rather unpronounced. An exemplary large part with a length of $250\,mm$ exhibits a shrinkage of $35\,\mu m$ ($0.014\,\%$).

With currently emerging larger machines and the trend to raise the pre-heating temperature in order to counter distortion problems, this may play a role in the future. However, in a questionnaire reported by SEIDEL (2016), the typical size of workpieces manufactured with LBM was reported to not exceed this build envelope. A more detailed model to distinguish between the different parts of shrinkage in an LBM process is provided by L. ZHANG et al. (2018). The characteristic differences are given as: from melting temperature, i.e. solidus, to the temperature level of the surrounding material, from this so-called process temperature to the holding, i.e. pre-heating temperature and lastly back to room or ambient temperature.

The study concludes that the size of the currently to-be-solidified layer determines which components of shrinkage are already corrected within the process.

Lastly, when using differing materials for build plate and workpiece, due to economical aspects, thermal expansion may result in a non-homogeneous shrinkage behavior: If the coefficient of thermal expansion differs significantly, stresses are introduced which in turn may lead to an alteration in the distortion behavior.

Thermal Stress Relief According to MERCELIS and KRUTH (2006), an LBM process will typically result in the workpieces having residual stresses up to yield strength. This distortion potential, stored as elastic strain, may negatively impact both subsequent processing steps as well as the operation phase by either leading to warpage when stresses are relieved or failure when the additional load stress exceeds the yield strength of the material. Thus, workpieces manufactured by LBM will typically be exposed to some thermal stress relief procedure wherein one of the following two mechanisms is used:

Disproportionate yield reduction If the relative reduction of the yield stress is disproportionately higher than that of the Young's Modulus, elastic strains over yield are converted into the plastic regime, resulting in a reduction of the stress level when returning to the initial temperature. DONG et al. (2014) provide the following equation for the elastic strain fraction that can be transferred to the plastic regime by simply heating to a certain temperature and cooling back down:

$$\delta\,\epsilon_{el} = \left(\sigma_y/E\right)_{T_{Room}} - \left(\sigma_y/E\right)_{T_{SRA}} \tag{3.1}$$

The magnitude of the effect is strongly material-dependent, and for the nickel-base alloy in their study, Inco 600, it was a negligible factor, i. e. approximately 5 % reduction in elastic strain and therefore stress was observed.

Creep mechanisms As mentioned in Subsection 2.2.1 on page 11, increased temperature levels may lead to the translation of elastic to plastic strain through viscous effects, i. e. creep phenomena. Since there is no external load in stress relief processes, only the elastic strain fraction, i. e. up to approximately 0.5 % for metals, is converted to creep strain (LÖHE and VÖHRINGER 2002, p. 60). The magnitude of a possible stress relief is dependent on the susceptibility of the material to creep, the duration of the annealing procedure and the initial levels of stress. While IN718 is creep resistant in the precipitation hardened state, the as-is state after LBM is more susceptible to creep (POPOVICH et al. 2018). KRAUSS (2016, p. 81) provides data for a simple bracket geometry manufactured via LBM under different processing conditions. In the corresponding study, subsequent process steps led to significantly increased form deviations compared to the as-built state for most of the parameter combinations.

SEIDEL (2016, pp. 99ff.) shows that a pre-heating temperature of 200 °C does not introduce significant creep strain, but for significantly increased temperature levels, i.e. pre-heating temperatures over 30 % of the homologous temperature, both mechanisms may become significant during the actual LBM process.

Effective Layer Thickness A fundamental effect that leads to a difference between geometrical and true surface is the actual solidification process. Assuming a packing density for the powder around 60 % and typical layer heights ranging up to 50 µm, the upper bound of this effect is assumed to be at 30 µm. Since the solidified layer thickness is lower than intended, the next powder layer will have an increased thickness and this will continue until the nominal (solidified) layer height is reached after approximately ten layers (SPIERINGS and LEVY 2009).

Self-Healing Effect The machine always melts the powder at the nominal position of the current layer. Thus, even if the workpiece distorts during the manufacturing, the position of the subsequent layer is corrected both in-plane (x and y) as well as in z-position. This effect is limited by the accuracy of the positioning system of the laser spot. The DIN 35224 requires it to be better than 0.06 mm for aerospace applications and, for this thesis, machines are assumed to adhere to this standard. Additionally, for small geometrical features, this effect is limited by the above mentioned mechanism of a reduced effective layer thickness.

The given mechanisms are summarized in Table 3.2.

Table 3.2: *Identified mechanisms for distortion in LBM, their estimated effect scale and size (◕ = small influence, ◑ = medium influence, ● = large influence)*

Mechanism	Estimated effect scale	Maximum estimated effect size
Temperature Gradient Mechanism	local	●
Cool-Down Phase Model	global	●
Solid state phase transformation	global	◑
Thermal expansion	global	◕
Thermal stress relief	global	◑
Effective layer thickness	local	◕
Self-healing effect	global	◕

3.1.4 Compensation Potentials

If distortion is identified as a process-inherent, non-avoidable and non-negligible influence of a process or a process chain, it is necessary to develop alleviation strategies. The compensation potential is ideally potent enough to balance out the distortion completely or to reduce it to an acceptable level, emphasizing the importance of suitable requirements engineering.

Support Design The most straightforward compensation potential to distortion is increasing the stiffness in the build job so that the stress-strain equilibrium shifts towards stresses (see Figure 2.3 on page 11). By creating bulky support structures with high load-bearing capabilities, distortion potential is stored. However, since this material is typically unwanted for the operation phase, the excess material needs to be machined, resulting in a waste of material, effort, cost and resources.

Process Temperature The driving mechanism behind the creation of stresses and distortions is the thermal gradient between the melted and the solidified material at pre-heating temperature. Thus, one promising approach is the increase of the base level of temperature for the whole build job by increasing the pre-heating temperature. SHIOMI et al. (2004), e. g., investigated how residual stress levels decreased due to a heating of the powder bed and subsequent heat treatments. Their results suggest a significant influence for the investigated steel, with residual stresses being reduced by 40 and 70 % respectively. The efficacy of this approach is similarly demonstrated for other materials, e. g. IN718 (SOCHALSKI-KOLBUS et al. 2015) or an aluminum-based alloy (BUCHBINDER et al. 2011). However, raising the temperature level does not only alter the development of residual stresses but also the microstructure of the resulting material. Components produced by LBM typically exhibit sufficient mechanical strength in comparison to wrought workpieces, but with less steep temperature gradients during and after the process, the microstructure will be affected and the workpieces will thus exhibit altered resistances to different types of mechanical loads. Whether this alteration is acceptable must thus be evaluated individually depending on material and use case. While subsequent heat treatments can be employed, depending on the requirements, it may not be possible to reach the desired material properties with the help of subsequent heat treatments. Additionally, heating the build plate to a temperature level that introduces a significant reduction of temperature gradients and providing enough thermal energy to maintain this state, poses both a technological and an economical challenge. While the technical barrier is easy to overcome, the additional monetary effort remains a hindrance.

Adjustment of the Energy Input As mentioned in Subsection 3.1.2, there are multiple studies concerning the effects of process parameter variations on the distortion potential. The results often include a recommendation for optimal parameter settings, i. e. leading to a minimum of distortion: MUNSCH (2013, p. 104) presents the feasibility and distortion reduction potential of multiple process parameter alterations, structured by dimensionality. Furthermore, it is suggested that hull-core-strategies should be employed to reduce distortion. The chosen benchmark parts could subsequently be manufactured within the required tolerances but the core region of the part exhibits altered mechanical properties (MUNSCH 2013, p. 84). Also, there is no quantitative comparison between the distortion before and after a change of the energy input.

SEIDEL (2016) showed that adjusting the energy input depending on the bulkiness of the

workpiece region can have a positive influence on the resulting deviation. In his study the final distortion of a blade primitive was reduced by 7 % by increasing the scan velocity in the filigree area of the workpiece. However, there was no investigation as to whether the microstructure was influenced by this adjustment. Similar results were achieved by KELLER (2017): The distortion of a bracket geometry was reduced by 10 to 20 % by applying an optimized, simulation-based heat input. The study also mentions that using custom exposure strategies, process stability may decrease due to less heat input homogenization.

In another study conducted by MÜLLER et al. (2015) the layer thickness and different types of exposure patterns were investigated. While it was possible to reduce distortions for cantilever geometries, the optimized process parameter settings did not lead to a reduced distortion of a more complex workpiece (MÜLLER et al. 2015, pp. 77ff.). Finally, AHMADI et al. (2017) suggest a machine learning approach to battle distortion in polymer parts: by training a neural network with data from an FE model for various processing conditions, an optimized set of parameters for the benchmark geometry could be identified. The transferability to metal parts was not investigated.

Additional Structures Another approach to change the distortion behavior of additively manufactured workpieces is the use of sacrificial material. This was first described by DENLINGER and MICHALERIS (2015) for a large but simple structure made by wire-based electron-beam additive manufacturing. Although the distortion reduction potential was found to be large, i. e. distortion was reduced by 91 %, there is only very limited applicability to the LBM process. Additionally, there is excess material which, similar to increased support structure volume, typically needs to be removed before the part transitions into the operation phase.

In order to avoid the use of excess material, there is also the idea to replace the sacrificial material with other workpieces that balance the development of stresses in the initial workpiece (ILLSTON 2016). The applicability of this approach, however, is again very limited and is basically restricted to specific geometries.

Pre-deformation The most intuitive approach to countering form deviations is to not reduce distortion but to pre-account for its effect. Consequently, machine manufacturers, from the start, allowed operators to provide scaling factors to account for volumetric shrinkage, i. e. countering the effects of the mechanism of thermal expansion, or shrinkage in this instance. Pre-deformation can, however, be extended to account for other effects as well, and multiple studies already investigated this possibility: BRANNER (2010) shows the potential of this method by comparing the form deviations of a linearly (scaled) and a non-linearly (FE model based) pre-deformed geometry. The results show that distortions can be reduced and the workpiece can be manufactured within the required tolerances. Also, it is mentioned that for an indirect sintering process, due to non-linearity, it may be necessary to iteratively apply the pre-deformation to reach a satisfying result (BRANNER 2010, p. 122). There is no investigation into the spread of the experimental results and the predictive capability of the simulation.

Similarly, SEIDEL (2016) provides results of a turbine primitive study, where the use of a pre-deformed geometry with an ad hoc scaling factor based on measurement results reduces the form deviations by 40 %. No information on variability and uncertainty is provided.

AFAZOV et al. (2017) present both measurement- and finite element method (FEM)-based pre-compensation mechanisms and reach satisfactory results with a homogeneous pre-deformation factor of -1: For a blade structure with an initial maximum form deviation of ±0.2 mm, both approaches lead to the form deviations lying within the tolerance range of ±0.075 mm after subsequent build-up. It is mentioned that an over-compensation of the measurement-based approach can be corrected via an adjusted pre-deformation factor. The study puts an emphasis on the need for exact geometry representation for a proper pre-deformation from both measured and simulated data. When coarse meshes are used, AFAZOV et al. (2017) suggest mapping the distortion to a refined surface mesh. This is also stressed in KELLER (2017), where a simulation-based pre-deformation is applied but yielded poor surface quality in certain areas due to problems with the triangulation accuracy. The model is implemented in two commercial FE codes and calibrated via a reference cantilever specimen by adjusting the thermal load until the displacements of FE model and experiment match. The methodology does not account for non-linear distortion behavior, variability or uncertainty. (AFAZOV et al. 2017)

Summary Table 3.3 provides an overview on how the presented compensation potentials relate to the carriers of distortion. For the latter, target geometry represents a special case, as no secondary quantity, like e.g. the mechanical property profile, is altered. If e.g. the temperature history is significantly influenced by elevating the process temperature level in general, the microstructure of the resulting workpiece and thus its mechanical properties are also likely to change.

Table 3.3: Identified compensation potentials and their relation to the carriers of distortion potential (○ = no influence, ◔ = small influence, ◑ = medium influence, ◕ = large influence, ● = paramount influence)

Carrier of distortion potential	Support design	Process temperature	Adjustment of the energy input	Additional structures	Pre-deformation
Target geometry	○	○	○	◔	●
Chemical composition	○	○	○	○	○
Microstructure	◔	◕	◔	○	○
Residual stresses	●	◑	◔	◔	◔
Temperature history	◑	●	◕	◑	◔
Mechanical history	◑	◔	○	◔	◔

In conclusion, solely pre-deformation offers a distortion compensation potential without interfering with secondary targets in a non-negligible way. However, since there is no easy

to use analytical model for the mechanisms presented in Subsection 3.1.3, simulation of the process is necessary.

3.2 Simulation of Laser Beam Melting

With many of the metal-based AM technologies sharing key characteristics of a welding process, the terminology and simulation approaches are similar, especially in the case of LBM. Since welding is a complex process with aspects of e. g. fluid dynamics, grain growth or elasto-plasticity, simulations typically only tackle a fraction of the involved physical phenomena. The established way of structuring and separating the respective simulation domains is to distinguish between structure, process and material simulation and provide suitable interface quantities if a coupling is necessary (see Figure 3.2). The same trinity makes sense for LBM simulation:

Process simulation In order to understand melt pool formation and behavior in different scenarios, researchers are working on the laser material interaction and the modeling of all relevant phenomena. However, there are still many challenges concerning the computational representation and the necessary material data even for single weld tracks (KING et al. 2015). Thus, the interface quantity for the structure simulation, i. e. the equivalent heat source, cannot be easily calculated for multiple layers or even larger cross-sections. Consequently, structure simulations mostly employ phenomenologically-based load application strategies.
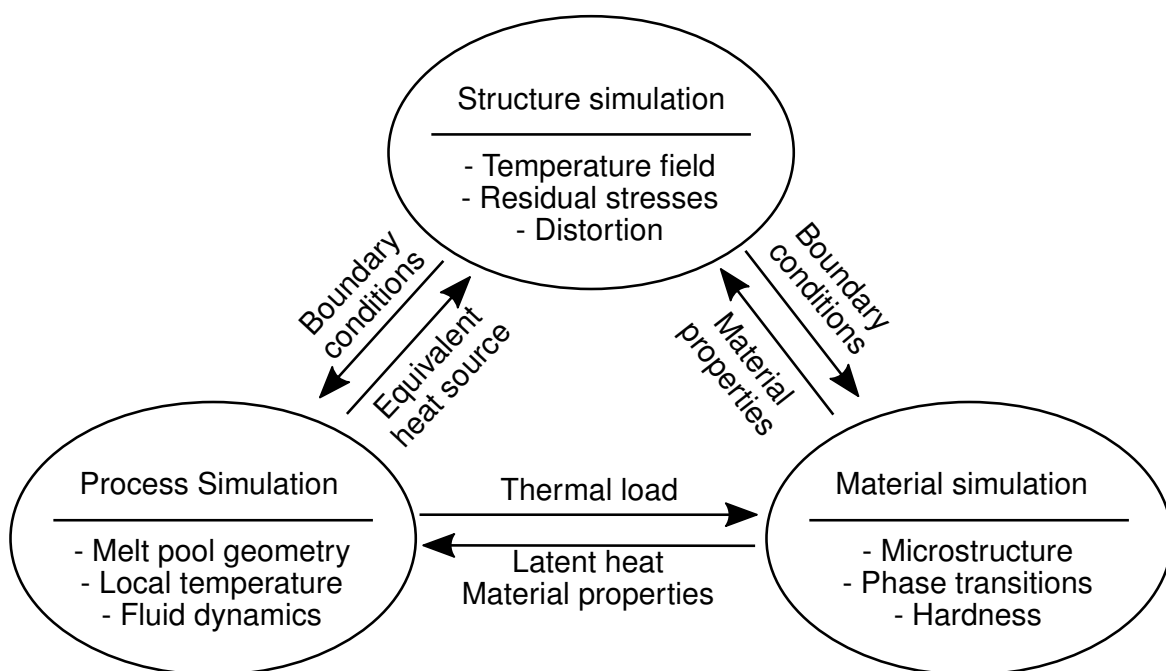
Figure 3.2: *The different aspects in welding simulations and their interrelations (adjusted from* RADAJ *(2002, p. 4))*

Material simulation In contrast to conventional processes, e. g. casting, where material is created in a well-controlled batch-wise process, with clearly defined boundary conditions, the high variability in the LBM process leads to novel challenges for the targeted material creation. In order to first gain an understanding of material forming processes and second predict and control said process, researchers make use of specific models: RAI et al. (2016) show that their coupled Cellular-Automaton-Lattice-Boltzmann-model is able to qualitatively predict grain structure via two-dimensional simulations of the build process. In the future, these predictions may be able to improve the result quality for the structure simulation by providing custom material properties, e. g. for filigree structures where microstructure differs from the bulk material.

Structure simulation As depicted in Figure 3.2 on the preceding page, structure simulation is intended to predict the thermo-mechanical behavior of the workpiece within the LBM process. Here, the main challenge is the representation of the covered time and length scales of the process: From the melt pool, which is situated in the micrometer- and microsecond-scale, to a typical part or build job in the range of up to a meter that may take up to multiple days. It is thus necessary to distinguish between simulations that use the actual layer dimensions for the build-up of small laboratory specimens in the range of multiple millimeters, i. e. meso-scale models, and those that compound actual layers in so-called layer compounds for the simulation of large workpieces. (CHIUMENTI et al. 2017) While the meso-scale models may work with interface data from both material and process simulation directly, workpiece-scale models require further simplification. Currently, there are two established ways to bridge this gap of scales: Either purely mechanically via the definition and application of an inherent strain vector or a mechanical layer equivalent (KELLER 2017; SIEWERT et al. 2018) or thermo-mechanically via a phenomenological heat source in the form of a direct temperature application that represents the melting process (SEIDEL 2016, p. 114). While SIEWERT et al. (2018) show that the purely mechanical approach may yield valid predictions for the distribution of near-surface residual stresses for simple parts, other studies suggest that there are geometrical restrictions on its transferability (BUGATTI and SEMERARO 2018).

For an exhaustive overview on current modeling efforts, the reader is referred to the respective literature (e. g. HU and MAHADEVAN (2017) and LIU et al. (2018)). Additionally, GOUGE and MICHALERIS (2017) provide a structured introduction to modeling the thermo-mechanical behavior in AM.

3.2.1 Reduced Thermo-mechanical Approach

This subsection presents the model of SEIDEL (2016), i. e. the direct precursor to the model developed within this thesis, in more detail. The underlying material properties for this model

are taken from experiments with comparable temperature and strain gradients, increasing congruency and comparability to the material behavior within the LBM processes. The mesh is generated by extruding selected machine data, i. e. common layer interface (CLI), in the build-up direction, creating hexahedronal elements. The accuracy of the geometry representation is therefore dependent on the number of layers that are combined in the layer compounds and a staircase effect cannot be avoided. This high initial deviation between computational mesh and CAD may hinder an effective usage for PD, as mentioned in the respective paragraph in Subsection 3.1.4 on page 30.

The heat source is realized as an instantaneous energy input via prescribed nodal temperatures for a, physically-based, very short (520 μs) duration on the top row of the respectively activated element layer. Thus, the effect from conduction during heating can be neglected and the energy input is dependent on both the element size, i. e. the number of compounded layers, and the shape function of the elements. For the used layer compound height of maximally 500 μm, predictions are, in general, in good agreement with experimental trials. However, computational effort is high with a prediction of distortion for an industrial use case requiring multiple days of simulation.

Additionally, an approach for a numerically efficient respect of other workpieces on the build plate is presented. The alteration of the thermal history with and without the surrounding workpieces is shown in silico. However, there is no information on whether the surrounding workpieces affect the distortion in the experiment and whether the simulation correctly predicts this effect when using the proposed methodology.

3.2.2 Modeling of Post-processes

While there are many modeling efforts for the LBM process itself, only a small number of studies investigate the representation of the further steps in the process chain before the operation phase (compare Figure 2.2 on page 7).

Heat Treatment Simulation The simulation of heat treatment processes is generally concerned with the combination of heat transfer, phase transformation and creep mechanisms. For the sole phenomenon of stress relief, simple models like the Norton model for the minimal creep rate are routinely employed (INOUE and ARIMOTO 1997; YAGHI et al. 2008). However, ALBERG (2003, p. 8) suggests using an interpolation model for improved accuracy if experiments from creep rupture tests at different stress and temperature levels are available. Finally, MAY et al. (2013) constitute that the strain-hardening formulation may provide better agreement to experiments under variable stress conditions. For the relaxation of near surface stresses, other approaches are used, but these are not considered for this thesis as the relaxation in the whole workpiece is of interest. There is no study on how the SRA process affects the residual stress level in a workpiece manufactured via LBM.

Workpiece Separation While there are very detailed models for separation processes, e. g. the chip removal process in metal cutting (SHET and DENG 2000), AM related research in this respect is mainly limited to the separation of the support structures of cantilever-like workpieces from the corresponding supports (PAPADAKIS et al. 2014). Similar to the activation of subsequent layers, the separation is performed by selectively deactivating the elements under the respective areas of the workpiece (NEUGEBAUER et al. 2014). There are no investigations into whether the separation method or direction plays a role for the resulting distortion.

3.3 Assessment of the Predictive Capability of Simulation Models

Since the use case for the developed methodology is the reduction of form deviations before experimental trials, the following section will discuss how to assess the predictive capability of a simulation model.

The prediction of an SRQ via a numerical model is subject to many sources of error: Besides direct modeling errors, variability and imperfect knowledge along with the, often faulty, assumption that the mean of all input values will yield the mean of the SRQ, may compromise the result integrity. If combined with e. g. an accidentally well fitting validation experiment, this may lead to an unjustified confidence in the predictive capability of the model. For a more robust and sound estimate of the actual knowledge of the system performance, methods from the areas of sensitivity analysis and uncertainty quantification are employed. With the numerous influences on the LBM process, KING et al. (2015, p. 23) suggest that it is necessary to quantify how sensitive simulation results are to input and material property variations.

3.3.1 Methodology

Since one of the core goals of assessing predictive capability is the creation of trust in the results, skepticism and documentation are important. Additionally, in order to avoid premature simplification, the following sequence for the respective activities and recommendations is advocated (OBERKAMPF and ROY 2010, pp. 555ff.):

1. Uncertainty identification: Identify uncertain variables and estimate whether the magnitude of their variation justifies considering them as uncertain. This uncertainty could stem from many sources, e. g. measurement error, improper modeling assumptions or missing information about the real system. A variable should be assumed to be uncertain unless there is knowledge or evidence suggesting otherwise.
2. Uncertainty characterization: Provide a formal description of the uncertainty in each variable. For some variables there may be enough data to provide a PDF, e. g. a uniform distribution, since all values are equally likely, but for others only an estimate from an expert along with boundaries is available.

3. Numerical error estimation: Quantify the effect of errors that are introduced by adjusting the problem in a way that a computer can solve it. From the numerous sources of error when a real-world problem is simplified into an executable model (OBERKAMPF and ROY 2010, pp. 584ff.), e. g. round-off errors, programming errors or just a faulty interpretation of the results, this thesis will focus on the discretization error within this aspect.

4. Uncertainty quantification (UQ): Propagate the uncertainties in the input variables through the model to obtain the uncertainty of the SRQ. The key goal of this step is to provide a more sophisticated report on what the analyst actually knows about the real value of the SRQ than a simple, e. g. scalar, prediction. The next section will provide more detailed information on the conduction of this step.

5. Model updating: Provide an improvement of the overall result correctness via suitable parameter adjustments. While the adjustment of material properties may have a very direct and predictable effect on the SRQ, e. g. yield strength on the residual stress distribution, only non-measurable, i. e. modeling or ad hoc, parameters are suitable targets in this step. Additionally, when model updating is conducted, a separation of the experimental information into calibration and validation data is necessary in order to avoid a so-called self-fulfilling prophecy. (OBERKAMPF and ROY 2010, pp. 624ff.)

6. Sensitivity analyis (SA): Identify and rank the most influential inputs (IOOSS and LEMAÎTRE 2015). The information from this step serves many purposes. For example, since UQ and SA require a high computational effort, the results may indicate how future analyses can be simplified without sacrificing integrity. Also, by ranking the contribution of different variables to the output uncertainty, it is possible to direct the focus of quality assurance investigations on the most relevant variables. Section 3.3.3 provides additional information and details on the conduction.

A variation to this sequence may be necessary when a model requires many (uncertain) input variables and/or exhibits high model execution cost. In this case, a so-called screening analysis may alleviate computational cost for both the UQ and SA with a controlled loss of accuracy (see Subsection 3.3.3).

3.3.2 Uncertainty Quantification

While there are other approaches to UQ, i. e. Bayesian inference and probabilistic methods, PBA exhibits one key advantage. It provides a method for not confounding epistemic and aleatory uncertainty. FERSON and GINZBURG (1996) provide explanations and examples on why separate handling of these uncertainty types may not only be beneficial but necessary: While variability may be canceled out between different variables, ignorance may contain systematic errors that may lead to a bias in the results. In essence, treating epistemic uncertainty as aleatory overstates the knowledge about the system. In turn, when all variability is simplified to ignorance, important knowledge is neglected and the prediction is not as precise as possible.

The method of PBA thus combines interval calculation for epistemicly uncertain variables with probabilistic methods for aleatory uncertainties. The actual propagation of the input uncertainty can be done via analytical, so-called stochastic expansion or Monte Carlo sampling (MCS) methods. However, for a separated propagation of aleatory and epistemic uncertainty only the computationally expensive MCS methods are suitable. Also, stochastic expansions require substantial modification of the computer code in order to be applied while MCS allows the model to remain a black box. (OBERKAMPF and ROY 2010, p. 600)

On the downside, since sampling can only provide an estimate of the true distribution, the resulting p-box deviates from its true value for a finite number of samples. However, with MCS being an unbiased estimator, there is no systematic error for a reasonable amount of samples. (OBERKAMPF and ROY 2010, p. 107)

For the segregation of the different uncertainty types, two possible methods are suggested:

- SUN et al. (2012) provide a general framework where each uncertainty is first converted into a p-box. Subsequently, a sample interval is drawn for all variables and the output range of the SRQ is determined by the minimum and maximum of the model output for the respective combination of input intervals. When no knowledge concerning the input-output relationship between a variable and the SRQ can be inferred, an optimization procedure is employed to ensure that the actual limits are found. This computationally expensive procedure should be avoided where possible. The resulting intervals can then be interpreted as empirical CDFs (see Figure 2.8c on page 18) respectively, forming the p-box for the SRQ.
- If there are no parameters that exhibit or contain ignorance and variability, OBERKAMPF and ROY (2010, p. 606) suggest two simple nested sampling loops with scalar samples: In the inner loop, the aleatory variables are sampled according to their PDF for one possible realization of epistemic variables. This results in a single CDF for the SRQ. By repeating this for multiple combinations of randomly sampled realizations of epistemic variables, a series of CDFs is generated, from which a p-box can be constructed (see Figure 3.3 on the next page). OBERKAMPF and ROY (2010, pp. 610ff.) also suggest the inclusion of model and numerical error in the resulting p-box by increasing the width between the limiting CDFs.

By using PBA, the results are also better suited to influence the future course of action: If the uncertainty is dominated by an epistemic character (represented by the width of the p-box), the result can be improved by adding knowledge in a focused way. However, if the aleatory character (represented by the breadth of the enveloping CDFs) dominates, major changes in the underlying design may be necessary to compensate for the influence of this variability (SUN et al. 2012).

Additionally, there is a distinction for uncertainties depending on their source. If there is limited knowledge about a problem, multiple alternatives for the modeling of different
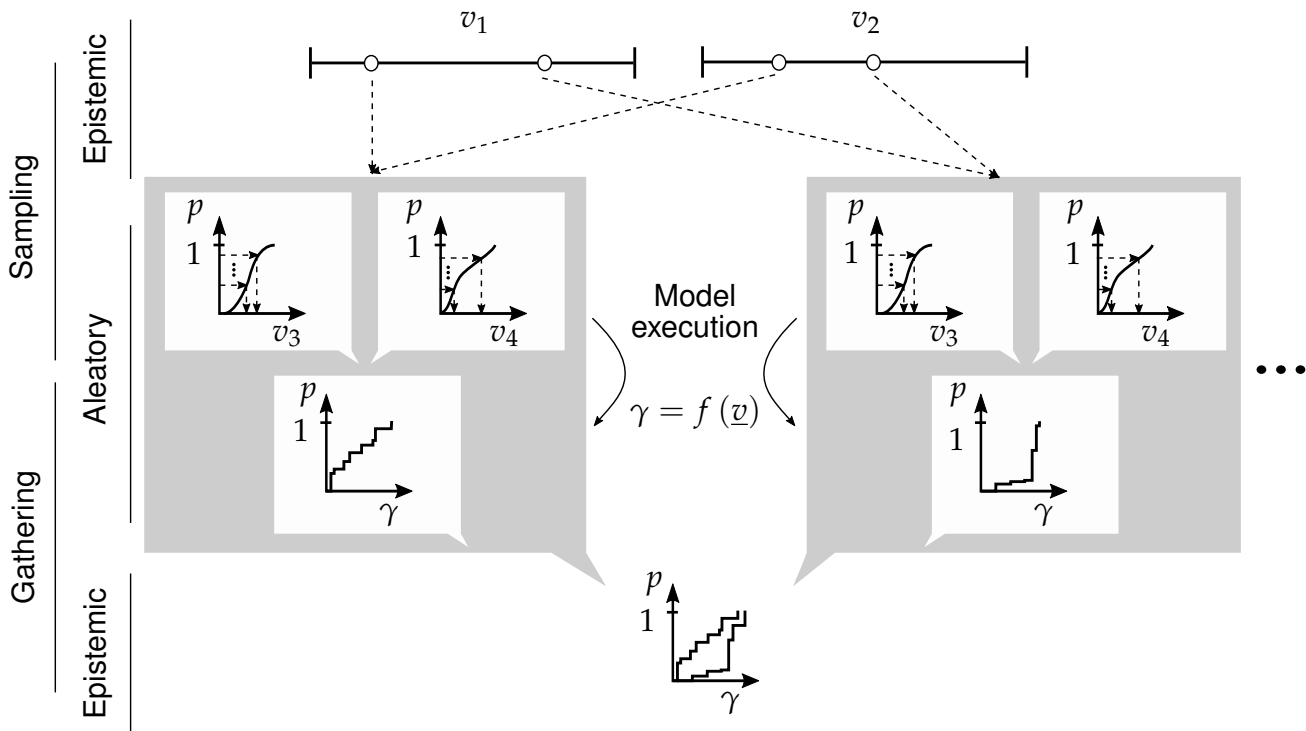
Figure 3.3: *Overview of UQ for four factors (v_1, v_2 epistemic and v_3, v_4 aleatory): samples are drawn from the (interval) epistemic variables in the outer loop and for each combination the aleatory variables are sampled according to their CDFs in the inner loop. Subsequently, the model is evaluated for each of these sample configurations and an individual empirical CDF is constructed for the SRQ for each combination of epistemic factors. The overall CDF is extracted as the hull of all CDFs (cf. Figure 2.7 on page 18).*

phenomena, e. g. the heat input, or the system as a whole may be suggested. This uncertainty in the formulation of the model is referred to as model uncertainty. In contrast, the resulting uncertainty in the SRQ stemming from the propagation of uncertain inputs, e. g. system inputs or boundary conditions, is simplified to input uncertainty.

3.3.3 Sensitivity Analysis

As mentioned above, there are different reasons for employing sensitivity analysis and, similarly, the used methodologies differ. One categorization criterion is the coverage of the input space: While earlier SA approaches mainly studied small input perturbations around the operating point of a model, i. e. so-called local analyses, recent research focuses on more global methods in order to yield a more complete picture of a variable's influence. Additionally, they can serve as stress tests for a model, since atypical combinations of input parameters are explored. (IOOSS and LEMAîTRE 2015)

Thus, only global SA methods are discussed in this thesis. For this class, IOOSS and LEMAîTRE (2015) provide an overview on the available methods and present a schematic to choose a suitable method based on the number of model evaluations and the regularity, i. e. the complexity, of the model. Additionally, they distinguish between so-called screening and

more precise variance-decomposition techniques that largely differ in the number of required model executions with the former only providing information on total effects. If no regularity for the model can be assumed, they conclude that the screening analysis should be conducted according to Morris' method (MORRIS 1991) and the Sobol' indices (SOBOL' 1993) should be used for a more precise information. Since the model that is used in this thesis exhibits both geometric and material non-linearities, discontinuity cannot be excluded. The next two sections explain the mentioned methods in more detail, but the reader is referred to the respective sources for the full mathematical derivations.

Screening Analysis The main reason for conducting screening analyses is the identification of negligibly relevant variables in order to exclude them from further analysis and thus reduce the computational effort. Instead of being highly accurate, the results of a screening analysis are required to be more robust and yield consistent results even for a low number of samples (IOOSS and LEMAÎTRE 2015).

Many engineering analyses use the so-called one-at-a-time (OAT) sampling strategy due to its simple implementation and interpretation (see Figure 3.4a). However, SALTELLI and ANNONI (2010) argument against its usage for SA due to its low coverage of the input space and poor performance to recognize interdependencies which may account for a significant portion of the variability especially in complex systems. As an alternative, MORRIS (1991) suggested the use of multiple OAT designs in order to alleviate these drawbacks and his method is currently considered best practice for screening analyses (SALTELLI and ANNONI 2010). See SALTELLI et al. (2002, p. 108) for a more detailed explanation on why this method is superior to other suggestions.

In essence, the method of Morris is conducted as follows: the input space is discretized into a lattice with a fixed number of levels for each variable, a random starting point is chosen and sample points are generated along a trajectory in the base directions with every variable changing its level once. In total, between $R = 10$ and $R = 50$ trajectories should be constructed (see Figure 3.4b, CAMPOLONGO et al. (2007)).

Subsequently, from the results of model executions at these sampling points, so-called elementary effects EE can be calculated along each of the edges of the trajectories. These effects

(a) OAT sampling   *(b) Trajectory sampling*   *(c) Winding stairs sampling*
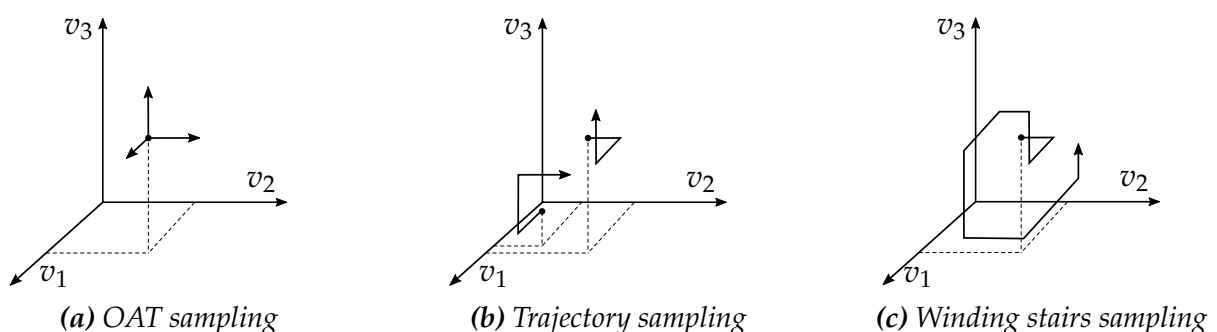
Figure 3.4: *Comparison of different sampling strategies*

relate the change of the SRQ to the change in the input parameter δ. Finally, the mean of all elementary effects μ_{Morris} or the mean of their absolute values μ^*_{Morris} as well as their standard deviation σ_{Morris} is used to classify the variables into three groups (see Table 3.4). For each v_k in $\underline{v}$ the quantities are computed as follows[7] (IOOSS and LEMAÎTRE 2015; MORRIS 1991):

$$EE_r = \frac{f(\underline{v} + \delta_r) - f(\underline{v})}{\delta_r} \tag{3.2}$$

$$\mu_{Morris} = \frac{1}{R} \sum_{r=1}^{R} EE_r \tag{3.3}$$

$$\mu^*_{Morris} = \frac{1}{R} \sum_{r=1}^{R} |EE_r| \tag{3.4}$$

$$\sigma_{Morris} = \sqrt{\frac{1}{R} \sum_{r=1}^{R} (EE_r - \mu_{Morris})^2} \tag{3.5}$$

The parameter μ^*_{Morris} was introduced to avoid falsely deeming a parameter negligible because the elementary effects cancel each other out across the input space (CAMPOLONGO et al. 2007). Also, in the original formulation (MORRIS 1991), the OAT designs were disjoint, but JANSEN et al. (1994) suggested the so-called winding stairs sampling: By connecting the OAT designs, additional elementary effects can be calculated from the same number of sample points (see Figure 3.4c).

The results are typically visualized in the μ_{Morris}-σ_{Morris}-plane (SALTELLI et al. 2002, p. 96) and since all resulting quantities are of the same dimension as the SRQ, the analyst can provide the cut-off between a small/negligible and a large/significant variable in a straightforward manner.

Table 3.4: Results of a Morris analysis and their interpretation; the definition of the threshold to discriminate between negligible and significant results is the responsibility of the analyst. (IOOSS and LEMAÎTRE (2015), ○ = negligible magnitude, ● = significant magnitude)

μ^*_{Morris}	σ_{Morris}	Explanation	Expendable
○	○	No influence on SRQ	yes
●	○	Large linear effect without interactions	no
●	●	Large non-linear effect with/without interactions	no
○	●		

However, similar to other screening methods, the results should mainly be used as a qualitative ranking mechanism rather than quantitatively asserting how much more important one variable is compared to the other. This is also true for the usage of UQ data for SA by systematically omitting uncertainties as suggested by FERSON et al. (2004). If quantitative

---

[7]Index k is omitted for improved readability.

data is required, more computationally expensive methods are necessary. (SALTELLI et al. 2002, p. 108)

Variance Decomposition When a model cannot be assumed to be linear or monotonic, variance decomposition or analysis of variance (ANOVA) methods are employed in order to perform SA. The basic underlying idea is ANOVA decomposition: when a function is defined on the unit hypercube, it can be expressed as a sum of its elementary parts, i. e. functions that are only dependable on a subset of the input vector:

$$f(\underline{v}) = f_0 + \sum_{k=1}^{d} f_k(v_k) + \sum_{k<l}^{d} f_{kl}(v_k, v_l) + f_{kl...d}(\underline{v}) \tag{3.6}$$

Then, a functional decomposition of its variance V is available, i. e. the total variance $V(f)$ can be expressed by the variance shares V_{kl} of the individual elementary parts (EFRON and STEIN 1981):

$$V(f) = \sum_{k=1}^{d} V_k() + \sum_{k<l}^{d} V_{kl}() + V_{kl...d}(). \tag{3.7}$$

The individual variance shares are thereby mutually exclusive, i. e. V_{12} only explains the variation explainable by the interaction of v_1 and v_2 and does not contain V_1 (ARCHER et al. 1997). By dividing Equation 3.7 by the total variance, the Sobol' indices result:

$$1 = \sum_{k=1}^{d} S_k + \sum_{k<l}^{d} S_{kl} + S_{kl...d}. \tag{3.8}$$

Since they add up to one, they can be interpreted as the share of variability, i. e. the sensitivity, of the SRQ to an individual elementary combination of variables $\underline{v}$. However, since there are $2^d - 1$ terms and it cannot be assumed that higher order interactions are negligible (ARCHER et al. 1997), HOMMA and SALTELLI (1996) introduced the total index S_T which contains the variance of all terms that a variable is part of. This ensures that no parameter is deemed negligible despite having significant influence even in interactions of higher order. In current practice, only first and total indices are routinely computed (IOOSS and LEMAÎTRE 2015). Additionally, total order indices are comparable to μ^*_{Morris} from a screening analysis (SALTELLI et al. 2002, p. 96).

In order to exactly compute the Sobol' indices, the solution of multi dimensional integrals for the respective variance shares is necessary. However, this is not possible, even for small models (SALTELLI 2002). Thus, estimators of the indices based on MCS were developed (IOOSS and LEMAÎTRE 2015): They rely on two sampling matrices A and B of size $n_{Samples} \times d$. Subsequently, two new matrices Ab and Ba are generated where one column, i. e. the sampling value for one factor, is replaced by the same one of the other matrix (see Figure 3.5 on the next page). For the factor v_2 this results in e. g.:

$$A = \begin{bmatrix} v_{11}^A & v_{21}^A & \cdots & v_{d1}^A \\ v_{12}^A & v_{22}^A & & v_{d2}^A \\ \vdots & & \ddots & \vdots \\ v_{1n_{Samples}}^A & v_{2n_{Samples}}^A & \cdots & v_{dn_{Samples}}^A \end{bmatrix} \qquad B = \begin{bmatrix} v_{11}^B & v_{21}^B & \cdots & v_{d1}^B \\ v_{12}^B & v_{22}^B & & v_{d2}^B \\ \vdots & & \ddots & \vdots \\ v_{1n_{Samples}}^B & v_{2n_{Samples}}^B & \cdots & v_{dn_{Samples}}^B \end{bmatrix}$$

$$Ab_2 = \begin{bmatrix} v_{11}^A & v_{21}^B & \cdots & v_{d1}^A \\ v_{12}^A & v_{22}^B & & v_{d2}^A \\ \vdots & & \ddots & \vdots \\ v_{1n_{Samples}}^A & v_{2n_{Samples}}^B & \cdots & v_{dn_{Samples}}^A \end{bmatrix} \qquad Ba_2 = \begin{bmatrix} v_{11}^B & v_{21}^A & \cdots & v_{d1}^B \\ v_{12}^B & v_{22}^A & & v_{d2}^B \\ \vdots & & \ddots & \vdots \\ v_{1n_{Samples}}^B & v_{2n_{Samples}}^A & \cdots & v_{dn_{Samples}}^B \end{bmatrix}.$$

Also, SALTELLI (2002) suggests using symmetries in order to only require *Ab* for a simplified estimator calculation. However, using both re-sampled matrices generally provides more accurate estimates (LILBURNE and TARANTOLA 2009). Additionally, as ARCHER et al. (1997, p. 110) mention, an estimate of sensitivity should always include an estimation towards its sampling variability. In order to provide this information, suggested methodologies include the use of e. g. random repetition (IOOSS et al. 2006) or bootstrap methods (ARCHER et al. 1997).

3.3.4 Uncertainty in Additive Manufacturing

The application of the presented technologies is also discussed with a focus on AM. HU and MAHADEVAN (2017) provide an insight into the current status, opportunities and needs of uncertainty management in AM and they present both experimental and model-based UQ efforts. Due to the high effort connected to experimental studies in AM, model-based UQ is the more favorable solution. Additionally, they suggest using Sobol' Indices for the reduction of the dimensionality of the variation problem in order to decrease numerical effort.
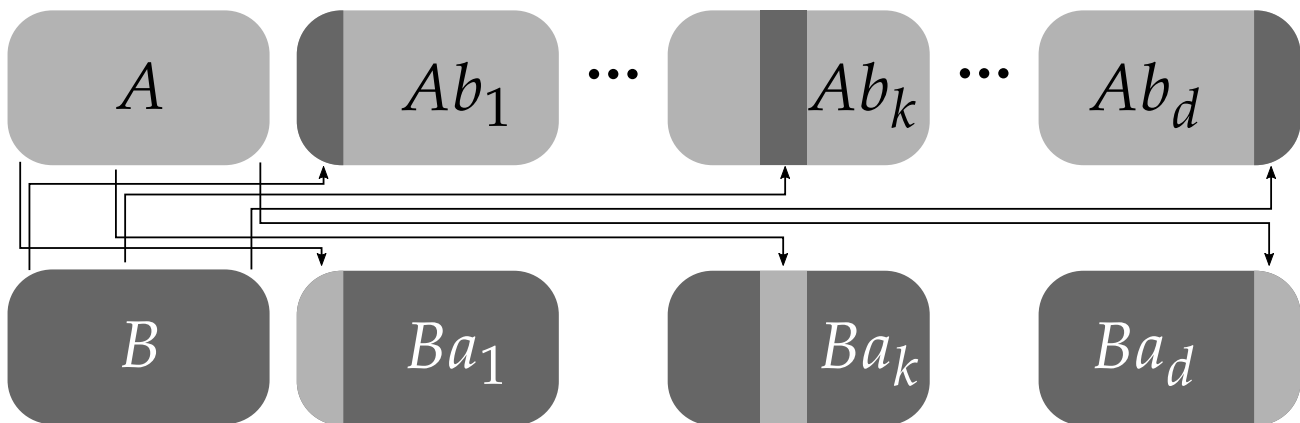
Figure 3.5: *Schematic of the build-up of sampling matrices for the estimation of Sobol' Indices; variations of the the initial sampling matrices A and B are generated by replacing individual columns from data of the respective other one.*

They conclude that there is a need to apply UQ and SA methods to validated multi-scale, multi-physics models of AMPs in order to advance the field.

Similarly, LOPEZ et al. (2016) recognize that while an increasing number of models are developed for AM, there is a common lack of indication about their variability and bias. They identify four main types of uncertainty within this context[8]: modeling assumptions (model uncertainty), unknown simulation parameters (input uncertainty), numerical errors, and measurement error in calibration data (lack of data validity). They present corresponding results for a melt pool width prediction model with a very fast execution time of 0.1 seconds. The 4000 samples are generated via MCS and the overall, so-called, validation uncertainty from different sources is calculated as the norm of the contributing factors of numerical, input and measurement uncertainty. There is no distinction between different types of uncertainty, i. e. aleatory and epistemic variables. However, the study highlights the necessity of correctly assessing uncertainty for the quantification of the predictive capability.

Lastly, MOSER (2017) provides a multi-scale simulation approach for LBM covering the particle and the powder bed scale. All predictions and results are accompanied by uncertainty estimates and the importance of providing the respective information is emphasized.

3.4 Research Gap

The management of form deviations in LBM is investigated by many researchers and there is constant progress towards the goal of FTR manufacturing. While there are other compensation mechanisms than PD, they affect secondary target quantities of the process in a non-negligible magnitude. However, for PD to become a robust tool for distortion management, some aspects need further investigation.

First, the coverage of simulation models should extend beyond the LBM process itself, as distortion is a quantity that is altered along the process chain. Thus, optimizing form accuracy for the as-built state may not provide sufficient results for the workpiece at a later phase. Additionally, models should provide explicit information on the applied verification and validation procedures. Second, there is only limited knowledge available on the variability of form accuracy and its predictability in AM. There are experimental studies that focus on dimensional stability for changing parameters and uncertainty is respected within the micro scale, but there is no systematic investigation concerning form deviation variability. Lastly, the available methods for PD do not account for non-linearity within the process and reveal a conflict between the required form accuracy of the mesh and the necessary computational effort. This thesis addresses all of theses challenges.

---

[8]The terms in brackets connect the mentioned types of uncertainty to the terminology used within this thesis.

4 Intended Added Value

The following paragraphs present the scope of this thesis, the corresponding goals as well as a classification.

4.1 Scope

This thesis is intended to contribute to the goal of FTR manufacturing in AM within the following surrounding conditions:

Design It is assumed that all possible design adjustments are already integrated and hence the initial design, i. e. the target geometry, is fixed. Additionally, the use of the simulation tool may provide benefit in scenario analyses, when e. g. a number of different design alternatives are to be compared.

Support The use and design of support structures will not be discussed, i. e. all workpieces are assumed to either not require support structures or to be designed with support structures made from bulk material.

Orientation The orientation of the workpiece may significantly affect distortion. For this thesis, it is assumed that the orientation is fixed or already optimized with respect to all relevant criteria, e. g. build job duration, necessary support volume or distortion potential, with a suitable cost function.

Data conversion Errors from data conversions on the way from CAD to actual workpiece are outside of the scope. While there are studies that show the challenges in this topic (ZENG et al. 2013), the providers of CAD systems are expected to solve these problems in the near future.

Optimization target The developed methodology functions as an optimization of form deviations in all individual points of the computational mesh, equally weighed. While it may be sufficient or even required for specific use cases to limit the adjustment of the input geometry in selected areas of the workpiece only, this is considered a subset of the intended methodology.

LBM process chain The steps subsequent to the separation of the workpiece from the build plate are not considered in this thesis (see Figure 2.2 on page 7).

Material All investigations were conducted with the material IN718. Most of the conclusions can be transferred to other materials, but e. g. the absence of plasticity from solid-state transformations needs to be reconsidered.

4.2 Goals

The overall goal is the development of a methodology for the management of form deviations and their reduction by simulative pre-deformation. Thus, the following functional top-level

goals are derived:

- The model is able to predict form deviations of industrially relevant workpieces along the LBM process chain with sufficient accuracy.
- The magnitude and influence of uncertainty is investigated and can be respected for the predictions. Information on the importance of uncertain factors can be extracted.
- The simulation result can be used to generate a pre-deformed geometry that exhibits less and/or smaller form deviations after manufacturing. The methodology should account for non-linearity and industrially relevant constraints, e. g. in terms of computational effort.

In order to provide measurable indicators, smart (DORAN 1981) subgoals need to be identified. Since the developed methodology is a digital pre-process, the classification scheme for software engineering requirements can be applied. The top-level goals mentioned above can then be broken down according to the categories of ISO/IEC 25010. However, only the most relevant quality criteria are included.

Functional Suitability This criterion summarizes i. a. aspects of functional correctness and completeness. In this respect, the developed model is required to

- integrate the relevant phenomena that are expected to contribute to the mechanical response in a non-negligble way,
- predict the trends of the residual stress state of the workpiece in the range of the measurement accuracy,
- provide estimates for the resulting form deviation with an error in the magnitude of the variability between samples,
- yield a comparable magnitude of variability in the SRQ from uncertain parameters and
- provide an optimized input design for manufacturing that exhibits significantly reduced form deviations compared to the initial design.

Performance Efficiency The main alternative to the provided methodology is a manufacturing-based trial-and-error optimization of the input design. In order to provide benefit, the model is thus required to

- yield predictions of form deviations faster than the actual build up time and
- demand significantly less (monetary) resources than the manufacturing-based process.

Reliability The main aspect of interest regarding this criterion is the maturity of the simulation model, i. e. the reliability under normal conditions. As mentioned in Subsection 2.3.2, maturity of a simulation model can be assessed by the PCMM. Since the intended use of the model is design support, the overall requirement is a maturity level of 1 if not mentioned otherwise. Thus, the method and the model are required to

- accurately represent the geometric fidelity of the parts to make it suitable for pre-deformation (here: maturity level 2),

- be physics-based for the important, i. e. the structural, process,
- provide and allow for unit and regression tests for code verification,
- include qualitative estimates on numerical effects on the SRQ,
- provide a quantitative accuracy assessment for workpieces that are similar to the intended applications as well as information on the experimental uncertainty from both measurement and variability and
- contain a quantification of sensitivities and the effect of uncertainties on the SRQ.

The remaining criteria (maintainability, portability, compatibility, usability and security) are more relevant for software engineering and, thus, the corresponding requirements are of optional character. However, adherence to these criteria may increase the suitability and long-term benefit of the developed model. The following chapters describe the steps undertaken to develop the proposed method within the framework of this thesis.

5 Distortion Simulation for Laser Beam Melting

In this chapter, a method to model the development of form deviations along the whole process chain is presented. First, the experimental setup, i. e. the used manufacturing system as well as the acquisition of SRQs, is defined. Subsequently, preliminary model identification experiments and their results are reported and the employed model for the LBM process is defined. Before the chapter is concluded by results of verification and validation tests, the model is extended to the stages of stress relief annealing and separation.

5.1 Extraction of System Response Quantities

The LBM process has many influencing parameters and, similarly, just as many quantities that could be considered as characteristic SRQs. These comprise among others: temperature, stress, plastic strain, form deviation, roughness, material composition, porosity, hardness and fracture toughness. Since the goal of the proposed methodology is the reduction of the overall form deviation of a workpiece, this quantity is considered the primary SRQ[9]. Additionally, as Figure 2.3 on page 11 depicts, the stresses complement the mechanical response of the workpiece and are thus also considered.

5.1.1 LBM Samples

All samples in the context of this thesis were built using one of the machines given in Table 5.1. The standard parameter settings of the machine manufacturer (EOS GmbH (EOS)) were used for all machines, but only the *EOS M270* works with a layer height of 20 µm. Additionally, the global scaling setting was deactivated since the simulation model is designed to include the shrinkage effect. In contrast, since the simulation is not designed to respect local effects, the beam offset was determined according to the specifications of the manufacturer and applied in all build jobs.

The used powder feedstock satisfies the chemical specifications of the alloy 2.4668, i. e. IN718, and was purchased from different suppliers (Oerlikon Metco Europe GmbH: Metco Add 718A, EOS GmbH: NickelAlloy IN718, TLS Technik GmbH & Co. Spezialpulver KG: Ni Alloy 718) and batches. The initial powder distribution is given with $d_{10} = 10\,\mu m$ and $d_{90} = 45\,\mu m$. However, these values may shift with progressing reuse.

---

[9]Even while the induction of strains is temperature-based, the thermal field is not a key SRQ as the distortion is dictated by the distribution of inherent strains. In future efforts, in-process temperature measurements, like the ones performed by CHIUMENTI et al. (2017), may be used to assess model suitability concerning this SRQ.

Table 5.1: Overview of the main properties of the used LBM machines

| Reference	Type	Operating organization	Maximum laser power in W	Layer height in μm
M270	EOS M270	*iwb*[a]	200	20
M400	EOS M400	*iwb*	1000	40
M280	EOS M280	MTU Aero Engines AG	400	> 20
M290	EOS M290	Ariane Group	400	40

[a] Institute for machine tools and industrial management of TU Munich, Institut für Werkzeugmaschinen und Betriebswissenschaften der TU München (iwb)

5.1.2 Acquisition of Form Deviations

As discussed in Section 2.2 on page 9, form deviation is not an SRQ of the simulation, only displacement is. For some simple structures like a cantilever with cut supports that almost exclusively experiences distortions in build-up direction, these quantities may be assumed to be equal with a high degree of certainty (MUNSCH 2013, pp. 71ff.). However, for more complex geometries and without the existence of a priori knowledge of undistorted areas of the workpiece, this comparability cannot be assumed.

Multiple strategies were investigated for their suitability to increase congruency between form deviations and displacements within this thesis, but no general methodology can be supplied: Besides being only available for the measurement directly after LBM, additional structures on the build plate are affected by the overall shrinkage from processing to ambient temperature. Another possibility is the introduction of marker structures into the workpiece. However, if they are large, they may affect distortion behavior and when they are small they either do not provide the necessary accuracy (apparent rotational errors in the comparison after alignment) or confound the errors from alignment and the difference between form deviations and distortion in a non-negligible way. Lastly, custom fitting strategies, i. e. 3-2-1 alignment with a plane, a vector and a point that are expected to only have negligible distortions, require a priori knowledge.

Thus, the following approach is taken for this thesis. For one geometry with a very distinct distortion mode, i. e. the turbine blade structure shown in Figure 5.1a, the maximum of the form deviation at the tip of the blade in the projection direction of the respective surface is assumed to be comparable to the maximum displacement. For another geometry, i. e. the panel structure shown in Figure 5.2a (courtesy of MTU Aero Engines AG), only direct comparisons between the simulation and the measurement result are deemed suitable. The alignment of both results was done via a best fit approach, resulting in a suitable indicator for the overall error of agreement. This quantity should, however, not be interpreted locally as a measure of the simulation error, since multiple types of error are confounded. Additionally, due to confidentiality reasons, only normalized deviation results are reported for the panel geometry. The reference is determined as the maximum form deviation of the as-built panel, manufactured on the *EOS M270*, compared to the CAD model.
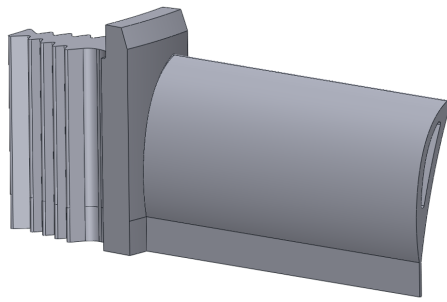
(a) Blade geometry

(b) Initial (light) and deformed (dark) blade geometry after LBM

Figure 5.1: *First benchmark workpiece for this thesis: (a) a simple turbine blade geometry and (b) its distortion behavior within the LBM process*

The acquisition of the workpiece form was performed using optical measurements with stripe light projection. However, metallic parts routinely exhibit reflective surfaces necessitating anti-reflection coating. This was performed via spray aeration of a TiO_2 suspension. The corresponding layer thickness was assessed to be lower than 15 µm even for a multiple of the passes that are necessary for a sufficient matting effect. Thus, the errors introduced by the coating itself as well as its variability were deemed negligible and have not been accounted for.

For all in-house measurements of form deviations, a Comet L3D 2M 3-D-Digitizer from Steinbichler Optotechnik[10]was used. A measurement system analysis was performed in order to quantify bias and variability of the measurements. Experiments with a gauge block of a defined length of 75.000 mm yielded a systematic bias of 10 µm and a standard deviation of 15 µm. While the bias was deemed to be negligible for the studies in this thesis, variability was accounted for by discretizing measurement values to multiples of the 95 % confidence

(a) Panel geometry

(b) Initial (light) and deformed (dark) panel geometry after LBM (see also Figure 5.7 on page 59)

Figure 5.2: *Second benchmark workpiece: (a) a panel structure with a height of approximately 150 mm from the aerospace sector and (b) a superposition of the initial and the distorted state after manufacturing via LBM*

---

[10]Today: Zeiss Optotechnik

interval of the reference measurement, i. e. approximately ± 2 standard deviations, i. e. 60 μm. This reduces the probability of drawing faulty conclusions from noisy data. The influence of different operators, i. e. varying measurement personnel, is neglected.

For all measurements conducted at external facilities, no estimate of the measurement error is available. Optical measurements conducted externally are assumed to provide similar accuracy as the in-house equipment. In contrast, tactile measurements are assumed to have negligible inaccuracies, i. e. results are reported with the resolution the equipment provides.

5.1.3 Determination of Residual Stresses

There are multiple methods to quantify the residual stress level in a specimen either directly via strain measurements or indirectly, e. g. via the resulting distortion when the mechanical equilibrium is shifted. In the context of this thesis, residual stresses were measured via neutron diffraction, since stress levels within the bulk material were to be determined. The respective studies are reported in detail in BAYERLEIN et al. (2016, 2018), but the most important findings are described in the following. With the beam time being the limiting factor in neutron diffraction experiments, a compromise between, e. g. the number of sampling points, positioning effort and signal-to-noise ratio due to attenuation by traveling through the sample medium, is necessary. For increased spatial coverage, a thin cuboid geometry $(40 \times 10 \times 40 \, \text{mm})$ was used as the specimen for both studies.

The measurements were performed at the STRESS-SPEC instrument in Garching, Germany. A wavelength of 1.55 Å was selected using the Si (400) monochromator, which allowed measuring the Ni$\{311\}$ reflection at a scattering angle of about 91°. The gauge volume was defined by a $2 \times 2 \, \text{mm}^2$ slit in the incoming beam and the radial collimator being opened to a 2 mm field of view for the diffracted beam.

The conversion from the position of the intensity maximum of the diffracted beam, i. e. the measured lattice spacing, into a strain was done via the measurement of a stress-free reference sample, i. e. the lattice spacing in the undistorted state for each respective axis. The evaluation of multiple candidates for a stress-free reference sample confirmed the recommendation of other studies (e. g. BRANNER (2010, p. 133) and WANG et al. (2017)) that small rods cut from a duplicate of the measurement specimen are most suitable (WEIRATHER et al. 2015). Using other candidates, e. g. small cylinders built on the same build plate, hollow cylinders (filled with powder) both as-built or after stress relieving, as the strain-free reference specimens, leads to non-physical stress results with non-negligible stress components close and normal to a free surface. SOCHALSKI-KOLBUS et al. (2015) confirm the unsuitability of powder specimens. However, with dimensions of $3 \times 3 \times 3 \, \text{mm}^3$, the rods cannot be assumed to be completely free of stresses, which may introduce errors. SOCHALSKI-KOLBUS et al. (2015) suggest that using additional constraints by balancing forces and moments across one or more cross-sections may provide an even better estimate of the stress-free lattice spacing.

However, due to the sparsity of the data collection points over the respective cross-sections in the performed experiments, this method was not applied.

Since the stress is a symmetric tensor, measurements are generally required in six orientations to determine the complete stress state. However, due to limited beam time, only three perpendicular strain components were measured for most positions. While this may not account for all of the stress in the sample, the calculation of these stress components is valid (WINHOLTZ and KRAWITZ 1996).

5.2 Model Identification Experiments

In this section, preliminary experiments concerning the influence of selected factors on the magnitude of form deviations are presented. These experiments are not meant to represent an exhaustive investigation, but to give supplementary information to other studies, e.g. KRAUSS (2016, pp. 68ff.).

5.2.1 Influences of Environmental Variables

The study consisted of three jobs of 18 turbine blade workpieces each (see Figure 5.3 on the next page): Two jobs were built on the *EOS M270* machine and as-built geometries were measured with the in-house Comet L3D 2M 3-D-digitizer. The remaining job was built on the *EOS M290* system and measured at Ariane Group. The investigated SRQ was determined from the measured geometry as mentioned in Subsection 5.1.2 on page 50. Figure 5.3b on the next page shows box plots[11]of the SRQ for the three build jobs. Providing mean and standard deviation is not sufficient since only the results for the first job on the *EOS M270* machine passed the Shapiro-Wilk test for normality (SHAPIRO and WILK 1965).

The results of a multiple linear regression model applied to the gathered data are shown in Table 5.2 on the following page, along with conclusions for the modeling efforts within this thesis. With a coefficient of determination R^2 of 0.60, the results suggest that there is a significant portion of random noise within the dataset that cannot be explained by the provided factors. This may either be due to a poor selection of factors, i.e. other systematic influences that were overlooked, due to low statistical power or due to inherent randomness in the system.

The large and significant effect of the machine type on the resulting distortion may be attributed either to a difference in the introduced plastic strains via altered temperature gradients (primary effect) or a difference in material properties leading to an altered mechanical
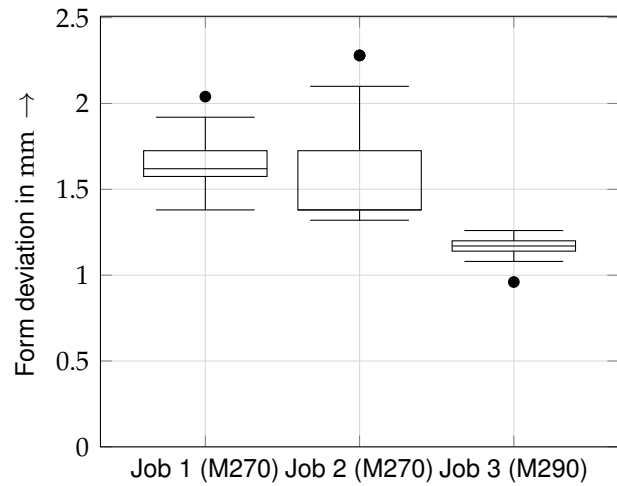
---

[11]All box plots in this document follow the convention of TUKEY (1977): The whiskers' maximum range is defined as ± 1.5 of the interquartile range, i.e. the range from the 75th to the 25th percentile. All values beyond this range are marked as outliers.
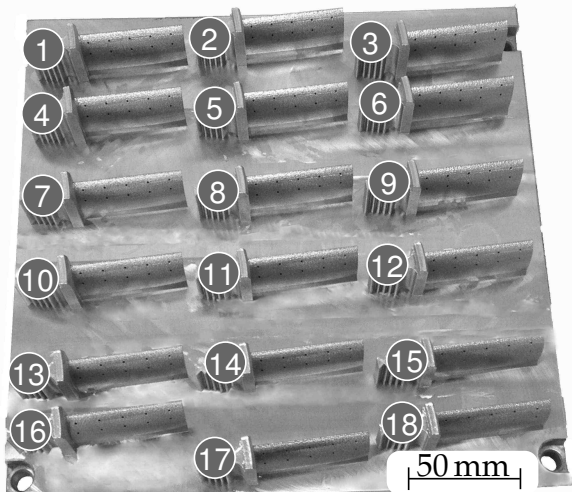
(a) Experimental result of the EOS M290 *job. For all jobs, the coating mechanism moved from right to left.*

(b) Summarized SRQ results for all positions grouped in build jobs

Figure 5.3: *Layout and results for the study on variability from environmental variables*

response to similar loads (secondary effect). The data gathered by KRAUSS (2016, p. 74), yielding e. g. an effect size of approximately 20 MPa for different layer heights (20, 30 and 40 μm) on the Young's Modulus, suggests that the effect of the difference in the layer thickness on the material properties is not sufficient to explain the magnitude of the determined effect in this thesis.

Table 5.2: *Results from a multiple linear regression model for the variability analysis: the factor "job" is not significant, but "machine" and "position" are. However, only the coefficient for "machine" is significantly higher than the assumed noise within the model.*

Factor	Coefficient	Standard error	p-value	Conclusion for the LBM model
Job	−0.097	0.068	0.160	The inclusion of job-based factors, e. g. humidity and temperature in the room, into the simulation is deemed unnecessary.
Machine	−0.330	0.118	0.007	The model should not be agnostic of machine-specific parameters.
Position	−0.015	0.005	0.006	The modeling of the build plate, its fixation state and the workpiece position is necessary (also suggested in SEIDEL (2016, p. 127)).

The significant difference from machine to machine is confirmed by DUNBAR et al. (2017). In their study, in-situ distortion measurements of $6.35 \times 6.35 \times 1.5 \, \text{mm}^3$ Ti-6Al-4V specimens are compared between a Renishaw and an EOS machine. The resulting difference of 10 % is reported alongside the differing thermal conditions and they conclude that machine specific distortion mitigation strategies are necessary. Since there is no data concerning the comparability of the resulting mechanical properties of the samples on the two respective machines,

no information discerning the relative importance of primary and secondary effect can be ascertained.

In order to investigate the variability in form deviation for an industrial use case, tactile inspection data from a production environment was collected. The variability within an observation period of twelve months is shown in Figure 5.4 together with the six sigma bounds and the respective tolerance range for this workpiece. The data is normalized by the target magnitude of the measured distance and the tolerance margin is not negligible. While there is significant variability, the six sigma bounds do not exceed the tolerance range. Thus, in this use case, it is not necessary to increase process stability by employing further methods of process control or quality assurance. However, for other workpieces with more rigid tolerance margins, this may be different. Additionally, it is apparent that there is a decrease in variability for later periods of observation. This may indicate that employed quality assurance measures successfully increased process stability for this workpiece. In summary, workpieces also exhibit varying degrees of form deviation within production environments, but the variability does not exceed the given tolerance range for the investigated case. A pre-deformation method may thus provide sufficient results without handling variability and only correcting for the overall bias (cf. Figure 2.9 on page 18).
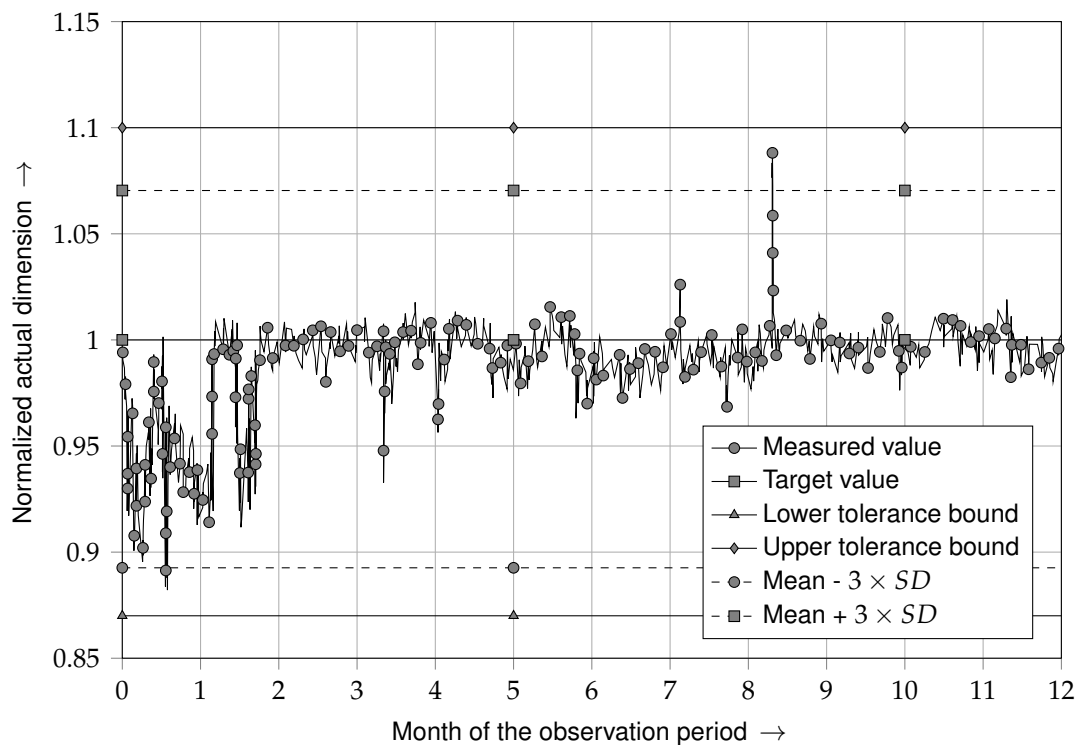
Figure 5.4: *Variability of form deviations for an industrially relevant workpiece at one measuring position for one year and three machines of the same type. A total of 850 workpieces was measured. The data were reconstructed from a provided plot with permission of the originator.*

5.2.2 Systematic Influence

Workpiece Spacing In order to quantify whether surrounding workpieces exert an influence on the resulting distortion of a workpiece, a study with the blade geometry and form following heat storages (see Figure 5.5b) was conducted and is described in this subsection. A total of six configurations with varying distance between workpiece and heat storages and two different thicknesses of the latter were manufactured on the *EOS M280* system (see Figure 5.5a). Table 5.3 shows the characteristics of the respective configurations and the resulting form deviation. For the measurements, the heat storages were milled off in order to allow optical data acquisition.

All specimens show the same distortion trend as the workpieces without heat storages (see Figure 5.5b) but with a significantly reduced magnitude. Due to the limited size of the study, no significant influence from either thickness or distance can be extracted. However, it is shown that surrounding workpieces may affect the distortion behavior in LBM. Thus, a model should be able to account for this influence as suggested by SEIDEL (2016, pp. 128ff.).

Distortions along the Process Chain As a second preliminary study, the form deviations of the two workpieces were analyzed over the course of the process chain. For the panel geometry, two different machines were used for the specimen generation (*EOS 270* and *EOS M280*) and the separation was realized via sawing and EDM, respectively.

Figure 5.6 on page 58 visualizes the results in the form of violin plots[12] for the form deviations at the respective stages. It is apparent, that the SRA process significantly alters the distortion distribution. All SRA procedures were conducted by MTU Aero Engines AG.

Also, the results suggest that the two employed separation (SEP) methods create distinctly differing responses in terms of form deviations for the investigated workpiece. These results

Table 5.3: Design and results of the conducted heat storage study. The given numbers refer to Figure 5.5a.

Number	Distance in mm	Thickness in mm	Form deviation at the flat side in mm
1	2.5	10	0.84
2	2.0	10	0.90
3	1.5	10	0.72
4	2.5	20	0.84
5	2.0	20	0.84
6	1.5	20	0.0[a]

[a] Workpiece and heat storage fused together at the end of the job

---

[12]Violin plots are a combination of the reduced statistic of a box plot with the detailed information of the local density estimate, i. e. a smoothed histogram (HINTZE and NELSON 1998)
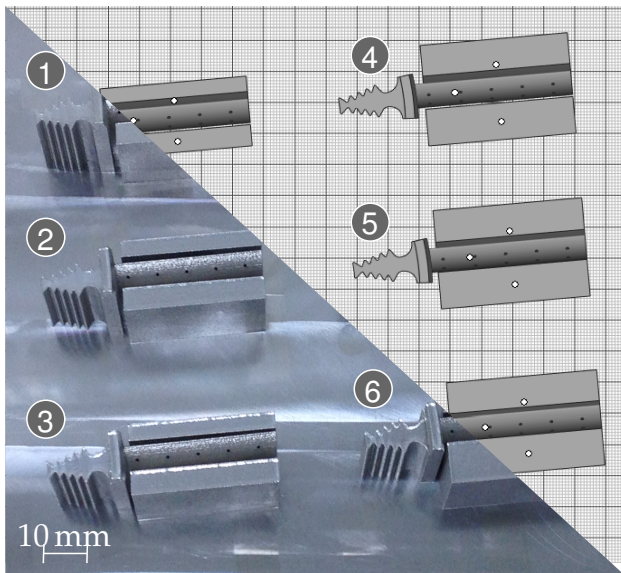
(a) *Overview of the study layout in (top/right) the job preparation software and (bottom/left) after job conclusion*
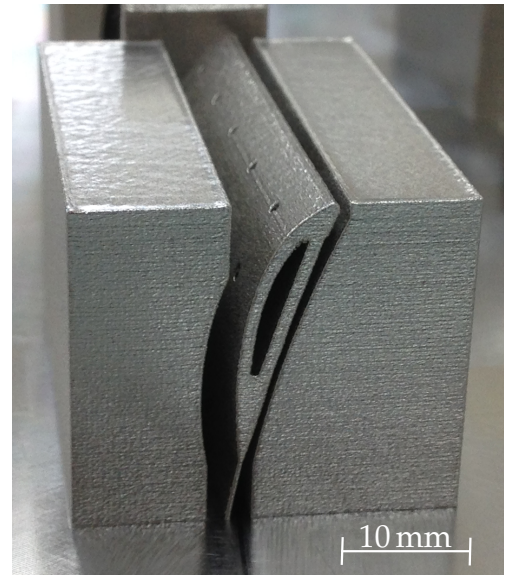
(b) *Compared to the equidistant design with respect to both heat storages, it is evident that the tip of the blade is distorted towards the flat side.*

**Figure 5.5:** *Illustrations of the heat storage study with the turbine blade geometry: (a) Six different configurations of workpiece and heat storages were built that vary in distance and thickness. (b)The typical distortion in the direction of the flat side of the turbine blade.*

suggest a non-negligible influence of the separation method on the distortion behavior. However, in order to determine the corresponding effect size and the respective confidence, a high number of experiments is necessary. This is outside the scope of this thesis.

If juxtaposed with Figure 5.7 on page 59, the difference in distortion behavior due to the manufacturing on different machines is apparent. While there are only small changes to the form of the workpiece built on the *EOS M280* during SRA, the other specimen exhibits a significant alteration. In contrast, the SEP procedure seems to affect the workpieces similarly with a bending around the middle axis in the front direction. This is apparent from the change in deviation on the upper and lower end of the front side in the positive direction and a reciprocal development on the back side for both workpieces. The artifacts on the bottom side of the *EOS M280* manufactured workpiece stem from the reduced height of the specimen because of the sawing process. Additionally, the results show the expected symmetry of the form deviations for a symmetrical workpiece. In summary, the evaluation of histogram information may provide more quantifiable results but is not suitable to be the sole basis for a comparison of form deviations. One additional source of variability stems from the furnace that was used for SRA. When in danger of loosing the vacuum for the procedure, it defaults to holding the current temperature, breaking the nominal heating and cooling cycle.

The difference in distortion behavior may stem from multiple sources and without a statistically sound experimental plan, no attribution can be conducted with certainty. However,
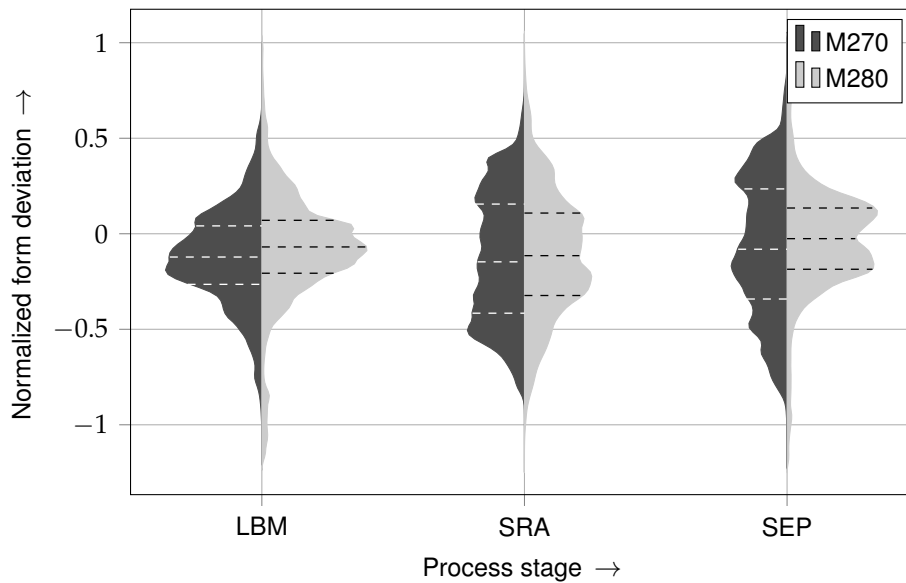
Figure 5.6: *Violin plots of the form deviations for the panel workpiece along the process chain for two different machines: For the states after build-up (LBM) and after stress relief annealing (SRA) the results suggest a similar distortion behavior for the two machines. In contrast, the distributions significantly differ for the state after SEP. Also, for both specimens, the SRA procedure results in an altered distribution of form deviations. The lines within the trace density estimates mark the quartiles of the distribution.*

with the similarity of the distortion results directly after the LBM process and the emerging spread after SRA, it is reasonable to assume that the residual stress state does account for the respective differences. The simulation model should thus be suitable to correctly predict the residual stress state of a workpiece.

Similarly, the blade geometry also shows varying levels of form deviation along the process chain (see Figure 5.8). An initial decrease after the heat treatment can be observed. After the SEP, however, the initial level of form deviation is restored. Additionally, an alternative process route via direct separation after the build-up was investigated. Here, the form deviation reaches a minimum, but since the process route does not include an SRA procedure, residual stress levels in the directly separated blade may still be substantial.

In a similar experiment by KRAUSS (2016, p. 80) with an industrial bracket structure, both the SRA and the SEP lead to increased form deviations compared to the as-built state. In summary, the formation of distortions along the process chain behaves non-linearly and is strongly dependent on the geometry. Thus, a suitable simulation model is necessary in order to predict this quantity.
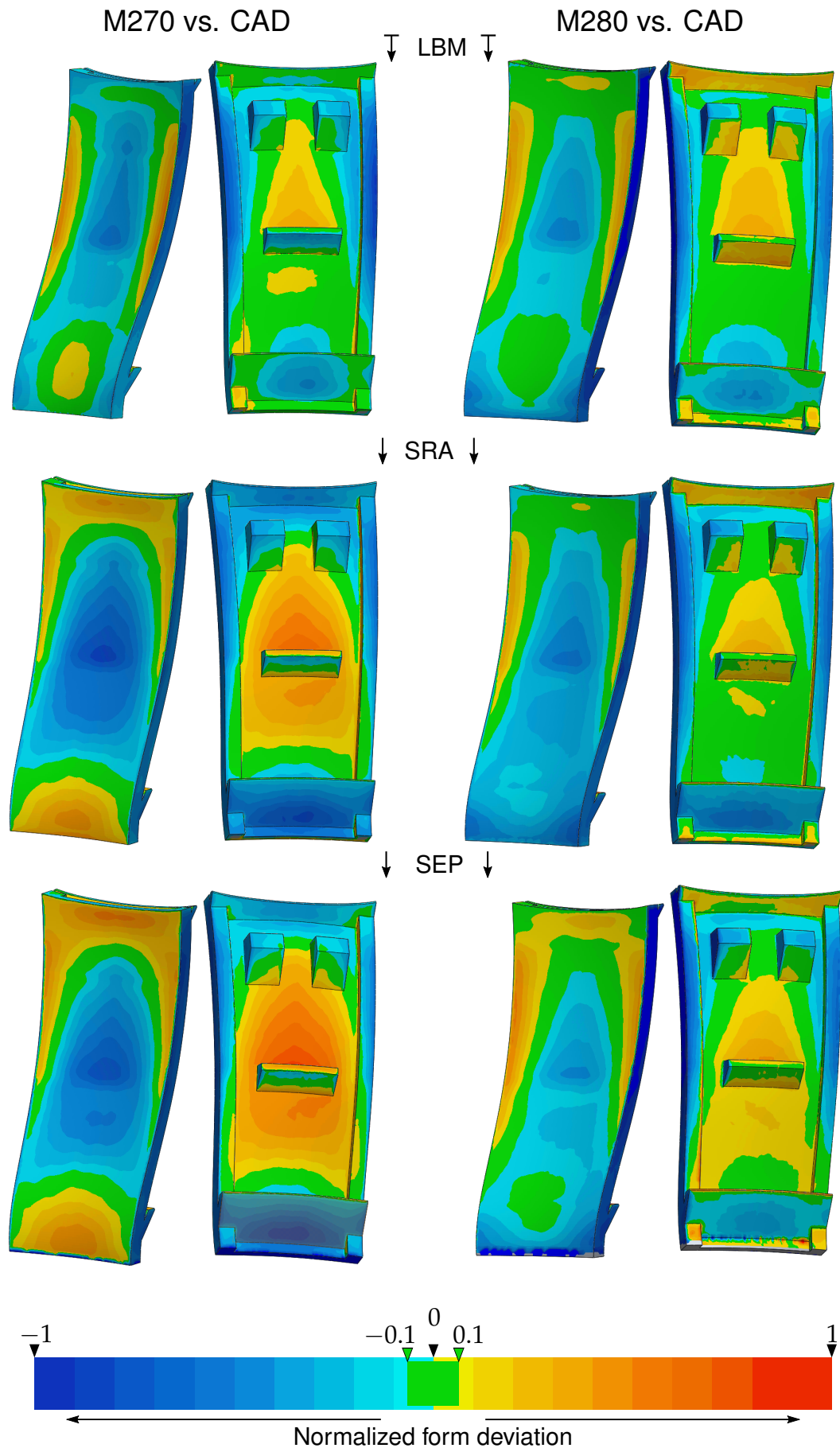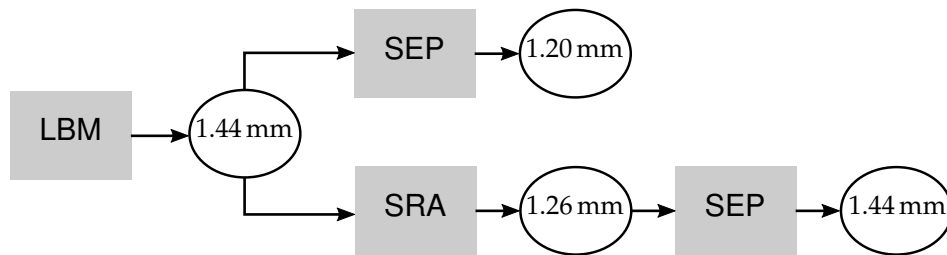
Figure 5.7: *Normalized form deviations of the panel geometry manufactured on (left) the* EOS M270 *and (right) the* EOS M280 *system for different stages of the process chain*

Figure 5.8: Maximum form deviation of the blade geometry for direct separation in comparison to a separation after stress relief annealing

5.3 Conceptual Model

The following paragraphs present the main modeling decisions and simplifications. The section is structured into the description of the modeled mechanisms and the initial and boundary conditions. The conceptual models for the underlying phenomena, i.e. heat transfer and structural mechanics, are omitted for conciseness. The reader is referred to the literature for the respective information (DHONDT 2005).

5.3.1 Modeled Mechanisms

As presented in Subsection 3.1.3, there are multiple mechanisms that dictate the distortion behavior of workpieces manufactured via LBM and they act on different scales. The goal of this thesis is to provide a management strategy that improves the global form deviations before the operation phase. While there may be use cases where local effects prohibit an in-tolerance manufacturing process, it is assumed that these are special cases that are not treated within this thesis, i.e. only the globally acting mechanisms are targeted for by the modeling efforts (compare Table 3.2 on page 28). This comprises the CDPM, the effects of thermal expansion and stress relief as well as the self-healing mechanism.

Additionally, the complex interaction of the laser beam and the powder surface is simplified to a phenomenological heat source, starting with the material at solidus temperature and subsequent cooling. This is deemed suitable as only solidified material exhibits mechanically relevant straining. The phenomenological approach leads to an interconnection of the conceptual and the numerical model. Thus, the heat source needs to be presented in the following section in more detail.

5.3.2 Initial and Boundary Conditions

The elements of the build plate are initialized at room temperature, i.e. $T_{Room} = 20\,°C$, in order to avoid the introduction of displacements from cooling from $T_{Pre} = 80\,°C$ to T_{Room}. Similarly, the elements of the workpiece are initialized at the temperature level of the heat affected zone, i.e. the process temperature T_{Pro} in order to respect the shrinkage when cooling down to T_{Room}. In order to quantify the respective temperature level, the results

of in-process temperature measurements by CHIUMENTI et al. (2017) in a Ti-6Al-4V LBM process are consulted. They determined T_{Pro} for a thin (5 mm) and a thick (40 mm) wall structure for a process with a preheating temperature of 100 °C to be approximately 150 °C and 220 °C, respectively. Since no corresponding results are available for IN718, the respective temperature level is arbitrarily defined as 200 °C due to the difference in T_{Pre} (100 °C vs. 80 °C). Due to its estimative nature, the quantity T_{Pro} is characterized as an ad hoc parameter. Since it dictates the driving temperature gradient, it is identified to represent the machine-specific primary effect of strain introduction and is marked as a suitable candidate for model updating.

The defined thermal boundary conditions are depicted in Figure 5.9: For all nodes on the bottom surface of the build plate, a fixed temperature of $T_{Pre} = 80$ °C is prescribed in order to model the controlled heating during the whole process. In addition, all nodes of the build plate are preheated to 80 °C within the first step. Additionally, several surfaces are attributed convective boundary conditions with a reference temperature of $T_{Conv} = 80$ °C:

- The cooling of the substrate caused by the inert gas flow is modeled in analogy to SEIDEL (2016, p. 119) with a convection coefficient of $h_{WP,top} = 10.6 \, \mathrm{W \, m^{-2} \, K^{-1}}$.
- A low thermal resistance is assumed for the heat transfer to the machine structure on the side of the plate via conduction. In order to avoid modeling the actual machine structure, this heat transfer is modeled as a convection with a correspondingly high convection coefficient of $h_{Plate,side} = 100 \, \mathrm{W \, m^{-2} \, K^{-1}}$.
- The heat transfer to the surrounding powder due to radiation and conduction is, for the same reason, also modeled as a convective heat exchange with the coefficient $h_{WP,side}$. However, the corresponding thermal resistance is assumed to have a high magnitude due to the low contact surface of the powder particles. Thus, for simulations with only a single workpiece, this influence is deemed negligible ($h_{WP,side} = 0 \, \mathrm{W \, m^{-2} \, K^{-1}}$). If, however, another workpiece is in close proximity, $h_{WP,side}$ is estimated according to Section A.3.

After conclusion of the LBM process in the simulation, the model cools down to room temperature. Details on the subsequent process of SRA are presented in Section 5.5.

The mechanical boundary conditions are as follows: During LBM the positions of the bore holes are fixed (consistent with the suggestions of SEIDEL (2016, p. 138), see Figure 5.10). The loosening of the corresponding screws is modeled via releasing the degrees of freedom at the bore holes and introducing a statically determined fixation on the bottom of the build plate at three of the four edges. Similarly, when the workpiece is separated from the build plate, this method is applied for both parts (build plate and workpiece) separately.

When stresses are introduced into the build plate that lead to non-negligible distortion, the displacement field of the workpiece may be significantly altered by a rigid body motion. Figure 5.10 on the following page visualizes the effect exemplarily for a global shrinkage of
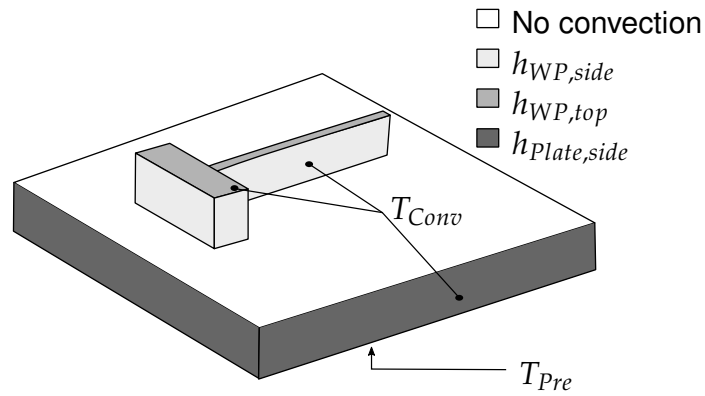
Figure 5.9: *Boundary conditions for the LBM simulation illustrated on a "T"-like workpiece on the cuboid build plate; the rectangle on the front side of the build plate represents a cutout so that the bottom surface of the build plate can be shown.*

the build plate. This may occur similarly for other modes of deformation of the build plate, possibly introducing another source of error into the comparison between form deviations and displacements. In this thesis, this source of error is controlled by either ensuring a negligible build plate distortion and thus a negligible influence on the SRQ (blade geometry) or only conducting direct comparisons to the measured data in combination with a best-fit alignment (panel geometry).
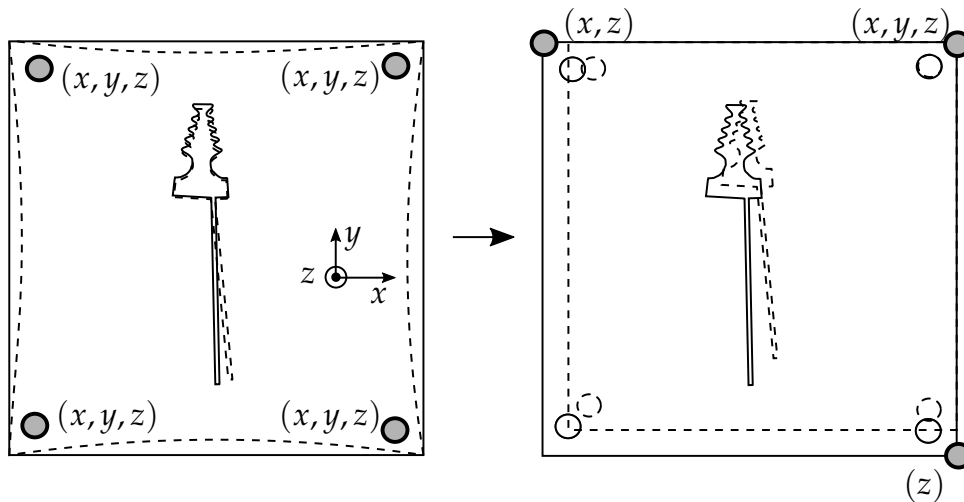
Figure 5.10: *Change in displacement results of the workpiece when the build plate exhibits form deviations; this example shows the effect when the build plate is subject to an overall shrinkage. By releasing the degrees of freedom at the bore holes and providing a statically determined fixation for the plate, the displacements of the workpiece are a superposition of the distortion and a rigid body motion of the workpiece. The magnitudes of both the distortion and the shrinkage are exaggerated and the blade and build plate size are disproportionate to allow for an unambiguous interpretation of the figure. The circles filled in gray mark the location for the fixed degrees of freedom that are given in parentheses. The solid lines represent the initial, the dashed ones the deformed configuration.*

5.4 Numerical Model

The simulation requires the defined conceptual model to be translated into an executable numerical model. In the following, the used methodology for the modeling of the material, the stepwise growing of the workpiece, the spatial discretization of the problem as well as the solution method are presented.

In this thesis, the underlying equations for the different phenomena, e. g. heat conduction and elasto-plasticity, were solved with the finite element (FE) method. All simulations were conducted with the three-dimensional structural finite element program CalculiX. The free (both libre and gratis as defined by FREE SOFTWARE FOUNDATION 2019) software uses the input deck format of the commercial program Abaqus, enabling simple verification runs. The equations are solved using the parallel direct sparse solver PARDISO from the Intel Math Kernel Library and nonlinear geometric effects are neglected[13]. Additionally, the method of summarizing multiple real layers into so-called layer compounds is employed.

5.4.1 Material Behavior

The material model for IN718 is taken from SEIDEL (2016). It was determined for standard process parameters on an *EOS M280* machine with a layer height of 20 µm. The model features temperature-dependent stress-strain curves gathered at strain rates that are comparable to the ones occurring within the LBM process. Additionally, λ and c are also given for the temperature range from T_{Room} to T_m. Thermal expansion is respected as a strain component α in combination with a fixed density. Similar information is provided for the material of the build plate (1.1730). The introduction of viscoplasticity, i. e. rate-dependent plasticity, is presented in Section 5.5.

5.4.2 Element Activation Strategy

One of the key characteristics of AM processes in general and also the LBM in particular is the sequential addition of material in order to create the final form of the workpiece. This is commonly realized within the simulation domain as an activation of the respective elements, which are held in a deactivated state until solidification. This deactivated state may either be implemented as the elements having negligible material properties or the corresponding nodes not being respected within the solution calculation. Another key characteristic is the self-healing effect mentioned in Subsection 3.1.3 on page 25: The powder is always melted at the nominal position irrespective of displacements of lower layers. In order to incorporate this effect, a so-called semi-quiet element activation procedure is suggested by AFAZOV et al. (2017). They employ two elastic materials: A very stiff material (10 000 GPa) in combination

---

[13]For further details on the implemented strain and stress theories, the reader is referred to DHONDT (2005).

with a fixation of two subsequent layers in order to provide the nominal position and a very soft (1 GPa) material to allow the current layer to distort without constraints.

The suggested methodology was modified within this thesis in such a way that no additional stresses are induced when the material properties are changed to the ones of the bulk material (see Figure 5.11). The self-healing effect is respected via fixing the nodes on the upper interface of the newly added layer compound before the conversion to bulk material. In step $(b - 2)$, the deactivated elements are activated with very soft elastic properties (10 GPa) in order to distribute the distortion across the layer compound. This greatly reduces the risk of numerical instabilities from distorted elements on the one hand and accounts for the continuous self-healing effect of the real process on the other. Subsequently, the elements are attributed ideally plastic properties so that any elastic strains, that would lead to stresses upon change to bulk material, are converted to plastic strains.

Otherwise, if a distortion in build-up direction is induced, the newly activated layers exhibit compressive stresses that accumulate over multiple layers, resulting in a jackknife-like distortion when the fixation of the topmost layer is finally removed. This behavior is observed for simulations of the distortion of the panel structure when the plastic intermediate step is omitted. An alternative solution to this problem is provided by PAPADAKIS and HAUSER (2017). They suggest the repositioning of not yet solidified elements after every step to their
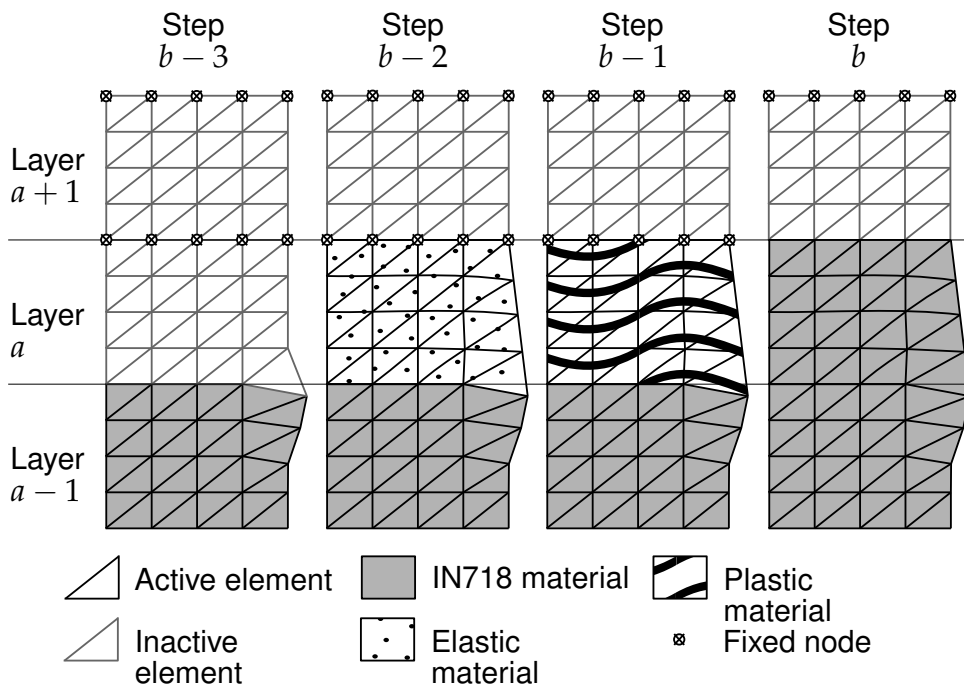
Figure 5.11: *Activation procedure for a robust and stress-free addition of a new layer of material: By distributing the distortion across the whole layer compound, numerical instabilities can be avoided. Additionally, the ideally plastic intermediate material guarantees a stress-free activation of the newly added layer.*

initial position. This may, however, lead to numerically unfit, i. e. distorted, elements for high displacements of the bottom layer.

5.4.3 Digital Data Chain

The targeted PD procedure represents a digital pre-process resulting in a new design that is expected to show significantly reduced form deviations after the manufacturing process. However, besides errors that stem from faulty predictions of the simulation model, there may also be errors resulting from a poor representation of the geometry by the computational mesh. In practice, i. e. in commercial solutions, an interpolation of the result on a representation of higher accuracy is conducted in order to minimize this source of error. This may lead to a satisfying result in some cases but the smoothing of the solution via interpolation may also introduce new errors. For this reason, a different approach is used in this thesis.

In order to avoid loosing fidelity of the geometry representation (one category for the PCMM), the mesh is created from the CAD model with tight constraints on the acceptable surface deviation. In order to retain the ability for a stepwise activation of layers, i. e. the layerwise structure of the mesh, two strategies can be employed (cf. SEIDEL (2016, pp. 56ff.)). First, it is possible to slice the CAD model before the actual meshing procedure. However, this poses a challenge to both the CAD and the meshing program, especially for thin layer compounds[14]. Second, the un-sliced CAD model can be meshed first and the elements can be sorted into slices subsequently. The main benefit of this solution is the straightforward meshing procedure. For this thesis, only linear and quadratic tetrahedral elements with a maximum aspect ratio of ten were used. The meshes were created via Altair's HyperMesh program with differing target element sizes of workpiece and build plate (see Figure 5.12a). However, the challenge is shifted to the slicing procedure. SEIDEL et al. (2013) suggest splitting elements or moving specific nodes to restore a planar interface between layers. However, both methods may lead to unsuitable element shapes (SEIDEL et al. 2013). In order to avoid this drawback, it is suggested to use non-planar layer interfaces, if necessary (see Figure 5.12).

The necessary attribution of elements to certain layers is realized by sorting them into the predefined layer pattern according to the z value of their center of gravity. Then, the interface is defined by the nodes that are shared by elements of two subsequent layers. The respective sets of nodes are required for a suitable fixation (see Figure 5.11 on the preceding page).

The advantage of such a mesh is its suitability for the generation of the pre-deformed design, since the robustness and success rate of the refit procedure are dependent on the level of initial mismatch. Additionally, for very tightly constrained meshes, i. e. meshes with a maximum

---

[14]For the panel workpiece, slicing of the CAD with layer heights lower than 0.5 mm resulted in program crashes. Similarly, meshing of layers smaller than 1 mm results in unmanageably large meshes due to the creation of multiple very small (smaller than 0.05 mm) edges by the segmentation operation.

(a) The meshed CAD geometry with the build plate

(b) Detailed display of every other layer
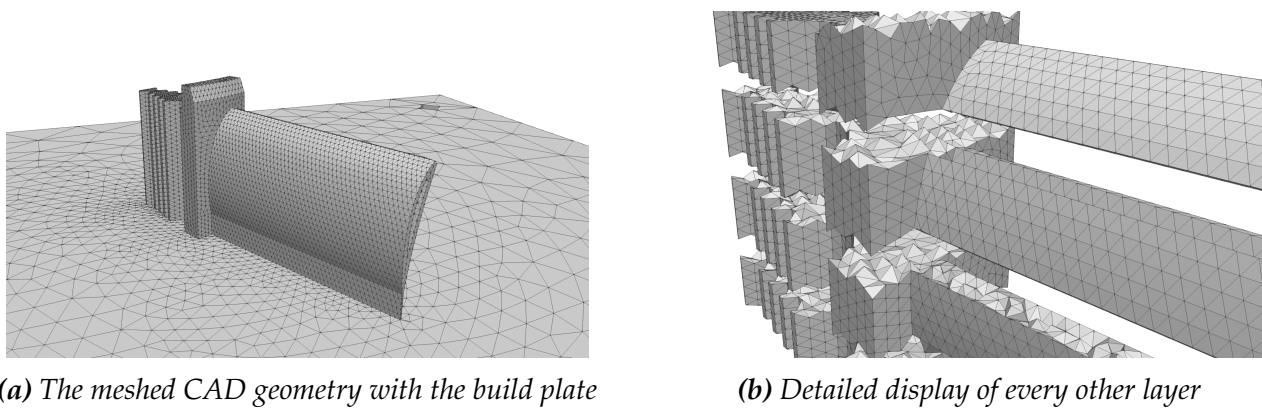
Figure 5.12: *Layerwise mesh sorting: (a) Starting from a tightly constrained mesh of the CAD model to avoid form deviations, layers are formed by all elements sharing a similar z-position of their center of gravity. (b) This results in crinkled interfaces.*

form deviation to the CAD model of less than 0.1 mm, a refit procedure may not be necessary at all. This is, however, connected to higher computational effort due to the finer spatial discretization.

5.4.4 Heat Input

The heat input in the model was designed along the recommendations of BRANNER (2010) and SEIDEL (2016) due to the promising results of these sources. In the respective workpiece-scale models, the heat input is modeled as an instantaneous application of the solidus temperature to the top nodes of the activated layer compound, which is represented as a single layer of elements. The amount of energy that is introduced thus depends on the shape function and size of the respective elements. With linear elements, a constant gradient is introduced over the element size in z-direction. The suitability of this heat input can be explained as an integration of the CDPM on the layer compound scale: Since the resolution of the layer compounds does not account for the subsequent shrinking of the combined layers, a linear temperature slope reintroduces this effect.

With the above mentioned adjustments to the spatial discretization and layer generation, i. e. crinkled interfaces and multiple layers of elements per layer compound, the heat source was redesigned in order to apply the linear gradient. The heat source is implemented as a user subroutine in CalculiX and the nodal temperatures are calculated according to the z-coordinate of the respective nodes of the activated layer compound. In contrast to previous models, the lower temperature level is not set at T_{Pre}, but at the process temperature T_{Pro}. Figure 5.13 on the facing page visualizes the given information in a two-dimensional example for some elements: The temperature for each node is determined by its local coordinate $\tilde{z}$. Since the gradient is fixed, there is no conduction during the heating phase.

This way of applying the temperature load almost entirely removes the dependency of the energy input on both the element order p_e and size l_e. Only the first element row of the

previously deposited layer receives a variable energy input, due to the prescribed T_{Pro} at the top nodes and variable element sizes.

The applicability of this simulative homogenization approach to the heat input is limited to modeling processing strategies that exhibit a similar homogenization via a rotation of the exposure pattern in the actual process. If there are special adjustments, the suitability and the validity of this approach may deteriorate. However, regular patterns with custom rules, e. g. the emerging strategy of only welding against the flow of the inert gas to avoid sputters landing on unsolidified material, may be respected by e. g. combining the approach with inherent strains that model the required asymmetry in the x-y-plane.

Besides this approach, different other types of heat sources were investigated but dismissed due to poor model accuracy. Providing a prescribed nodal temperature to the top nodes, i. e. the interface nodes, and supplying sufficient time for a temperature gradient to build up over multiple layers, led to a prediction of faultily low levels of residual stresses, i. e. not exceeding 250 MPa, in the cuboid workpiece.

5.4.5 Solution Method

The calculation of the resulting displacements and residual stresses is conducted as a sequentially coupled thermal and thermo-mechanical simulation, similar to e. g. SEIDEL (2016, p. 123). The temporal discretization is chosen according to a fitted function and the time steps are scaled with a similarity factor in order to reduce the error introduced by the application of layer compounds (ZELLER 2019). For further details on the thermal simulation the reader is referred to ZELLER (2019).

The parallel direct sparse solver Intel MKL Pardiso was employed for both the thermal and the structural simulation. Since there are no limitations from either CalculiX or the solver, the number of threads for the respective simulations was chosen based on experience and the
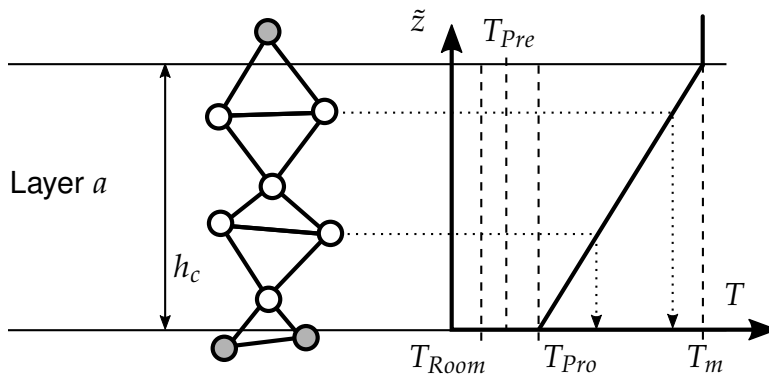
Figure 5.13: *The implemented linear heat source: The ratio of the local coordinate $\tilde{z}$ to the layer compound height h_c determines the prescribed temperature along the slope from process temperature T_{Pro} to melting temperature T_m. The linear slope is not extrapolated for nodes that are beyond the nominal layer compound dimensions (marked gray).*

number of degrees of freedom (DOFs). For small (less than ten thousand DOFs) simulation models, excessive parallelization leads to significantly prolonged calculation times due to problem splitting and thread creation overhead.

5.5 Simulation of Stress Relief Annealing

After the LBM process, workpieces typically exhibit high levels of residual stresses, even exceeding the initial yield strength, as plastification has occurred within the process (BAYERLEIN et al. 2016; SOCHALSKI-KOLBUS et al. 2015). The stress reduction within the SRA process can be divided into the two stages of the heating of the workpiece and the actual annealing at the target temperature. During heating, stress relief is mainly induced by a disproportionate reduction of Young's modulus and yield strength (RADAJ 2002, p. 317). However, for IN718, the potential for stress relief without creep mechanisms is rather low (approximately 5 %), similar to the alloy IN600 (2.4816) investigated by DONG et al. (2014) (see Figure 5.14 and Equation 3.1 on page 27). Creep mechanisms are dictating the strain and stress redistribution in IN718 during SRA . Since residual stresses are, in general, inhomogeneously distributed within the workpiece, the assumption of a uniform reduction of stress levels without a change in deformation cannot be guaranteed. This is also supported by the studies according to Section 5.2, in which the distortion behavior was altered through SRA. While the macroscopic phenomenon within SRA is relaxation, the local behavior is dictated by creep mechanisms. In order to determine a suitable model for the simulation, creep rupture tests were conducted.

5.5.1 Creep Model Identification Experiments

In the following paragraphs, the experimental design and the results of the conducted creep rupture tests are presented.
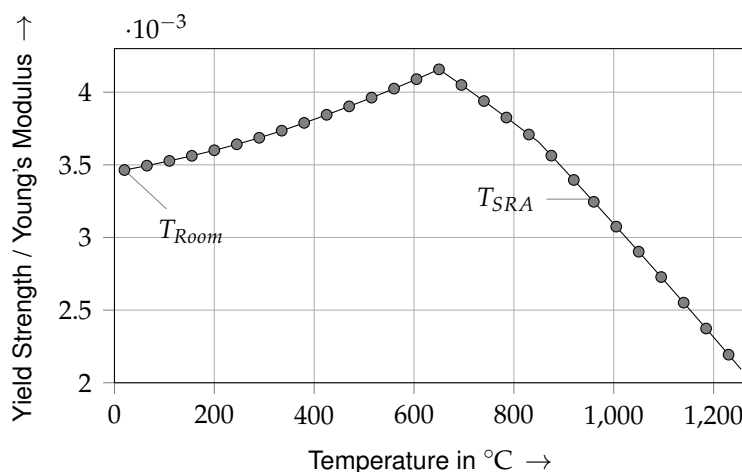

Figure 5.14: Overview on stress reduction potential from material side

Specimens The samples were built as $\varnothing 20\,\text{mm} \times 120\,\text{mm}$ rods with their axis coinciding with the *z*-axis on the *EOS M270* system with nominal parameters. Due to economic constraints, no specimens for repeat tests were built, i. e. the identified curves are based on one specimen per stress and temperature combination. Additionally, since the microstructure of the specimens was intended to properly reflect the state after the LBM process, no stress relief annealing was conducted prior to the creep rupture tests. Consequently, pre-existing residual stresses in the specimens from the build-up process may have added to the applied load stresses, contributing to the uncertainty of the true stress.

However, even without an SRA, the microstructural state of the specimens may not properly reflect the intended state after LBM: Experimental procedures typically involve the heat up of the specimen and the subsequent dwelling on this temperature level for a certain period of time in order to ensure that the entire specimen has reached the temperature level. This may already constitute a heat treatment if the microstructure is not stable at the target temperature, which is the case for IN718 at the respective test temperatures. Additionally, this heat treatment may also affect the level of residual stresses.

Experiments The experiments were conducted at the material testing laboratory, Materialprüfungsanstalt (MPA) Darmstadt. The main design variables in the experiments are temperature and applied stress. With SRA being conducted at 955 °C and SEIDEL (2016, p. 100) showing that there there is significant creep above 700 °C, the corresponding temperature range was chosen. Since there is limited information on the behavior of as-built IN718 at this temperature range, the loading stresses were chosen successively based on the generated knowledge of each experiment in close collaboration with the MPA. The resulting temperature and load levels are given in Table 5.4 along with the time to rupture.

The creep rupture specimens were machined at MPA to $\varnothing 6.7\,\text{mm}$ and tested according to DIN EN ISO 204 while the relaxation specimen was machined to $\varnothing 7.9\,\text{mm}$ and the experiment was conducted according to DIN EN 10319-1.

Table 5.4: *Temperature and stress levels for the creep rupture tests.The loading within the temperature levels is reported in the sequence of the actual tests to document the successive selection process.*

Experimental Condition	Setting											
Temperature in °C	755	755	755	755	855	855	855	855	955	955	955	955
Nominal stress in MPa	400	600	350	500	200	400	150	285	140	100	120	85
Time to rupture in h	23.1	0.7	48.0	4.1	8.1	0.0	40.3	0.5	0.3	3.0	0.8	7.4

Creep Rate Results Prior to the machining, the hardness of all specimens was determined. The tests showed consistent hardness results in the range of 303 and 309 HV30. The results are provided as measured strain with respect to the passed time, i. e. ϵ versus t. The data was processed as follows: The true stress was calculated by respecting the tapering of the

specimens with the temperature dependent ν and the measured strain ϵ. The fraction of the strain related to creep ϵ_{cr} was then calculated by subtracting the elastic strain ϵ_{el} from the total strain ϵ. Lastly, the creep strain rate $\dot{\epsilon}_{cr}$ was determined as the temporal gradient of the creep strain ϵ_{cr}.

Additionally, the provided information of the accuracy of the strain measurement (0.01 %) was converted to a relative error and respected as uncertainty of the creep strain rate under the assumption that the time is, in comparison to the strain, measured perfectly accurately. Only little information is available for the estimation of other error sources, e.g. inherent variability between samples and the variability from the known anisotropy within LBM. For this thesis, the spread of ±12 % in material strength determined by SEIDEL (2016, p. 101) is assumed to be transferable to the creep resistance. Both uncertainty terms were combined via Gaussian error propagation and visualized exemplarily in Figure 5.15 as gray bands. Since the magnitude is negligible, the uncertainty information is omitted for all following plots.

The results for the $\dot{\epsilon}_{cr}$-ϵ_{cr}-curves are provided in Figures 5.15 to 5.17. All diagrams show the absence of a stationary creep regime. Instead, the specimens exhibit a continuously increasing creep rate for growing creep strains, indicating changes in the microstructure (RÖSLER et al. 2012, p. 391).

The result for the relaxation test is shown in Subsection 5.5.3 together with the predictions of the developed creep model.

5.5.2 Model

Without external load, creep strain ϵ_{cr} can only occur up to the level of elastic strains ϵ_{el} present in the material (see Figure 2.4a on page 13). Thus, the model is only required to
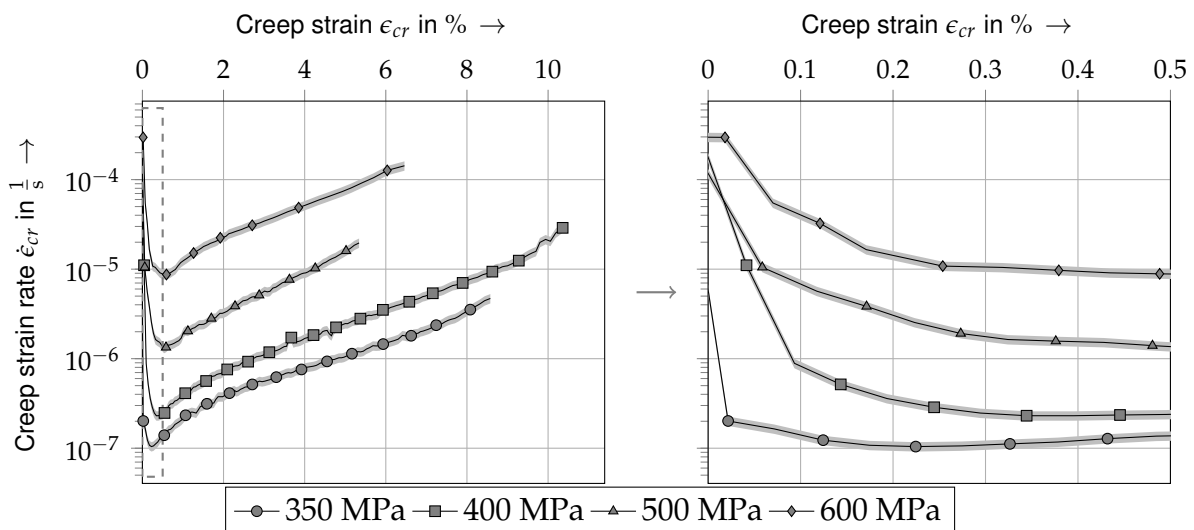
Figure 5.15: *Results of the creep rupture experiments at 755 °C for the whole strain range and magnified for the range of 0.0 to 0.5 % creep strain. The gray bands represent the uncertainty from the measurement and an estimate of variability.*
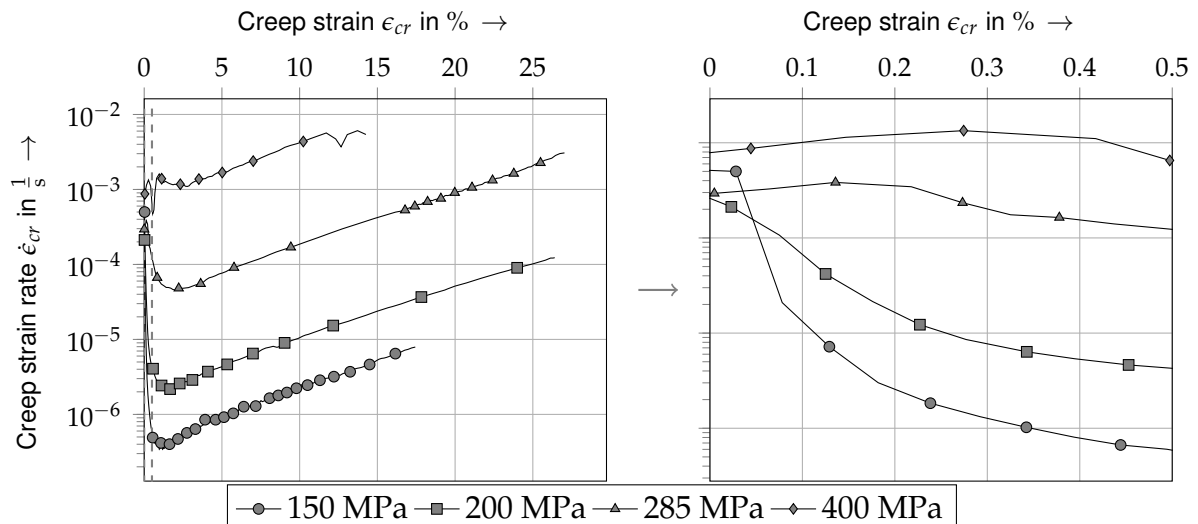
Figure 5.16: *Results of the creep rupture experiments at 855 °C for the whole strain range and magnified for the range of 0.0 to 0.5 % creep strain.*

provide valid predictions for the range from 0 to 0.5 %. Since a hydrostatic loading does not lead to creep straining, the von-Mises stress σ_{vM} is used as the equivalent stress, i. e. the driving force, since it is defined in a way that a hydrostatic stress state is equal to zero.

First, common models from the literature are investigated concerning their suitability: However, the models of Norton and Bailey as well as the one suggested by Garofalo do not show sufficient congruency with the measured data even when fitted with uncertainties respected via orthogonal distance regression. (GAROFALO 1965; NORTON 1929)

Thus, a regression model was built based on suitable transformations of the input quantities obtained from literature. This is similar to the approach of CASTELLANOS et al. (2010) where the fitting parameters for the Garofalo equation exhibited strain dependencies. Similarly,
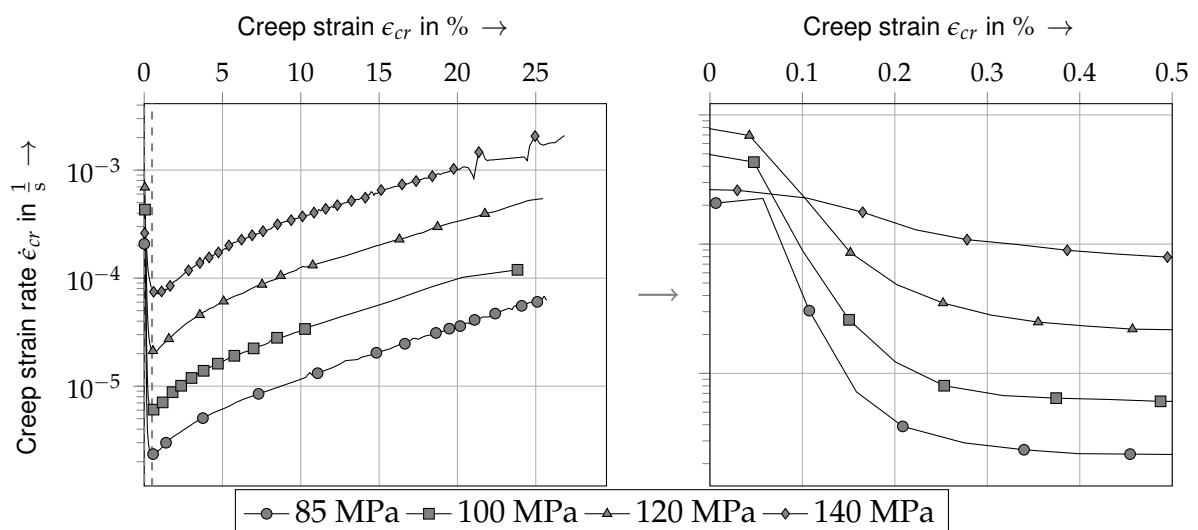
Figure 5.17: *Results of the creep rupture experiments at 955 °C for the whole strain range and magnified for the range of 0.0 to 0.5 % creep strain.*

ALBERG (2003, p. 8) also suggests using linear interpolation of creep rupture results. The assumed creep model is in the form of:

$$log(\dot{\epsilon}_{cr}) = f\left(\log(\sigma_{vM}), \frac{1}{T}, \epsilon_{cr}\right) . \tag{5.1}$$

The regression analysis was performed with the software Visual X-sel 13. Terms up to cubic order as well as interdependencies are permitted, and the input quantities were normalized. The fitting procedure yields the following phenomenological relation for $[\sigma_{vM}] = $ MPa, $[T] = $ K and $[\epsilon_{cr}] = \frac{mm}{mm}$ with a coefficient of determination of $R^2 = 95\%$ (values given in Table 5.5):

$$\begin{aligned} log(\dot{\epsilon}_{cr}) = &K_c + K_\epsilon \times \epsilon_{cr} + K_{\epsilon 2} \times \epsilon_{cr}{}^2 + K_{\epsilon 3} \times \epsilon_{cr}{}^3 + K_T \times \frac{1}{T} + K_{T2} \times \frac{1}{T^2} + \\ &K_\sigma \times \log(\sigma_{vM}) + K_{\sigma 2} \times \log(\sigma_{vM})^2 + K_{\sigma 3} \times \log(\sigma_{vM})^3 + \\ &K_{\epsilon,T} \times \epsilon_{cr} \times \frac{1}{T} + K_{\sigma\epsilon} \times \log(\sigma_{vM}) \times \epsilon_{cr} + K_{\sigma,T} \times \log(\sigma_{vM}) \times \frac{1}{T} . \end{aligned} \tag{5.2}$$

Table 5.5: Factors for the regression model

Factors 1	K_c	K_ϵ	$K_{\epsilon 2}$	$K_{\epsilon 3}$	K_T	K_{T2}	K_σ
Values 1	-13.25×10^1	-86.89×10^1	22.48×10^4	-17.81×10^6	23.86×10^4	-20.31×10^7	48.95

Factors 2	$K_{\sigma 2}$	$K_{\sigma 3}$	$K_{\epsilon,T}$	$K_{\sigma\epsilon}$	$K_{\sigma,T}$
Values 2	-31.83	4.16	-21.37×10^5	75.71×10^1	40.38×10^3

The Figures 5.18 to 5.20 show that the model is well suited to provide adequate estimates of the respective creep rates at varying levels of accumulated creep strain for the stress and temperature levels. Additionally, the stress and temperature dependencies of the model are given in Figure 5.21 on the facing page in order to demonstrate its suitability.

The SRA procedure is typically conducted with the workpiece still connected to the build
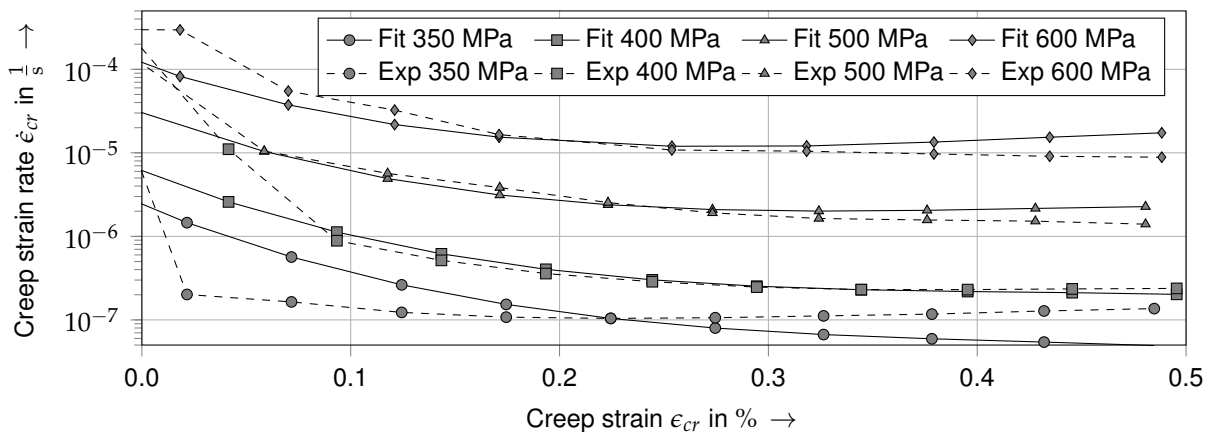
Figure 5.18: Fitting result for the creep experiments at 755 °C

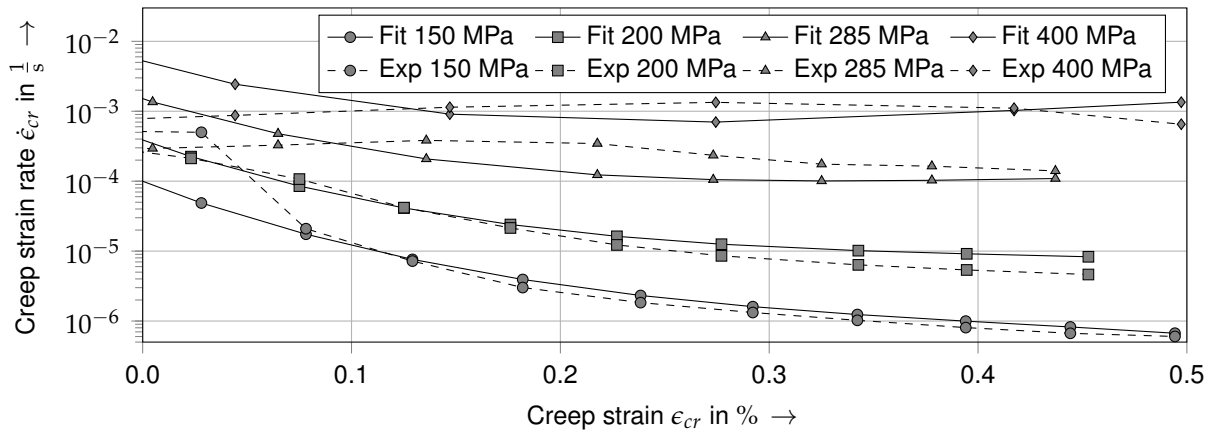**Figure 5.19:** *Fitting result for the creep experiments at 855 °C*
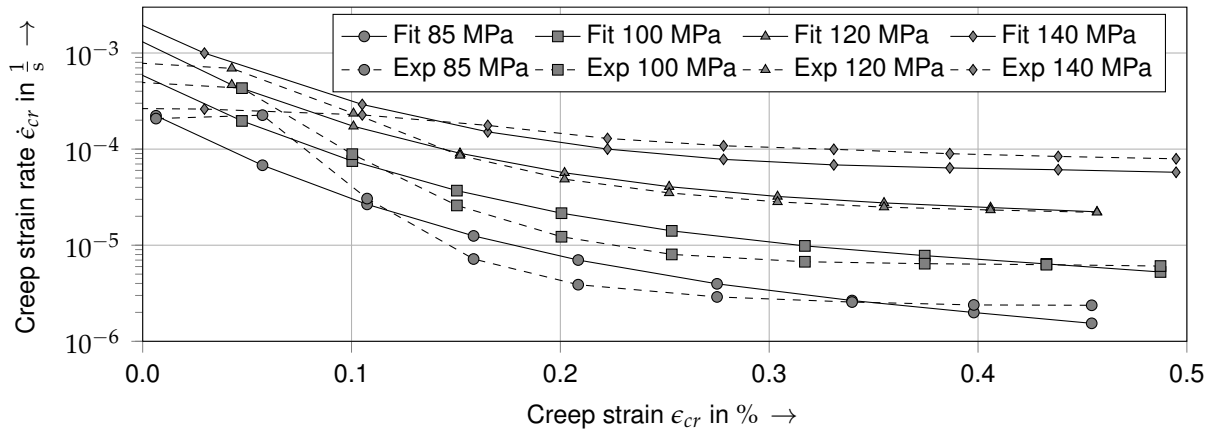

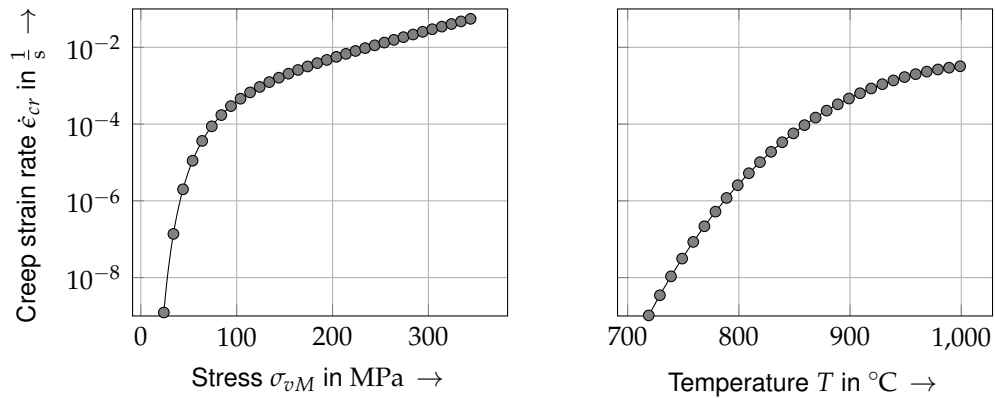**Figure 5.20:** *Fitting result for the creep experiments at 955 °C*

Figure 5.21: *Behavior of the regression model for the creep strain rate $\dot{\epsilon}_{cr}$ plotted over (left) stress σ_{vM} and (right) temperature T for the settings: $\epsilon_{cr} = 0.3\,\%, \sigma_{vM} = 150\,\mathrm{MPa}, T = 955\,°C$*

plate. Thus, the creep behavior of the build plate also has to be modeled in order for stresses on the interface between workpiece and build plate to be able to change. This was realized with a simplified Norton model, since the exact stress relaxation behavior of the build plate is not the focus of this thesis and only limited experimental data for the build plate material were available:

$$\dot{\epsilon}_{cr} = A \times \sigma^n \quad . \tag{5.3}$$

The parameters were chosen as $n = 1.0$ and $A = 2.0 \times 10^{-7}\,\mathrm{s}^{-1}\,\mathrm{MPa}^{-n}$ at $755\,\mathrm{°C}$ as well as $5.0 \times 10^{-7}\,\mathrm{s}^{-1}\,\mathrm{MPa}^{-n}$ at $955\,\mathrm{°C}$.

5.5.3 Application

The model was implemented via a user subroutine in CalculiX. The modeling of viscous phenomena is explicitly activated for certain steps and can be combined with plastic behavior. However, viscoplasticity is modeled as an over-stress model in CalculiX, i. e. only stresses above yield induce creep strains. As this does not correctly model the behavior for IN718, the yield stress is reduced to zero for all viscous calculation steps, resulting in a viscoelastic model. Thus, plastic and viscous behavior are modeled as either-or alternatives. The possible hardening effect from plastic deformation is respected, nevertheless, as the program does not distinguish between creep and plastic strain.

The model was first tested by reproducing the conducted relaxation experiment: A specimen was heated to the testing temperature ($955\,\mathrm{°C}$) and strained to a predefined level ($0.3\,\%$). The force was continuously measured, providing data for the stress decrease over time. The maximum measured stress at the beginning of the test was $169\,\mathrm{MPa}$. The model of this experiment was simulated with the implemented creep model and the stresses were extracted from and averaged over four representative elements in the middle of the specimen. Figure 5.22 on the next page shows the results of both experiment and model for the whole testing period of $86\,000\,\mathrm{s}$, i. e. approximately one day. Considering that this load scenario is already an extrapolation for the model (only load stresses up to $140\,\mathrm{MPa}$ were used for model calibration at $955\,\mathrm{°C}$) and the inherent uncertainty of creep experiments, the agreement is deemed sufficient for this thesis. However, the execution time of the implemented creep routine is significantly higher, i. e. it is 20 times that of the Norton model that is included in CalculiX. This was not improved further, but with code optimizations, a comparable speed to the native creep routine can be expected.

The second benchmark is the simulation of the SRA procedure for the cuboid specimen. It is intended to test whether the model is able to provide a realistic transient stress development in the workpiece. Due to a loss of vacuum in the experiment, two $1\,\mathrm{h}$ holding stages at 450 and $650\,\mathrm{°C}$ occurred during heating. This, compared to the defined single slope heating process,
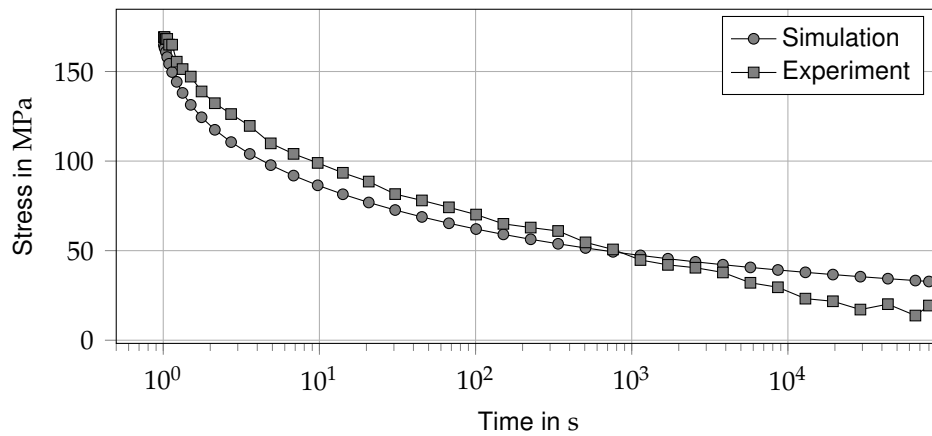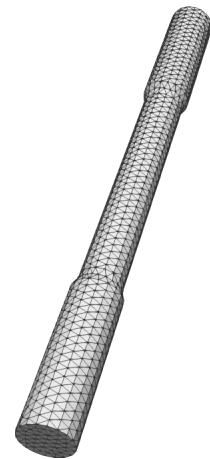
(a) *Stress relaxation* **(b)** *Computational model*

Figure 5.22: *Simulative and experimental result for the relaxation experiment at* 955 °C *and a straining of* $\epsilon = 0.3\%$*; (a) plot of the results and (b) model of the relaxation specimen*

altered thermal load was replicated in the model. Figure 5.23 on the following page shows how the modeled creep mechanisms provide a significant stress relief for this specimen. The heat transfer in the oven was simplified in the model by applying the heating process as prescribed nodal temperatures for the whole workpiece. Additionally, no solid state phase transformation of the build plate was respected. Unfortunately, no experimental data is available for validation purposes, but the observed behavior is in line with the expected outcome: maximum stresses exhibit a higher gradient than average stresses and both are continuously lowered during the heating phases. The stresses reach a (local) minimum during the respective holding phases with the driving force for creep coming to a halt. The main stress decrease is induced during the heat up to the highest temperature level. Upon cooldown, the remaining elastic strains lead to an increase of the stresses due to the growing material stiffness. The minimum stresses remain negligible over the course of the process and both the average (485 to 27 MPa) and the maximum (965 to 129 MPa) stress level are significantly reduced. Further results for the panel and blade geometry are mentioned in Section 5.7.
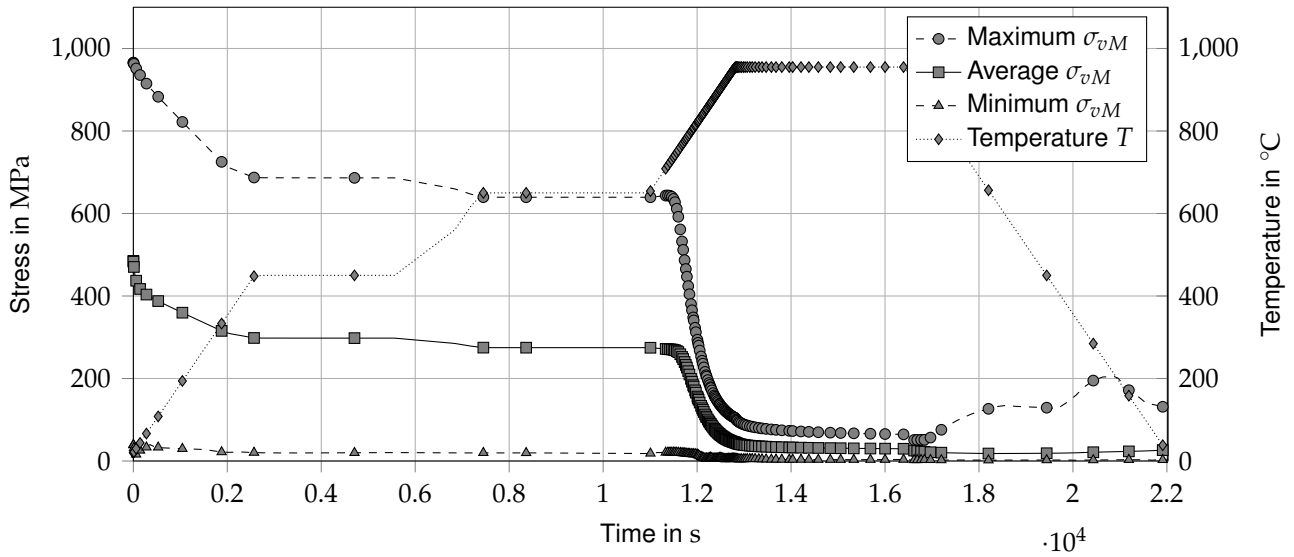
Figure 5.23: *Stress and temperature history for the SRA procedure of the cuboid geometry: Stresses are lowered during the heating phase, remain at a low level during the holding phase and increase when the initial material stiffness is restored upon cooldown.*

5.6 Verification

In order to ensure the suitability of the chosen numerical model, different verification studies were conducted with the panel and the blade workpiece. For conciseness, the following paragraphs only provide information on a mesh convergence study with respect to l_e and h_c. Other implemented tests, e. g. a so-called degenerate test (SARGENT 2013) with isothermal conditions that is required to yield zero displacements for all nodes or simple unit tests, are not discussed.

For a discrete numerical solution, more accurate results should be obtained by refining the mesh, i. e. decreasing l_e or increasing the order of the elements p_e. In order to investigate the behavior of the developed simulation model in this regard, the discretization error was determined for variable configurations. For the evaluation of the discretization error, the grid convergence index (GCI) *GCI* by ROACHE (1994) was employed. The *GCI* is determined from the results of a coarse (f_c) and a fine (f_f) mesh, the corresponding refinement factor r_f defined by the cube root of the ratio of the element counts, the order of accuracy of the numerical model p_e and a safety factor F_s according to:

$$GCI = \frac{F_s}{r_f^{p_e} - 1} \left| f_c - f_f \right|.$$ (5.4)

The recommended safety factor of $F_s = 3$ was chosen for all estimates of the *GCI* in this thesis. The given formulation yields a conservative estimate of the discretization error in the units of the solution, i. e. mm for form deviations. Additionally, the relative *GCI* was determined by dividing the *GCI* by the magnitude of the SRQ.

The investigated SRQs are the maximum displacement magnitude for the blade and the magnitude of the displacement at position 5 (see Figure 5.24) for the panel geometry. Additionally, the effect of the height of the layer compounds h_c was investigated. To this end, the convergence study of the panel geometry was expanded to incorporate both different l_e and h_c values. Tables 5.6 and 5.7 provide the results of the mesh convergence studies for the blade and the panel geometry, respectively. All studies were conducted with first order elements.

Table 5.6: *Results from the mesh convergence study with the blade geometry for a layer compound height of $h_c = 2$ mm, i. e. 18 layers; since the mesh is unstructured, a constant refinement factor cannot be ensured.*

l_e in mm	Number of elements in the model	Refinement factor	SRQ in mm	*GCI*	Relative *GCI* in %	Runtime in h[a]
1.0	80 836	N/A[b]	1.17	N/A	N/A	0.3
0.5	311 926	1.57	1.62	2.375	147	1.7
0.4	954 349	1.45	1.64	0.133	8	7.1
0.25	2 016 506	1.28	F[c]	N/A	N/A	N/A

[a] Running on a normal workstation (Intel Xeon E5-2687W) with 5 cores per simulation
[b] N/A = not applicable
[c] F = Simulation failed at material property change from plastic to bulk material.

Table 5.7: *Results from the mesh convergence study with the panel geometry for two exemplary layer compound heights; since the mesh is unstructured, a constant refinement factor cannot be ensured.*

h_c in mm	l_e in mm	Number of elements in the model	Refinement factor	SRQ in mm	*GCI*	Relative *GCI* in %	Runtime in h[a]
2	4.0	36 468	N/A	0.234	N/A	N/A	0.5
	2.0	74 042	1.27	0.390	1.76	451	0.8
	1.0	293 309	1.58	0.388	0.01	3	3.1
	0.5	1 559 137	1.75	0.396	0.03	8	15.1
1	4.0	36 468	N/A	0.244	N/A	N/A	0.6
	2.0	74 042	1.27	0.379	1.52	401	1.7
	1.0	293 309	1.58	0.413	0.18	42	5.5
	0.5	1 559 137	1.75	0.420	0.03	7	51.1

[a] Running on a normal workstation (Intel Xeon E5-2687W) with 5 cores per simulation.

The same characteristic is observed for a more complete picture of the distortion behavior of the panel, i. e. the root mean square (RMS) of nine characteristic evaluation positions (see Figure 5.24 on the next page). The results for a full factorial study with $h_c = [1, 2, 4, 6]$ and $l_e = [0.5, 1, 2, 4]$ are visualized in Figure 5.25 on the following page.

In summary, the results show that the solution converges for both geometries and that coarse meshes already yield suitable estimates of the qualitative distortion trend for the investigated
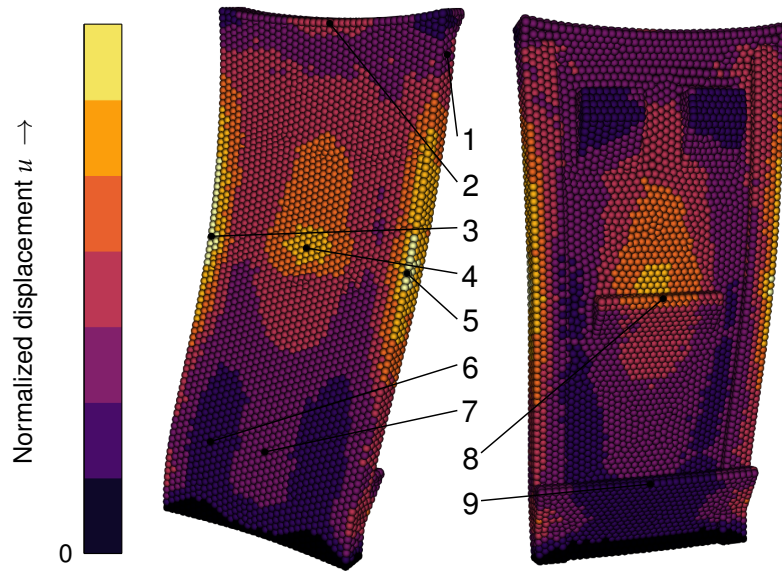
Figure 5.24: *Evaluation positions for the determination of the RMS; the visualization shows the results of the simulation with $l_e = 2$ mm and $h_c = 4$ mm. The solution is depicted as a colored sphere for each integration point ("point Gaussian" representation in the visualization software Paraview)*

geometries. However, there is a significant discretization error concerning the magnitude for simulations with coarse meshes. Also, both the simulation results and the convergence behavior exhibit a dependency on the value of h_c: With more layers being aggregated in layer compounds, the resulting distortion is underestimated. In order to limit this effect, h_c should not exceed 2 mm. Thus, for the following simulations a h_c of 2 mm was used, if not mentioned otherwise. Also, the average element edge length l_e should not exceed the height of the layer compounds h_c in order to allow for a suitable energy introduction.
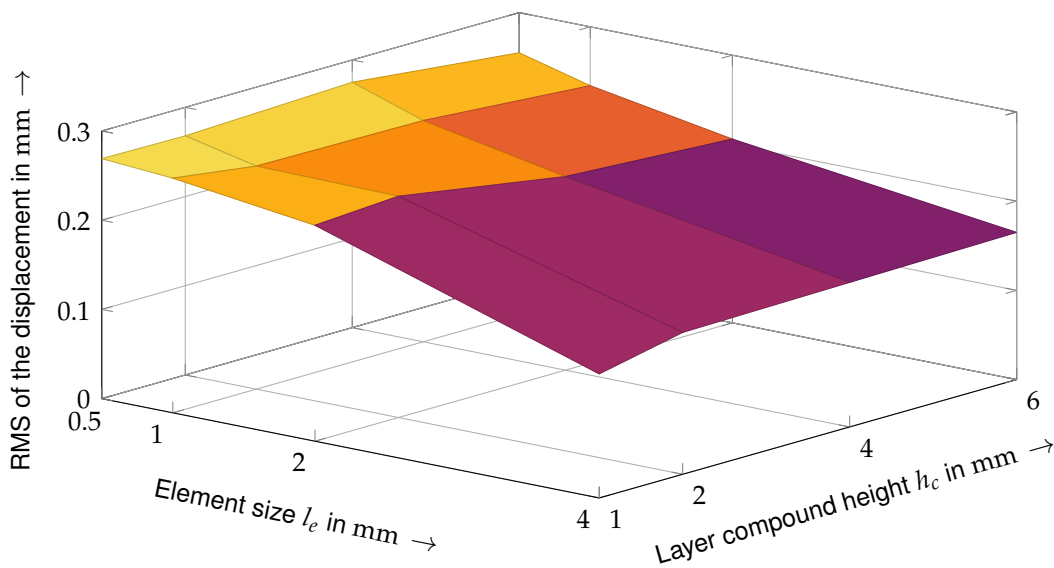
Figure 5.25: *Simulation results for the RMS of nine evaluation points for the panel geometry (see Figure 5.24 for the positions of these points).*

5.7 Validation

The following paragraphs present comparisons between the predictions of the model and experimental data. The goal is to determine wheter there is congruency between simulative predictions and measured data as defined in Subsection 2.3.1.

5.7.1 Residual Stresses

The generation of the validation data was performed in two measurement series and published together with supplementary data: The first study compared results of the hole drilling method and X-ray as well as neutron diffraction measurements with simulation results (BAY-ERLEIN et al. 2016). For the second measurement series, the transient build-up of stresses within the cuboid specimens and the build plate as well as the magnitude of possible shear stresses marked the focus (BAYERLEIN et al. 2018). The reader is referred to the respective sources for in-depth information, since only a subset of the information is used for model validation in this thesis (see Figure 5.26). All samples were built on the *EOS M270*.

Figure 5.27 on page 81 shows a comparison between the simulative and the experimental results for the three stress components coinciding with the symmetry axes of the specimen. The simulation results were obtained from a mesh with a target element edge length of $l_e = 1\,\text{mm}$, layer compounds with a height of $h_c = 2\,\text{mm}$ and an element order of $p_e = 1$, i. e. linear elements. The simulation data was gathered by a random sampling of 100 points within a sphere located at the nominal measurement position and exhibiting a radius of $2\,\text{mm}$. The variability of the results, i. e. the sample standard deviation, is provided as uncertainty bands for each sampling line within the plots. They can additionally be interpreted as a measure of the sensitivity of the results to a positioning error.
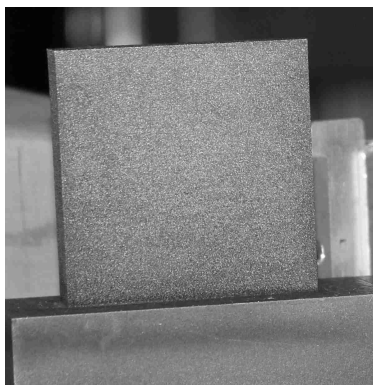
(a) Sample workpiece from one of the measurement campaigns
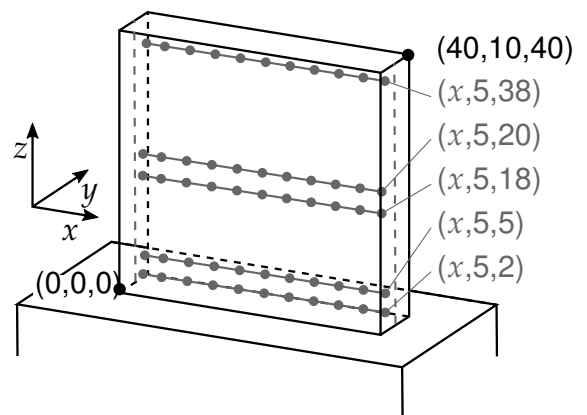
(b) The coordinate system and the measurement lines (gray)

Figure 5.26: *The specimen ($40 \times 10 \times 40\,\text{mm}^3$) and a schematic representation of the study for the comparison of simulated and measured stresses (adjusted from* BAYERLEIN *et al. (2016))*

As expected, due to higher gradients in border regions, simulative variability increases towards the free surfaces, i. e. $x = 0\,\text{mm}$ and $40\,\text{mm}$ as well as $z = 40\,\text{mm}$. The comparison to the experimental data shows that the predicted stresses are in sufficient agreement with the measured values: There are only singular points, e. g. σ_{yy} at $x = 2\,\text{mm}$ and $z = 20\,\text{mm}$, where the deviation exceeds $100\,\text{MPa}$.

A more qualitative overview on the predicted distribution of residual stresses in the workpiece is provided in Figure 5.28 on page 82. In addition to the outline of the geometry, only the elements of the respective measurement paths are plotted.

Lastly, the non-negligible magnitude of shear strains in the upper edge regions of the cuboid workpiece, as presented in BAYERLEIN et al. (2018), are similarly predicted by the simulation (without depiction). However, due to the very limited experimental data, i. e. only two measurement positions, no further assessment is provided.
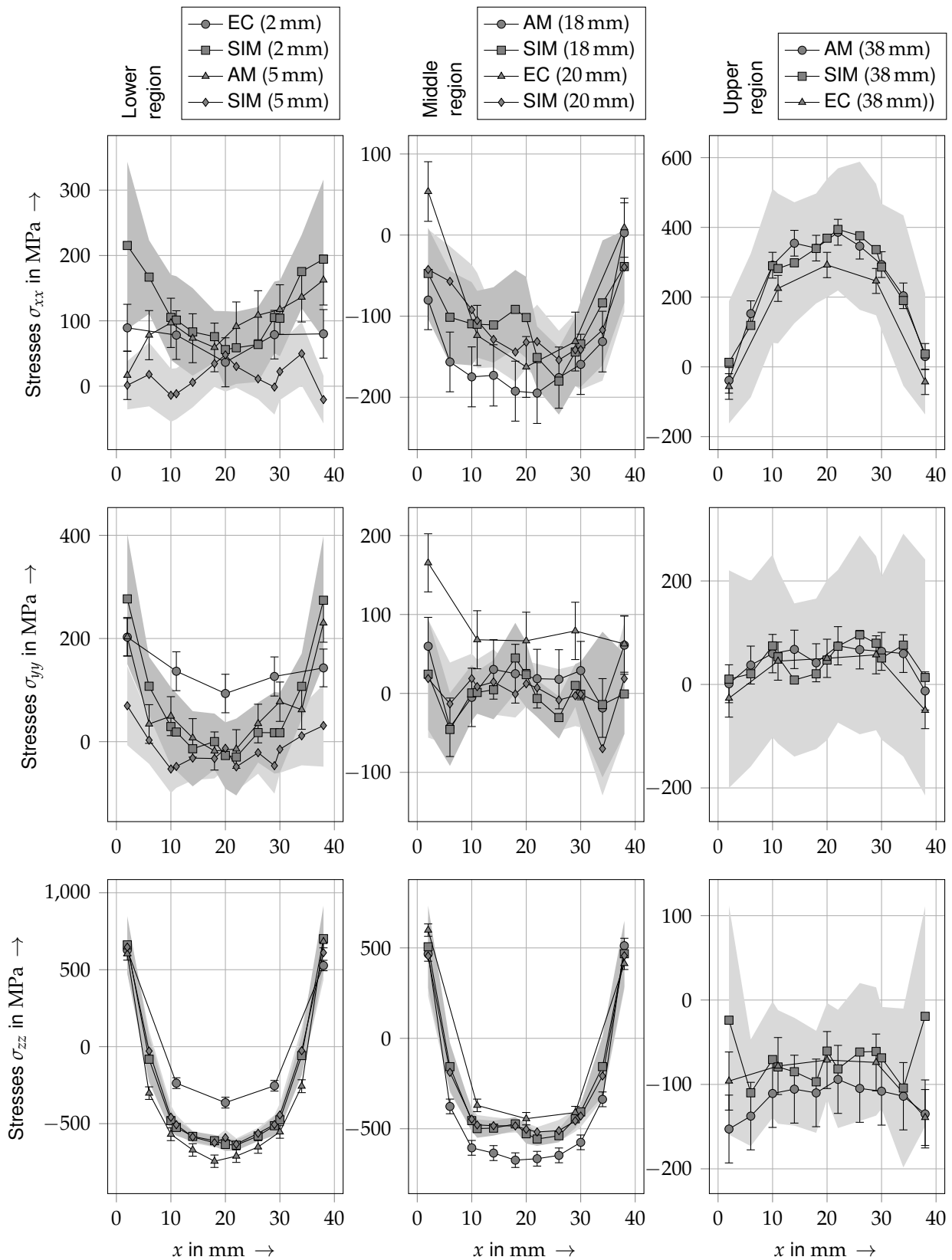
***Figure* 5.27:** *Residual stress distribution in the cuboid geometry from two measurement campaigns (EC =* BAYERLEIN *et al. (2016), AM =* BAYERLEIN *et al. (2018), uncertainty given by error bars) and the simulation (SIM, uncertainty visualized as value bands); each row contains the results for a certain stress component, i. e.* σ_{xx}, σ_{yy} *and* σ_{zz} *and the columns represent the lower, middle and upper measurement region (compare Figure 5.26 on page 79). The connecting lines are solely for easier readability and do not represent actual data. The more lightly marked uncertainty band always refers to the lower (in z-direction) measurement line.*
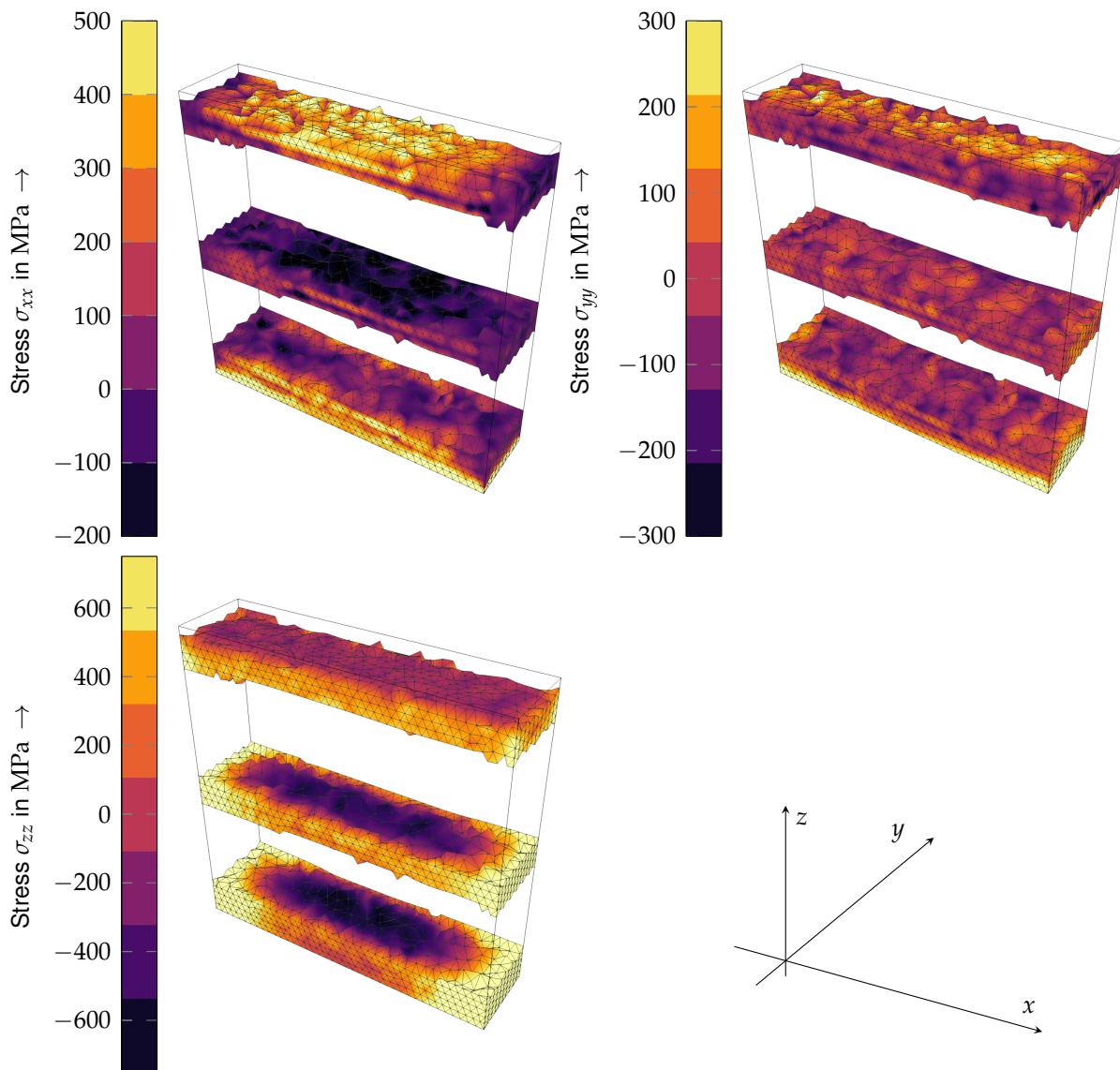
Figure 5.28: *Depiction of the simulation results for the residual stress distribution in the cuboid geometry after build-up; for better comparability, the result is only plotted for elements with a z-position of their center of gravity between 0 and 4 mm, 18 and 20 mm as well as 37 and 38 mm.*

5.7.2 Form Deviation

The capability of the simulation tool to predict form deviations was investigated by comparisons to the two defined benchmark workpieces. Since multiple machines were used for the generation of the workpieces, a choice of the point of reference was necessary. As mentioned above, the material model in the simulation is based on results from samples manufactured on an EOS *EOS M280* machine with a layer height of 20 μm. Accordingly, the data of the *EOS M270* (same layer height) or the *EOS M280* (same machine type, e. g. inert gas flow) could serve as reference points and the results for both machines are provided in the following.

Panel geometry The results of the predicted and the measured form deviations is summarized in Figure 5.29 on page 84. The mismatch for the prediction is in the same range as the

deviation between the two different machines. However, the direction of the mismatch shows that the workpiece built on the *EOS M270* deviates further from the predicted outcome. The artifacts at the bottom of the workpiece stem from sawing (*EOS M280*) and EDM (*EOS M270*), respectively, and are thus located at different heights.

The results suggest that the main error is introduced by a suboptimal modeling of the SRA process, since the magnitude of the mismatch increases significantly at this stage. However, the given tolerance range is very small in order to allow for a more quantitative assessment of mismatches. For the actual use case, the tolerance range is significantly less strict, i. e. larger.

Blade Geometry   For the blade geometry, multiple validation cases are presented: the simulation result after different process steps, the modeling of the influence of heat storages (cf. Figure 5.5 on page 57) as well as the simulation of multiple workpieces on one build plate.

First, it is necessary to quantify the level of mismatch between the maximum of the displacement u and the respective form deviation $\underline{\Delta}$. Since there are multiple mismatched surfaces for the hollow blade structure in a normal three dimensional comparison, a spline was designed on the tip of the blade and compared to the edge of the CAD geometry. With the simulation providing $u_{max} = 1.62\,\text{mm}$ and the comparison yielding $\underline{\underline{\Delta}}_{max} = 1.6127\,\text{mm}$, the difference between the two quantities is deemed negligible.

When the computational result for the form deviation after LBM is compared to the outcome of the experimental studies visualized in Figure 5.3 on page 54, the model prediction shows agreement with the trials run on the *EOS M270*. Since the material model is derived from data gathered from specimens manufactured with a layer height of $20\,\mu\text{m}$, the model seems adequate. However, in addition to an estimate of the average form deviation, a decision maker may require the model to also provide an estimate of the variability of the result. The next chapter will thus provide an in-depth analysis of the uncertainty in the simulation and corresponding sensitivities for this state of the workpiece.

Similarly to the panel geometry, the form deviation was also investigated along the process chain. However, the results of only one specimen are available due to the limited availability of the heat treatment equipment. A laboratory furnace was used for the SRA in this study. Additionally, due to the high computational effort of the implemented creep routine, a coarse mesh of the blade with $l_e = 1\,\text{mm}$ was used for the simulative prediction. In addition to the typical process chain, a direct separation without an SRA procedure was also investigated. The corresponding results and the states of the workpiece are summarized in Figure 5.30 on page 85. For the direct separation, the model correctly predicts the lowering of form deviations. In contrast, the model does not correctly predict the re-emerging form deviations in the separation step after SRA for the normal process chain.

The next study was intended to examine whether the simulation tool is able to model the influence of the heat storages on the resulting form deviation. Therefore, three ways to
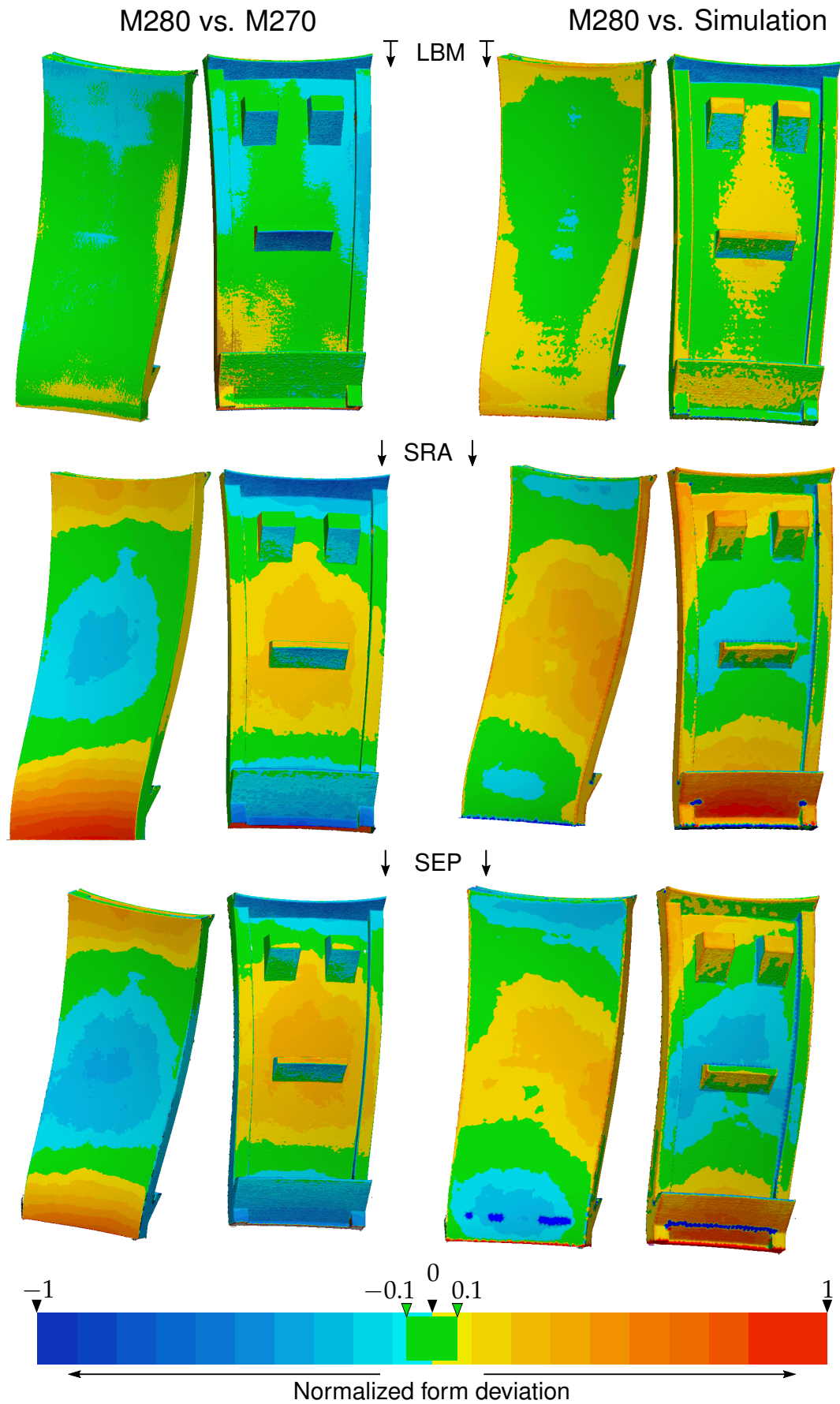
Figure 5.29: *Comparison of the difference of the form deviations between workpieces manufactured on two machines (EOS M280 vs. EOS M270) versus the difference between the simulated prediction and one of the experimental results (EOS M280 vs. Simulation).*
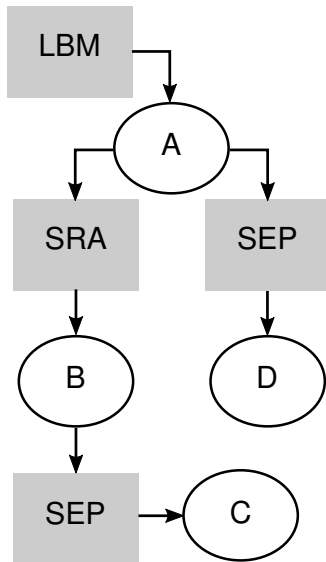
(a) *States of the workpiece*

(b) *SRQ at the defined states from (a)*

Figure 5.30: *Form deviations of one blade workpiece and its simulative prediction over two possible process chains; the values 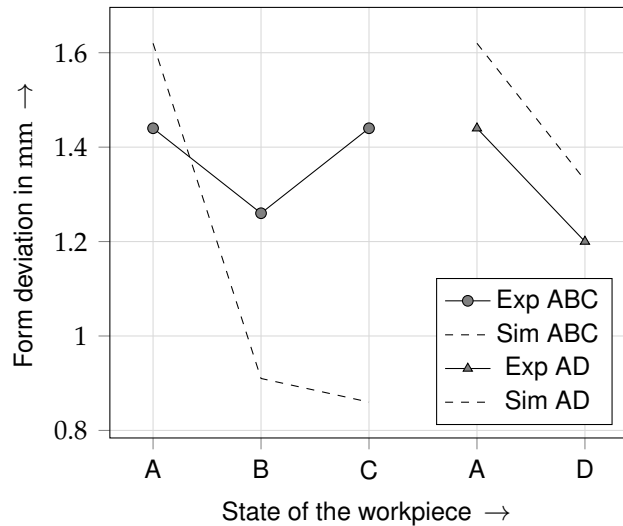for B, C and D were generated by scaling them according to the ratio of the maximum displacement in A obtained from a simulation with a fine and one with a coarse mesh (cf. Table 5.6 on page 77).*

respect the surrounding material are compared: including the heat storages in the simulation, increasing the temperature level of the process (T_{Pro}) as well as adding a convective boundary condition on the side surfaces of the workpiece. The respective parameters, the results and the experimental reference are summarized in Table 5.8.

- Including the heat storages in the simulation exhibits a negligible influence on the development of form deviations in the blade workpiece. This suggests that the interaction of parts via the build plate may not be the main driver for the influence.
- Phenomenologically, it is reasonable to assume that the main effect of heat storages is the increase of the temperature level of the process for the respective workpieces. However, for the given study, an increase of T_{Pro} leads to an inverse effect compared to the one observed in the experiment. Thus, for the given modeling approach, raising T_{Pro} cannot be deemed suitable.
- The last alternative under investigation is the simplification of the complex heat exchange between the two workpieces as well as the separating powder layer to a convective load on the side of the workpiece. The chosen parameters are based on a simple model obtained from conduction measurements of the powder and significant simplifications due to the omission of thermal contacts. For full details, see Section A.3 on page 154 of the appendix. The simulation with the adjusted model yields results that match the trend observed in the experiments. This may represent a physically motivated and numerically efficient way to model the influence of other workpieces being built in close proximity to the workpiece under investigation.

Table 5.8: *Results for different simulations and experiments in order to model the influence of heat storages being built alongside the blade geometry. For all simulations a layer compound height $h_c = 2\,\mathrm{mm}$ and an element target length $l_e = 1\,\mathrm{mm}$ was used. The SRQ γ was determined as the maximum displacement of the blade geometry.*

	Description	Geometry	T_{Pro} in °C	T_{Conv} in °C	$h_{WP,side}$ in $\frac{\mathrm{mW}}{\mathrm{mm^2\,K}}$	γ in mm	Relative magnitude in %
Simulation	Nominal simulation	Blade	200	80	0	1.17[a]	100
	Full simulation of heat storages	Blade and heat storages	200	80	0	1.15	98
	Increased T_{Pro}	Blade	300	80	0	1.34	113
	Increased convective influence	Blade	200	200	14.1×10^{-3}	1.04	88
Experiment	Median of blades in Job 3	Blade	-	-	-	1.17[a]	100
	Blade number 5	Blade and heat storages	-	-	-	0.84	72

[a] The agreement of nominal simulation result and experimental value is coincidental and likely due to two errors cancelling each other out: The coarse mesh leads to an overestimation of the stiffness, resulting in an altered displacement behavior. Additionally, the simulation is built on material information for a layer height of 20 μm, but the specimens were manufactured with 40 μm.

Lastly, the systematic influence of the position of a workpiece in a job with multiple specimens was investigated. To this end, a simulation model of the build job with 18 blade workpieces was generated and simulated. However, limitations of the computational hardware prohibited the simulation on a fine mesh. The shown results were produced for a model with $l_e = 1\,\mathrm{mm}$ and a layer compound height of $h_c = 3\,\mathrm{mm}$. The results of the study are visualized in Figure 5.31 on the next page, showing that both model and experiment exhibit a similar trend for the different positions. However, the correlation coefficient $R^2 = 56\,\%$ indicates that there is significant noise within the data. Nevertheless, the simulation shows a promising behavior for multi-workpiece build jobs.
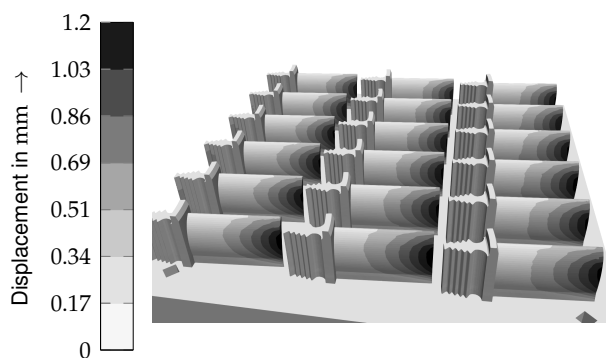
(a) Simulation result for a build job with 18 blades
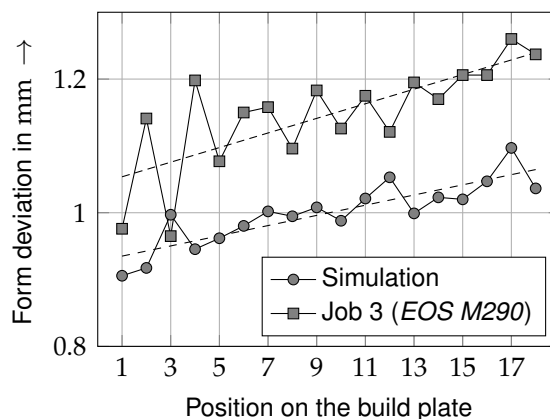
(b) Comparison of form deviations between simulation and experiment with corresponding trend lines

Figure 5.31: *Comparison of the measured and predicted form deviations with respect to the placement on the build plate; the underestimation of the displacement magnitude is likely to stem from the use of a coarse mesh with $l_e = 1\,\text{mm}$ and a layer compound height of $h_c = 3\,\text{mm}$. (a) The simulation result exhibits small differences between the individual workpieces. (b) When compared to e. g. Job 3 on the EOS M280, the simulated trend of the variation shows some agreement with the experiment. The numbering of the positions can be taken from Figure 5.3 on page 54*

5.8 Summary

In this chapter, a new simulation model for the prediction of form deviations in the process chain of LBM was presented. Model identification experiments enabled the preselection of relevant modeling factors with e. g. the position of the workpiece on the build plate exhibiting a significant effect. The developed FE-based model features a novel activation strategy and a slicing strategy suitable for representing industrially relevant workpieces with high shape accuracy. Additionally, the SRA process was investigated and successfully simulated with a regression-based creep model. The concluding sections show promising verification and validation results concerning both defined SRQs, i. e. residual stresses and form deviations. However, due to the deterministic nature of the simulation model, the experimental spread of e. g. the distortion results cannot be reproduced. Thus, the method of PBA is introduced and its application to the simulation model in order to improve the prediction of experimental outcomes is explained in the next chapter.

6 Predictive Capability

While the results in Chapter 5 suggest that the developed simulation model is able to provide an accurate estimate for the form deviation of workpieces manufactured via LBM, the full range of experimental results cannot be explained with the deterministic model. Thus, in the following sections, variabilities and uncertainties are moved into focus. In order to expand the predictive capabilities of the developed model to also provide estimates for e. g. the variability of the results, the PBA framework for non-deterministic predictions was employed. Additionally, using sensitivity analysis, information on the major drivers for variability are investigated, allowing for an effective application of quality assurance methods. Lastly, a method for the perpetuation of the respective efforts is suggested.

There are investigations on the predictive capability for some micro scale models (LOPEZ et al. 2016; MOSER 2017), but, due to the numerical effort and the oftentimes high monetary effort due to costly licenses, no comparable investigations are conducted for workpiece-scale models. Since the usage of the simulation tool that was developed within the context of this thesis does not incur licensing fees and the studies can be parallelized, the respective investigations become feasible.

6.1 Methodology

The overall methodology for the assessment of the predictive capability is based on the suggestion of OBERKAMPF and ROY (2010) presented in Section 3.3.1 on page 35. The following subsections provide additional information on the methods chosen for the respective steps within this methodology. The topics of uncertainty identification and characterization are specific to the scope of the study and thus presented in the next section (6.2).

6.1.1 Screening

Due to the high dimensionality of the model, a screening analysis is applied in order to reduce the computational effort with only a reasonable loss of confidence in the results. This is also confirmed by the suggestions of IOOSS and LEMAÎTRE (2015) for the choice of SA methods: If non-linear behavior of the model is expected and the computational cost is high, screening should be conducted prior to a quantitative analysis via the determination of Sobol' indices (SIs).

Since there is no suitable a priori knowledge about the regularity of the model, the method of MORRIS (1991) was chosen for the screening analysis. A winding stairs sampling scheme was implemented in order to maximize the efficiency of the study design. The input space is constructed from the interval boundaries of the epistemic factors as well as the 5th and

the 95th percentile of the aleatory factors. The samples are generated randomly without respecting the PDFs of the aleatory factors, effectively resulting in the assumption of uniform distributions for all factors.

The results for the different factors are investigated in terms of the established quantities of σ_{Morris} and μ^*_{Morris}. Only factors that exhibit a significant magnitude, i.e. surpassing a threshold, are respected for the subsequent analyses.

6.1.2 Uncertainty Quantification

The method of PBA was employed for UQ since, first, no adjustments to the simulation model are intended and, second, the method is able to handle the model as a black box with discrete input and output quantities. Additionally, the method allows to distinguish between uncertainty from inherent variability and that of missing knowledge.

For this thesis, model form uncertainty, i.e. uncertainty in the formulation of the model, is not investigated (see Subsection 6.2.1 for further details). Thus, the quantification of the output uncertainty is provided by a propagation of the input uncertainty through the model. This is also referred to as forward UQ. Since the model does not allow the propagation of p-boxes but discrete samples, MCS was employed to approximate the CDFs via suitable empirical probability density functions (EDFs). In the following, EDFs based on MCS and the respective distributions of the SRQ after propagation are referred to as CDFs in order to separate them from the experimentally gathered EDFs.

For the method of PBA, the relevant factors are first categorized into epistemic and aleatory kind. Subsequently, using the nested loop structure suggested by OBERKAMPF and ROY (2010, pp. 606ff.), the samples from epistemic factors can be differently managed and evaluated, compared to those of the aleatory factors. This is necessary as there is no probability connected to an epistemic sample. It is merely one possible realization, i.e. while the samples are being generated under the assumption of a uniform distribution, the results are not aggregated but simply provided as possible alternatives. Consequently, if a highly non-linear behavior of the simulation model with respect to a factor has to be kept in mind, a high number of samples may be necessary.

The generation of the p-box follows the scheme given in Figure 3.3 on page 38: The sampling of the aleatory variables is performed via the method of inversion transform sampling in order to respect their PDFs (ANGUS 1994). By creating uniformly random samples and projecting them onto the CDF in question, samples following the respective distribution are generated. Within the inner loop, individual CDFs are obtained for one combination of epistemic realizations. They, in turn, provide the p-box via their envelope (see Figure 2.7 on page 18). However, this resulting p-box is also an estimate, since the CDFs are generated by MCS, i.e. they, too, are only estimates of the true distributions.

Additionally, independence between the factors is assumed, since the handling of epistemic dependencies is not yet understood (OBERKAMPF and ROY 2010, p. 572). This constitutes a simplification, especially for the material properties that may correlate significantly.

With the model in question exhibiting high computational cost and both types of uncertainties requiring a reasonable amount of samples, only factors that are estimated to provide relevant contributions to the output uncertainty should be included in the study. This emphasizes the need for and the role of a suitable screening analysis.

6.1.3 Sensitivity Analysis

In order to provide a measure of the importance of individual factors concerning the output uncertainty, a sensitivity analysis is conducted. To this end, the method of SOBOL' (1993) is employed. As mentioned in Chapter 3, it constitutes a standard for global sensitivity analysis and is capable of yielding reliable results even for underlying models of high complexity, i.e. significant factor interactions. By ranking the input factors according to their contribution to the output uncertainty, future quality assurance or experimental characterization efforts can be efficiently directed.

There are various estimators for both the first order (S_1) and the total order (S_T) SIs. For this thesis, the estimators suggested by TARANTOLA et al. (2006) based on the design of SALTELLI (2002) were chosen. In a comparative study by LILBURNE and TARANTOLA (2009), these estimators exhibited the best performance due to their use of symmetries in sampling vectors. Additionally, in order to avoid a loss of accuracy in the determination of the indices for less important factors, the suggestions of KUCHERENKO et al. (2011) are respected by using an alternative, more numerically robust, form of the equation.

Additionally, the averages of the suggested estimators, e.g. eight for S_1, are calculated and used. Since the individual estimators are positively and negatively correlated in pairs, the average is, in general, more accurate (LILBURNE and TARANTOLA 2009).

The chosen estimators use both arrays of matrices with replaced columns, i.e. *Ab* and *Ba*. Lastly, all model outputs are normalized by, first, centralizing via subtraction of the mean and second, dividing by the standard deviation.

For easier readability of the following equations,

- *Y* stands for the normalized SRQ for a given sampling vector denoted as its subscript,
- E_x represents the short form of the expectation operator, i.e. $\frac{1}{n_{Samples}} \sum_{1}^{n_{Samples}}$ for a discrete sampling scheme, i.e. MCS and
- the index for the current factor k is omitted.

Each first order index S_1 is then determined as the average of its eight estimators:

$$8 \times S_1 =$$

$$\frac{E_x[Y_A(Y_{BA} - Y_B)]}{E_x[Y_A^2] - E_x[Y_A]E_x[Y_B]} + \frac{E_x[Y_B(Y_{AB} - Y_A)]}{E_x[Y_B^2] - E_x[Y_A]E_x[Y_B]} +$$

$$\frac{E_x[Y_A(Y_{BA} - Y_B)]}{E_x[Y_B^2] - E_x[Y_A]E_x[Y_B]} + \frac{E_x[Y_B(Y_{AB} - Y_A)]}{E_x[Y_A^2] - E_x[Y_A]E_x[Y_B]} + \quad (6.1)$$

$$\frac{E_x[Y_{BA}(Y_A - Y_{AB})]}{E_x[Y_{BA}^2] - E_x[Y_{BA}]E_x[Y_{AB}]} + \frac{E_x[Y_{AB}(Y_B - Y_{BA})]}{E_x[Y_{AB}^2] - E_x[Y_{BA}]E_x[Y_{AB}]} +$$

$$\frac{E_x[Y_{BA}(Y_A - Y_{AB})]}{E_x[Y_{AB}^2] - E_x[Y_{BA}]E_x[Y_{AB}]} + \frac{E_x[Y_{AB}(Y_B - Y_{BA})]}{E_x[Y_{BA}^2] - E_x[Y_{BA}]E_x[Y_{AB}]} .$$

Similarly, the total order index of a given factor is determined by solving:

$$4 - 4 \times S_T =$$

$$\frac{E_x[Y_A(Y_{AB} - Y_B)]}{E_x[Y_A^2] - E_x[Y_A]E_x[Y_B]} + \frac{E_x[Y_B(Y_{BA} - Y_A)]}{E_x[Y_B^2] - E_x[Y_A]E_x[Y_B]} + \quad (6.2)$$

$$\frac{E_x[Y_{AB}(Y_A - Y_{BA})]}{E_x[Y_{AB}^2] - E_x[Y_{BA}]E_x[Y_{AB}]} + \frac{E_x[Y_{BA}(Y_B - Y_{BA})]}{E_x[Y_{BA}^2] - E_x[Y_{BA}]E_x[Y_{AB}]} .$$

In order to provide an estimate of the sampling variability for these indices, the method of so-called jackknife re-sampling is used: By systematically determining a quantity from all $(n_{Samples} - 1)$ subsamples, an unbiased estimate of the variability is gained. (QUENOUILLE 1949; TUKEY 1958)

6.1.4 Sampling

Since both UQ and SA rely on MCS, a large number of samples is necessary to provide meaningful results. Thus, for this thesis, both sampling schemes are combined to decrease the overall number of model evaluations by combining the hierarchical structure of UQ with the arrangement of samples into the matrices: i.e. A, B, Ab and Ba for SA. Under the assumption that the factors are independent, there is no violation of the properties of UQ. In essence, the matrices A and B are constructed like a normal sampling matrix for a UQ analysis. Since extended estimators are used in this thesis, two arrays of matrices Ab and Ba with individually interchanged columns are generated (see Figure 3.5 on page 42), resulting in an overall of $2 \times d + 2$ sampling matrices. In this sampling scheme, an exemplary column occurs in $d + 1$ matrices. With the combined sampling matrices exhibiting these repetitions, the significance of the UQ results is reduced accordingly.

In order to quantify the sampling error from using MCS, the following equation is employed (ANG and TANG 2007):

$$\text{error in \%} = 200 \times \sqrt{\frac{1-p}{n_{Samples}}} \, . \tag{6.3}$$

While this error converges rather slowly, it is independent from the number of factors (OBERKAMPF and ROY 2010, p. 605).

Additionally, the determination of SIs is based on variance operators, which are not defined for epistemic variables as their realizations are not connected to a probability. As mentioned before, the samples for epistemic variables are generated via a random number generator, effectively yielding a uniform PDF. Since, in contrast to PBA, the chosen method for SA does not handle these factors differently, this implicit assumption may lead to erroneous results. Although this is common practice in engineering applications, the corresponding results should still be handled with care.

6.1.5 Handling of Simulation Fails

Since the input parameter combinations created in the following studies significantly deviate from the nominal model parameterization, convergence of the simulation cannot be ensured, potentially resulting in missing SRQ data. This raises the topic of the handling of such failed simulation attempts. For this thesis, the corresponding runs are documented and they were excluded from further analysis. This may decrease the statistical power for a given number of samples.

Additionally, the distribution of failed simulations with respect to the factor realizations may provide hints on systematic problems with e. g. the defined input sampling intervals. As an example, the assumption of a normal distribution of the Poisson's ratio ν may be sensible but lead to physically implausible samples above 0.5 for higher temperatures. In such a case, the distribution of failed simulations will show a systematic behavior if analyzed with respect to the sampling factor.

6.2 Scope

This thesis cannot provide an exhaustive analysis for all possible types of workpieces, processing parameters or materials. The following explanations define the scope of the conducted study. First, potential sources are identified and characterized, subsequently the concrete study is presented and, lastly, some remarks considering the numerical error are given.

6.2.1 Uncertainty Identification

The basis of determining which factors should be considered as uncertain is skepticism. If a factor can a priori not be deemed to be fixed, exhibit negligible uncertainty or have no or insignificant influence on the SRQ of interest, it should be considered uncertain. For complex systems, this assumption should be carefully considered as there may be interactions that are not anticipated by the analyst.

The first possible source of uncertainty is given by the geometric representation of the model. For the presented approach of the creation of the numerical mesh (see Subsection 5.4.3 on page 65), no simplification of the CAD geometry is conducted and the meshing algorithm is constrained to not create secant deviations larger than 0.1 mm. The effect of possible variations of the meshing procedure, e. g. with different tools, on the SRQ is thus assumed to be negligible. However, the meshing may be relevant concerning the numerical error as presented in Subsection 6.2.4.

In contrast, the uncertainty of material parameters and boundary conditions cannot be dismissed. Even for a standardized material like IN718, both the spread of the alloy composition itself as well as custom processing parameters may lead to different mechanical properties of the resulting workpiece and consequently the SRQ. Similarly, the boundary conditions, especially within the thermal domain, are dependent on processing conditions that may vary significantly between machines and build job configurations.

As mentioned above, model uncertainty is not investigated within this thesis. However, since only a small fraction of the involved physics is modeled, this may be of interest for future studies.

6.2.2 Uncertainty Characterization

When characterizing uncertainty for the use within the PBA methodology, it is essential to distinguish between variability due to missing knowledge, i. e. epistemic, and that due to inherent fluctuations, i. e. aleatory. While epistemic uncertainty should be reducible by collecting further information, aleatory uncertainty can only be more correctly defined.

An example for this difference can be given by the melting point for IN718: If there is no additional information on a provided material other than that it meets the alloy requirements, the melting point of the alloy can vary significantly and cannot be characterized by a CDF. It is only known that the actual value falls within the set interval boundaries. If, in contrast, the material is e. g. obtained from only one supplier with a defined process, a CDF can be extracted by determining the melting point for a sufficient amount of samples for a given confidence level. Additionally, an SA may provide the information whether this effort is

sensible, i. e. whether the reduction of the uncertainty in the SRQ for this factor does provide sufficient cost effectiveness.

Since the provided methodology comprises an additional screening analysis without the epistemic-aleatory distinction, the direction of the efforts may already be decided at this stage. However, since the chosen method does only provide qualitative results, caution is necessary. In this thesis, the uncertainties were defined before the screening analysis.

Therefore, interval boundaries and CDFs are defined for the epistemic and the aleatory factors, respectively. While there are scenarios in which more complex types may be beneficial, only purely epistemic or aleatory input uncertainties are used, i. e. no p-boxes. Table 6.1 on the next page summarizes all included factors, the respective characterization and the corresponding source. Due to the high effort necessary to obtain CDFs with high confidence, assumptions were employed for the aleatory factors within this thesis: Only material properties are of aleatory nature, all corresponding factors follow a normal or a truncated normal distribution and the observed extremal values denote the 5 and 95 % marks. The corresponding observations are taken from the literature. All other factors are of epistemic nature. For material properties that no observations are reported for, a generic variation of $\pm 10\,\%$ is estimated with the exception of ν being limited to only a reduction through variance to ensure physically plausible values, i. e. below 0.5.

6.2.3 Study Design

While the variability of the geometry is assumed to be negligible, an influence of the type of workpiece cannot be dismissed a priori. Thus, the screening analysis is conducted for both benchmark workpieces, i. e. blade and panel, and the results are compared to provide an indication on this sensitivity. However, since experimentally determined EDFs only exist for the blade, UQ and SA were only conducted for this workpiece.

The nominal simulation result for the blade is visualized in Figure 6.1a alongside the nodes at which the SRQ is evaluated (Figure 6.1b). The SRQ is determined as the mean of the magnitude of the displacement at these five nodes. The simulations were conducted with a model with an average edge length of the elements $l_e = 0.5\,\text{mm}$ and a layer compound height of $h_c = 2\,\text{mm}$. Similarly, for the panel, the SRQ was determined as the mean of the magnitude of the displacement of five nodes at the side of the panel, i. e. at position 5 in Figure 5.24 on page 78 for a model with $l_e = 1\,\text{mm}$ and $h_c = 2\,\text{mm}$.

The results of the screening, i. e. μ^*_{Morris} and σ_{Morris} as well as the relative ranking of the factors, were subsequently used to determine the input for UQ and SA. The corresponding thresholds for the incorporation of a factor into the further analyses were chosen very stringently, i. e. as $\mu^*_{Morris} \geq 10\,\mu\text{m}$ and $\sigma_{Morris} \geq 20\,\mu\text{m}$, respectively.

Table 6.1: *Uncertain input factors and their characterization; for all temperature-dependent quantities, the adjustments were applied to all temperature levels.*

Description	Symbol	Type	Value	Unit	Source
Young's Modulus	E	A[1]	norm($\pm\,28\,\%$)[2]	GPa	VEREIN DEUTSCHER INGENIEURE E.V. (VDI 3405 2.2)
Yield stress	σ_y	A	norm($\pm\,12\,\%$)	MPa	SEIDEL (2016, p. 101)
Poisson's ratio	ν	A	truncnorm($-\,10\,\%$)[3]	-	Estimate, natural limit
Specific heat capacity	c	A	norm($\pm\,10\,\%$)	$\mathrm{mJ\,t^{-1}\,K^{-1}}$	Estimate
Density	ϱ	A	norm($\pm\,10\,\%$)	$\mathrm{t\,mm^{-3}}$	Estimate
Conductivity	λ	A	norm($\pm\,10\,\%$)	$\mathrm{mW\,mm^{-1}\,K^{-1}}$	Estimate
Thermal expansion coefficient	α	A	norm($\pm\,10\,\%$)	$\mathrm{K^{-1}}$	Estimate
Melting point	T_m	E[4]	$[1075, 1260]$	°C	ANTONSSON and FREDRIKSSON (2005) and POTTLACHER et al. (2002)
Pre-heating temperature	T_{Pre}	E	$[75, 85]$	°C	Estimate of the uncertainty in a temperature measurement
Reference temperature for the convection	T_{Conv}	E	$[70, 120]$	°C	Estimate of the possible increase in overall build chamber temperature
Temperature in the heat affected zone	T_{Pro}	E	$[80, 250]$	°C	Estimate of different ambient conditions
Film coefficient for the top side of the workpiece	$h_{WP,top}$	E	$[5.8, 17.8] \times 10^{-3}$	$\mathrm{mW\,mm^{-2}\,K^{-1}}$	SEIDEL (2016, p. 119) and uncertainty of inert gas flow velocity $[0;3]\,\mathrm{m\,s^{-1}}$
Film coefficient for the side of the workpiece	$h_{WP,side}$	E	$[0, 6.4]$	$\mathrm{mW\,mm^{-2}\,K^{-1}}$	See A.3 on page 154
Film coefficient for the side of the build plate	$h_{Plate,side}$	E	$[0, 1000]$	$\mathrm{mW\,mm^{-2}\,K^{-1}}$	Range from perfect insulator to perfect conductor

[1] A = aleatory uncertainty

[2] norm(κ) = normal distribution with 95 %-interval κ around the mean; thus, for a large enough number of samples, only 5 % of the values deviate more than κ, i.e. 1.96 times the standard deviation SD, from the mean.

[3] truncnorm(κ) = truncated normal distribution with 95 %-interval κ; the sign of κ characterizes the not cut-off arm of the distribution.

[4] E = epistemic uncertainty

(a) *Nominal result*

(b) *Nodes for SRQ extraction*
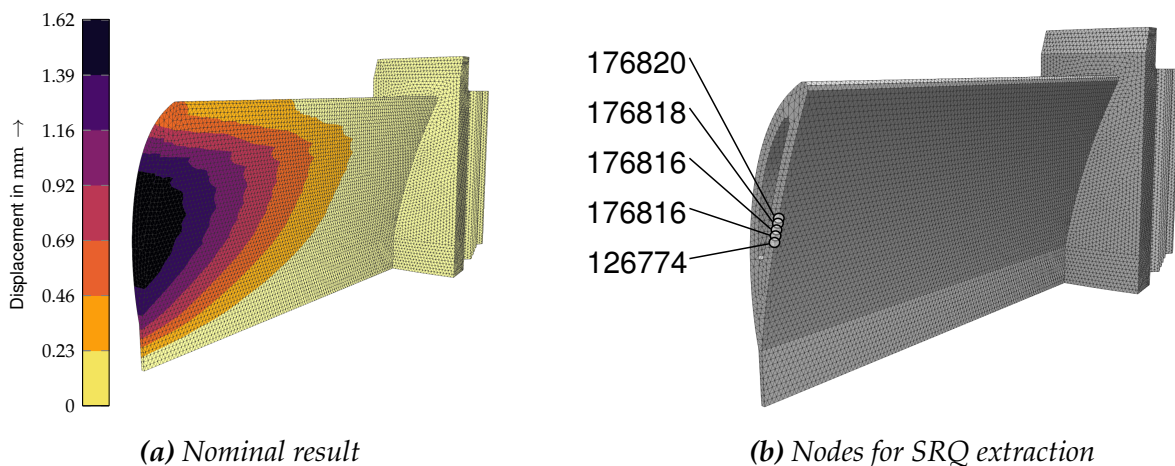
Figure 6.1: *Estimate on predictive capability for the example of the turbine blade: (a) the nominal simulation result showing a maximum displacement magnitude at the tip of the blade of 1.62 mm. (b) The SRQ is generated by averaging the displacement magnitude at the position of the five marked nodes. For this simulation, this selection and averaging also yields 1.62 mm.*

6.2.4 Numerics

The mesh convergence study presented in Section 5.6 on page 76 shows that there is a significant discretization error when using a coarse mesh of the blade geometry. However, the difference in the SRQ is only marginal for finer meshes that exhibit a minimum of two elements over the thickness of the thin features. While OBERKAMPF and ROY (2010, p. 324) recommend incorporating the determined discretization error as an epistemic uncertainty within the analysis, this is omitted for the prototypical study presented here.

In an industrial use case that is used as the basis for a grave decision, a conservative approach like the GCI should be used as an estimate and respected as mentioned above within the analysis. The reduction of the numerical error does not pose a significant challenge in an industrial scenario since it exclusively affects the computational effort of the study. This is, however, only true if none of the auxiliary steps requires manual effort. For the developed simulation tool, no user interaction is required in case all simulations are conducted on the machine on which the samples are generated. If multiple execution hosts are to be used, the tool allows a structured import and export of sampling and SRQ data, respectively. While this could be further simplified by employing a suitable job scheduler / load balancer software to distribute the computational load, only manual load distribution was conducted for this thesis.

In the academic setting of this thesis, three workstations with 30 logical cores each were performing seven simulations in parallel with four cores dedicated to each process. For the UQ study, results from 700 samples were thus obtained in approximately two days, with a runtime of 1.5 h per simulation. This significantly surpasses the manufacturing time of a single blade but is in the same range as the whole process chain from the CAD to the evaluated form deviations even for a streamlined process and a single blade.

6.3 Results

This section presents the results of the different stages of the investigations on the predictive accuracy of the developed simulation model. First, the results from the screening analysis are presented, providing the scope for the remaining investigations. Subsequently, the results of the UQ and the SA are presented in detail.

6.3.1 Screening

For the preliminary sensitivity analysis according to MORRIS (1991), a total of 23 OAT trajectories were chained, resulting in 300 simulations for the identified factors. The results are organized by workpiece.

Blade An overview of the sampling distribution of both failed and successful simulation runs is provided in Figure 6.2 on the next page. It is evident that the sampling strategy is not based on the respective PDFs as e. g. the samples for ν do not conform to a truncated normal distribution. An analysis of the failed simulations suggests a non-systematic influence of the factors on the stability of the simulation, except for the melting point T_m. For this factor, higher temperatures can be correlated with a less stable simulation.

The corresponding results are given in Figure 6.3 on page 100 and the following observations occurred:

- The simulation results show a significant influence of the input variability on the SRQ with an absolute effect μ^*_{Morris} of the process temperature T_{Pro} amounting to 37 % of the magnitude of the SRQ of the nominal case.
- A comparison of the maximum σ_{Morris} and μ^*_{Morris} suggests that the direct effects of the factors are more prominent than the interactions.
- The majority of factors exhibits a μ_{Morris} higher than or equal to zero, i. e. on average sampling the factor at a non-nominal position leads to an increase in the SRQ for the provided sampling range.
- There are multiple factors with a near negligible influence, i. e. exhibiting both a small σ_{Morris} and μ^*_{Morris}.

In summary, the screening results suggest that a subset of the uncertain input factors is sufficient to describe the model variability. Applying the threshold defined in Subsection 6.2.3, eight factors were respected for the subsequent analyses: $h_{WP,side}$, T_{Conv}, T_m, T_{Pro}, σ_y, E, ν and α. However, the upper end of the range for $h_{WP,side}$ is only reached when workpieces are being built in close proximity, i. e. with gaps of 2 mm. In an industrial setting, similar to the experiments conducted in this thesis, larger spacings are employed which significantly shifts the possible range of the heat transfer on the side of the workpieces towards the lower end. Consequently, both $h_{WP,side}$ and T_{Conv} were not respected for the further analyses. The methodology, however, correctly marked the potential importance of the factors when the full ranges are considered. Thus, if no information about the distance between workpieces is available, both factors should be included.

Panel As mentioned above, the screening analysis was repeated with the panel workpiece. The sampling was taken directly from the study of the blade, i. e. no re-sampling was conducted. In contrast to the blade workpiece, no simulation run failed for this geometry, suggesting workpieces with filigree areas are more sensitive to deviations from the nominal parameters. The results for the panel workpiece are provided in Figure 6.4 on page 100.

The following conclusions can be drawn:

- The absolute magnitude of all effects and interactions is significantly lower than for the blade workpiece.
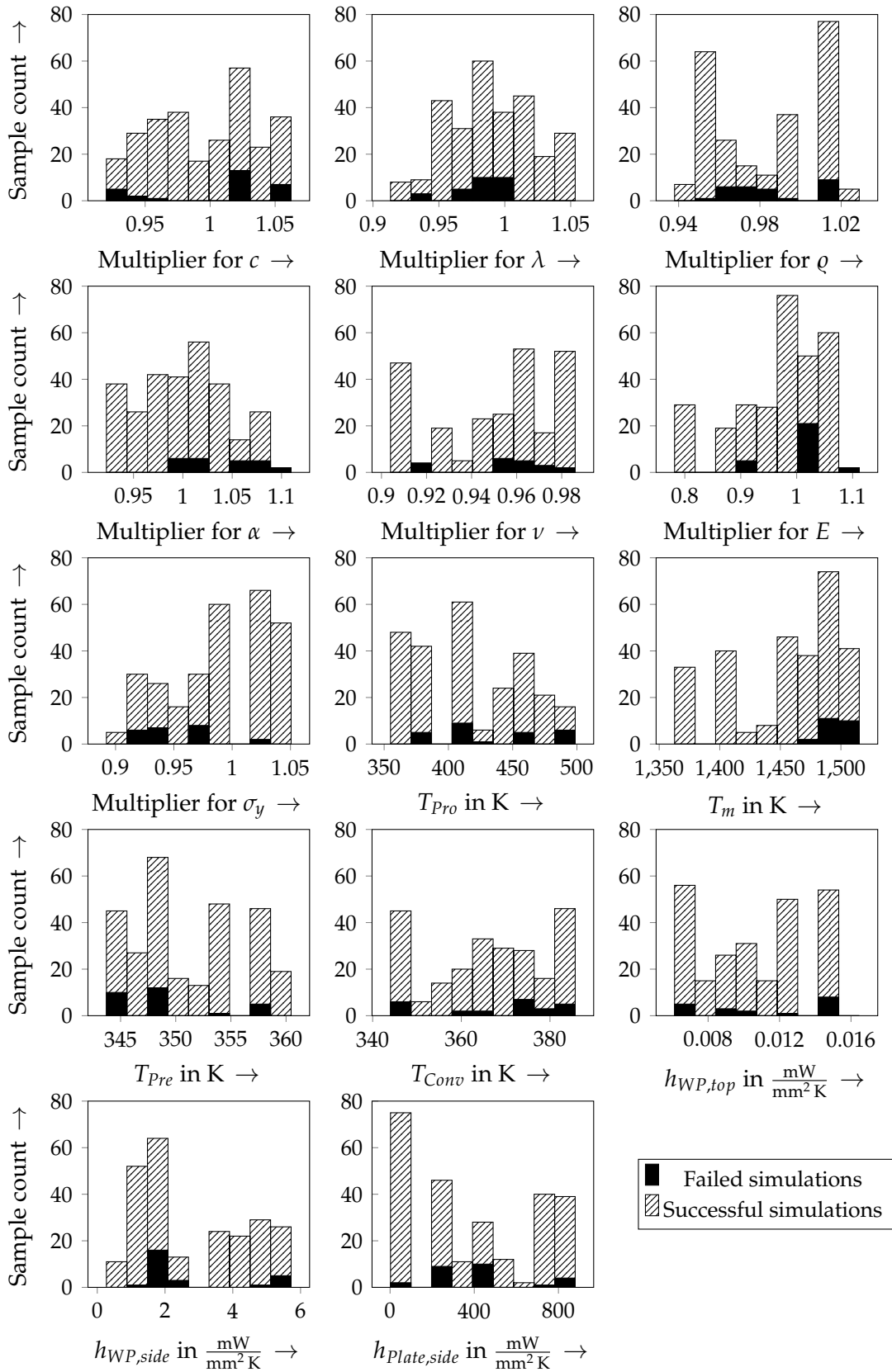
Figure 6.2: *Sampling overview for the screening study of the blade workpiece; failed simulations are marked black. The CDFs were not evaluated for the sampling of the aleatory factors, i. e. a uniform distribution is inherently assumed by the employed random number generator for all factors.*
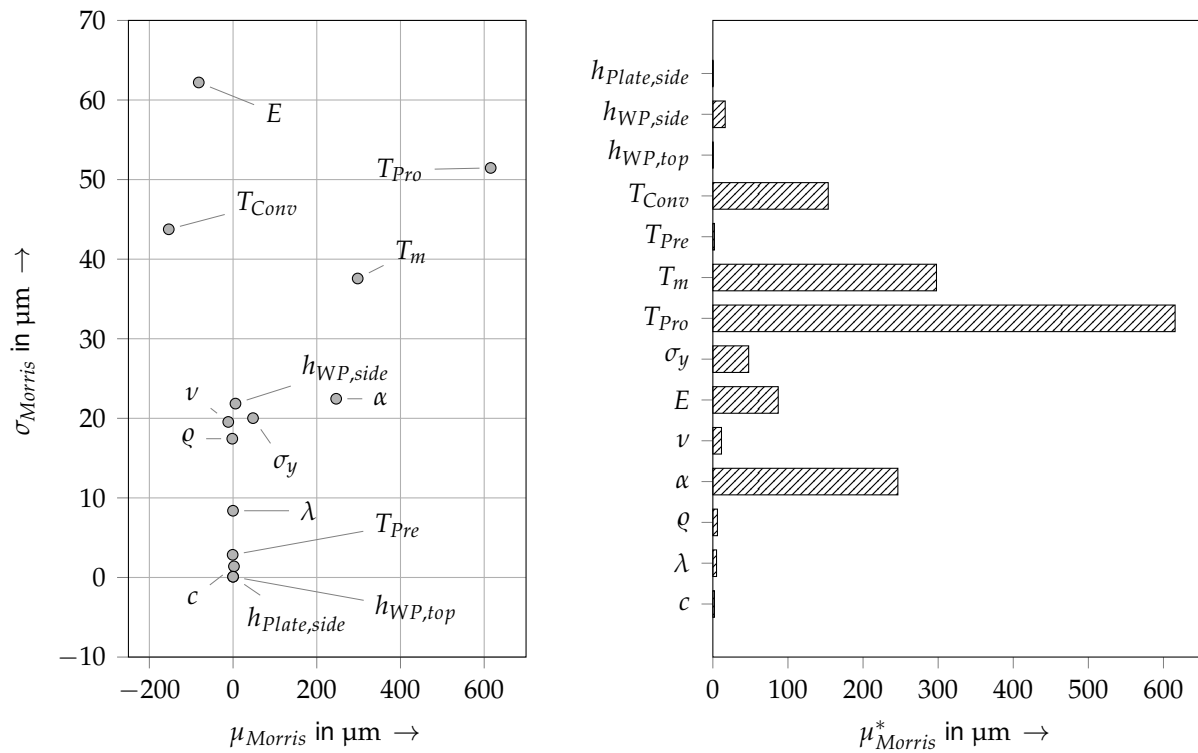
Figure 6.3: *Results of the screening analysis for the blade workpiece (left) in the μ_{Morris}-σ_{Morris}-plane and (right) their absolute magnitude μ^*_{Morris}; for a highly nonlinear contribution, e.g. for ν, μ_{Morris} does not properly reflect the importance of the factor.*
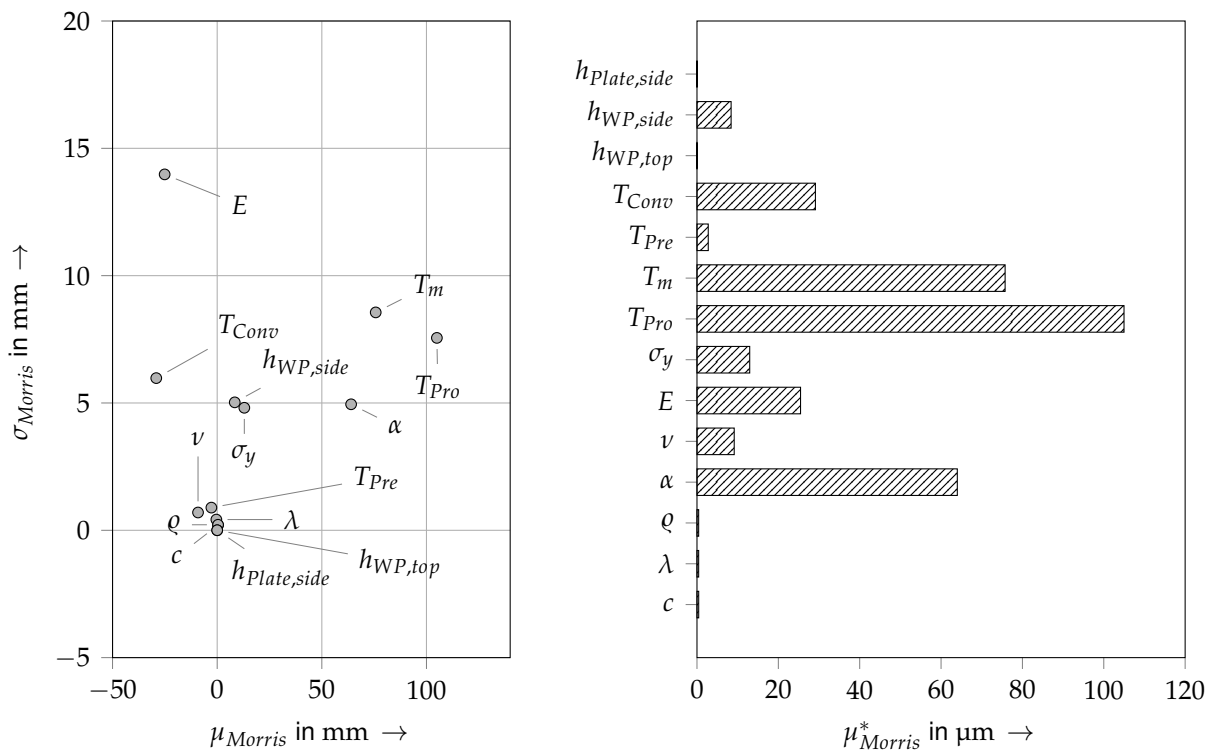
Figure 6.4: *Results of the screening analysis for the panel workpiece: in the μ_{Morris}-σ_{Morris}-plane (left) and their absolute magnitude μ^*_{Morris} (right)*

- The ratio of the magnitude of the variability (largest μ^*_{Morris}) with respect to the magnitude of the nominal displacement ($0.105\,\text{mm}/0.388\,\text{mm} = 27\,\%$) is similar to that of the blade workpiece ($0.615\,\text{mm}/1.62\,\text{mm} = 38\,\%$).
- The ranking of the most important factors is equivalent for the major contributors (T_{Pro}, T_m, α, T_{Conv}, E and σ_y) and similar for the subsequent factors (e. g. ν and T_{Pre}).

In conclusion, the comparison of both results suggests that the geometry does not significantly alter the structure of the drivers of uncertainty in the SRQ for this simulation model. However, the confidence that can be placed in this statement is limited as no analysis of the sampling variability was conducted, which, if added, would contradict the preliminary nature by adding numerical effort.

6.3.2 Uncertainty Quantification

For the UQ only the six factors that were previously identified as the most relevant were used and no adjustments to their uncertainty characterizations were carried out. The number of base samples for the epistemic and the aleatory factors are chosen as 5 and 10, respectively. With the sampling strategy by SALTELLI (2002), the resulting 700 samples contain only 100 independent samples for the aleatory variables, resulting in a sampling error of approximately 20 %. A pure PBA-based sampling strategy with 700 independent samples could reduce this error to approximately 7 %. However, new samples would then be necessary to generate the SIs.

The results are visualized as individual CDFs in Figure 6.5 on the following page along with the resulting p-box that is extracted as their envelope (cf. Figure 2.7 on page 18). In this study, the result is dominated by epistemic uncertainty, as the distance between the boundary CDFs significantly exceeds the lateral extent of both curves individually. This is in line with the results of the screening where the two most relevant factors (T_{Pro}, T_m) are of epistemic nature. Additionally, most of the CDFs could be approximated by linear slopes, which would represent uniform PDFs. This suggests a non-linearity of the simulation model, since the distribution changes from input to output quantity. The varying step heights of the CDFs can be explained by missing results for failed simulations. Table 6.2 on page 104 contains the share of successfully concluded simulation runs for all conducted studies in this chapter. No conclusions should be drawn from the distribution of the individual CDFs in the p-box, since there is no probability associated with the realizations, i. e. the combination of samples of the epistemic factors.

6.3.3 Model Accuracy Assessment

This subsection is dedicated to the investigation of the degree to which the model predictions and the experimental data match. There are different metrics to present the accuracy of a
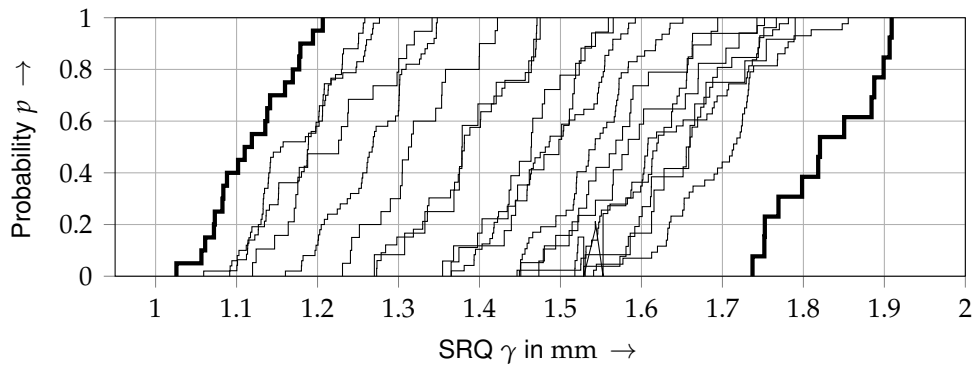
Figure 6.5: Resulting CDFs for the study with the blade workpiece; from a total of 700 simulations, 20 CDFs of the unique combinations of epistemic factors were constructed and plotted (thin). Additionally, the hull of this family of curves, i. e. the p-box, is marked (thick).

simulation model. As an example, OBERKAMPF and ROY (2010, pp. 529ff.) suggest using and reporting the non-overlapping area between prediction and experiment to quantify the level of disagreement. However while it is a sophisticated metric, this quantity, referred to as the area metric, is not easily accessible and does not contain all the information that a graphical representation can provide. The same holds true for other metrics, including typical standards like e. g. the distance of the maximum value to the mean in terms of standard deviations. In consequence, plots are provided for the assessment of model accuracy instead of a reduced metric in this thesis.

Additionally, in the following, accuracy is distinguished from precision[15]. Otherwise, in order to make the model more accurate, it would suffice to simply increase ignorance to correctly predict the range in which observations may fall. For example, by largely increasing the uncertainty in the input factors, a range for the prediction between 0 and 20 mm may result, covering all experimentally observed results. However, for the intended use, it is usually required to not only get a correct but also a precise estimate of an SRQ in order to provide benefit. The precision of the prediction should thus also be considered when evaluating model accuracy results.

The results for the UQ study are depicted in Figure 6.6 on the facing page and described in the following. The lower bound of the prediction matches the experimental observations very well. For the upper bound of the SRQ distribution, the simulation results and the experimental observations largely differ in the estimate of the likelihood of both small (< 1.5 mm) and large deformations (> 2 mm). Due to the limited experimental basis, this does not necessarily point to defects in the model. But if additional experiments confirmed this mismatch, the precision of the model should be the focus point for additional modeling efforts. The accuracy, i. e. the degree to which the experimental results fall within the prediction of the model, may already

---

[15]In essence, precision describes the degree to which the variability of the results can be predicted, while accuracy is related to the remaining bias between prediction and actual result (see Figure 2.9 on page 18).

be at a suitable level for the intended use, with only rather unlikely (probability lower than approximately 10 %) outcomes not being predicted. These values may also be explainable with partial ruptures of the support-to-workpiece transition that the model is not designed to respect.

Depending on the use case, the provided information may not be deemed suitable to support a decision. The likelihood that the resulting maximum form deviation is lower than 1.4 mm can only be stated as being between 0 and 100 %. However, in order to increase the usefulness of the simulative predictions, model updating may be conducted.

6.3.4 Model Updating

The results from Section 5.2 on page 53 show that the two different machine types lead to a significant difference in both the average and the variability of form deviations for the blade geometry. The workpieces produced on the *EOS M290* system, which is part of an industrial process chain and thus subject to far more stringent quality control procedures, exhibit significantly reduced variability in form deviation. Since these differences may be of significant interest for industrial users, the model should be able to predict these differences when provided with suitable inputs. In order to test this behavior, the input ranges were adjusted to more closely resemble the actual conditions for the respective machines.

First, it is assumed that the industrial process is running with a well controlled feedstock leading to little to no variability in the metallurgical properties, e. g. the melting point T_m. Since, however, variations of thermal and mechanical properties also stem from anisotropy, no significant reduction of variability is assumed in the remaining material properties. Second, the ad hoc quantity, i. e. the process temperature T_{Pro}, is fixed to different levels. From the results of the screening study, an increase in T_{Pro} is known to have a rather linear and positive effect on displacement (low $\frac{\sigma_{Morris}}{\mu_{Morris}}$ and positive μ^*_{Morris}). Thus, in order to better reflect the lower displacement results on the *EOS M290*, a reduced magnitude of T_{Pro} can be employed.
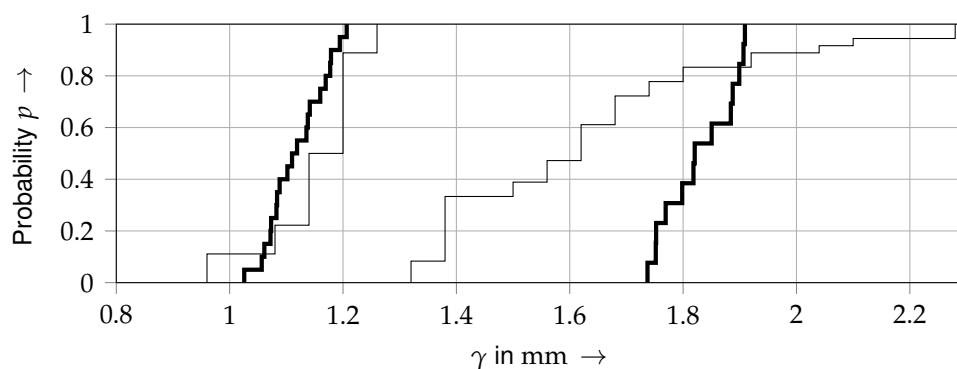
Figure 6.6: *Comparison of simulative (thick) and experimental results (thin) for the turbine blade study; the simulative prediction contains the experimental outcomes with the exception of very high and very low displacements.*

In consequence, a process temperature of $T_{Pro} = 200\,°C$ was chosen for the *EOS M270*. All other input factors are equivalent to the full study. In contrast, to update the model to better reflect the reality on the *EOS M290*, the following parameters were assumed: $T_{Pro} = 80\,°C$ and $T_m = 1250\,°C$. Since these are ad hoc choices, the generated data represents a verification rather than a validation procedure. The remaining factors are not constrained since the contributions of metallurgy cannot be separated from those of anisotropy.

Since the exclusion of factors reduces the numerical effort, an increased number of base samples could be generated for the two studies (see Table 6.2). The chosen sampling frequencies led to sampling errors of 12 % for the *EOS M270* and 28 % for the *EOS M290*. Also, a comparable fraction of simulations failed with respect to the previous study (see Table 6.2).

Table 6.2: Information on the sampling strategies and the success rates for the conducted studies

Workpiece	Study description	Epistemic base samples	Aleatory base samples	Number of simulations	Share of successful simulations in %
Panel	Screening	-	-	300	100
Blade	Screening	-	-	300	91
	UQ	5	10	700	84
	UQ for *EOS M270*	8	16	1536	85
	UQ for *EOS M290*	-	20	240	83

The results of the UQ analysis for the study tailored to the *EOS M270* are provided in Figure 6.7a on the facing page. As expected, since the input space is a subset of the previous study, the very high SRQ values are still not within the prediction and the epistemic fraction of the uncertainty is significantly reduced. However, in comparison to the previous study (see Figure 6.6 on the previous page), the desired shift of the predicted form deviation to larger magnitudes is evident. Additionally, the precision of the prediction is raised, especially for the SRQ range from 1.5 to 1.8 mm[16].

Similarly, Figure 6.7b displays the results for the *EOS M290*. Since this study only contains aleatory factors, only one CDF for the prediction of the SRQ was generated. The result suggests a rather linear overestimation of the form deviations by the simulation model with an average error of approximately 0.2 mm. In comparison to the non-calibrated study, it is apparent that the newly generated prediction does not coincide with the lower boundary of the p-box and consequently exhibits significantly increased mismatch. It may be sensible to further improve the model updating process for this machine, if additional experiments confirm the given experimental EDF of the SRQ. Possible targets include, in this case, the

---

[16]The experimental EDF indicates, for example, that 80 % of the specimens show a maximum deviation lower than 1.8 mm. Without model updating, the prediction could only suggest this fraction to be between 40 and 100 % (see Figure 6.6 on the preceding page). In contrast, the calibrated model yields an improved estimate of this fraction of approximately 90 %.

material parameters, since the layer height of the machine is different from the one that was used to manufacture the material testing specimens. However, depending on the use case, a conservative estimate of the form deviations, that includes some room for error in post-processing, may also be suitable.

In an additional study, the effect of a change in process temperature on the quantity of the residual stresses was investigated with the help of the cuboid specimen. No significant differences were observed between settings of $T_{Pro} = 80\,°\text{C}$ and the nominal setting from the previous simulation, i. e. $T_{Pro} = 200\,°\text{C}$. This suggests that, at least in the given range, the process temperature provides a suitable target for calibration, as it does not affect secondary quantities.

6.3.5 Sensitivity Analysis

Due to the chosen sampling method, which was suggested by SALTELLI (2002), the results of the previous studies can also be used for a quantitative SA. To this end, the S_1 and S_T indices were determined for the respective factors. Additionally, as mentioned in Subsection 6.1.3, jackknife re-sampling is used to generate information on the sampling variability of the determined indices. For each factor, 40 jackknife samples (JS) were generated.

The results of this analysis for the non-calibrated study are provided in Figure 6.8 on the next page with the values for the full sample and all subsample configurations. According to this information, the main share of the variance, approximately 85 %, can be explained by only two factors, i. e. T_{Pro} (49 %) and E (36 %). The remaining four quantities exhibit only marginal first order indices but are part of non-negligible interdependencies. The sampling variability is significant, with e. g. S_T of E being subject to changes of approximately 40 %. However, since the segmentation of negligible and non-negligible SIs is independent of this variability, no change in the conclusion can be expected. In comparison to the results of the screening study (see the μ^*_{Morris} magnitudes in Figure 6.3 on page 100), conducted with the method of

(a) EOS M270 *(b)* EOS M290
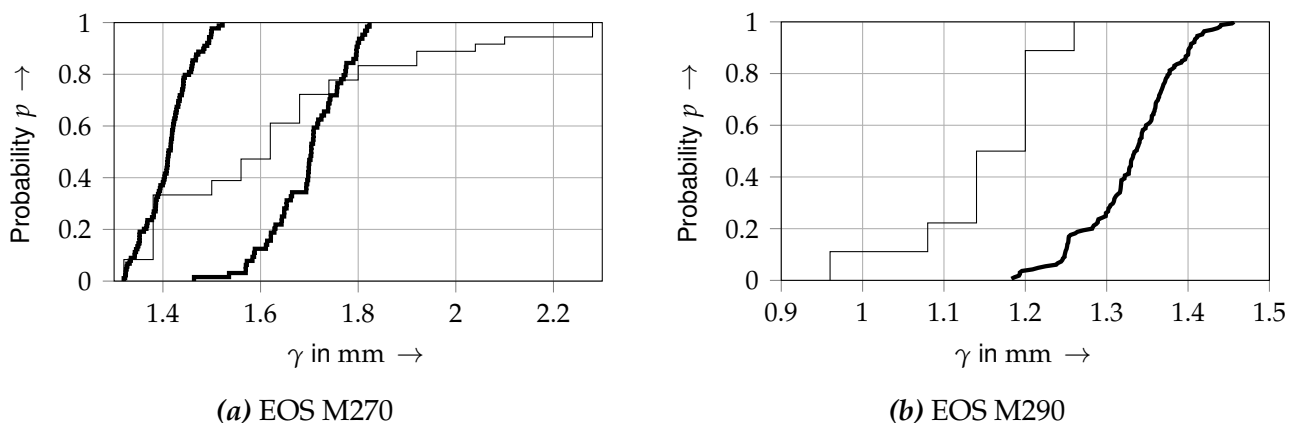
Figure 6.7: *Prediction of the probability after model updating (thick) and experimental EDF for the form deviation (thin) of workpieces on different machines to be below a given threshold*

MORRIS (1991), the ranking of factors is altered. The role of E is significantly increased, while the variance share of T_m is diminished. Since the screening method was conducted with a reduced number of samples, this mismatch is explicable. The large influence of E via mixed terms, i.e. the difference between S_T and S_1, is, in contrast, well predicted by the screening analysis with a large σ_{Morris}.

In order to investigate the stability of these variance shares, the study tailored to the *EOS M270* is also evaluated according to the specified methodology (see Figure 6.9). For the fixed value of T_{Pro}, the results from the quantitative SA resemble those of the screening analysis more closely: the ranking of the importance of the factors is analogous and the effect of interdependencies, described by $(S_T - S_1)$ and σ_{Morris}, is small with respect to the isolated effects, i.e. S_1 and μ^*_{Morris}. The dominant influence is given by T_m, followed by α and E. The remaining factors contribute negligibly.

In summary,

- the screening method by MORRIS (1991) provided suitable estimates for the relative importance of the factors and the nature of the effects (isolated vs. in interdependencies),
- the number of samples should be increased to raise the confidence in the results (analogous to the UQ),
- the presented sensitivities are suitable indicators for the sensible direction of experimental and modeling effort to increase the predictive capability and
- the suitability of T_{Pro} for model updating is confirmed by its large share of variance.
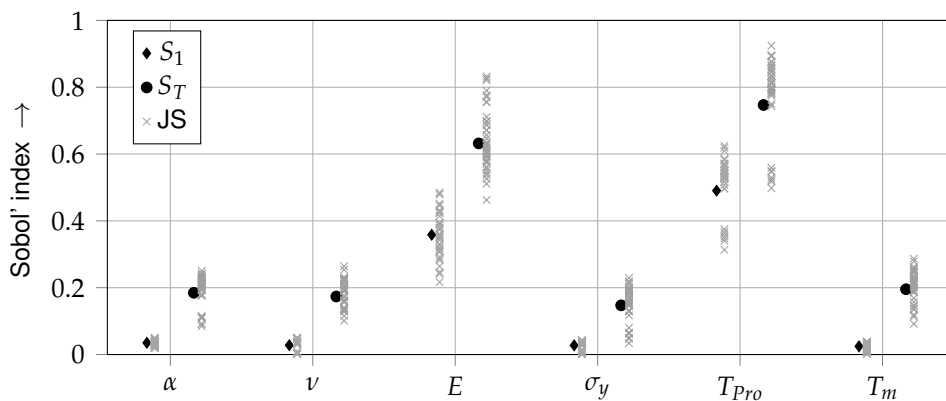
Figure 6.8: *Results for the SA for the investigated simulation model and the prediction of form deviations for the blade workpiece; the 40 jackknife samples (JS) marked by crosses denote the result for the corresponding index (S_1 and S_T) if a subsample of ($n_{Samples} - 1$) was used.*
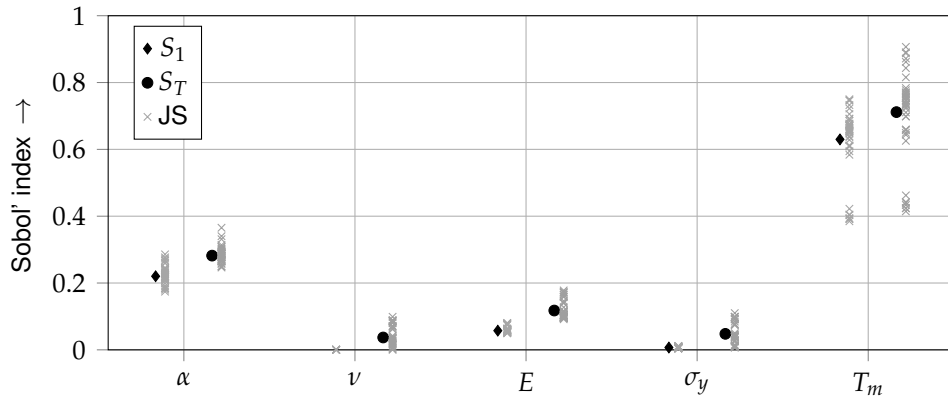
Figure 6.9: *Sobol' indices for the study tailored to the* EOS M270: T_m *shows a paramount influence*

6.4 Summary

By respecting uncertainties in the model and material parameters, non-deterministic simulation results that better represent the inherent variability of experimental outcomes can be obtained. For this chapter, a methodology consisting of a screening analysis with a winding stairs sampling scheme as well as a UQ based on the PBA and a sensitivity analysis based on the determination of SIs was employed. The screening analysis, conducted for the panel and the blade workpiece, enabled the identification of the most relevant factors for the subsequent studies. The form deviation results of the UQ show promising agreement with the experimental outcomes for the blade workpiece, especially if model updating is conducted to account for machine differences. Lastly, the more detailed sensitivity analysis confirms and expands the results of the screening and enables a more effective direction of effort for decreasing uncertainty. Additionally, the study shows that the high numerical effort for the generation of non-deterministic results necessitates a careful study design. Subsequently, the application of the simulation model to reduce form deviations after manufacturing is presented in the next chapter.

7 Pre-deformation

According to the descriptions in this chapter, the predictions of the developed simulation model were used in a digital pre-process to reduce form deviations after manufacturing (AM). As pointed out in the introduction (see Figure 1.2 on page 2), an approach relying on simulative models offers advantages over a strategy based on experimental trial-and-error principles in terms of economics, usability and lead time. However, the success of the methodology is dependent on the underlying simulation model providing accurate predictions for the form deviations. If correctly modeled, all carriers of distortion potential are possible handles for compensation by applying them in an inverse fashion (ZOCH 2012).

Differently put, the framework itself represents a general purpose algorithm that can be applied to other processes and other materials by simply switching the used simulation model. For this thesis, only the pre-deformation of the target geometry is investigated due to its almost exclusive effect on the target geometry (cf. Table 3.3 on page 31). The concept is illustrated in Figure 7.1: instead of avoiding distortion, which is oftentimes not possible, the input geometry is adjusted in a way that the displacements lead to a workpiece within tolerances after manufacturing.
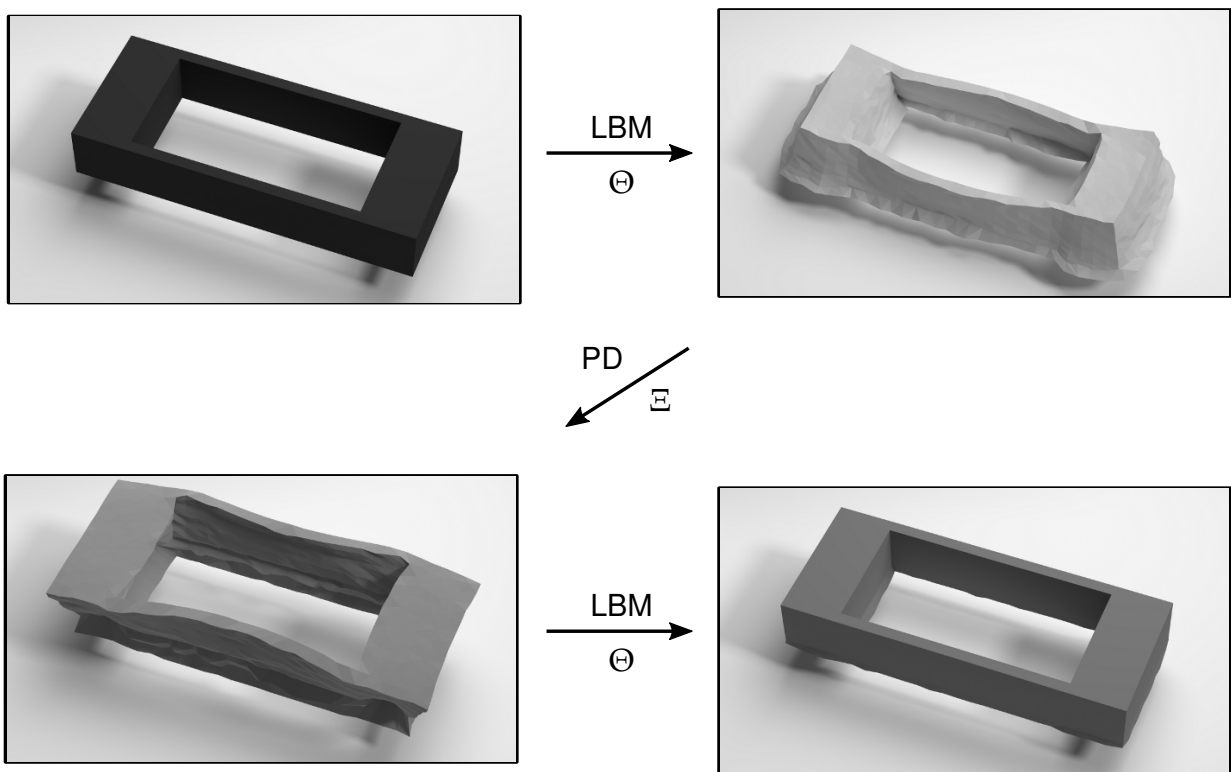
Figure 7.1: *Overview of the PD process: The workpiece exhibits form deviations from the target geometry after the LBM process. With the information on how the workpiece behaves during LBM a pre-deformation function Ξ is constructed that provides an improved input design that only exhibits negligible form deviations after the manufacturing.*

7.1 Methodology

The goal of this methodology is the determination of a pre-deformed set of coordinates, i. e. a configuration $\underline{\underline{x}}_{opt}$, so that the magnitude of form deviations after the manufacturing process does not exceed the given tolerance range. This is translated into an optimization problem where the sum of all form deviations $\underline{\underline{\Delta}}$ is the objective function that should be minimized. Additionally, the abort criterion is defined as a threshold on the maximum of all form deviations.

7.1.1 Constraints

The methodology of PD alters the geometry of the workpiece. Thus, the interfaces to other components in the build process, i. e. the build plate and potential support structures, may also be altered if not handled separately. Specifically, if e. g. the interface to the build plate was reduced, the risk of a build failure, whether by missing cohesion or excessive distortion due to reduced stiffness, may be significantly increased. Thus, the in-plane form of the interface may be altered, but the bottommost surface is constrained to remain within the x-y-plane. This is implemented by excluding the z-position of the nodes coinciding with both workpiece and build plate from the optimization.

7.1.2 Assumptions

One main assumption for the following methodology is that the point distance between the ideal, i. e. undeformed, position x_{target} and the resulting position x' is representative of the form deviation $\underline{\underline{\Delta}}$. For a comparison, there are two sources of mismatch (cf. Figure 2.5 on page 14):

- The determination of form deviation depends on the projection direction and is thus in general not collinear to the displacement vector. In order to minimize the error from this mismatch, the convergence target for the optimization is set stringently, i. e. to $10\,\mu m$.
- A rigid body motion of the workpiece due to a distortion of the build plate may introduce significant deviations between displacement and form deviation in general (see Figures 2.5 on page 14 and 5.10 on page 62). However, since the determination of $\underline{\underline{\Delta}}$ does not rely on projections but can be directly generated from the coordinates of corresponding nodes of the computational mesh, this effect will not lead to wrong results. Nevertheless, excessive rigid body translation or rotation will lead to numerical problems as the workpiece-build plate-interface is fixed in the z-plane. It is thus beneficial to use a state of the simulation model as the target for the optimization that is likely not to exhibit rigid body motion of the workpiece compared to its initial position. For this thesis, the state with the build plate still being fixed by screws is chosen for this reason.

The other main assumption is the existence of non-linearity within the process, i. e. applying an inverse deformation does not result in a perfect manufacturing output (see Subsection 3.1.4). See Section 7.3 for an a posteriori investigation into the validity of this assumption.

The alteration of nodal positions may lead to the applied temperature boundary condition no longer representing a gradient in z-direction only (BAYERLEIN et al. 2015). However, comparisons of optimization routines with and without a re-simulation of the thermal field for each optimization cycle showed, that the influence is marginal. Consequently, the thermal simulation is only conducted once and the results are used for all subsequent thermo-mechanical simulations.

Additionally, as mentioned in Subsection 3.1.2, support structures are assumed to either not be necessary or to be designed as bulk material. For bulky support structures, the respective geometry is considered to be part of the workpiece and is included within the PD methodology. If the support may not be altered, since e. g. the interface is realized with tooth-like structures, the methodology may be adjusted to either treat this interface similarly to the one between build plate and workpiece or to prevent movement of the nodes of the interface in all coordinate directions.

7.1.3 Iterative approach

In order to reach an optimal solution $\underline{x}_{opt}$, an iterative approach is employed, generating an improved solution $\underline{x}_{i+1}$ by further pre-deforming the geometry with the remaining form deviation according to:

$$\underline{x}_{i+1} = \underline{x}_i - \underline{\Delta}_i \quad \text{or} \tag{7.1}$$

$$= \underline{x}_i - \left(\underline{x}'_i - \underline{x}_{target} \right) \tag{7.2}$$

$$= \underline{x}_{target} - u_i \quad \text{with} \quad \underline{x}'_i = \underline{x}_i + u_i \,. \tag{7.3}$$

These equations relate to both all points of the geometry and all three coordinate directions. The optimization itself is performed independently for each individual point and coordinate. The coordinates are only combined for the abort criterion, i. e. whether all form deviations are within the tolerance range, which is determined as the point distance. The iterative procedure is depicted in Figure 7.2.

Additionally, Figure 7.3 on the following page visualizes the mentioned quantities for the one-dimensional case: a point P will be transformed from its initial position, i. e. synonymous with the target position x_{target}, to another position by the displacement u_0. If the form deviation $\underline{\Delta}_0$ is outside the specified tolerance range Tol, the pre-deformation function Ξ uses the deviation $\underline{\Delta}_0$ to change the subsequent input position x_1. The displacement from the LBM process will then result in an output position x'_1 that is, in general, closer to the target. If the result does
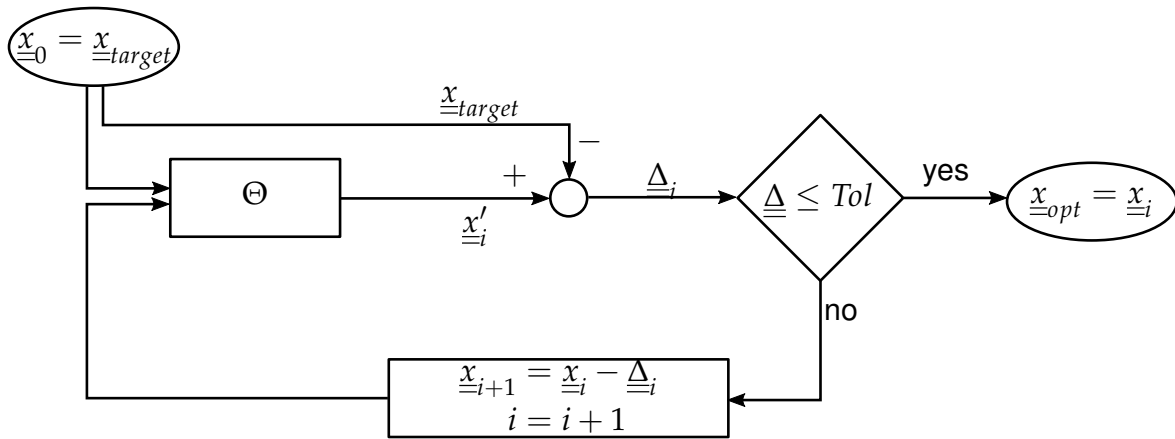
Figure 7.2: Overview of the PD workflow

not lie within the tolerance range, the PD can be repeated until a satisfactory result in terms of form deviations is found. Here, this configuration is found after the second PD.

Mathematically, this iterative procedure represents a fixed-point iteration (see BAYERLEIN et al. (2015) for details) of the pre-deformation function Ξ: the optimum is reached when an additional run does not change the input design anymore. There may be cases where this approach leads to divergence, i.e. where form deviations of specific points increase in subsequent runs due to high non-linearity. For these cases, the iterative procedure may be adjusted by, e.g. using a smaller step size as $\underline{\underline{\Delta}}_i$ for the pre-deformation. This could be realized via a reduction factor that is multiplied with the form deviation before inversely applying it, if a divergence is detected. However, no benchmark geometry showed this behavior.

Figure 7.3: Schematic representation of the definitions for pre-deformation simplified to one dimension: The pre-deformation function Ξ is applied until all form deviations are within the tolerance range. Accordingly, the input position geometry x_i approaches its fix point x_{opt}.

Additionally, the descriptive quantity of the pre-deformation factor ξ is introduced:

$$\xi_i = \frac{\underline{x}_{target} - \underline{x}_i}{\underline{\underline{\Delta}}_1} = \frac{\underline{x}_{target} - \underline{x}_i}{\underline{x}'_1 - \underline{x}_1} \quad . \tag{7.4}$$
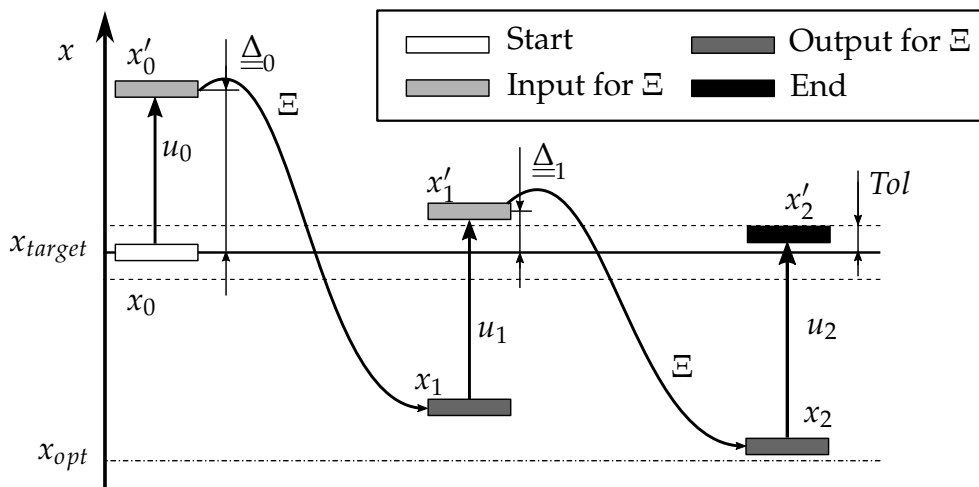
By comparing the lastly resulting pre-deformation to the initial form deviation, it is possible to quantify the level of non-linearity in the process. For example, if a point's form deviation after the build-up is determined as 2 mm, and a deformation of -2 mm is necessary in order for the point to lie within tolerance after the build-up, the process has no non-linearity and ξ is -1. If, on the other hand, a deformation of -3 mm is necessary, the process is non-linear and the pre-deformation is 50 % higher than expected from a linear process, resulting in a ξ of -1.5.

7.1.4 Pre-Scaling

If the result of the pre-deformation cannot be used as manufacturing input, the PD algorithm should provide suitable data for a refit. Since the complexity of this operation is highly dependent on the level of mismatch between the two sets of data, pre-scaling the geometry correctly minimizes the respective gaps. Since computer-aided engineering (CAE) tools routinely allow for the provision of three independent scaling factors for the three spatial coordinates, a least-squares algorithm is used to determine the best values for the components of the pre-scaling vector $\underline{\psi}$ (see Section A.2 on page 153 in the Appendix for the corresponding equations).

This methodology equates to separating the shrinkage from the distortion part of the form deviation. By pre-scaling the CAD-model, the initial difference between the two sets of data can be minimized, improving the conditions for the refit. Additionally, for bulky workpieces, a pre-scaling may already be sufficient to reach a sufficiently low magnitude of the overall form deviations after manufacturing.

7.2 Data chain

This section introduces the data chain related to a simulation-based PD strategy, which is, in essence, an optional digital pre-process, since both input and output of the PD are of digital nature. In contrast to the previous section, the suggested implementation may change significantly, as other programs and tools may become available. Specifically, if isogeometric analysis (IGA) can be established as a general purpose simulation tool, data chains for CAE will be drastically simplified (HUGHES et al. 2005). However, the solution of thermo-mechanical problems currently relies on discretization in the form of computational meshes or particles. Thus, the data chain consists of three major transitions:

CAD $\rightarrow$ FEM ($\underline{\bar{x}} \rightarrow \underline{\hat{x}}$) For the FEM, it is necessary to generate a mesh from the CAD geometry. Since the developed methodology targets a global, i. e. for all points, optimization of the form deviation, the mesh should be an accurate representation of the CAD model in all areas of the workpiece. To this end, the tolerance for the node-to-surface distance was not allowed to exceed 50 μm. For practical applications it stands to reason that only those areas with high GD&T requirements are accurately represented in the computational model, reducing the numerical effort. All geometries are meshed using a CAE tool, more specifically Altair HyperMesh, but there are many alternative software packages available, including open source programs like netgen.

FEM $\rightarrow$ FEM$_{\text{optimal}}$ ($\underline{\hat{x}} \rightarrow \underline{\hat{x}}_{opt}$) The methodology described in the previous section was employed to gain the optimized input geometry. While the data also contains nodes within the volume, only the surface was used in the subsequent step, including all internal surfaces, e. g. channels.

FEM$_{\text{optimal}}$ $\rightarrow$ CAD$_{\text{optimal}}$ ($\underline{\hat{x}}_{opt} \rightarrow \underline{\bar{x}}_{opt}$) As mentioned in Chapter 5, this step may be omitted if the mesh was created with sufficient form accuracy. In this case, the surface description of the mesh may directly be used within the normal pre-processing for a build job. If the mesh is unsuitable, both the optimized simulation result, i. e. its surface description, and the initial CAD geometry are used to gain the optimized CAD model. For this step, no suitable alternative to the commercial solution Geomagic Design X could be identified. The tolerance range for the refit was set to 50 μm for all studies.

With distortion evolving over multiple process steps, it is necessary to define the target state for the form deviation minimization. By using e. g. $\underline{x}'_{LBM}$ as the target state, the distortion after the whole process $\underline{x}'_{HT}$ may not exhibit satisfactory form deviations. As mentioned above, the step with the build plate still being held in place by screws was selected for the simulations in this thesis.

7.3 Results

In order to check the convergence behavior of the developed methodology, the reduction of the form deviations of the two benchmark workpieces was analyzed. Additionally, experimental trials with pre-deformed input designs were conducted that enable a qualitative and quantitative comparison of the merit of the proposed methodology. This section is divided by workpiece type, i. e. panel and blade.

7.3.1 Panel Workpiece

In order to investigate the non-linearity of the distortion behavior of this workpiece, the developed PD methodology was compared to a simple pre-scaling version, comparable to the measurement-based approach: instead of allowing individual values of ξ to vary for every

node, it is constrained to three fixed values, one each for the three axes for all nodes. This is equivalent to the current industry practice of shrinkage correction by inversely applying the measured overall size change to the nominal design, with an adjusted scaling factor in the three coordinate directions. The panel workpiece was meshed with $l_e = 1\,\mathrm{mm}$ resulting in a mesh of linear elements with 57 388 nodes. The simulation was performed on a normal workstation (Intel Xeon E5-2687W) with 10 cores in parallel and it took a total of eight hours to complete for all three iterations.

Figure 7.4 shows the residual deviations for both optimizers over the course of the simulation iterations. By allowing a non-uniform distribution of ζ, the set target deviation of $10\,\mu\mathrm{m}$ was met for all nodes after three iterations. In contrast, if the pre-deformation factor ζ is restricted to a uniform distribution, e. g. approximately 1.135 in this case, the deviations cannot be lowered beyond a certain magnitude (normalized maximum deviation of 0.2) in this benchmark. The final distribution of ζ illustrates the degree of non-linearity (see Figure 7.5 on the following page).

The difference in the possible form adjustments also leads to a discrepancy in the recommended scaling factors[17]. For the uniform optimization, the overall shrinkage of the workpiece in the process requires a globally oversized design: the corresponding scaling factors for an easier refit of the geometry are: 0.41 %, 0.011 % and 0.059 %. In contrast, for the non-uniform ζ, the recommend factors are: 0.356 %, -0.215 % and 0.063 %.

Since the pre-scaling approach did not yield sufficient form accuracy in the simulation, only the non-uniform solution was experimentally examined. The pre-deformed geometry for the build-up study was generated directly from the simulation result without an additional
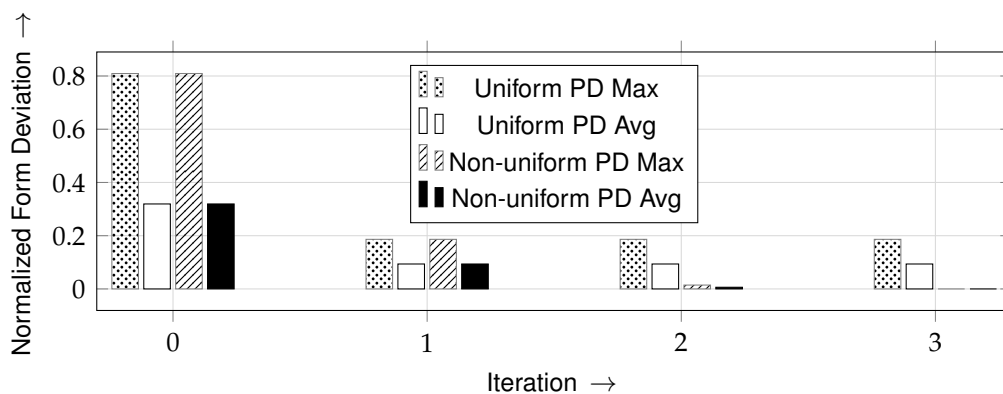
Figure 7.4: *Remaining maximum normalized form deviation of the benchmark geometry panel for uniform and non-uniform pre-deformation: while the non-uniform solution reaches a satisfactory result after three iterations, the uniform approach cannot further decrease the deviation. The optimization was aborted after five unsuccessful iterations in this case.*

---

[17]For easier readability, the scaling factors are given as deltas to one. Thus, a factor of 1.0041 is provided as 0.41 %.
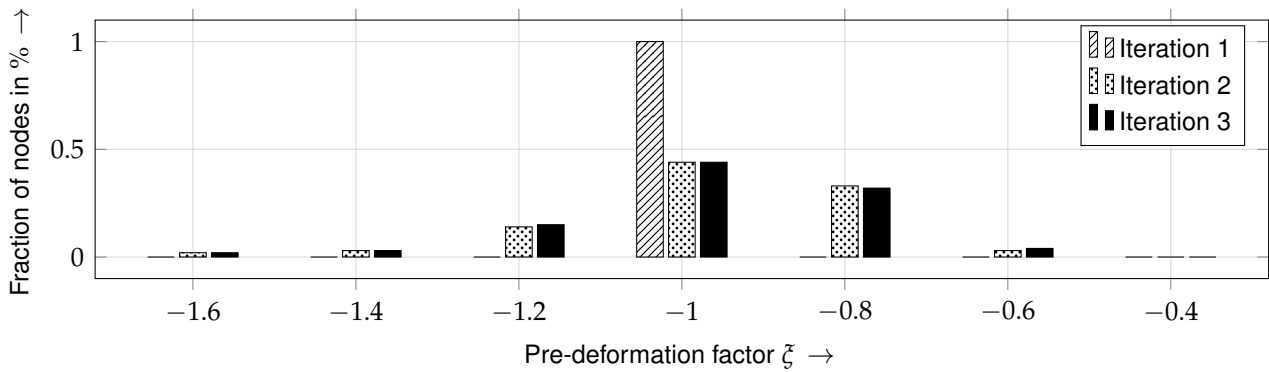
Figure 7.5: *Distribution of the pre-deformation factor for three iterations of the panel geometry; the iterations after the initial inversion with a uniform factor exhibit a broadened distribution that only undergoes small alterations until convergence.*

refitting procedure. Thus, a standard-tesselation-language (STL) representation of the final, converged input design was generated from the numerical mesh and provided to the build preparation software for placement and orientation. No additional parameters besides the design were changed and both workpieces were built on the *EOS M270* system. Figure 7.6 on the next page shows the measured form deviations for both the initial and the pre-deformed design with respect to the nominal, i.e. the target, geometry.

The optimized design shows a better overall form accuracy, but some areas exhibit remaining form deviations in general or overcompensation (front, middle) in particular. However, without statistically significant investigations, it is hard to quantify whether these local mismatches are due to a systematic error or variability from the manufacturing process. The results suggest that the pre-deformation procedure is also suitable for large workpieces that exhibit significant distortion and shrinkage. Additional studies are necessary to provide a statistically sound analysis.
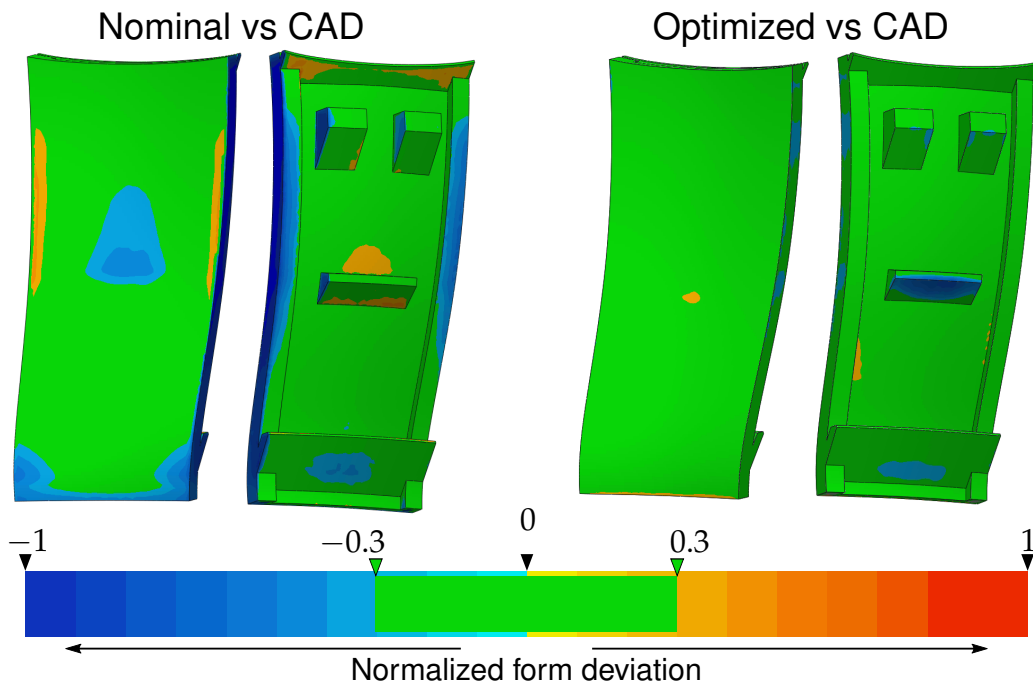
Figure 7.6: *Comparison of form deviations after LBM between the nominal and an optimized input design for the panel workpiece; in contrast to the depiction in previous figures, the overall tolerance was tripled in order to represent a more industrially relevant scenario.*

7.3.2 Blade Workpiece

A similar study was conducted with the blade workpiece, only without the uniform PD. It was meshed with $l_e = 0.4\,\text{mm}$ resulting in a mesh of linear elements with 139 060 nodes. However, due to the high distortion of the geometry, the pre-deformation is more susceptible to numerical instabilities. The nominal study could indeed not be successfully concluded, with reproducible simulation aborts on the second iteration due to non-convergence in the switch to bulk material (cf. Figure 5.11 on page 64) for a layer with a mass jump. Consequently, the material definition of IN718 was adjusted by removing the definition of the plastic behavior at melting temperature T_m. This resulted in a negligible alteration to the prediction of the displacements of e. g. 5 μm for the maximum displacement, but a more robust simulation procedure, enabling the iterative optimization for the blade workpiece. The simulation was performed on a normal workstation (Intel Xeon E5-2687W) with 10 cores in parallel and it took a total of 14 hours to complete for all three iterations.

The convergence behavior is shown in Figure 7.7 on the next page along with the defined tolerance range for the convergence of the optimization of 50 μm. The major share of form deviations was already corrected with a simple inversion of the deformation, leaving a maximum $\underline{\underline{\Delta}}$ of 270 and 70 μm on average. At this stage, approximately 30 % of nodes still exhibited a final position outside the tolerance range. The subsequent run reduced this fraction to 14 % of the nodes with a maximum $\underline{\underline{\Delta}}$ of 65 μm before all nodes were optimized in the third iteration.
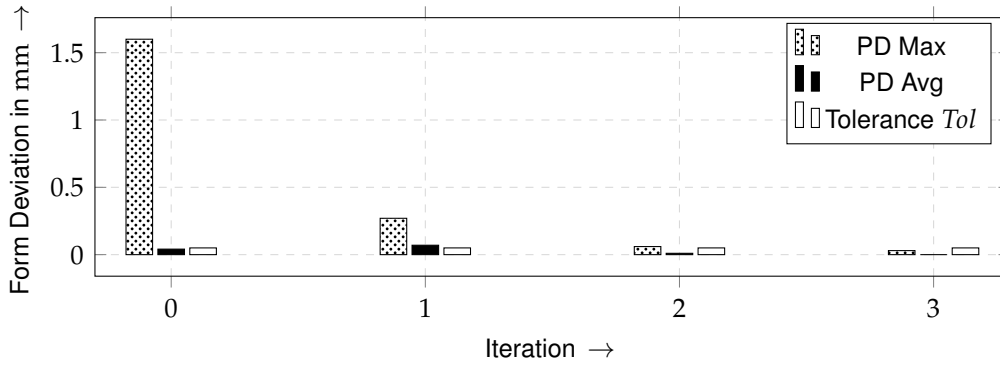
Figure 7.7: Convergence of the simulated remaining form deviations for the blade workpiece

Figure 7.8 shows that the blade workpiece also required a non-uniform ξ in order to reach form deviations within the tolerance range. However, the spread is significantly lower compared to the panel workpiece, which may be due to the difference in size of the two workpieces, since the amount of shrinkage correction depends on the distance of a respective point from the center of gravity. It could also be explained by the more distinct mode of deformation in the blade geometry.

These simulative results were, again, validated against experimental results. Additionally, in order to investigate the merit of the iterative method of pre-deformation, the experimental study for the blade workpiece was expanded to include (values in brackets refer to the number of samples built for this design):

- the nominal design (18),
- the pre-deformed design (18),
- a simple inverted design (3),
- a scaled version of the pre-deformed design (3) and, lastly,
- a pre-deformed design for a simulation with reduced T_{Pro} of 80 °C (3).

Similar to previous jobs, the workpieces were placed randomly across the build plate and oriented in the same direction for all of them and for all jobs of 18 blades each (cf. Figure

Figure 7.8: Distribution of the pre-deformation factor for four iterations of the blade workpiece

5.3a on page 54). For the build job, the most detailed simulation of the blade workpiece with $l_e = 0.4$ mm and $h_c = 1$ mm was used. The scaled version of the optimized geometry was generated by scaling the final difference between pre-deformed and ideal geometry by 120 %.

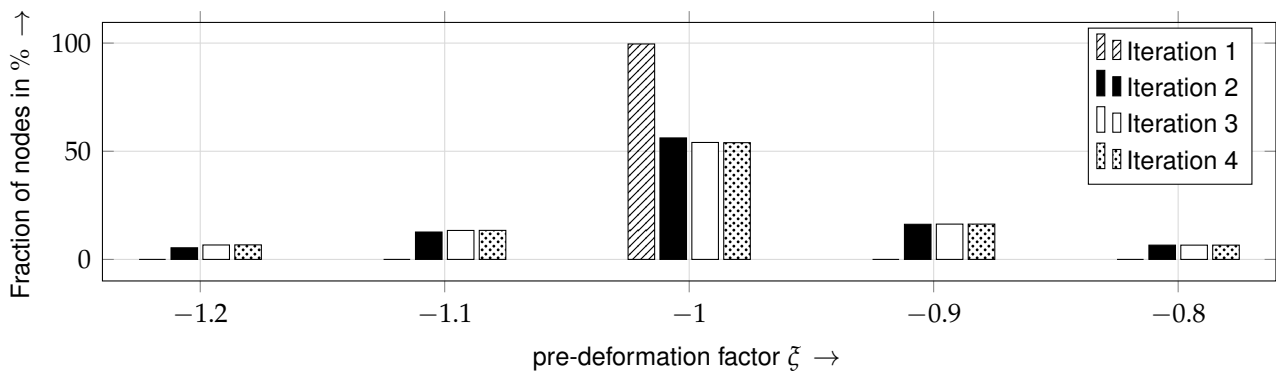The inspection of the manufacturing result showed that five pre-deformed blades ruptured at the transition from support to workpiece in the filigree part at the tip of the blade (see Figure 7.9). All corresponding workpieces were located at the outer region of the build plate. In an a posteriori analysis, the respective areas were predicted to exhibit disproportionately high plastic strain by the simulation, too. However, failure could not be predicted since the simulation model does not contain any crack initiation criteria. In the future, it might be sensible to warn the operator if the plastic strains surpass an appropriate strain threshold or even include a simple model for crack initiation in order to avoid such failure modes. The corresponding workpieces were excluded from further investigations.

Figure 7.10 provides a qualitative overview of the form deviations of the different configurations for three representative workpieces. For a quantitative comparison, three distinct evaluation points were identified, but, due to the high degree of distortion and the closely neighboring surfaces for the hollow blade, no proper matching of the surfaces was reached for point 1 in the nominal design case. Therefore, the respective measurements for this position were dropped.

For all remaining blades, the form deviation was determined as the shortest distance between the defined points on the nominal and the corresponding surface of the measured geometry with the help of the Control X software by Geomagic. The results are presented in the box plots in Figure 7.11a for the two remaining positions 2 and 3 and the different configurations.

For the position on the side of the blade, employing the optimized design reduced both the magnitude and variability of the form deviation compared to the simple, inverted design. The scaled version shows further improvement, suggesting that the simulation underestimated
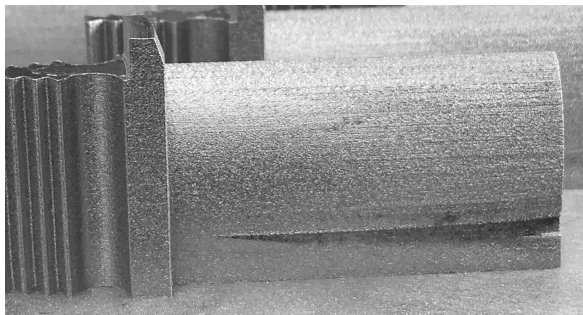
(a) Large defect

(b) Varying levels of defect for different blades

Figure 7.9: *Overview of defects that occurred during the build up of the blade workpieces on the* EOS M400.

(a) Nominal design *(b) Inverted design* *(c) Optimized design*
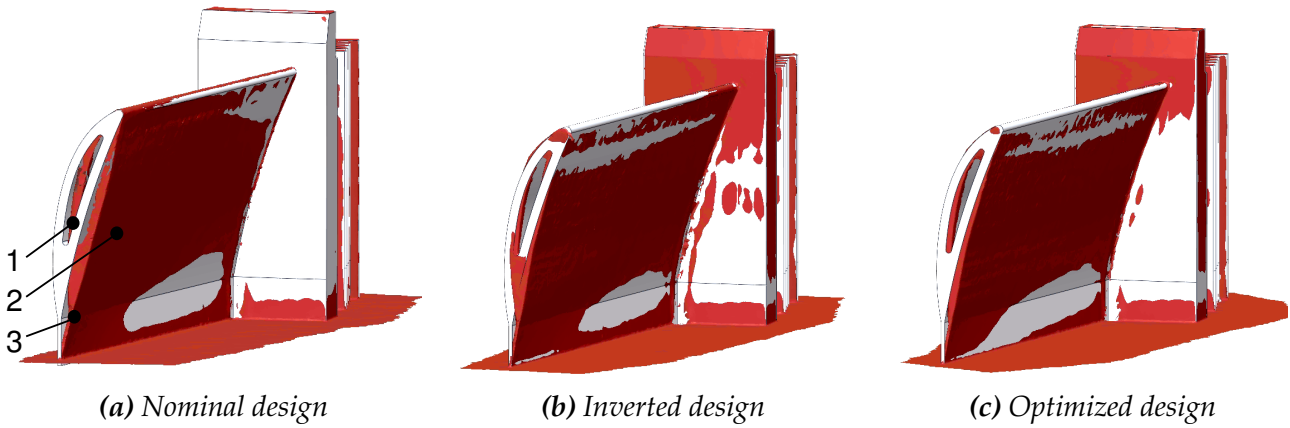
Figure 7.10: *Comparisons of nominal (light) and as-manufactured (red or dark) geometries of the different configurations of the blade workpiece; the investigated points of interest (1, 2 and 3) for the quantitative comparison are marked in (a). Qualitatively, only the improvement of the dimensional accuracy in comparison between the manufacturing result of the nominal design and the two others is apparent.*

the real distortion on this machine. This is in line with the results of the UQ study (see Figure 6.7a). Compared to the nominal design, an average reduction of the form deviation by 72 % was reached at this location. The evaluation point at the transition between support and blade shows a similar ranking of the designs, but with a significantly reduced overall improvement magnitude. Here, the average of the form deviation was decreased by only 25 %.

This difference in efficacy can be explained by a poor local prediction of the SRQ as a result of an insufficiently fine mesh for this transition. Due to the low thickness of the structure, i. e. 0.4 mm, only one element was constructed over the thickness, resulting in an unphysical stiffening of the structure.

(a) Form deviations in point 2 *(b) Form deviations in point 3*
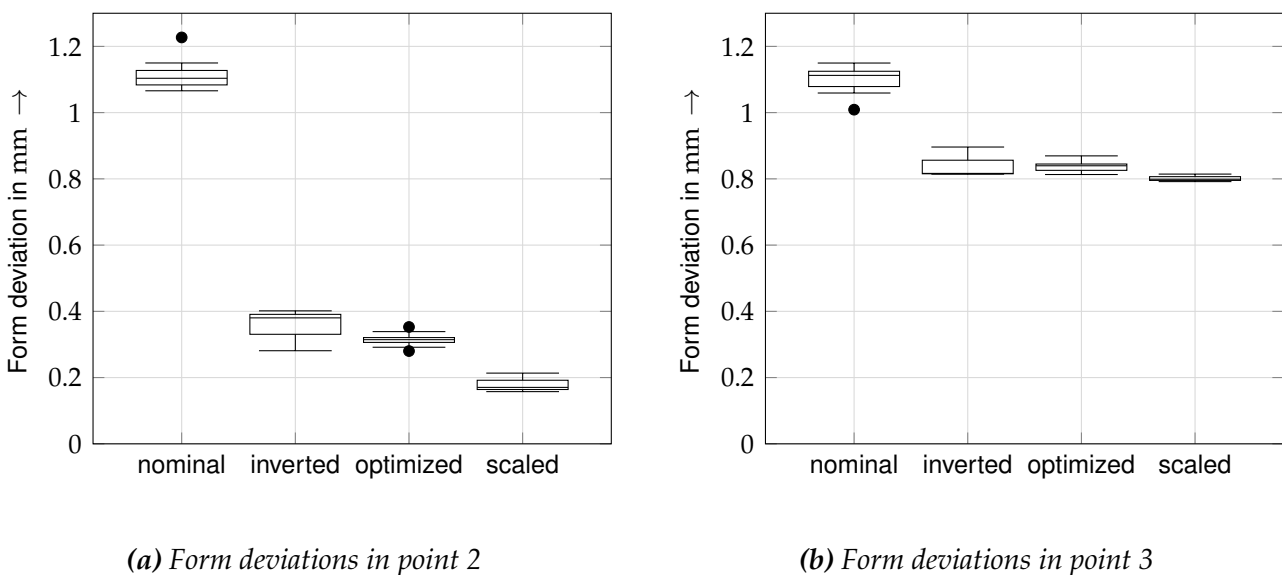
Figure 7.11: *Boxplot comparison between form deviation at the straight side of the blade for the nominal geometry (nominal), a simple inversion of the warpage (inverted), the optimized version (optimized) and, lastly, a by 120 % scaled version of the optimized geometry (scaled)*

In summary, the pre-deformation shows promising results, but it can only correct the distortion from effects that the underlying model accounts for. However, with increasing usage and generated experimental data, the model is expected to provide a very good estimate for an FTR design.

7.3.3 Challenges

While the results from the developed methodology are promising, there are also challenges that may deteriorate the ease of use:

- An accurate representation of the geometry of complex workpieces for the FEM is always connected to high numbers of nodes and elements, which may lead to an unacceptable computational effort. In the context of this thesis, this was counteracted by manually loosening restrictions on form accuracy of the mesh to areas of the workpiece with less strict requirements from a quality assurance (QA) perspective.
- For geometries with thin geometry features or, more general, geometries that feature closely located surfaces, the matching of target and actual position may be faulty. The benchmark part of the turbine blade primitive exhibited this behavior with the outer surface of the convex side being matched with an inner surface. Thus, in order to provide a refitted CAD model, a stepwise approach was applied: by first refitting the initial model to a computational result with only 50 % of the actual pre-deformation and subsequently refitting this model to the fully pre-deformed geometry, the problem was circumvented.
- Since the nodal positions are independently optimized, the elements may be arbitrarily distorted. This may lead to bad aspect ratios or even a negative Jacobian, resulting in a failure of subsequent simulation runs. If necessary, the mesh must be repaired, e. g. in a CAE tool, before restarting the simulation.

7.4 Summary

This chapter presents experimental results that underline the suitability of the developed digital pre-process for managing form deviations in LBM by pre-deformation. An iterative procedure was developed and implemented in order to reliably reach a new workpiece design that, after manufacturing, only exhibits marginal deviations from the intended target design. The application of this pre-deformation method led to significantly reduced form deviations for the panel and blade workpieces, with the additional iterations after the initial inversion providing an increase of approximately 10 % in accuracy. However, the form deviations were only slightly reduced at the support-to-workpiece interface of the blade geometry. This can be explained by the simplified, stiffening meshing of the thin support structure. The chapter is concluded by a description of the aforementioned and other challenges for the application of simulation-based pre-deformation. Details on the efficacy, efficiency and the long-term benefits of the developed approach are given in the next chapter.

8 Discussion

This chapter is structured into three sections highlighting the levels of added benefit from applying the developed methodology. The following sections target specific requirements, as set out in Chapter 4, with efficacy being related to the functional suitability as its sole benchmark quantity. Subsequently, the efficiency of the methodology is investigated mainly in terms of (monetary) resource utilization but also time behavior and capacity as mentioned in ISO/IEC 25010. Lastly, the effectiveness of managing form deviations with a digital pre-process is discussed by evaluating additional criteria as well as the long-term suitability.

8.1 Efficacy - Managing Form Deviations

As a first step, the presented methodology is evaluated solely on the basis of the resulting technological benefit. This evaluation is divided into, first, understanding and predicting form deviations and, second, compensating and correcting these deviations.

8.1.1 Predictive Capability

The results in Chapters 5 and 6 show that the simulation model is able to predict the trend and magnitude of form deviations within the experimental variability. Similar results for validation trials are provided by other simulation models but without information on experimental variability (AFAZOV et al. 2017; KELLER 2017; SEIDEL 2016). However, uncertainty in the form of intra- and inter-machine differences cannot be deemed negligible for the management of form deviations when the manufacturing conditions are not stringently controlled. The proposed method of PBA to incorporate the uncertainties from missing knowledge and inherent variability into the prediction of the SRQ shows promising results for the investigated workpiece, i.e. the blade geometry. The trend and magnitude of the variability of form deviations can be estimated as a p-box that avoids both implicitly assuming knowledge and providing excessively conservative estimates.

With the limited experimental data, input uncertainties, especially concerning material properties, are mainly based on estimates and assumptions. This impedes a quantitative assessment as well as a stringent evaluation of whether the simulation model exhibits sufficient predictive capability for the intended use. However, the applications in this thesis show that the methodology is applicable and viable and that the gathered information can be used for both steering model improvement processes (SA) and decision making (UQ). No similar study is reported in the literature for macroscopic form deviations.

Lastly, when comparing the results and the effort of the employed methods for SA, the congruency of the results of the screening (MORRIS 1991) compared to the method of SOBOL'

(1993) in combination with the low difference of first and total order SIs emphasizes the suitability of the former for preliminary studies. For the study presented in this thesis, confounding the sampling strategy for UQ and SA may have provided less benefit than solely conducting UQ with a sampling scheme tailored to the PBA only.

8.1.2 Improving Dimensional Accuracy by Pre-Deformation

The suitability of the compensation of form deviations via simulation-based PD was already confirmed by multiple studies, e. g. AFAZOV et al. (2017), BRANNER (2010), KELLER (2017), and SEIDEL (2016). However, this thesis represents the first investigation into the efficacy of multiple PD passes; a strategy suggested by BRANNER (2010). The results support the expected increase in form accuracy by accounting for non-linearity within the process, although only a tenth of the effect size compared to the initial inversion (see Figure 7.11a; optimization provides a further improvement of 0.07 mm compared to the initial decrease of 0.72 mm).

In comparison to the mentioned studies, the proposed simulation and PD strategy was tested for larger workpieces (> 100 mm) and larger deformations (> 1 mm). While BUGATTI and SEMERARO (2018) suggest that varying geometries may pose a challenge for the inherent strain method, the quality of the results from the thermo-mechanical simulation approach does not deteriorate for the investigated scenarios.

Lastly, the results emphasize that for an SRQ with inherent variability, reducing the form deviations beyond a fixed threshold may not be possible in a reproducible fashion. Thus, SA and UQ can also be considered for PD usage scenarios, resulting e. g. in an estimate on how reliably a tolerance criterion is reached.

8.2 Efficiency - Cost and Benefit

This section is intended to answer the question as to whether the added value of the presented methodology is economically viable. To this end, the financial aspects involved in both the simulation-based PD methodology as well as the conventional variant, relying on machine occupancy, are discussed. The corresponding process steps are depicted in Figure 8.1.

Other measures for increasing dimensional accuracy that target different drivers of distortion potential, e. g. adding support structures, are not included in this comparison due to them interfering with secondary quantities and performance indicators (see Table 3.3 on page 31).

8.2.1 Cost Model

In order to generate quantitative data, a simplified model for the cost savings of switching to a simulation-based pre-processing strategy is developed. All information is provided for the *as-is* status of the developed simulation tool. Further development may significantly
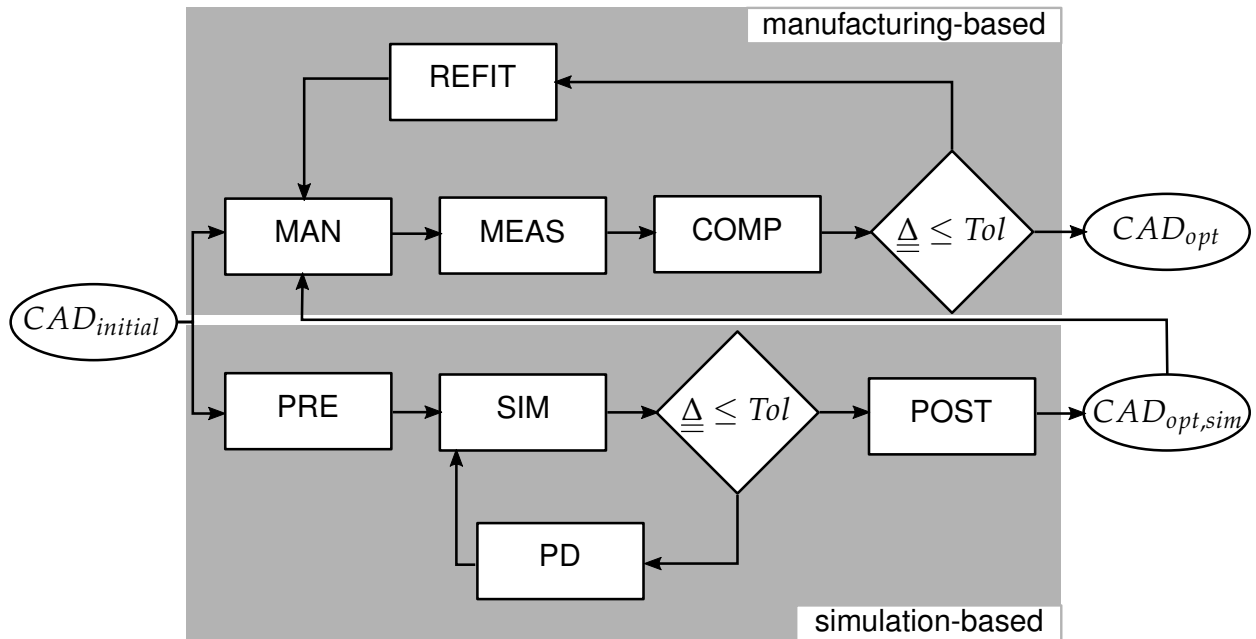
Figure 8.1: *Comparison between a manufacturing- and a simulation-based process chain for PD; the depicted abbreviations are used for the cost model: refit(REFIT), manufacturing (MAN), measurement (MEAS), comparison between actual and target geometry (COMP), pre-processing (PRE), simulation (SIM), pre-deformation (PD), post-processing (POST).*

alter all aspects. The used data and the equations of the cost model are summarized in Table 8.1 on the following page. The following list presents the reasoning behind the non-linear relationships:

- The effort of pre-processing includes the generation of a suitable mesh. With the extreme temperature gradients occurring in the simulation, special care for elements with aspect ratios smaller than 20 is necessary which may lead to very high effort, especially for complex workpieces.
- The simulation effort is assumed to scale linearly with the number of simulation development cycles although the thermal simulation is only performed once. This is due to the thermo-mechanical fraction of the simulation requiring significantly more computational effort.
- An increasing complexity of the workpiece necessitates more nodes for an accurate representation. The size of the matrices scales quadratically with the number of nodes, which is used as an estimate for the effort scaling of the simulation, although there may be solvers that exhibit better scaling behavior. Exemplarily, the calculated simulation effort of around 200 h per cycle, i. e. more than a week, for a very complex part ($c \approx 10$), is in line with experience from industrially relevant workpieces.
- The comparison procedure scales less than linearly with the complexity.

The hourly rate of an AM machine is based on the calculation of KRAUSS (2016), but other sources, e. g. BAUMERS et al. (2016), yield results of the same magnitude. The model was implemented in Python and cost savings for different scenarios, i. e. values for i_{sav}, i_{sim} and

Table 8.1: Input data and used model for the cost savings analysis

Description	Symbol	Value	Unit	Source
Costs for a CAE engineer	K_{CAEE}	70	€/h	Assumption
Costs for an AM operator	K_{AMO}	50	€/h	Assumption
Costs for a measurement expert	K_{ME}	70	€/h	Assumption
Costs for the measurement equipment	K_{MME}	20	€/h	Assumption
Costs for a workstation	K_{WS}	1.5	€/h	AMAZON (2018)
Costs for an AM machine	K_{AMM}	20	€/h	KRAUSS (2016, p. 169)
Costs for the raw material	K_{RM}	570	€	Estimate[1]
Costs for a CAE package, e. g. Altair Hypermesh	K_{HM}	2.5	€/h	Estimate[2]
Costs for a re-engineering software, e. g. Geomagic Design X	K_{GDX}	2.5	€/h	Estimate[2]
Costs for a software for comparison of target and actual comparison, e. g. Geomagic Control X	K_{GCX}	2.5	€/h	Estimate[2]
Complexity factor	c	[1; 10]	-	Definition[3]
Number of necessary development cycles	i_{nec}	$[1; \infty[$	-	Definition[4]
Number of saved development cycles	i_{sav}	$[0; i_{nec} - 1]$	-	Definition[5]
Number of simulated development cycles	i_{sim}	$[1; \infty[$	-	Definition[6]
Costs for the simulation-based pre-processing	K_{PRE}	$c \cdot 5\,\mathrm{h} \cdot (K_{CAEE} + K_{WS} + K_{HM})$	€	Model
Costs for the actual simulation	K_{SIM}	$c \cdot 1\,\mathrm{h} \cdot K_{CAEE} + c^2 \cdot 2\,\mathrm{h} \cdot K_{WS} \cdot i_{sim}$	€	Model[7]
Costs for the simulation-based post-processing	K_{POST}	$c \cdot 1\,\mathrm{h} \cdot (K_{CAEE} + K_{WS} + K_{GDX})$	€	Model
Cost for the simulation-based development cycle	$K_{SIM,tot}$	$K_{PRE} + K_{SIM} + K_{POST}$	€	Model
Costs for the manufacturing of the part	K_{MAN}	$K_{AMO} \cdot 2\,\mathrm{h} + K_{AMM} \cdot 15\,\mathrm{h} + K_{RM}$	€	Model[8]
Costs for the measurement procedure	K_{MEAS}	$c \cdot 2\,\mathrm{h} \cdot (K_{ME} + K_{MME})$	€	Model
Costs for the comparison between actual and target geometry	K_{COMP}	$\sqrt{c} \cdot 2\,\mathrm{h} \cdot (K_{CAEE} + K_{WS} + K_{GCX})$	€	Model
Costs for the refit from measurement data	K_{REFIT}	$c \cdot 2\,\mathrm{h} \cdot (K_{CAEE} + K_{WS} + K_{GDX})$	€	Model
Cost for the manufacturing-based development cycle	$K_{MAN,tot}$	$K_{MAN} + K_{MEAS} + K_{COMP} + K_{REFIT}$	€	Model
Cost savings for the simulation-based process chain	K_{CS}	$i_{sav} \cdot K_{MAN,tot}(c) - K_{SIM,tot}(c, i_{sim})$	€	Model

[1] An assumed workpiece size of $130x130x130\,\mathrm{mm}^3$ with 30 % of the volume filled (SEIDEL 2016, p. 40) leads to a workpiece volume of around $660\,\mathrm{cm}^3$. With a density of approximately $8.71\,\mathrm{kg\,dm^{-3}}$ and a material price of $100\,€/\mathrm{kg}$, approximately $570\,€$ worth of raw material per workpiece should be respected. All other costs of the LBM process are respected in K_{AMM}.

[2] Based on license costs of $\approx 10\,\mathrm{k}€/\mathrm{year}$.

[3] The complexity factor increases with the number of surfaces, edges, radii and other elements that require special attention during CAE. A simple cylinder relates to $c = 1$, while $c = 10$ represents a very complex workpiece that requires hundreds of thousands of nodes for an accurate representation in an FE model.

[4] Depending on workpiece geometry and many other features, workpieces may need several iterations of redesign before tolerances can be reached (see Figure 8.1).

[5] If the simulation provides a better input geometry to the maufacturing process, all but one manufacturing-based loops may be saved.

[6] It can not be assumed that the simulation can save as many manufacturing-based iterations as it needs to converge in silico. Additionally, if a simulation-based pre-processing strategy is employed for a workpiece that does not require any redesign, the effort for the simulation is still incurred.

[7] The numerical effort is expected to scale more than linearly with the complexity, i. e. the discretization effort.

[8] In this simplified model, optimizing the form deviations after LBM, opposed to after the whole process chain (see Figure 2.2 on page 7), is assumed to also yield satisfying results for the state after all subsequent steps.

c were obtained. Figure 8.2 summarizes the cost savings from the simulation-based PD approach for different scenarios and in dependence of workpiece complexity.

8.2.2 Conclusions on Resource Utilization

The developed cost model shows a differentiated picture on cost savings for multiple scenarios. Most significantly, it shows that blindly applying a digital pre-processing strategy may incur additional costs. The number of saved development cycles provides the most significant effect on cost savings. If an experienced operator expects the workpiece not to experience any issues with form deviation, the effort for simulation should be saved, especially for complex parts. If only one manufacturing development cycle can be saved, only less complex workpieces may provide a viable use case for simulation-based pre-deformation. For more than one such cycle, the cost-effectiveness increases with workpiece complexity. Additionally, a significantly increased number of simulative development cycles only has a marginal effect on cost savings, compared to the effect of complexity and number of saved manufacturing-based development cycles.

This analysis also shows that high licensing costs for commercial software may compromise the cost-effectiveness of this methodology, when not looking at secondary benefits. However, if an optimization of the form deviations after LBM does not provide satisfactory results after all subsequent processes, i.e. the whole process chain needs to be respected in the manufacturing-based approach, a positive K_{CS} is much more likely for all scenarios.
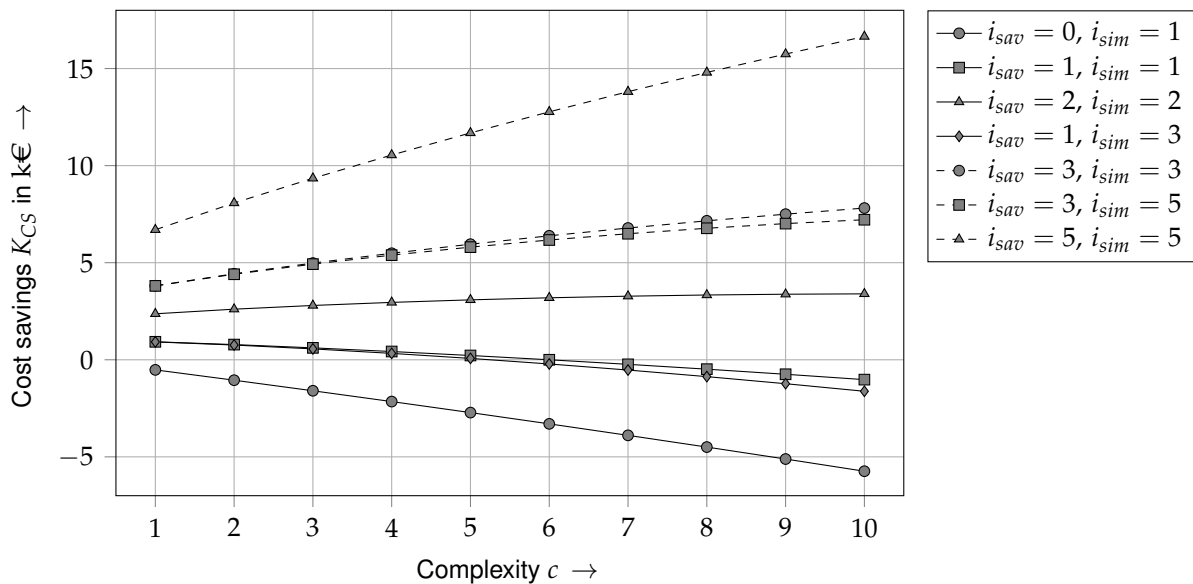
Figure 8.2: *Cost savings for different scenarios with relation to the workpiece complexity; if the simulation cannot provide an improved design suggestion, the simulation-based process will only incur costs (increasing with the number of simulation cycles i_{sim}), which in turn depend on the workpiece complexity. Contrarily, if multiple iterations can be saved (i_{sav}) by the digital pre-process, significant cost savings can be expected.*

8.2.3 Other Benefits

The benefits of a simulation-based PD are, however, not limited to possible monetary advantages. For workpieces that exhibit a certain level of complexity, a measurement-based pre-deformation may not be feasible at all. Also, by increasing the speed of feedback on the manufacturing suitability of designs, better overall designs are possible in a given time frame. These temporal advantages may, depending on the use case or scenario, even be more relevant than monetary ones, see Section 1.1. In comparison to previous solutions, e.g. SEIDEL (2016), the time behavior (cf. ISO/IEC 25010) of the simulation could be improved by an altered heat source modeling, enabling the usage of larger layer compounds, significantly reducing simulation effort. The goal of yielding deformation predictions faster than the actual build process was reached for all workpieces, i.e. 3 vs. 33 hours for the panel and 5 vs. 7 hours for the blade.

Additionally, capacity may also be a key aspect. Scaling computational resources is straightforward with either marginal (no confidentiality requirements, enabling the use of cloud resources) or low investment costs (confidentiality requires in-house solution). On the other side, scaling machine capacities is either connected to high overhead costs for external build-up or potentially prohibitive investment costs and lead times if in-house resources are already used to capacity.

8.3 Effectiveness - Long-Term Benefit and Transferability

In order to evaluate this aspect, different frames of reference are investigated: in the first subsection, the reached maturity of the developed model is evaluated in order to provide an estimate on the predictive capabilities for the intended use. Subsequently, Subsection 8.3.2 provides details on the transferability of the methods and tools to other processes and materials. Finally, this section is concluded by an investigation into the impact the presented research may have on industrial supply chain scenarios, in which AM is a viable alternative to established manufacturing techniques.

8.3.1 Predictive Capability Maturity

This subsection represents a self-assessment according to the PCMM (see Appendix A.4 on page 155 and the set out targets in Chapter 4). The number in brackets denotes the maturity level at which the model is evaluated in the given aspect.

Representation and geometric fidelity (2) In general, apart from a discretization required for a numerical mesh, the model accurately represents the geometry. However, summarizing real layers into layer compounds was necessary to reach suitable calculation times. The methodology for the meshing was developed in close collaboration with

an industrial partner and the information from relevant sources (AFAZOV et al. 2017; KELLER 2017) was respected.

Physics and material model fidelity (1) Both the thermal and the structural simulation are physics based, but only the most relevant phenomena are modeled. A one-way coupling was deemed suitable and some of the boundary conditions were calibrated using data from related systems.

Code verification (1) The codes of both the FE program and the simulation model were checked by unit and regression tests. Additionally, software quality assurance methods were continuously applied.

Solution verification (1) The input and output was only verified by the analysts, but both at an industrial partner and at the research facility. A quantitative assessment of numerical effects on the SRQ of interest, i. e. form deviation, suggested a justifiable magnitude.

Model validation (2) Quantitative model validation was performed for both SRQs of interest and experimental uncertainties were characterized for two workpieces at differing levels of statistical power. For the primary SRQ, i. e. form deviation, comparative studies at the industrial partner were performed. The results for the residual stress distributions were published and properly peer reviewed.

UQ and SA (1) Aleatory and epistemic uncertainties were segregated and separately propagated for the primary SRQ. However, only limited data for their characterization was available, necessitating estimates for most of the factors. Two different methods of SA, qualitative and quantitative, were applied. However, no stringently conducted evaluation of numerical effects on the outcome of the corresponding studies was performed.

In summary, the aspired level of maturity of 1 for a simulation model that is intended to support workpiece design, was reached in all aspects and exceeded in some. Next, the following paragraphs describe how the methods in this thesis may provide additional benefit beyond the presented use cases.

8.3.2 Transferability

While the results of Chapter 5 are connected to LBM and IN718, the methods presented in Chapters 6 and 7 are independent of the model and thus the process and the material. If a mapping of an input geometry to a deformed geometry is available, PD may be applied in the presented fashion and conducting a PBA will increase knowledge about the system.

Naturally, all modeling choices need to be reevaluated when moving to other use cases: for a different material, it is necessary to adapt the material model, i. e. gather new experimental data, include steady state phase changes or switch to a viscoplastic behavior during the build-up phase. BRANNER (2010), e. g., provides corresponding model descriptions for steel. Other processes may require switching the sequential to a two-way coupling of the thermal

and the thermo-mechanical simulation. For new scenarios, uncertainties of both the model and the experiments should, however, be reevaluated as well.

8.3.3 Supply Chain Integration

The added value of the presented methodology can also be investigated with regards to the typical supply chain scenarios that AM is expected to thrive on. Table 8.2 presents seven such scenarios and provides explanations on how the work in this thesis contributes to their viability.

Table 8.2: Relation of pre-deformation to typical supply chain scenarios for AM (scenarios taken from SENVOL LLC *(2017))*

Supply Chain Scenario	Description "Why is AM a viable option?"	Relation to this work
Expensive to manufacture	Workpieces with a high price-per-weight ratio are likely to be suitable candidates for the replacement of conventional with additive manufacturing.	By increasing confidence that the required tolerances can be reached and not require extensive build studies, AM cost effectiveness and the likelihood of companies risking the shift to AM processes is increased.
Long lead times	Long development cycles require confidence and financial cushions until a positive cash flow is reached.	By alleviating the way to FTR-manufacturing, lead times can be further reduced and thus the associated risks better contained.
High inventory costs	Long-term support for spare parts, i. e. stock in general, is one of the seven types of waste as defined by lean management (MCCARTHY and RICH 2015, p. 31). AMPs provide opportunities for on-demand manufacturing, greatly reducing the need for stock-keeping.	If the workpiece in question is already manufactured via AMPs, this thesis may provide suitable approaches to identify drivers of distortion. Additionally, if the part is manufactured conventionally, employing the methodology developed in this thesis may lower the barrier to switch to a suitable AMP and thus profit from the corresponding advantages.
Sole-sourced from suppliers	If critical parts are only available from one source, shifting to an AMP may facilitate qualifying other suppliers, minimizing the supply chain risk.	
Remote locations	The transport of products is another one of the seven types of waste (MCCARTHY and RICH 2015, p. 31). AMPs may allow production on-site.	
High import/export costs		
Improved functionality	With AMPs providing novel design opportunities, e. g. bionic structures, at almost no additional cost, there will be more and more viable business cases as experience with these manufacturing technologies increases.	By increasing the predictability of the process, designers will have a lower barrier to make use of the design freedom offered by AM.

9 Conclusion

9.1 Summary

The success of AM technologies in the production sector is currently hindered by multiple obstacles and issues. One of them is the adherence to strict requirements for form deviations both in terms of absolute magnitude and variability. In order to resolve these issues, this thesis contributes a computational model to predict and manage form deviation in the LBM process as well as an approach to handle the corresponding variability and uncertainty. However, instead of avoiding distortion, it is accepted and compensated for in order to reduce form deviations.

For an unambiguous terminology, Chapter 2 provides definitions for all relevant aspects that are covered in this thesis. Subsequently, in Chapter 3, the methodology of distortion engineering is employed to cluster and evaluate related research efforts concerning form deviations and distortion in AM. Additionally, previous works concerned with the simulation of LBM as well as the assessment of predictive capability are discussed. The intended added value, formulated in Chapter 4, is presented in the following three chapters.

First, driven by model identification experiments, an FE model for the prediction of form deviations in LBM was developed. A new phenomenological heat source was employed that greatly reduces the dependency of the SRQ magnitude on the number of summarized layers in the model. In order to increase the usability of the simulation result for pre-deformation with a higher form accuracy of the computational mesh, a new CAD model based meshing strategy without the need for planar inter-layer interfaces was developed. Additionally, a viscoplastic model for the post-process of stress relief annealing was derived from creep measurements. Due to microstructure alterations, no standard creep model could be fitted to a suitable level of congruency, necessitating the use of a regression model. The overall simulation model was then validated against the form deviation of two workpieces across the process chain, as well as the residual stress distribution of a simple cuboid geometry.

Second, the deterministic prediction of the simulation model was contrasted to the results of the preliminary experiments, exhibiting a non-negligible magnitude of manufacturing variability. In order to resolve this mismatch, the method of probability bounds analysis from the domain of uncertainty quantification as well as different sensitivity analysis methods were employed as described in Chapter 6. When respecting the inherent variability in the material parameters and the missing knowledge concerning some of the modeling parameters, the spread of the experimental results can be explained. It is shown that providing the average of all input quantities may not provide an accurate estimate on the average of the SRQ and that, in general, a more detailed analysis is necessary to communicate the actual knowledge about

the system. Additionally, the conducted sensitivity analysis provides a quantitative estimate on how to best reduce the variability in the SRQ.

Lastly, Chapter 7 presents an iterative approach to generate a pre-deformed version of the input design that is expected to not exhibit form deviations that exceed the given tolerance range. Here, necessary boundary conditions for an industrial application are given. Experimental studies showed that the iterative approach is beneficial to further reduce form deviations compared to a simple inversion. In a study with the blade benchmark workpiece, the average maximum form deviation was reduced by up to 72 %.

The findings are subsequently discussed in Chapter 8 in terms of their efficacy (direct effect only), their efficiency (cost-benefit-ratio) and their effectiveness (long-term benefit). While the proposed methodology should always provide technical merit, the economical viability is not given in all cases. Especially for very complex workpieces that are not expected to experience form deviations out of tolerance after manufacturing, the digital pre-process may incur significant cost. However, for workpieces that otherwise require multiple build-up studies, simulation-based pre-deformation is an economically promising opportunity. The proposed strategy will benefit from future refinements of the simulation model and, thus, also be relevant in long-term scenarios. Also, understanding the interplay of variabilities in input and output quantities may be used for process improvements if the model is sufficiently accurate.

9.2 Outlook

The developed simulation model should be expanded to better handle workpieces that exhibit filigree areas. With the current approach of direct CAD meshing, prohibitively high element counts may be generated. Possible strategies comprise homogenization techniques for regular geometries like the commonly used block-like support structures or sub-modeling approaches for irregular ones. Also, meshing accuracy may be more directly related to form deviation requirements for certain areas of a workpiece, by e. g. loosening restrictions in areas that are machined later.

In order to improve the significance of the investigations into uncertainty, a largely increased data base is necessary that can likely only be realized by collaborative efforts. Additionally, the computational effort of simulation models should be further minimized. For a decision making process, it may be more sensible to employ models that only cover the most relevant phenomena of a process and conduct non-deterministic studies than to construct highly sophisticated models that run for weeks at a time. Similarly, meta-models may be able to bridge the gap between the required and the current performance of simulation models for distortion prediction in AM. For their generation, sensitivity analysis can provide valuable hints on which aspects to cover.

Lastly, improving the manageability of form deviation is only one integral part to enable AM to be a viable alternative to commercial manufacturing at large scales and in demanding scenarios. There are many challenges surrounding the creation, the detectability and the effect of defects at the material scale that need to be solved in order to provide confidence in the load bearing capabilities of additively manufactured workpieces. Additionally, it will be necessary for designers to alter their way of thinking and be provided with the right tools to fully make use of the potential of AM.

Bibliography

AFAZOV et al. 2017
Afazov, S.; Denmark, W. A.; Lazaro Toralles, B.; Holloway, A.; Yaghi, A.: Distortion prediction and compensation in selective laser melting. *Additive Manufacturing* 17 (2017) Supplement C, pp. 15–22. ISSN: 2214-8604. DOI: `10.1016/j.addma.2017.07.005`.

AHMADI et al. 2017
Ahmadi, A.; Movahhedy, M. R.; Akbari, J.: Optimization of process parameters for reducing warpage in selected laser sintering of polymer parts. *Additive Manufacturing* (2017). ISSN: 2214-8604. DOI: `10.1016/j.addma.2017.10.018`.

ALBERG 2003
Alberg, H.: Material modelling for simulation of heat treatment. Licentiate dissertation. Luleå, Sweden: Luleå tekniska universitet. 2003.

AMATO et al. 2012
Amato, K. N.; Gaytan, S. M.; Murr, L. E.; Martinez, E.; Shindo, P. W.; Hernandez, J.; Collins, S.; Medina, F.: Microstructures and mechanical behavior of Inconel 718 fabricated by selective laser melting. *Acta Materialia* 60 (2012) 5, pp. 2229–2239. ISSN: 13596454. DOI: `10.1016/j.actamat.2011.12.032`.

AMAZON 2018
Amazon, ed. (2018): *Amazon WorkSpaces Pricing*. URL: `https://aws.amazon.com/de/workspaces/pricing/` (visited on 07/31/2018).

ANG and TANG 2007
Ang, A. H.-S.; Tang, W. H.: *Probability concepts in engineering: Emphasis on applications in civil & environmental engineering*. 2. ed. Hoboken, NJ: Wiley. 2007. ISBN: 978-0-471-72064-5.

ANGUS 1994
Angus, J. E.: The Probability Integral Transform and Related Results. *SIAM Review* 36 (1994) 4, pp. 652–654. ISSN: 0036-1445. DOI: `10.1137/1036146`.

ANTONSSON and FREDRIKSSON 2005
Antonsson, T.; Fredriksson, H.: The effect of cooling rate on the solidification of INCONEL 718. *Metallurgical and Materials Transactions B* 36 (2005) 1, pp. 85–96. ISSN: 1073-5615. DOI: `10.1007/s11663-005-0009-0`.

ARCHER et al. 1997

Archer, G. E. B.; Saltelli, A.; Sobol', I. M.: Sensitivity measures, anova-like techniques and the use of bootstrap. *Journal of Statistical Computation and Simulation* 58 (1997) 2, pp. 99–120. ISSN: 0094-9655. DOI: `10.1080/00949659708811825`.

BAHILL and GISSING 1998

Bahill, A. T.; Gissing, B.: Re-evaluating systems engineering concepts using systems thinking. *IEEE Transactions on Systems, Man and Cybernetics, Part C (Applications and Reviews)* 28 (1998) 4, pp. 516–527. ISSN: 10946977. DOI: `10.1109/5326.725338`.

BAUMERS et al. 2016

Baumers, M.; Dickens, P.; Tuck, C.; Hague, R.: The cost of additive manufacturing: machine productivity, economies of scale and technology-push. *Technological Forecasting and Social Change* 102 (2016) Supplement C, pp. 193–201. ISSN: 0040-1625. DOI: `10.1016/j.techfore.2015.02.015`.

BAYERLEIN et al. 2015

Bayerlein, F.; Zeller, C.; Zaeh, M. F.; Weirather, J.; Wunderer, M.; Seidel, C.: Improving cost effectiveness in additive manufacturing – Increasing dimensional accuracy in laser beam melting by means of a simulation supported process chain. In: *ANSYS Conference & 33. CADFEM Users' Meeting* (Bremen, Germany, June 24–26, 2015). 2015, pp. 1–9.

BAYERLEIN et al. 2016

Bayerlein, F.; Zeller, C.; Wunderer, M.; Weirather, J.; Schmid, M.; Seidel, C.; Zaeh, M. F.; Hessert, R.; Schlick, G.; Uihlein, T.; Hofmann, M.: Validation of modeling assumptions for the buildup simulation of laser beam melting on the basis of the residual stress distribution. In: *Proceedings of the VII European Congress on Computational Methods in Applied Sciences and Engineering* (Crete Island, Greece, June 5–10, 2016). 2016.

BAYERLEIN et al. 2018

Bayerlein, F.; Bodensteiner, F.; Zeller, C.; Hofmann, M.; Zaeh, M. F.: Transient development of residual stresses in laser beam melting – A neutron diffraction study. *Additive Manufacturing* 24 (2018), pp. 587–594. ISSN: 2214-8604. DOI: `10.1016/J.ADDMA.2018.10.024`.

BRANNER 2010

Branner, G.: Modellierung transienter Effekte in der Struktursimulation von Schichtbauverfahren. Dissertation. München: Technical University of Munich. 2010.

BUCHBINDER et al. 2011

Buchbinder, D.; Schilling, G.; Meiners, W.; Pirch, N.; Wissenbach, K.: Untersuchung zur Reduzierung des Verzugs durch Vorwärmung bei der Herstellung von Aluminiumbauteilen mittels SLM. *RTejournal - Forum für Rapid Technologie* 8 (2011). ISSN: 1614-0923.

BUGATTI and SEMERARO 2018

Bugatti, M.; Semeraro, Q.: Limitations of the Inherent Strain Method in Simulating Powder Bed Fusion Processes. *Additive Manufacturing* (2018). ISSN: 2214-8604. DOI: `10.1016/j.addma.2018.05.041`.

CAMPOLONGO et al. 2007

Campolongo, F.; Cariboni, J.; Saltelli, A.: An effective screening design for sensitivity analysis of large models. *Environmental Modelling & Software* 22 (2007) 10, pp. 1509–1518. ISSN: 13648152. DOI: `10.1016/j.envsoft.2006.10.004`.

CASAVOLA et al. 2008

Casavola, C.; Campanelli, S. L.; Pappalettere, C.: Preliminary investigation on distribution of residual stress generated by the selective laser melting process. *The Journal of Strain Analysis for Engineering Design* 44 (2008) 1, pp. 93–104. ISSN: 0309-3247. DOI: `10.1243/03093247JSA464`.

CASTELLANOS et al. 2010

Castellanos, J.; Rieiro, I.; Carsí, M.; Ruano, O. A.: Analysis of Garofalo equation parameters for an ultrahigh carbon steel. *Journal of Materials Science* 45 (2010) 20, pp. 5522–5527. ISSN: 0022-2461. DOI: `10.1007/s10853-010-4610-5`.

CHIUMENTI et al. 2017

Chiumenti, M.; Neiva, E.; Salsi, E.; Cervera, M.; Badia, S.; Moya, J.; Chen, Z.; Lee, C.; Davies, C.: Numerical modelling and experimental validation in Selective Laser Melting. *Additive Manufacturing* 18 (2017) Supplement C, pp. 171–185. ISSN: 2214-8604. DOI: `10.1016/j.addma.2017.09.002`.

DENLINGER and MICHALERIS 2015

Denlinger, E. R.; Michaleris, P.: Mitigation of distortion in large additive manufacturing parts. *Proceedings of the Institution of Mechanical Engineers, Part B: Journal of Engineering Manufacture* 231 (2015) 6, pp. 983–993. ISSN: 0954-4054. DOI: `10.1177/0954405415578580`.

DENLINGER and MICHALERIS 2016

Denlinger, E. R.; Michaleris, P.: Effect of stress relaxation on distortion in additive manufacturing process modeling. *Additive Manufacturing* 12, Part A (2016), pp. 51–59. ISSN: 2214-8604. DOI: `10.1016/j.addma.2016.06.011`.

DENLINGER et al. 2015

Denlinger, E. R.; Heigel, J. C.; Michaleris, P.; Palmer, T. A.: Effect of inter-layer dwell time on distortion and residual stress in additive manufacturing of titanium and nickel alloys. *Journal of Materials Processing Technology* 215 (2015), pp. 123–131. ISSN: 09240136. DOI: `10.1016/j.jmatprotec.2014.07.030`.

Bibliography

DIN 4760

Gestaltabweichungen, Berlin: Beuth. 1982.

DIN EN 10319-1

Metallische Werkstoffe - Relaxationsversuch unter Zugbeanspruchung: Teil 1: Prüfverfahren für die Anwendung in Prüfmaschinen, Berlin: Beuth. 2003.

DIN EN 10302

Warmfeste Stähle, Nickel- und Cobaltlegierungen, Berlin: Beuth. 2008.

DIN 35224

Schweißen im Luft- und Raumfahrzeugbau - Abnahmeprüfung von pulverbettbasierten Laserstrahlmaschinen zur additiven Fertigung, Berlin: Beuth. 2016.

DIN EN ISO 204

Metallische Werkstoffe – Einachsiger Zeitstandversuch unter Zugbeanspruchung – Prüfverfahren, Berlin: Beuth. 2017.

DHONDT 2005

Dhondt, G.: *The finite element method for three-dimensional thermomechanical applications*. Chichester, UK: Wiley. 2005. ISBN: 9780470857526. DOI: `10.1002/0470021217`.

DoD 5000.59

DoD Modeling and Simulation (M&S) Management, Department of Defense. 2007. URL: `http://www.esd.whs.mil/Portals/54/Documents/DD/issuances/dodd/500059p.pdf`.

DONG et al. 2014

Dong, P.; Song, S.; Zhang, J.: Analysis of residual stress relief mechanisms in post-weld heat treatment. *International Journal of Pressure Vessels and Piping* 122 (2014), pp. 6–14. ISSN: 03080161. DOI: `10.1016/j.ijpvp.2014.06.002`.

DORAN 1981

Doran, G. T.: There's a SMART way to write management's goals and objectives. *Management review* 70 (1981) 11, pp. 35–36.

DUNBAR et al. 2017

Dunbar, A. J.; Denlinger, E. R.; Gouge, M. F.; Simpson, T. W.; Michaleris, P.: Comparisons of laser powder bed fusion additive manufacturing builds through experimental in situ distortion and temperature measurements. *Additive Manufacturing* 15 (2017) Supplement C, pp. 57–65. ISSN: 2214-8604. DOI: `10.1016/j.addma.2017.03.003`.

Efron and Stein 1981

Efron, B.; Stein, C.: The Jackknife Estimate of Variance. *The Annals of Statistics* 9 (1981) 3, pp. 586–596. ISSN: 00905364.

Ekmekci 2007

Ekmekci, B.: Residual stresses and white layer in electric discharge machining (EDM). *Applied Surface Science* 253 (2007) 23, pp. 9234–9240. ISSN: 01694332. DOI: `10.1016/j.apsusc.2007.05.078`.

Farshidianfar et al. 2016

Farshidianfar, M. H.; Khajepour, A.; Gerlich, A. P.: Effect of real-time cooling rate on microstructure in Laser Additive Manufacturing. *Journal of Materials Processing Technology* 231 (2016), pp. 468–478. ISSN: 09240136. DOI: `10.1016/j.jmatprotec.2016.01.017`.

Ferson and Ginzburg 1996

Ferson, S.; Ginzburg, L. R.: Different methods are needed to propagate ignorance and variability. *Reliability Engineering & System Safety* 54 (1996) 2-3, pp. 133–144. ISSN: 09518320. DOI: `10.1016/S0951-8320(96)00071-3`.

Ferson et al. 2004

Ferson, S.; Hajagos, J.; Tucker, W. T.: Probability bounds analysis is a global sensitivity analysis. In: *International Conference on Sensitivity Analysis of Model Output (SAMO)* (Santa Fe, NM, Mar. 8–11, 2004). 2004, pp. 211–220.

Free Software Foundation 2019

Free Software Foundation, ed. (2019): *What is free software?* URL: `https://www.gnu.org/philosophy/free-sw.en.html` (visited on 02/22/2019).

Garofalo 1965

Garofalo, F.: *Fundamentals of creep and creep-rupture in metals: (Creep and creep rupture in metals and alloys, fundamental information for instruction and reference)*. New York: MacMillan. 1965.

Gouge and Michaleris 2017

Gouge, M.; Michaleris, P.: *Thermo-Mechanical Modeling of Additive Manufacturing*. Saint Louis, MO: Elsevier Science. 2017. ISBN: 9780128118207.

Hintze and Nelson 1998

Hintze, J. L.; Nelson, R. D.: Violin Plots: A Box Plot-Density Trace Synergism. *The American Statistician* 52 (1998) 2, pp. 181–184. ISSN: 00031305. DOI: `10.1080/00031305.1998.10480559`.

Bibliography

HOMMA and SALTELLI 1996
Homma, T.; Saltelli, A.: Importance measures in global sensitivity analysis of nonlinear models. *Reliability Engineering & System Safety* 52 (1996) 1, pp. 1–17. ISSN: 09518320. DOI: `10.1016/0951-8320(96)00002-6`.

HU and MAHADEVAN 2017
Hu, Z.; Mahadevan, S.: Uncertainty quantification and management in additive manufacturing: current status, needs, and opportunities. *The International Journal of Advanced Manufacturing Technology* 93 (2017) 5-8, pp. 2855–2874. ISSN: 0268-3768. DOI: `10.1007/s00170-017-0703-5`.

HUANG et al. 2015
Huang, Y.; Leu, M. C.; Mazumder, J.; Donmez, A.: Additive Manufacturing: Current State, Future Potential, Gaps and Needs, and Recommendations. *Journal of Manufacturing Science and Engineering* 137 (2015) 1, p. 014001. ISSN: 1087-1357. DOI: `10.1115/1.4028725`.

HUGHES et al. 2005
Hughes, T.; Cottrell, J. A.; Bazilevs, Y.: Isogeometric analysis: CAD, finite elements, NURBS, exact geometry and mesh refinement. *Computer Methods in Applied Mechanics and Engineering* 194 (2005) 39–41, pp. 4135–4195. ISSN: 0045-7825. DOI: `10.1016/j.cma.2004.10.008`.

HUTCHINGS et al. 2005
Hutchings, M. T.; Withers, P. J.; Holden, T. M.; Lorentzen, T.: *Introduction to the characterization of residual stress by neutron diffraction*. 1. ed. Boca Raton: CRC Press Taylor & Francis Group. 2005. ISBN: 9780415310000. DOI: `10.1201/9780203402818`.

ILLSTON 2016
Patent: 20160271699. 2016. Illston, T.: "Additive Fertigung".

INOUE and ARIMOTO 1997
Inoue, T.; Arimoto, K.: Development and implementation of cae system "hearts" for heat treatment simulation based on metallo-thermo-mechanics. *Journal of Materials Engineering and Performance* 6 (1997) 1, pp. 51–60. ISSN: 1059-9495. DOI: `10.1007/s11665-997-0032-1`.

ISO/IEC Guide 98-3
Guide to the expression of uncertainty in measurement, Geneva, Switzerland: ISO. 2010.

ISO/IEC 25010
Systems and software engineering - System and software Quality requirements and Evaluation (SQuaRE) - System and software quality models, Geneva, Switzerland: ISO. 2011.

ISO 14638
Geometrical product specifications (GPS) – Matrix model, Geneva, Switzerland: ISO. 2015.

IOOSS and LEMAÎTRE 2015
Iooss, B.; Lemaître, P.: A Review on Global Sensitivity Analysis Methods. In: *Uncertainty Management in Simulation-Optimization of Complex Systems*. Vol. 59. Operations Research/Computer Science Interfaces Series. Boston, MA: Springer US. 2015, pp. 101–122. ISBN: 978-1-4899-7546-1. DOI: `10.1007/978-1-4899-7547-8_5`.

IOOSS et al. 2006
Iooss, B.; van Dorpe, F.; Devictor, N.: Response surfaces and sensitivity analyses for an environmental model of dose calculations. *Reliability Engineering & System Safety* 91 (2006) 10-11, pp. 1241–1251. ISSN: 09518320. DOI: `10.1016/j.ress.2005.11.021`.

JANSEN et al. 1994
Jansen, M. J. W.; Rossing, W. A. H.; Daamen, R. A.: Monte Carlo Estimation of Uncertainty Contributions from Several Independent Multivariate Sources. In: *Predictability and Nonlinear Modelling in Natural Sciences and Economics*. Vol. B 11. Dordrecht and Boston: Kluwer Academic Publishers. 1994, pp. 334–343. ISBN: 978-94-010-4416-5. DOI: `10.1007/978-94-011-0962-8_28`.

KELLER 2017
Keller, N.: Verzugsminimierung bei selektiven Laserschmelzverfahren durch Multi-Skalen-Simulation. Dissertation. Bremen: University of Bremen. 2017.

KING et al. 2015
King, W. E.; Anderson, A. T.; Ferencz, R. M.; Hodge, N. E.; Kamath, C.; Khairallah, S. A.; Rubenchik, A. M.: Laser powder bed fusion additive manufacturing of metals; physics, computational, and materials challenges. *Applied Physics Reviews* 2 (2015) 4, p. 041304. DOI: `10.1063/1.4937809`.

KOLARIK et al. 2009
Kolarik, K.; Ganev, N.; Pala, Z.; Barcal, J.; Bakalova, T.; Svanter, M.: Investigation of macroscopic Residual Stresses Distribution after Progressive Machining of Tool Steels. *MM Science Journal* 2009 (2009) 04, pp. 160–162. ISSN: 18031269. DOI: `10.17973/MMSJ.2009_12_20091203`.

KRAUSS and ZAEH 2013
Krauss, H.; Zaeh, M. F.: Multi-target Optimization and Process Window Analysis in Selective Laser Melting of High-performance Parts. In: *International Conference on Production Research ICPR 22 - Conference Proceedings* (Iguassu Falls, Brazil, July 28–Aug. 1, 2013). 2013.

KRAUSS 2016
Krauss, H.: Qualitätssicherung beim Laserstrahlschmelzen durch schichtweise thermografische In-Process-Überwachung. Dissertation. Munich: Technical University of Munich. 2016.

Bibliography

KROL 2019

Krol, T. A.: Beitrag zur simulationsgestützten Steigerung der Bauteilmaßhaltigkeit für laserbasierte Strahlschmelztechnologien. Dissertation. Munich: Technical University of Munich. 2019.

KUCHERENKO et al. 2011

Kucherenko, S.; Feil, B.; Shah, N.; Mauntz, W.: The identification of model effective dimensions using global sensitivity analysis. *Reliability Engineering & System Safety* 96 (2011) 4, pp. 440–449. ISSN: 09518320. DOI: 10.1016/j.ress.2010.11.003.

LILBURNE and TARANTOLA 2009

Lilburne, L.; Tarantola, S.: Sensitivity analysis of spatial models. *International Journal of Geographical Information Science* 23 (2009) 2, pp. 151–168. ISSN: 1365-8816. DOI: 10.1080/13658810802094995.

LIU et al. 2018

Liu, J.; Jalalahmadi, B.; Guo, Y. B.; Sealy, M. P.; Bolander, N.: A review of computational modeling in powder-based additive manufacturing for metallic part qualification. *Rapid Prototyping Journal* 24 (2018) 8, pp. 1245–1264. ISSN: 1355-2546. DOI: 10.1108/RPJ-04-2017-0058.

LÖHE and VÖHRINGER 2002

Löhe, D.; Vöhringer, O.: Stability of Residual Stresses. In: *Handbook of residual stress and deformation of steel*. Ed. by. Materials Park, Ohio: ASM International. 2002, pp. 54–69. ISBN: 0871707292.

LOPEZ et al. 2016

Lopez, F.; Witherell, P.; Lane, B.: Identifying Uncertainty in Laser Powder Bed Fusion Additive Manufacturing Models. *Journal of Mechanical Design* 138 (2016) 11, p. 114502. ISSN: 1050-0472. DOI: 10.1115/1.4034103.

MAY et al. 2013

May, D. L.; Gordon, A. P.; Segletes, D. S.: The Application of the Norton-Bailey Law for Creep Prediction Through Power Law Regression. In: *Proceedings of the ASME Turbo Expo: Turbine Technical Conference and Exposition* (San Antonio, TX, June 3–6, 2013). New York, NY: ASME. 2013, V07AT26A005. ISBN: 978-0-7918-5526-3. DOI: 10.1115/GT2013-96008.

MCCARTHY and RICH 2015

McCarthy, D.; Rich, N.: *Lean TPM: A blueprint for change*. Second edition. Amsterdam: Elsevier Butterworth-Heinemann. 2015. ISBN: 9780081001103.

MEINERS 1999

Meiners, W.: Direktes selektives Laser Sintern einkomponentiger metallischer Werkstoffe. Dissertation. RWTH Aachen. 1999.

MERCELIS and KRUTH 2006

Mercelis, P.; Kruth, J.-P.: Residual stresses in selective laser sintering and selective laser melting. *Rapid Prototyping Journal* 12 (2006) 5, pp. 254–265. ISSN: 1355-2546. DOI: `10.1108/13552540610707013`.

MORRIS 1991

Morris, M. D.: Factorial Sampling Plans for Preliminary Computational Experiments. *Technometrics* 33 (1991) 2, p. 161. ISSN: 00401706. DOI: `10.2307/1269043`.

MOSER 2017

Moser, R. D.: Multi-scale computational modeling of selective laser melting for process improvements. Dissertation. Texas: The University of Texas at Austin. 2017.

MUGWAGWA et al. 2018

Mugwagwa, L.; Dimitrov, D.; Matope, S.; Yadroitsev, I.: Influence of process parameters on residual stress related distortions in selective laser melting. In: *Procedia Manufacturing*. Vol. 21. 2018, pp. 92–99. DOI: `10.1016/j.promfg.2018.02.099`.

MÜLLER et al. 2015

Müller, B.; Witt, G.; Töppel, T.; Hoeren, K. P. J.: Eigenspannungen und Verzüge im Strahlschmelzprozess - Untersuchung der verschiedenen Einflüsse und Maßnahmen zur Reduzierung: Final Report. *Forschungsvereinigung Schweißen und verwandte Verfahren e.V.* (2015) DVS 13.003.

MUNSCH 2013

Munsch, M.: Reduzierung von Eigenspannungen und Verzug in der laseradditiven Fertigung. Dissertation. Göttingen: Hamburg University of Technology. 2013.

NEUGEBAUER et al. 2014

Neugebauer, F.; Keller, N.; Ploshikhin, V.; Feuerhahn, F.; Köhler, H.: Multi Scale FEM Simulation for Distortion Calculation in Additive Manufacturing of Hardening Stainless Steel: 4th International Workshop on Thermal Forming and Welding Distortion. In: *Proceedings of the IWOTE'14: 4th International Workshop on Thermal Forming and Welding Distortion* (Bremen, Germany, Apr. 9–10, 2014). 2014.

NITSCHKE-PAGEL and WOHLFAHRT 2002

Nitschke-Pagel, T.; Wohlfahrt, H.: Residual Stresses in Welded Joints – Sources and Consequences. *Materials Science Forum* 404-407 (2002), pp. 215–226. ISSN: 1662-9752. DOI: `10.4028/www.scientific.net/MSF.404-407.215`.

Bibliography

NORTON 1929
Norton, F. H.: *The creep of steel at high temperatures*. New York: McGraw-Hill. 1929.

OBERKAMPF and ROY 2010
Oberkampf, W. L.; Roy, C. J.: *Verification and validation in scientific computing*. New York: Cambridge University Press. 2010. ISBN: 978-0-511-90875-0.

PAPADAKIS and HAUSER 2017
Papadakis, L.; Hauser, C.: Experimental and computational appraisal of the shape accuracy of a thin-walled virole aero-engine casing manufactured by means of laser metal deposition. *Production Engineering* 11 (2017) 4-5, pp. 389–399. ISSN: 0944-6524. DOI: `10.1007/s11740-017-0746-3`.

PAPADAKIS et al. 2014
Papadakis, L.; Loizou, A.; Risse, J.; Bremen, S.; Schrage, J.: A computational reduction model for appraising structural effects in selective laser melting manufacturing: A methodical reduction proposed for time-efficient finite element analysis of larger components in Selective Laser Melting. *Virtual and Physical Prototyping* 9 (2014) 1, pp. 17–25. ISSN: 1745-2759. DOI: `10.1080/17452759.2013.868005`.

PARIS et al. 2016
Paris, H.; Mokhtarian, H.; Coatanéa, E.; Museau, M.; Ituarte, I. F.: Comparative environmental impacts of additive and subtractive manufacturing technologies. *CIRP Annals* 65 (2016) 1, pp. 29–32. ISSN: 0007-8506. DOI: `10.1016/j.cirp.2016.04.036`.

POPOVICH et al. 2018
Popovich, V. A.; Borisov, E. V.; Heurtebise, V.; Riemslag, T.; Popovich, A. A.; Sufiiarov, V. S.: Creep and Thermomechanical Fatigue of Functionally Graded Inconel 718 Produced by Additive Manufacturing. In: *TMS 2018 147th Annual Meeting & Exhibition Supplemental Proceedings*. Vol. 53. The Minerals, Metals & Materials Series. Cham, Germany: Springer International Publishing. 2018, pp. 85–97. ISBN: 978-3-319-72525-3. DOI: `10.1007/978-3-319-72526-0_9`.

POTTLACHER et al. 2002
Pottlacher, G.; Hosaeus, H.; Kaschnitz, E.; Seifter, A.: Thermophysical properties of solid and liquid Inconel 718 Alloy. *Scandinavian Journal of Metallurgy* 31 (2002) 3, pp. 161–168. ISSN: 0371-0459.

QUENOUILLE 1949
Quenouille, M. H.: Problems in Plane Sampling. *The Annals of Mathematical Statistics* 20 (1949) 3, pp. 355–375. ISSN: 0003-4851. DOI: `10.1214/aoms/1177729989`.

RADAJ 2002

Radaj, D.: Eigenspannungen und Verzug beim Schweißen - Rechen- und Meßverfahren. *Stahlbau* 71 (2002) 7, pp. 542–543. ISSN: 00389145. DOI: `10.1002/stab.200201720`.

RAI et al. 2016

Rai, A.; Markl, M.; Körner, C.: A coupled Cellular Automaton–Lattice Boltzmann model for grain structure simulation during additive manufacturing. *Computational Materials Science* 124 (2016), pp. 37–48. ISSN: 09270256. DOI: `10.1016/j.commatsci.2016.07.005`.

REPPER 2010

Repper, J.: Einfluss mikroskopischer Eigenspannungen auf die makroskopische Eigenspannungsanalyse mittels Neutronenbeugung. Dissertation. Munich: Technical University of Munich. 2010.

REPPER et al. 2012

Repper, J.; Hofmann, M.; Krempaszky, C.; Regener, B.; Berhuber, E.; Petry, W.; Werner, E.: Effect of macroscopic relaxation on residual stress analysis by diffraction methods. *Journal of Applied Physics* 112 (2012) 6, p. 064906. ISSN: 0021-8979. DOI: `10.1063/1.4752877`.

ROACHE 1994

Roache, P. J.: Perspective: A Method for Uniform Reporting of Grid Refinement Studies. *Journal of Fluids Engineering* 116 (1994) 3, p. 405. ISSN: 00982202. DOI: `10.1115/1.2910291`.

RÖSLER et al. 2012

Rösler, J.; Harders, H.; Bäker, M.: *Mechanisches Verhalten der Werkstoffe*. 4th edition. Wiesbaden: Springer. 2012. ISBN: 978-3-8348-2241-3. DOI: `10.1007/978-3-8348-2241-3`.

RUST 2015

Rust, W.: Theory and Numerics of Creep. In: *Non-Linear Finite Element Analysis in Structural Mechanics*. Cham: Springer International Publishing. 2015, pp. 181–208. ISBN: 978-3-319-13379-9. DOI: `10.1007/978-3-319-13380-5_7`.

SALTELLI 2002

Saltelli, A.: Making best use of model evaluations to compute sensitivity indices. *Computer Physics Communications* 145 (2002) 2, pp. 280–297. ISSN: 00104655. DOI: `10.1016/S0010-4655(02)00280-1`.

SALTELLI and ANNONI 2010

Saltelli, A.; Annoni, P.: How to avoid a perfunctory sensitivity analysis. *Environmental Modelling & Software* 25 (2010) 12, pp. 1508–1517. ISSN: 13648152. DOI: `10.1016/j.envsoft.2010.04.012`.

Bibliography

SALTELLI et al. 2002

Saltelli, A.; Tarantola, S.; Campolongo, F.; Ratto, M.: *Sensitivity Analysis in Practice*. Chichester, UK: John Wiley & Sons, Ltd. 2002. ISBN: 0470870931. DOI: `10.1002/0470870958`.

SAND2007-5948

Predictive capability maturity model for computational modeling and simulation, Albuquerque: Sandia National Laboratories. 2007. URL: `https://cfwebprod.sandia.gov/cfdocs/CompResearch/docs/Oberkampf-Pilch-Trucano-SAND2007-5948.pdf`.

SARGENT 2013

Sargent, R. G.: Verification and validation of simulation models. *Journal of Simulation* 7 (2013) 1, pp. 12–24. ISSN: 1747-7786. DOI: `10.1057/jos.2012.20`.

SEIDEL 2016

Seidel, C.: Finite-Elemente-Simulation des Aufbauprozesses beim Laserstrahlschmelzen. Dissertation. Munich: Technical University of Munich. 2016.

SEIDEL et al. 2013

Seidel, C.; Zaeh, M. F.; Weirather, J.; Wunderer, M.; Krol, T. A.; Schilp, J.; Groth, C.; Stroebele, B. S.: Simulation of the laser beam melting process – an approach for an efficient geometry modelling of complex lightweight parts. In: *Proceedings DGM LightMAT 2013*. 2013.

SENVOL LLC 2017

Senvol LLC: *Additive Manufacturing: 7 Supply Chain Scenarios: Understanding the opportunities and benefits in order to qunatify the buseness implications of adapting additive manufacturing*. URL: `http://senvol.com/additive-manufacturing/` (visited on 11/16/2017).

SEYDA et al. 2017

Seyda, V.; Herzog, D.; Emmelmann, C.: Relationship between powder characteristics and part properties in laser beam melting of Ti–6Al–4V, and implications on quality. *Journal of Laser Applications* 29 (2017) 2, p. 022311. ISSN: 1042-346X. DOI: `10.2351/1.4983240`.

SHAPIRO and WILK 1965

Shapiro, S. S.; Wilk, M. B.: An analysis of variance test for normality (complete samples). *Biometrika* 52 (1965) 3-4, pp. 591–611. ISSN: 0006-3444. DOI: `10.1093/biomet/52.3-4.591`.

SHET and DENG 2000

Shet, C.; Deng, X.: Finite element analysis of the orthogonal metal cutting process. *Journal of Materials Processing Technology* 105 (2000) 1-2, pp. 95–109. ISSN: 09240136. DOI: `10.1016/S0924-0136(00)00595-1`.

SHIOMI et al. 2004
Shiomi, M.; Osakada, K.; Nakamura, K.; Yamashita, T.; Abe, F.: Residual Stress within Metallic Model Made by Selective Laser Melting Process. *CIRP Annals* 53 (2004) 1, pp. 195–198. ISSN: 0007-8506. DOI: `10.1016/S0007-8506(07)60677-5`.

SIEWERT et al. 2018
Siewert, M.; Neugebauer, F.; Epp, J.; Ploshikhin, V.: Validation of Mechanical Layer Equivalent Method for simulation of residual stresses in additive manufactured components. *Computers & Mathematics with Applications* (2018). ISSN: 08981221. DOI: `10.1016/j.camwa.2018.08.016`.

SOBOL' 1993
Sobol', I. M.: Sensitivity Estimates for Nonlinear Mathematical Models. *Mathematical Modeling and Computational Experiments* 1 (1993) 4, pp. 407–414.

SOCHALSKI-KOLBUS et al. 2015
Sochalski-Kolbus, L. M.; Payzant, E. A.; Cornwell, P. A.; Watkins, T. R.; Babu, S. S.; Dehoff, R. R.; Lorenz, M.; Ovchinnikova, O.; Duty, C.: Comparison of Residual Stresses in Inconel 718 Simple Parts Made by Electron Beam Melting and Direct Laser Metal Sintering. *Metallurgical and Materials Transactions A* 46 (2015) 3, pp. 1419–1432. ISSN: 1073-5623.

SPECIAL METALS CORPORATION 2018
Special Metals Corporation, ed. (2018): *INCONEL alloy 718*. URL: `http://www.specialmetals.com/assets/smc/documents/inconel_alloy_718.pdf` (visited on 07/24/2018).

SPIERINGS and LEVY 2009
Spierings, A.; Levy, G.: Comparison of density of stainless steel 316L parts produced with Selective Laser Melting using different powder grades. In: *Proceedings of the Solid Freeform Fabrication Symposium* (Austin, TX, Aug. 3–5, 2009). 2009.

STEUER 2018
Steuer, M.: *EOS to offer Amphyon simulation software to its Additive Manufacturing customers*. URL: `http://www.metal-am.com/eos-to-offer-amphyon-simulation-software-to-its-additive-manufacturing-customers/` (visited on 10/03/2019).

SUN et al. 2012
Sun, S.; Fu, G.; Djordjević, S.; Khu, S.-T.: Separating aleatory and epistemic uncertainties: Probabilistic sewer flooding evaluation using probability box. *Journal of Hydrology* 420-421 (2012), pp. 360–372. ISSN: 00221694. DOI: `10.1016/j.jhydrol.2011.12.027`.

Bibliography

TARANTOLA et al. 2006

Tarantola, S.; Nardo, M.; Saisana, M.; Gatelli, D.: A new estimator for sensitivity analysis of model output: An application to the e-business readiness composite indicator. *Reliability Engineering & System Safety* 91 (2006) 10, pp. 1135–1141. ISSN: 09518320. DOI: `10.1016/j.ress.2005.11.048`.

THOMAS 2009

Thomas, D.: The development of design rules for selective laser melting. Dissertation. Cardiff: University of Wales. 2009.

THOMPSON et al. 2016

Thompson, M. K.; Moroni, G.; Vaneker, T.; Fadel, G.; Campbell, R. I.; Gibson, I.; Bernard, A.; Schulz, J.; Graf, P.; Ahuja, B.; Martina, F.: Design for Additive Manufacturing: Trends, opportunities, considerations, and constraints. *CIRP Annals* 65 (2016) 2, pp. 737–760. ISSN: 0007-8506. DOI: `10.1016/j.cirp.2016.05.004`.

TROSCH et al. 2016

Trosch, T.; Strößner, J.; Völkl, R.; Glatzel, U.: Microstructure and mechanical properties of selective laser melted Inconel 718 compared to forging and casting. *Materials Letters* 164 (2016), pp. 428–431. ISSN: 0167577X. DOI: `10.1016/j.matlet.2015.10.136`.

TUKEY 1958

Tukey, J. W.: Bias and confidence in not quite large samples (abstract). *The Annals of Mathematical Statistics* 29 (1958) 2, pp. 614–623. ISSN: 0003-4851. DOI: `10.1214/aoms/1177706647`.

TUKEY 1977

Tukey, J. W.: *Exploratory data analysis*. Addison-Wesley series in behavioral science. Reading, Mass.: Addison-Wesley. 1977. ISBN: 0201076160.

V&V10

Guide for verification and validation in computational solid mechanics, New York: ASME. 2006.

VDI 3405 2.2

Laser beam melting of metallic parts: Material data sheet nickel alloy material number 2.4668, Berlin: Beuth. 2017.

VRANCKEN 2016

Vrancken, B.: Study of Residual Stresses in Selective Laser Melting. Dissertation. KU Leuven, Belgium. 2016.

WANG et al. 2017

Wang, Z.; Denlinger, E.; Michaleris, P.; Stoica, A. D.; Ma, D.; Beese, A. M.: Residual stress mapping in Inconel 625 fabricated through additive manufacturing: Method for neutron diffraction measurements to validate thermomechanical model predictions. *Materials & Design* 113 (2017), pp. 169–177. ISSN: 02641275. DOI: `10.1016/j.matdes.2016.10.003`.

WEBER and LAKOMIEC 2017

Weber, M.-A.; Lakomiec, M.: Additive Fertigung für die industrielle Produktion. *ZWF Zeitschrift für wirtschaftlichen Fabrikbetrieb* 112 (2017) 11, pp. 741–744. ISSN: 0947-0085. DOI: `10.3139/104.111809`.

WEIRATHER et al. 2015

Weirather, J.; Bayerlein, F.; Zeller, C.: Understanding Residual Stress States of Laser Beam Melted Inconel718-Parts: Experimental Report. (unpublished). Heinz Maier-Leibnitz Zentrum. 2015.

WINHOLTZ and KRAWITZ 1996

Winholtz, R. A.; Krawitz, A. D.: The effect of assuming the principal directions in neutron diffraction measurement of stress tensors. *Materials Science and Engineering: A* 205 (1996) 1–2, pp. 257–258. ISSN: 09215093. DOI: `10.1016/0921-5093(95)10040-7`.

WOLBERG 2006

Wolberg, J.: *Data Analysis Using the Method of Least Squares: Extracting the Most Information from Experiments*. Berlin, Heidelberg: Springer. 2006. ISBN: 978-3-540-31720-3. DOI: `10.1007/3-540-31720-1`.

YAGHI et al. 2008

Yaghi, A. H.; Hyde, T. H.; Becker, A. A.; Sun, W.: Finite element simulation of welding and residual stresses in a P91 steel pipe incorporating solid-state phase transformation and post-weld heat treatment. *The Journal of Strain Analysis for Engineering Design* 43 (2008) 5, pp. 275–293. ISSN: 0309-3247. DOI: `10.1243/03093247JSA372`.

ZELLER 2019

Zeller, C.: Adaption of Numerical Methods to the Specific Requirements of the Thermal Simulation in Laser Beam Melting. Dissertation. Munich: Technical University of Munich. 2019.

ZENG et al. 2013

Zeng, K.; Patil, N.; Gu, H.; Gong, H.; Pal, D.; Starr, T.; Stucker, B.: Layer by Layer Validation of Geometrical Accuracy in Additive Manufacturing processes. In: *Proceedings of the Solid Freeform Fabrication Symposium* (Austin, TX, Aug. 12–14, 2013). 2013, pp. 76–87.

D. ZHANG et al. 2015
Zhang, D.; Niu, W.; Cao, X.; Liu, Z.: Effect of standard heat treatment on the microstructure and mechanical properties of selective laser melting manufactured Inconel 718 superalloy. *Materials Science and Engineering: A* 644 (2015), pp. 32–40. ISSN: 09215093. DOI: `10.1016/j.msea.2015.06.021`.

L. ZHANG et al. 2018
Zhang, L.; Zhang, S.; Zhu, H.; Hu, Z.; Wang, G.; Zeng, X.: Horizontal dimensional accuracy prediction of selective laser melting. *Materials & Design* 160 (2018), pp. 9–20. ISSN: 02641275. DOI: `10.1016/j.matdes.2018.08.059`.

ZOCH 2012
Zoch, H.-W.: Distortion engineering – interim results after one decade research within the Collaborative Research Center: Distortion Engineering – ein Zwischenbericht nach einem Jahrzehnt des Sonderforschungsbereichs. *Materialwissenschaft und Werkstofftechnik* 43 (2012) 1-2, pp. 9–15. ISSN: 1521-4052.

Appendix

A.1 Supervised Theses

Multiple student theses were supervised by the author that contributed to the results presented in this document (see Table A.1). The students' work is highly appreciated and their contribution to this thesis is acknowledged.

Table A.1: *List of student theses that were supervised and contributed to the work in this dissertation*

Author	Title	Type[a]
Bante, Lukas	Quality Control for a Simulation Model through Continuous Verification and Validation	BT
Bewerunge, Moritz	Prozessfähigkeit von Laserstrahlschmelzanlagen im Bezug auf die Bauteilform	BT
Bodensteiner, Fabian	Analysis of residual stresses and their transient development in selective laser melting by neutron diffraction	TP
Brunhuber, Fabian	Fertigung und Vermessung von Validierungsbauteilen für die Simulation des Laserstrahlschmelzens	BT
Lindenmeyer, Adrian	Unsicherheitsbewertung und Sensitivitätsanalyse eines Simulationsmodells für das Laserstrahlschmelzen	TP
Looschen, Christian	Versionsbasierte, automatisierte Validierung und Verifizierung eines Simulationsmodells	BT
Roth, Lukas	Simulative Vordeformation für das Laserstrahlschmelzen - Modellkalibrierung und -validierung	TP
Scherer, Dominik	Prozessstabilitäts- und Maßhaltigkeitsuntersuchungen im Hinblick auf das additive Verfahren des Laserstrahlschmelzens zur Fertigung von Raumfahrtkomponenten	MT
Viermetz, Fabian	Modellierung des Spannungsarmglühens von laserstrahlgeschmolzenen IN718 Bauteilen	TP
Vogel, Daniel	Design, Manufacturing and Measuring of Benchmark Parts for the Validation of a Build-up Simulation for Laser Beam Melting	TP
Yan, Aobo	Verzugsbeherrschung beim Laserstrahlschmelzen durch simulative Vordeformation	MT

[a] BT = Bachelor's Thesis, TP = Term Paper, MT = Master's Thesis

A.2 Pre-Scaling

This section provides the derivation of the equations to determine the three individual components for the pre-scaling vector $\underline{\psi}$. In order to increase readability, all symbols in the following equations are denoted without the respective subscript of the coordinate direction. The least squares problem is given by minimizing the objective function Obj that is defined as the sum of the squared residuals Res_j, assuming that there is no error in the quantity (WOLBERG 2006,

p. 34). In the context of this thesis, these residuals are defined as the mismatch between the pre-deformed geometry and the pre-scaled coordinate for all points:

$$\min Obj = \min \sum_j Res_j{}^2 = \min \sum_j \left(x_{opt} - \Psi(x_{target}, \underline{\psi}) \right)^2 \tag{A.1}$$

$$= \min \sum_j \left(x_{opt} - \underline{\psi} \times x_{target} \right)^2 . \tag{A.2}$$

According to WOLBERG (2006, p. 45) the solution is obtained by setting the derivative of the objective function to zero and solving for the model parameters, i.e. $\underline{\psi}$ in this case:

$$\frac{\delta Obj}{\delta \underline{\psi}} \overset{!}{=} 0 \tag{A.3}$$

$$-2 \times \sum_j Res_j \times \frac{\delta \Psi}{\delta \underline{\psi}} \overset{!}{=} 0 \tag{A.4}$$

$$\sum_j \left(Res_j \times x_{target,j} \right) = 0 \tag{A.5}$$

$$\sum_j x_{opt,j} x_{target,j} - \psi \times \sum_j x_{opt,j}{}^2 = 0 \tag{A.6}$$

$$\psi = \frac{\sum_j x_{opt,j} \times x_{target,j}}{\sum_j x_{opt,j}^2} \tag{A.7}$$

This algorithm is applied to all coordinate directions independently, with one exception: As the z-coordinates of the nodes coinciding with both build plate and workpiece are not used for the pre-deformation, the corresponding nodes are skipped for the calculation of suitable factors.

A.3 Convection on the Side of the Workpiece

In order to simplify the heat transfer through the powder surrounding the workpiece, the complex mix of convection, conduction and radiation was simplified to a purely convective phenomenon. The estimate for the $h_{WP,side}$ was determined as the ratio of the conductivity of the material and the distance to the reference temperature level, i.e. the convection temperature. For the conductivity of the powder, a thousandth of the respective property of bulk material was assumed. The temperature dependency of λ was respected.

For the heat storage study, the temperature T_{Conv} is 200 °C, the λ of powder was assumed and the distance to the reference temperature (here: the heat storage) was 1 mm, resulting in $h_{WP,side} = 14.1 \times 10^{-3}\,\text{mW}\,\text{mm}^{-2}\,\text{K}^{-1}$.

In contrast, a far more conservative estimate was employed for the UQ study. In order not to underestimate the heat transfer and in consequence prematurely ignoring its effect for

further studies, the conductivity of bulk material was chosen as the frame of reference. In combination with a justifiable minimum distance of the workpieces of $2\,\mathrm{mm}$, a maximum for the $h_{WP,side}$ of $6.4\,\mathrm{mW\,mm^{-2}\,K^{-1}}$ was obtained.

A.4 Predictive Capability Maturity Model

The PCMM is a method that allows for a structured assessment of the maturity of a modeling effort. It provides attributes that characterize different levels of maturity in six relevant dimensions that can be used for a self-assessment. The corresponding information is reprinted in Table A.2 for convenience.

Table A.2: Full definition for the PCMM (adjusted from SAND2007-5948)

Maturity element	Maturity level 0 Low consequence, minimal M&S impact, e. g. scoping studies	Maturity level 1 Moderate consequence, some M&S impact, e. g. design support	Maturity level 2 High consequence, high M&S impact, e. g. qualification support	Maturity level 3 High consequence, decision-making based on M&S, e. g. qualification or certification
Representation and geometric fidelity What features are neglected because of simplifications or stylizations?	• Judgment only • Little or no representational or geometric fidelity for the system and BCs	• Significant simplification or stylization of the system and BCs • Geometry or representation of major components is defined	• Limited simplification or stylization of major components and BCs • Geometry or representation is well defined for major components and some minor components • Some peer review conducted	• Essentially no simplification or stylization of components in the system and BCs • Geometry or representation of all components is at the detail of "as built", e.g., gaps, material interfaces, fasteners • Independent peer review conducted
Physics and material model fidelity How fundamental are the physics and material models and what is the level of model calibration?	• Judgment only • Model forms are either unknown or fully empirical • Few, if any, physics-informed models • No coupling of models	• Some models are physics based and are calibrated using data from related systems • Minimal or ad hoc coupling of models	• Physics-based models for all important processes • Significant calibration needed using separate effects tests (SETs) and integral effects tests (IETs) • One-way coupling of models • Some peer review conducted	• All models are physics based • Minimal need for calibration using SETs and IETs • Sound physical basis for extrapolation and coupling of models • Full, two-way coupling of models • Independent peer review conducted
Code verification Are algorithm deficiencies, software errors, and poor SQE practices corrupting the simulation results?	• Judgment only • Minimal testing of any software elements • Little or no SQE procedures specified or followed	• Code is managed by SQE procedures • Unit and regression testing conducted • Some comparisons made with benchmarks	• Some algorithms are tested to determine the observed order of numerical convergence • Some features & capabilities (F&C) are tested with benchmark solutions • Some peer review conducted	• All important algorithms are tested to determine the observed order of numerical convergence • All important F&Cs are tested with rigorous benchmark solutions • Independent peer review conducted

Appendix

Maturity element	Maturity level 0	Maturity level 1	Maturity level 2	Maturity level 3
Solution verification Are numerical solution errors and human procedural errors corrupting the simulation results?	• Judgment only • Numerical errors have an unknown or large effect on simulation results	• Numerical effects on relevant SRQs are qualitatively estimated • Input/output (I/O) verified only by the analysts	• Numerical effects are quantitatively estimated to be small on some SRQs • I/O independently verified • Some peer review conducted	• Numerical effects are determined to be small on all important SRQs • Important simulations are independently reproduced • Independent peer review conducted
Model validation How carefully is the accuracy of the simulation and experimental results assessed at various tiers in a validation hierarchy?	• Judgment only • Few, if any, comparisons with measurements from similar systems or applications	• Quantitative assessment of accuracy of SRQs not directly relevant to the application of interest • Large or unknown experimental uncertainties	• Quantitative assessment of predictive accuracy for some key SRQs from IETs and SETs • Experimental uncertainties are well characterized for most SETs, but poorly known for IETs • Some peer review conducted	• Quantitative assessment of predictive accuracy for all important SRQs from IETs and SETs at conditions/geometries directly relevant to the application • Experimental uncertainties are well characterized for all IETs and SETs • Independent peer review conducted
Uncertainty quantification and sensitivity analysis How thoroughly are uncertainties and sensitivities characterized and propagated?	• Judgment only • Only deterministic analyses are conducted • Uncertainties and sensitivities are not addressed	• Aleatory and epistemic (A&E) uncertainties propagated, but without distinction • Informal sensitivity studies conducted • Many strong UQ/SA assumptions made	• A&E uncertainties segregated, propagated and identified in SRQs • Quantitative sensitivity analyses conducted for most parameters • Numerical propagation errors are estimated and their effect known • Some strong assumptions made • Some peer review conducted	• A&E uncertainties comprehensively treated and properly interpreted • Comprehensive sensitivity analyses conducted for parameters and models • Numerical propagation errors are demonstrated to be small • No significant UQ/SA assumptions made • Independent peer review conducted

A.5 Used Software

For this thesis, different software packages were used for the production of both the content as well as the documentation. The following list provides information on the respective versions.

- Content
  - SuSe Linux 12 Service Pack 1
  - Python 3.4.7
  - CalculiX CrunchiX 2.14 with custom adjustments
  - PARDISO solver from the Intel Math Kernel Library 11.3.3.210
  - Altair HyperMesh 14.0
- Documentation
  - Paraview 5.5.10
  - Inkscape 0.92
  - Gimp 2.10
  - TikzEdt 0.2.3.0
  - TeXstudio 2.12.0
  - MikTeX x64 2.9
  - $\mathrm{\LaTeX\,2_\varepsilon}$